

Antonio Baldi · Sharlotte L. B. Kramer  
Fabrice Pierron · John Considine · Sven Bossuyt  
Johan Hoefnagels *Editors*

# Residual Stress, Thermomechanics & Infrared Imaging and Inverse Problems, Volume 6

Proceedings of the 2019 Annual Conference on  
Experimental and Applied Mechanics



---

# Conference Proceedings of the Society for Experimental Mechanics Series

*Series Editor*

Kristin B. Zimmerman  
Society for Experimental Mechanics, Inc.  
Bethel, CT, USA

The Conference Proceedings of the Society for Experimental Mechanics Series presents early findings and case studies from a wide range of fundamental and applied work across the broad range of fields that comprise Experimental Mechanics. Series volumes follow the principle tracks or focus topics featured in each of the Society's two annual conferences: IMAC, A Conference and Exposition on Structural Dynamics, and the Society's Annual Conference & Exposition and will address critical areas of interest to researchers and design engineers working in all areas of Structural Dynamics, Solid Mechanics and Materials Research.

More information about this series at <http://www.springer.com/series/8922>

---

Antonio Baldi • Sharlotte L. B. Kramer • Fabrice Pierron  
John Considine • Sven Bossuyt • Johan Hoefnagels  
Editors


# Residual Stress, Thermomechanics & Infrared Imaging and Inverse Problems, Volume 6

Proceedings of the 2019 Annual Conference on Experimental  
and Applied Mechanics

*Editors*

Antonio Baldi  
Department of Mechanical, Chemical  
and Materials Engineering  
University of Cagliari  
Cagliari, Sardinia, Italy

Fabrice Pierron  
University of Southampton  
Southampton, Hampshire, UK

Sven Bossuyt   
Advanced Manufacturing and Materials group  
Aalto University  
Aalto, Finland

Sharlotte L. B. Kramer  
Sandia National Laboratories  
Albuquerque, NM, USA

John Considine  
Forest Products Laboratory  
USDA, Forest Service  
Madison, WI, USA

Johan Hoefnagels  
Eindhoven University of Technology  
Eindhoven, NB, Netherlands

ISSN 2191-5644                      ISSN 2191-5652 (electronic)  
Conference Proceedings of the Society for Experimental Mechanics Series  
ISBN 978-3-030-30097-5              ISBN 978-3-030-30098-2 (eBook)  
<https://doi.org/10.1007/978-3-030-30098-2>

© Society for Experimental Mechanics, Inc. 2020

This work is subject to copyright. All rights are reserved by the Publisher, whether the whole or part of the material is concerned, specifically the rights of translation, reprinting, reuse of illustrations, recitation, broadcasting, reproduction on microfilms or in any other physical way, and transmission or information storage and retrieval, electronic adaptation, computer software, or by similar or dissimilar methodology now known or hereafter developed.

The use of general descriptive names, registered names, trademarks, service marks, etc. in this publication does not imply, even in the absence of a specific statement, that such names are exempt from the relevant protective laws and regulations and therefore free for general use.

The publisher, the authors, and the editors are safe to assume that the advice and information in this book are believed to be true and accurate at the date of publication. Neither the publisher nor the authors or the editors give a warranty, express or implied, with respect to the material contained herein or for any errors or omissions that may have been made. The publisher remains neutral with regard to jurisdictional claims in published maps and institutional affiliations.

This Springer imprint is published by the registered company Springer Nature Switzerland AG  
The registered company address is: Gewerbestrasse 11, 6330 Cham, Switzerland

---

## Preface

*Residual Stress, Thermomechanics & Infrared Imaging and Inverse Problems* represents one of six volumes of technical papers presented at the 2019 SEM Annual Conference and Exposition on Experimental and Applied Mechanics organized by the Society for Experimental Mechanics and held in Reno, NV, June 3–6, 2019. The complete proceedings also include volumes on *Dynamic Behavior of Materials; Challenges in Mechanics of Time-Dependent Materials, Fracture, Fatigue, Failure and Damage Evolution; Advancement of Optical Methods & Digital Image Correlation in Experimental Mechanics; Mechanics of Biological Systems and Materials & Micro- and Nanomechanics; Mechanics of Composite, Hybrid and Multifunctional Materials*.

Each collection presents early findings from experimental and computational investigations on an important area within experimental mechanics; Residual Stress, Thermomechanics and Infrared Imaging, and Inverse Problems being some of these areas.

Residual stresses are self-balanced stress fields induced during most materials processing procedures, for example, welding/joining, casting, thermal conditioning, and forming. Their hidden character often causes them to be underrated or overlooked. However, they profoundly influence structural design and substantially affect strength, fatigue life, and dimensional stability. Thus, they must be taken seriously and included in practical applications.

In recent years, the applications of infrared imaging techniques to the mechanics of materials and structures have grown considerably. The expansion is marked by the increased spatial and temporal resolution of the infrared detectors, faster processing times, much greater temperature resolution, and specific image processing. The improved sensitivity and more reliable temperature calibrations of the devices have meant that more accurate data can be obtained than were previously available.

Advances in inverse identification have been coupled with optical methods that provide surface deformation measurements and volumetric measurements of materials. In particular, inverse methodology was developed to more fully use the dense spatial data provided by optical methods to identify mechanical constitutive parameters of materials. Since its beginnings during the 1980s, creativity in inverse methods has led to applications in a wide range of materials, with many different constitutive relationships, across material heterogeneous interfaces. Complex test fixtures have been implemented to produce the necessary strain fields for identification. Force reconstruction has been developed for high strain rate testing. As developments in optical methods improve for both very large and very small length scales, applications of inverse identification have expanded to include geological and atomistic events. Researchers have used in situ 3D imaging to examine microscale expansion and contraction and used inverse methodologies to quantify constitutive property changes in biological materials.

Cagliari, Italy  
Albuquerque, NM, USA  
Southampton, Hampshire, UK  
Madison, WI, USA  
Aalto, Finland  
Eindhoven, Netherlands

Antonio Baldi  
Charlotte L. B. Kramer  
Fabrice Pierron  
John Considine  
Sven Bossuyt  
Johan Hoefnagels

---

# Contents

<b>1 Regularization Uncertainty in Slitting Residual Stress Measurement</b> .....	1
Mitchell D. Olson, Adrian T. DeWald, and Michael R. Hill	
<b>2 Walkthrough and History of the Virtual Fields Method</b> .....	9
Michel Grédiac	
<b>3 Low-Cost Thermoelastic Stress Analysis</b> .....	15
Melissa Weihrauch, Ceri Middleton, Richard Greene, and Eann Patterson	
<b>4 The Effect of Residual Stress on Aluminum Strength Using Thermoelastic Stress Analysis</b> .....	21
Wei-Cheng Shen, Shiang-Jiun Lin, Yan-Bing Huang, Xue-Lin Ji, and Wei-Yu Zeng	
<b>5 Calibration of Anisotropic Plasticity Models with an Optimized Heterogeneous Test and the Virtual Fields Method</b> .....	25
J. M. P. Martins, S. Thuillier, and A. Andrade-Campos	
<b>6 One-Dimensional Heat Source Reconstruction Applied to Phase Transforming Superelastic Ni-Ti Wire</b> .....	33
Antoine Jury, Xavier Balandraud, Luděk Heller, Eduardo Alarcon, and Miroslav Karlik	
<b>7 Coupled NIRT/3D-DIC for a FEMU Identification of the Thermo-Mechanical Behavior of Zr-4 Claddings Under Simulated Reactivity Initiated Accident</b> .....	41
T. Jailin, N. Tardif, J. Desquines, M. Coret, M.-C. Baietto, T. Breville, P. Chaudet, and V. Georgenthum	
<b>8 Residual Stresses at Critical Locations in Additively-Manufactured Components</b> .....	49
Christopher R. D’Elia, Michael R. Hill, Michael E. Stender, and Christopher W. San Marchi	
<b>9 Identification of Constitutive Parameters Governing the Hyperelastic Response of Rubber by Using Full-Field Measurement and the Virtual Fields Method</b> .....	59
A. Tayeb, J.-B. Le Cam, M. Grédiac, E. Toussaint, F. Canévet, E. Robin, and X. Balandraud	
<b>10 Intermethod Comparison and Evaluation of Near Surface Residual Stress in Aluminum Parts Subject to Various Milling Parameters</b> .....	67
Christopher R. Chighizola, Christopher R. D’Elia, and Michael R. Hill	
<b>11 Inversion of Residual Stresses in Silicon Wafer from Surface Deflection Measurements</b> .....	75
Yuri Obata and Satoru Yoneyama	
<b>12 Evaluating the Coefficient of Thermal Expansion of Electronic Board Using the Virtual Fields Method</b> .....	83
Yohei Kanai, Shuichi Arikawa, Satoru Yoneyama, and Yasuhisa Fujimoto	
<b>13 Identification of Constitutive Parameters from Full Thermal and Kinematic Fields: Application to Hyperelasticity</b> .....	89
S. Charlès and J.-B. Le Cam	
<b>14 Calorific Analysis of a Granular System Made in Shape Memory Alloy</b> .....	95
Tanapon Yachai, Rym Boufayed, Pawarut Jongchansitto, Itthichai Preechawuttipong, and Xavier Balandraud	

<b>15</b>	<b>Dynamic VFM to Identify Viscoplastic Parameters. Analysis of Impact Tests on Titanium Alloy</b> . . . . .	<b>101</b>
	Thomas Fourest, Pascal Bouda, Bertrand Langrand, Delphine Notta-Cuvier, Éric Markiewicz, Lloyd Fletcher, and Fabrice Pierron	
<b>16</b>	<b>Test Design for Identification from Full-Field Measurements: A Concise Review</b> . . . . .	<b>105</b>
	Fabrice Pierron	
<b>17</b>	<b>Stress Determination for Granular Materials Using TSA: An Inverse Approach</b> . . . . .	<b>111</b>
	Mohammad Yousefi, Xavier Balandraud, and Wael A. Samad	
<b>18</b>	<b>Evaluation of Fatigue Crack Growth Behavior and Effect of Repair Work Based on Thermoelastic Stress Analysis for Steel Bridge Members</b> . . . . .	<b>119</b>
	Takahide Sakagami, Daiki Shiozawa, Yuki Terauchi, Noriyasu Arima, Yoshiaki Mizokami, and Masahiro Hayashi	
<b>19</b>	<b>Analysis of Deformations in Crush Tests of Lithium Ion Battery Cells</b> . . . . .	<b>123</b>
	Marco Sasso, Golam Newaz, Marco Rossi, Attilio Lattanzi, and Sanket Mundhe	
<b>20</b>	<b>In-situ Thermal Monitoring of Printed Components During Rapid Prototyping by Fused Deposition Modeling</b> . . . . .	<b>131</b>
	K. Pooladvand, A. D. Salerni, and C. Furlong	
<b>21</b>	<b>Development of an Inverse Identification Method for Identifying Constitutive Parameters by Metaheuristic Optimization Algorithm: Application to Hyperelastic Materials</b> . . . . .	<b>141</b>
	G. Bastos, A. Tayeb, N. Di Cesare, J.-B. Le Cam, and E. Robin	
<b>22</b>	<b>MIMO Input Derivations, Optimizing Input Force Against Output Accuracy</b> . . . . .	<b>147</b>
	Arup Maji	
<b>23</b>	<b>Evaluation of Sensitivity-Based Virtual Fields for Non-Linear Parameter Identification Including DIC Filtering Effects</b> . . . . .	<b>153</b>
	Pascal Lava, Jevan Furmanski, Alexander Marek, Francis M. Davis, and Fabrice Pierron	
<b>24</b>	<b>Identification of Inhomogeneous Plastic Constitutive Models of Friction Stir Welded Aluminum Alloy Sheets Using Virtual Fields Method</b> . . . . .	<b>157</b>
	Chanyang Kim, Jin-Hwan Kim, and Myoung-Gyu Lee	
<b>25</b>	<b>Accuracy Improvement of Thermoelastic Stress and Dissipation Energy Measurement by Motion Compensation with Optical-Infrared Synchronous Measurement</b> . . . . .	<b>163</b>
	Yuji Uchid, Daiki Shiozawa, Mitsuhiro Hori, Kazuki Kobayashi, and Takahide Sakagami	





# Chapter 1

## Regularization Uncertainty in Slitting Residual Stress Measurement

Mitchell D. Olson, Adrian T. DeWald, and Michael R. Hill

**Abstract** This paper describes the development of an uncertainty estimate for slitting residual stress measurement. The uncertainty estimate includes a newly developed uncertainty estimate related to the smoothing used in the stress calculation procedure called the regularization uncertainty. This work describes the approach to define the regularization uncertainty, shows the usefulness of the uncertainty estimate in a numerical experiment. The uncertainty estimate is shown to meet an acceptance criterion that compares the calculated (measured) stress  $\pm$  its uncertainty estimate to the true value for the numerical experiment. This work shows the regularization uncertainty estimate to be a necessary contributor to the uncertainty in slitting and additionally the uncertainty estimate developed here reasonably predicts the uncertainty present in slitting method measurements.

**Keywords** Uncertainty · Slitting method · Crack compliance method · Residual stress · Integral method · Regularization · Repeatability · Precision

### Introduction

Slitting [1], hole-drilling [2], and ring-coring [3] are all established residual stress measurement techniques that determine a residual stress versus depth profile using measurements of deformation (typically strain at a given location) caused by cutting-induced release of residual stress. Measured deformation versus depth data are used to calculate a residual stress versus depth profile, most commonly using the *integral method* [4–7], which uses a numerical inverse. In a typical residual stress calculation, a regularization parameter is used to control smoothing of the deformation data that is useful in mitigating the amplification of measurement uncertainty in the computed residual stress versus depth profile. Because the appropriate value of the regularization parameter is unknown to the experimenter, and the value assigned significantly affects the residual stress computed, there is a need to quantify the uncertainty associated with the regularization parameter.

The objective of this work is to develop an improved residual stress uncertainty estimator for the slitting method by incorporating uncertainty associated with the regularization parameter. Typical uncertainty estimates for slitting are inadequate because they ignore this type of error, as noted recently by Prime [8]. A numerical experiment (with a known residual stress state) is performed to determine the relationship between measurement error and the selection of the regularization parameter. The numerical experiment guides the development of the regularization uncertainty estimate and provides some context to judge its usefulness.

---

Submitted for presentation at SEM 2019 Annual Conference and Exposition on Experimental and Applied Mechanics, Reno, NV, June 3–6, 2019.

---

M. D. Olson (✉) · A. T. DeWald  
Hill Engineering, LLC, Rancho Cordova, CA, USA  
e-mail: [mrhill@ucdavis.edu](mailto:mrhill@ucdavis.edu)

M. R. Hill  
Department of Mechanical and Aerospace Engineering, University of California, Davis, CA, USA

## Methods

### Slitting Method Overview

A useful summary of the theoretical background for the stress calculations performed in a slitting method residual stress measurement is given in [7]. To fix ideas, consider a slitting experiment in a rectangular plate of length  $L$ , width  $W$ , and out of plane thickness  $B$ , as shown in Fig. 1.1. The residual stress to be evaluated is a profile of the residual stress component acting along the length of the plate as a function of depth,  $\sigma_{xx}(y)$ . The slitting measurement consists of cutting a slit into the test specimen in small increments of depth at the specimen mid-length,  $x = L/2$ , in Fig. 1.1. At each increment of cut depth  $h_i$ , the initial residual stresses redistribute and cause deformation that is recorded after each cut depth increment, often using a strain gage located at the back face of the slitting measurement plane (e.g., centered at  $(x, y) = (L/2, W)$ ). The strain versus slit depth data are used to calculate residual stress.

The uncertainty in the calculated residual stress due to the uncertainty in the measured strain data has previously been established by Prime and Hill [9] for both Legendre polynomials as well as unit pulse basis functions and is not described here for brevity. The work here proposes an improved slitting method uncertainty estimator that adds an additional term to account for uncertainty associated with the selection of the regularization parameter, called the *regularization uncertainty*. With the addition of regularization uncertainty, the total uncertainty is taken as the root of the sum of squares (RSS) of the two uncertainty sources

$$U_{\sigma, \text{tot}}^2 = U_{\sigma, \varepsilon}^2 + U_{\sigma, \text{reg}}^2. \quad (1.1)$$

where  $U_{\sigma, \text{total}}$  is a vector of total uncertainty,  $U_{\sigma, \varepsilon}$  is a vector of uncertainty in stress resulting from the uncertainty in the measured strains,  $U_{\sigma, \text{reg}}$  is a vector of uncertainty in stress resulting from the choice of the regularization.

For a specific value of the regularization parameter,  $\alpha = \hat{\alpha}$ , the regularization uncertainty is established by assessing a set of residual stress versus depth results computed using different values of  $\alpha$  near  $\hat{\alpha}$  (i.e., different amounts of regularization), which defines the sensitivity of the computed residual stress to  $\alpha$ . Each member of the set of residual stress results is computed for a range of  $\alpha$  called  $\alpha_{\text{subset}}$ . The range  $\alpha_{\text{subset}}$  is defined by two key characteristics, the number of values that it contains,  $M$ , and the range of  $\alpha$  that it spans. The present work uses a logarithmically spaced set of  $M = 60$  values of  $\alpha$  spanning a range  $\alpha_{\text{subset}} = [\hat{\alpha} \pm R]$  where  $R = 1.5$ . A vector of regularization uncertainty versus depth,  $U_{\sigma, \text{reg}}$ , is then defined as the standard deviation of the set of residual stress values at each depth computed for the different values of  $\alpha$  in  $\alpha_{\text{subset}}$

$$U_{\sigma, \text{reg}}(\hat{\alpha}) = \sqrt{\frac{1}{M-1} \sum_{i=1}^M [\sigma_i - \bar{\sigma}]^2} \quad (1.2)$$

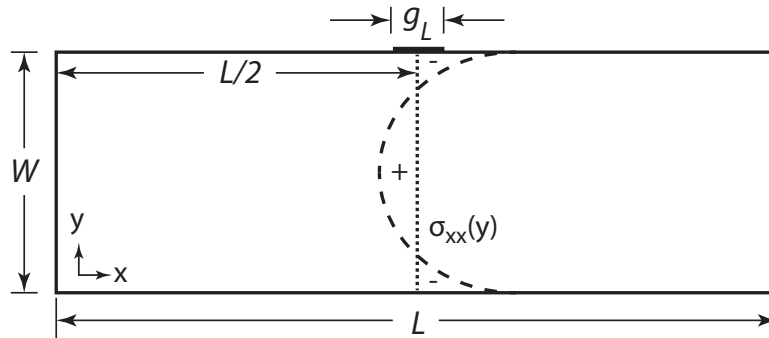


**Fig. 1.1** Diagram of a typical slitting measurement. The measurement plane is at  $x = L/2$  and incrementally cuts the sample from  $y = 0$  to  $W$  to measure  $\sigma_{xx}(L/2, y)$ . The strain gage has a length of  $g_L$  and is affixed to the back face of the specimen at  $(x, y) = (L/2, W)$ .  $B$  is the out of plane thickness

where the vectors  $\sigma_i$  reflect the stresses computed for the range  $\alpha_{\text{subset}}$  and  $\bar{\sigma}$  is the average residual stress versus depth vector computed for the range  $\alpha_{\text{subset}}$  (the bracketed terms on the right side of Eq. (1.2) are vectors, and the square and square root operations are performed element-by-element).

### Slitting Numerical Experiment

To determine whether the regularization uncertainty as defined above was a useful predictor of regularization error, a numerical experiment was performed. The numerical experiment consisted of three steps. In the first step, a residual stress distribution (initialized residual stress) was chosen and introduced as an initial condition in an elastic finite element stress analysis of the plate shown in Fig. 1.1, and then strain versus slit depth data were extracted from the model. This defined the numerical experiment strain. The initialized residual stress was a parabolic shape similar to the residual stress profile that might be achieved from quenching [10], defined using a second order Legendre polynomial.

$$\sigma_{xx}(y) = 100 \left[ 3(2y/W - 1)^2 - 1 \right] / 2 \text{ MPa} \quad (1.3)$$

The stress analysis used commercial software [11] and had the geometry shown in Fig. 1.1 with  $L = 3W$  and a strain gage of size  $g_L = 0.01W$ . The simulated slit was at  $x = L/2$  and had a slit width of  $0.001W$ . Elements were removed from the mesh to simulate cut depths from  $h_l = 0.02W$  to  $h_{49} = 0.98W$  in cut depth increments of  $0.02W$ . The model used a refined, biased mesh where the node spacing was  $0.0033W$  at the cut plane and increased to  $0.01W$  at  $x = 0$  and  $x = L$  with a total number of elements of 115,600. Each element was a two-dimensional, plane strain quadrilateral with biquadratic displacement interpolation. The elastic material properties were  $E = 70,000 \text{ GPa}$ , and  $\nu = 0.3$ . The computed initial residual stress (at zero slit depth) is shown in Fig. 1.2a, and strain as a function of slit depth is shown in Fig. 1.2b.

The second step of the numerical experiment determined the compliance matrix. The stress analysis used to generate the compliance matrix used the same approach and model as was used for the first step, but with constant stress (unit pulses) applied over each cut depth increment and for each cut depth (instead of the initialized residual stress distribution at each cut depth).

In the third step of the numerical experiment, noise was added to the numerical experiment strain and residual stress and uncertainties were calculated for a range of  $\alpha$  values. The added noise was normally distributed with a magnitude of  $1 \mu\epsilon$  (Fig. 1.3). The strain precision was set to  $e = 0.5 \mu\epsilon$ . Since the numerical experiment used a known residual stress, the error arising from the added noise could be directly determined and provides a useful benchmark to assess the proposed uncertainty estimator.

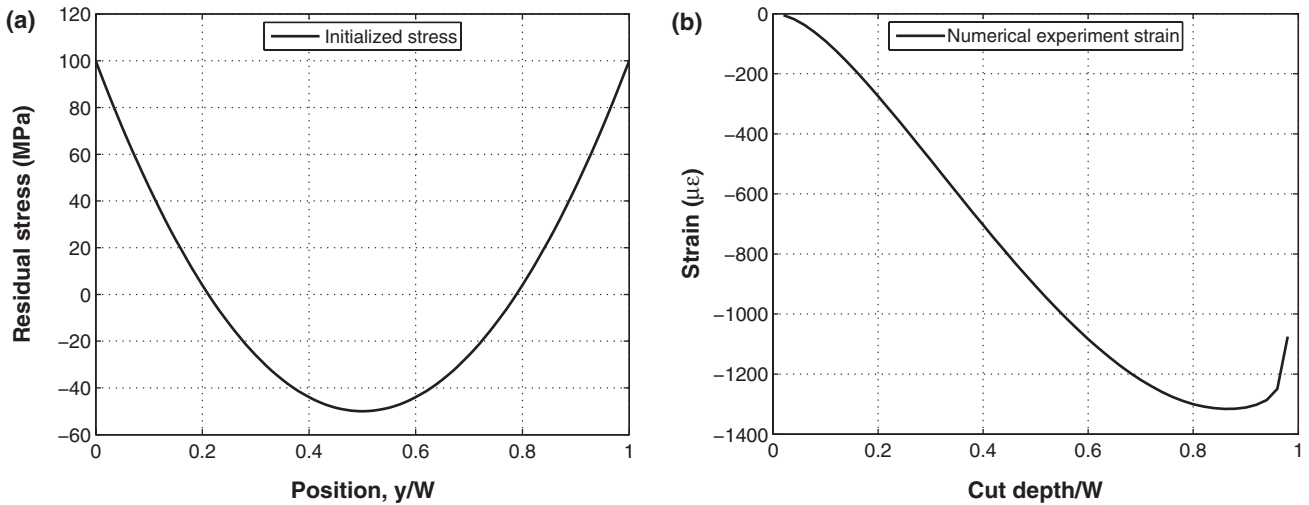
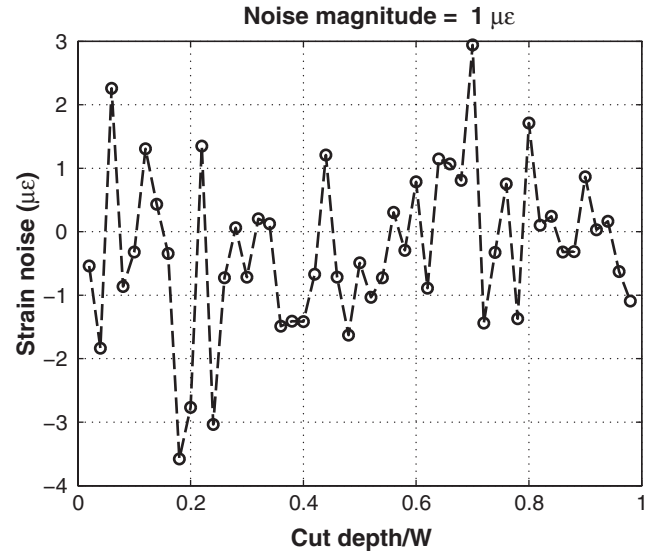


Fig. 1.2 Data for the numerical experiment: (a) initialized residual stress and (b) numerical experiment strain

**Fig. 1.3** Data for the numerical experiment: noise added to the numerical experiment strain



## Results

### Numerical Experiment

The calculated residual stress from the numerical experiment with various levels of regularization and the associated misfits can be seen in Fig. 1.4. The calculated residual stresses (Fig. 1.4a) show that very low regularization ( $\alpha = -15$ ) results in residual stress with large fluctuations that arise from the added noise. Use of more positive values of  $\alpha$  are effective in mitigating the effect of the added noise and provide better approximation of the initialized residual stress. However, more positive  $\alpha$  increases the misfit in strain (Fig. 1.4b), and when high regularization is chosen the large misfit indicates the calculated residual stress profile is overly smoothed. The strain misfit for the chosen value of  $\alpha$  closely resembles the added noise.

The estimated measurement uncertainties from the numerical experiment with various levels of regularization are shown in Fig. 1.5. The regularization uncertainty  $U_{\sigma, \text{reg}}$  (Fig. 1.5a) is low (nearly zero) for a low  $\alpha$  value, moderate for the chosen  $\alpha$  value (peak uncertainties around 2 MPa), and large for a high  $\alpha$  value (peak uncertainties around 6 MPa). The low  $U_{\sigma, \text{reg}}$  for low  $\alpha$  occurs because the calculated residual stress is relatively insensitive to values of  $\alpha$  within  $\alpha_{\text{subset}}$ . The uncertainty in stress due to strain uncertainty  $U_{\sigma, \epsilon}$  (Fig. 1.5b) is high for a low  $\alpha$  value (peak uncertainties around 19 MPa). This occurs because the calculated residual stress is sensitive to noise without regularization. For the chosen or high values of  $\alpha$ ,  $U_{\sigma, \epsilon}$  is low (peak uncertainties around 1 MPa). The total uncertainty in residual stress  $U_{\sigma, \text{tot}}$  (Fig. 1.5c) follows  $U_{\sigma, \epsilon}$  for low  $\alpha$  value, and  $U_{\sigma, \text{reg}}$  for the chosen and high  $\alpha$  values.

The maximum and RMS values of  $U_{\sigma, \epsilon}$ ,  $U_{\sigma, \text{reg}}$  and  $U_{\sigma, \text{tot}}$  are shown as functions of  $\alpha$  for the numerical experiment in Fig. 1.6a. The maximum and RMS values of uncertainty each follow similar trends.  $U_{\sigma, \text{reg}}$  is low for highly negative  $\alpha$ , increasing to a maximum, decreasing to a local minimum, and then increasing again.  $U_{\sigma, \epsilon}$  is constant for highly negative  $\alpha$  values, decreasing to a local minimum, and then increasing again.  $U_{\sigma, \text{tot}}$  follows the uncertainty due to strain uncertainty,  $U_{\sigma, \epsilon}$ , for highly negative  $\alpha$  values and follows the regularization uncertainty for the most positive  $\alpha$  values.

The maximum and RMS error in stress for the numerical experiment is shown in Fig. 1.6b (solid lines), where error at each depth is the calculated residual stress minus the initialized residual stress. The error is large and constant for highly negative  $\alpha$ , decreases with increasing  $\alpha$  to a minimum and then increases. Figure 1.6b shows that  $U_{\sigma, \text{tot}}$  follows the trend of the error and is larger than the error near the minimum uncertainty. Furthermore, the minimums of uncertainty and error occur at similar  $\alpha$  values. This shows  $U_{\sigma, \text{tot}}$  is a useful predictor of error.

The calculated residual stress at the chosen  $\alpha$  value is shown in Fig. 1.7a for the numerical experiment. The calculated residual stress matches well the initialized residual stress. The total uncertainty provides a good approximation of the error overall, as shown in Fig. 1.7b, with both having a maximum value at the initial cut depth (1.7 MPa error and 2.0 MPa total uncertainty) and uncertainty and error falling between 1.5 and 0.25 MPa at larger cut depths. Regularization and strain uncertainties are both significant contributors to the total uncertainty.

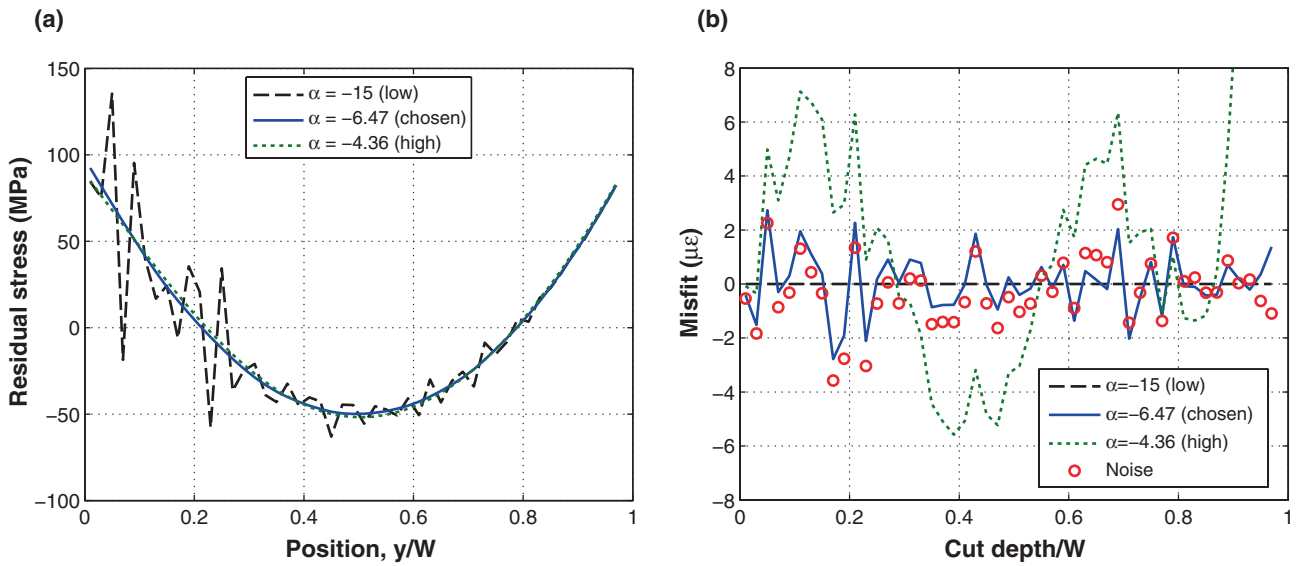


Fig. 1.4 Results for the numerical experiment with various choices of  $\alpha$ : (a) calculated residual stress and (b) resulting misfit and applied noise

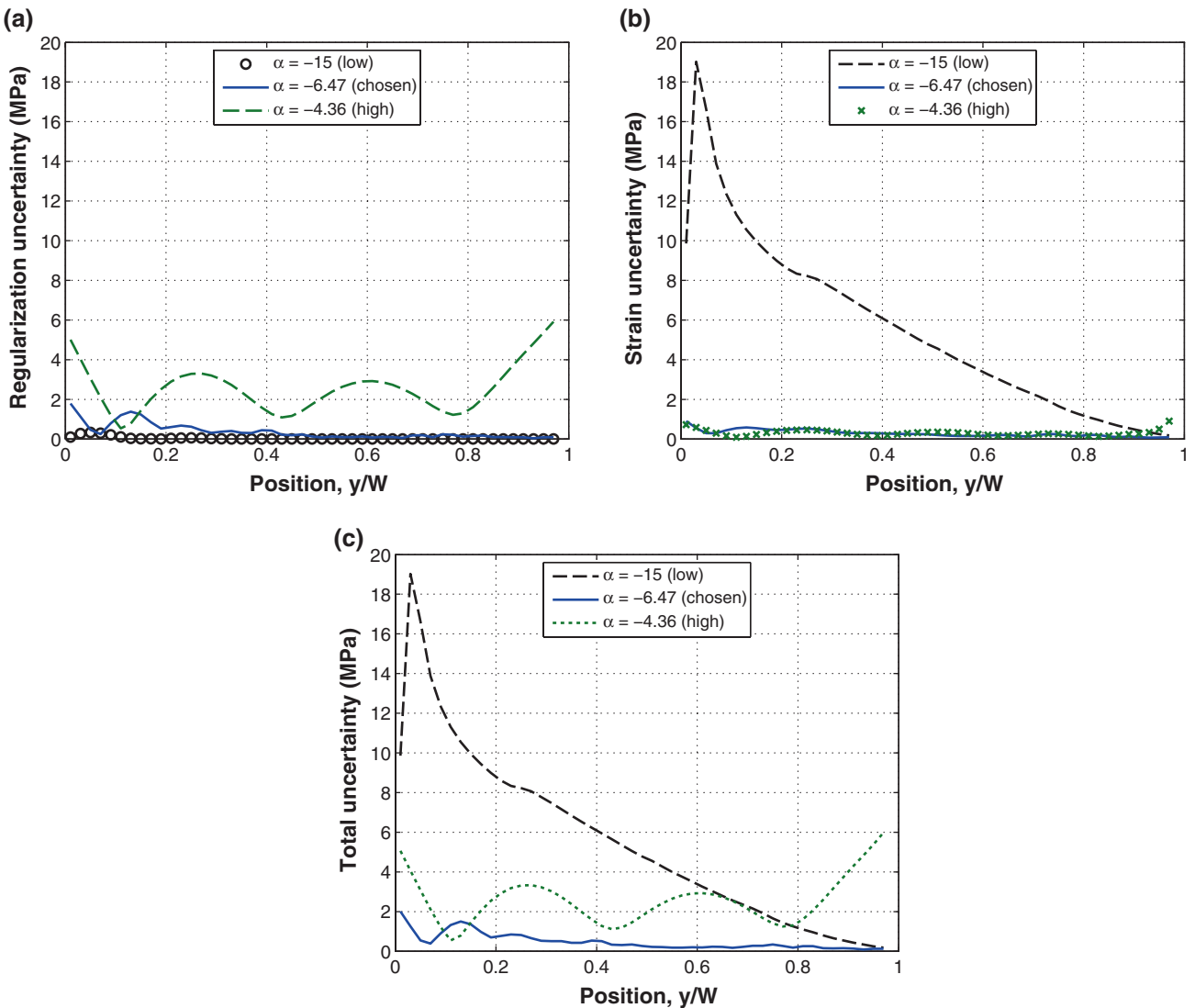
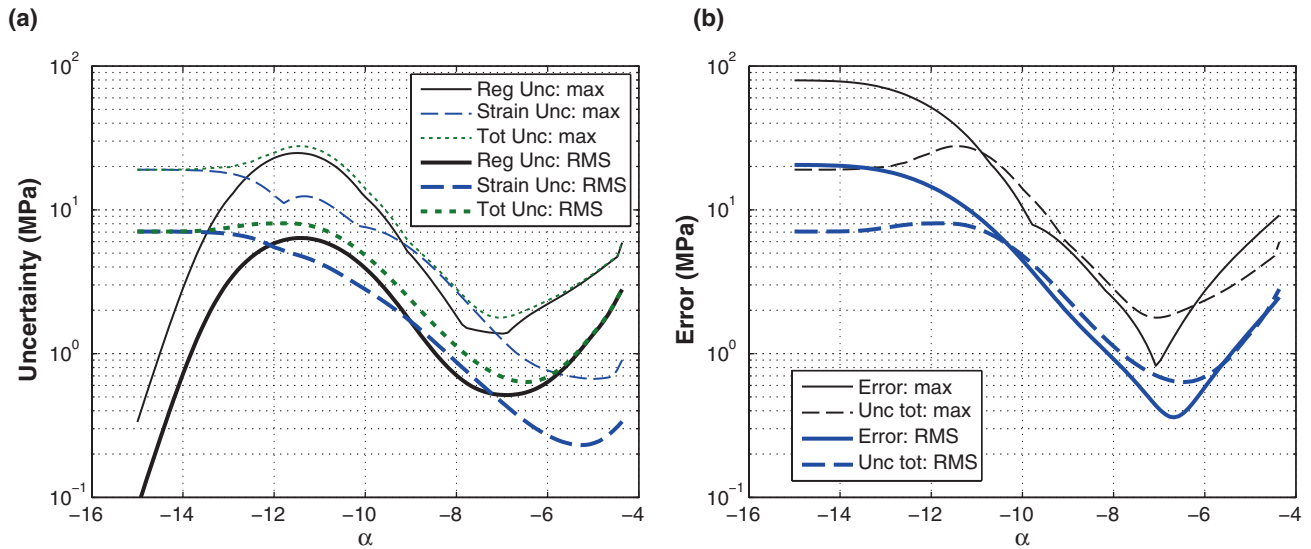
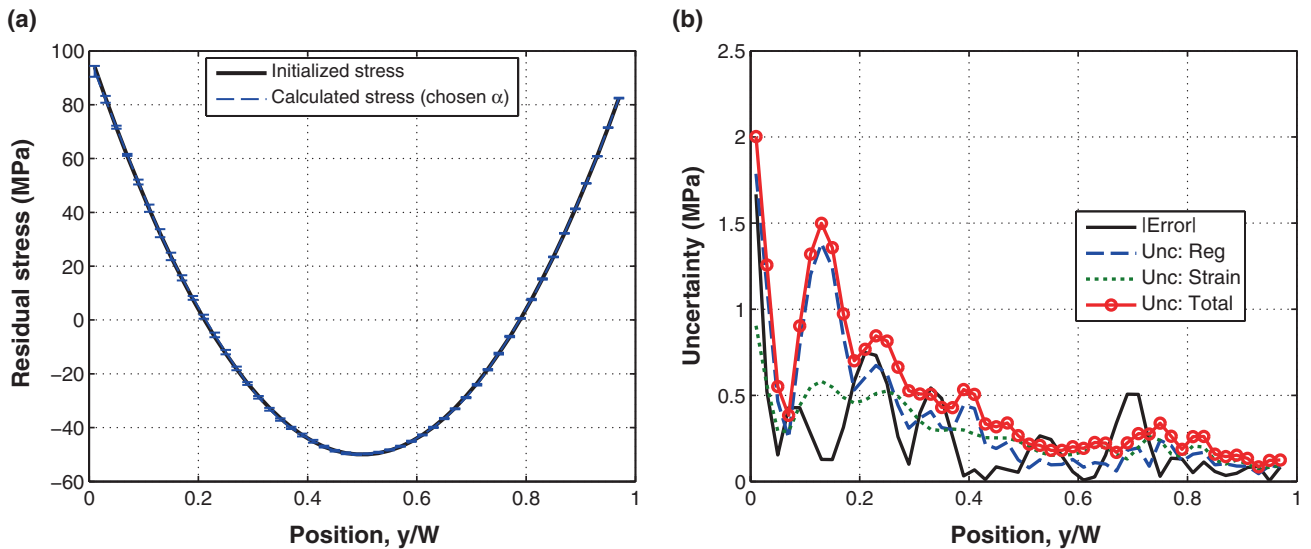


Fig. 1.5 Uncertainties in stress for the numerical experiment for a range of  $\alpha$  values: (a) regularization, (b) strain, and (c) total uncertainty



**Fig. 1.6** Results for the numerical experiment: (a) Maximum and RMS regularization, strain, and total uncertainty as a function of  $\alpha$  and (b) maximum and RMS error and total uncertainty



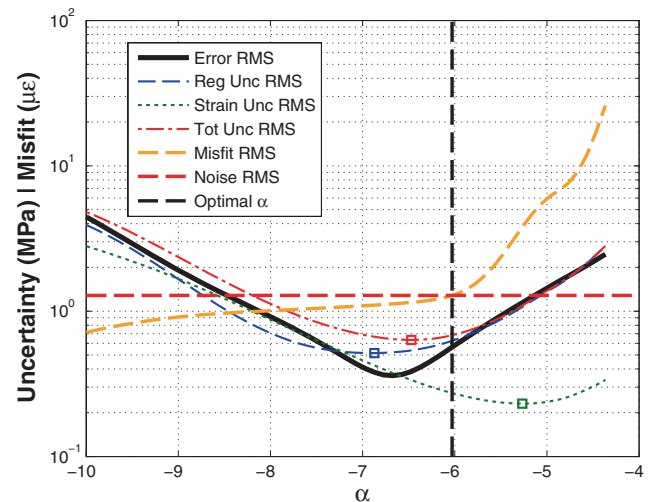
**Fig. 1.7** Results for the numerical experiment: (a) initialized and calculated residual stress, and (b) uncertainty and error

The calculated residual stress  $\pm$  the total uncertainty in Fig. 1.7 contains the initialized residual stress at 81.6% of points. Over 50 additional assessments with independent, noisy data added to the initialized strain, the calculated residual stress  $\pm$  the total uncertainty includes the initialized stress at 73.0% of points. This is nominally consistent with the level of agreement that would be expected if the uncertainty followed a normal distribution (68% of points within  $\pm$  one standard deviation).

## Discussion

The numerical experiment provides useful information to inform a strategy for selection of an appropriate value of regularization parameter since the noise in the data and error in residual stress are known. A pragmatic way to define an optimal amount of regularization is to determine the value of  $\alpha$  where the RMS misfit matches the RMS added noise. For the

**Fig. 1.8** Results for the numerical experiment as a function of  $\alpha$ : RMS error and uncertainties in stress



numerical experiment, the RMS values of error, uncertainties, and misfit are plotted as functions of  $\alpha$  in Fig. 1.8; also indicated are the RMS of added noise and the optimal  $\alpha$  (where the RMS misfit is equal to the RMS noise). The optimal  $\alpha$  occurs at  $\alpha \approx -6$ . It is noteworthy that this working definition of an optimal  $\alpha$  does not provide for a minimum error in residual stress; this occurs at  $\alpha \approx -6.7$ . Furthermore, Fig. 1.8 shows that the RMS total uncertainty are minimized near the value of  $\alpha$  where the RMS error is a minimum.

## Summary

This work provides a new uncertainty estimator for the slitting method of residual stress measurement that accounts for regularization uncertainty. The improved uncertainty estimator was demonstrated and tested in the context of a numerical experiment, which show that the uncertainty estimator reasonably predicts error and meets the defined acceptance criterion. The numerical experiment shows that reporting only uncertainty due to measurement imprecision is anti-conservative. The work shows that uncertainty in regularization is an important contributor to the uncertainty in residual stress found using slitting (and likely other mechanical residual stress measurements) and that minimization of uncertainty provides a way to select a value of the regularization parameter.

## References

1. M.R. Hill, The slitting method, in *Practical Residual Stress Measurement Methods*, ed. By G.S. Schajer (Wiley, West Sussex, 2013), pp. 89–108
2. ASTM, *E837 – 08: Test Method for Determining Residual Stresses by the Hole-Drilling Strain-Gage Method* (ASTM International, West Conshohocken, 2009)
3. G.S. Schajer, P.S. Whitehead, Hole drilling and ring coring, in *Practical Residual Stress Measurement Methods*, ed. By G.S. Schajer (Wiley, Chichester, 2013), pp. 29–64
4. G.S. Schajer, Measurement of non-uniform residual stresses using the hole-drilling method. Part II - practical application of the integral method. *J. Eng. Mater. Technol.* **110**, 344–349 (1988)
5. M. Barsanti, M. Beghini, C. Santus, A. Benincasa, L. Bertelli, Integral method coefficients and regularization procedure for the ring-core residual stress measurement technique. *Adv. Mater. Res.* **996**, 331–336 (2014)
6. M. Beghini, L. Bertini, L.F. Mori, Evaluating non-uniform residual stress by the hole-drilling method with concentric and eccentric holes. Part I. definition and validation of the influence functions. *Strain* **46**(4), 324–336 (2010)
7. G.S. Schajer, M.B. Prime, Use of inverse solutions for residual stress measurements. *J. Eng. Mater. Technol.* **128**(3), 375–382 (2006)
8. M.B. Prime, The inadequacy of uncertainty estimation in residual stress measurements. Presented at the residual stress summit 2017, Dayton, OH, USA.
9. M.B. Prime, M.R. Hill, Uncertainty, model error, and order selection for series-expanded, residual-stress inverse solutions. *J. Eng. Mater. Technol.* **128**(2), 175–185 (2006)
10. W.M. Sim, *Residual Stress Engineering in Manufacture of Aerospace Structural Parts* (Airbus SAS, Filton, 2009)
11. Abaqus/Standard, “Version 6.10.” Simulia Inc., Providence, RI, USA (2010)



## Chapter 2

# Walkthrough and History of the Virtual Fields Method

Michel Grédiac

**Abstract** This paper presents the history of the Virtual Fields Method, an identification method developed 30 years ago in order to identify constitutive parameters from full-field measurements. This method was initially proposed in the case of bending plate problems, but it has progressively been adapted to many other testing configurations. In this paper we look back at the first developments of the method and highlight the main problems that were progressively tackled, especially in terms of increasing complexity of the constitutive equations that were considered, and improvement of the identification technique itself to make it more efficient.

**Keywords** Full-field measurement · Identification · Material characterization · Principle of virtual work · Virtual fields method

### Introduction

The Virtual Fields Method is an identification method, which has been developed in order to identify parameters from fields of displacement/strain measurements. It is based on the principle of virtual work. Its main feature is that the resolution of the direct problem, namely numerically calculating the distribution of the displacement and strain fields in the specimen under test, is not required during the identification process. Originally developed during the late 1980s to characterize the elastic properties of composite materials, this method has since then been progressively improved and used in various cases of identification problems. The objective of this paper is to recall the origins of this method and to set out the main milestones in its development, with a special emphasis on the different hurdles that were progressively overcome.

### The First Beginnings

The starting point is the PhD work of the author [1] performed during the late 1980s under the supervision of late Pr. Alain Vautrin. The objective of this work was to characterize the six independent bending rigidities of a thin composite (and thus anisotropic) plate by performing only one test. Classic material characterization procedures such as the tensile or the three-point bending tests are based on configurations for which closed-form solutions for the displacement/strain/stress distributions as functions of the constitutive parameters are available. In this case, three stiffnesses at most are involved in the response of the specimen, so no more than three parameters can be measured at the same time. It means that one test is not sufficient with this type of approach when anisotropic materials are to be characterized. On the contrary, if the test is performed on one plate in which heterogeneous strain/curvature fields occur, a greater number of parameters are involved in the response, and these parameters are therefore potentially identifiable. The underlying benefit of this type of approach is that the number of tests is reduced, the ultimate case being one test only. This also paves the way for similar, but more complicated situations for which heterogeneous strain fields are unavoidable because they automatically take place in the specimen. This situation arises for instance in heterogeneous materials, when the strain field fluctuates from one constituent to another because of local changes of stiffness, or in materials with gradient properties such as solders or welding seams, where the local mechanical properties continuously spatially change.

---

M. Grédiac (✉)

Université Clermont Auvergne, SIGMA, Institut Pascal, UMR CNRS 6602, Clermont-Ferrand, France

e-mail: [michel.grediac@univ-bpclermont.fr](mailto:michel.grediac@univ-bpclermont.fr)



With the type of test described above, the main problem is that displacement/strain/stress distributions are generally not modeled by a closed-form solution. The challenge to be faced for solving this problem is twofold. The first challenge is of a practical nature since the displacement and strain components shall be measured at a sufficient number of points to reflect the actual heterogeneous response of the specimen. Ideally, full-field measurements shall be used to perform such measurements. In [1], this first problem was resolved by using deflectometry, a full-field measurement technique based on the observation of a regular pattern by reflection over the surface of the specimen [2]. The second problem is that some suitable identification procedure shall be used in order to link the measurements and the sought parameters in order to eventually retrieve the latter. The natural reflex for solving this problem is to rely on the finite element method. Indeed this method provides the displacement/strain field over the surface of the specimen, assuming that the geometry of the specimen, the boundary conditions and the material properties are correctly modeled. The latter being the unknowns for this identification problem, a cost function can be iteratively minimized with respect to these parameters. This technique, often referred to as Finite Element Model Updating (FEMU), has been proposed first in [3] for composite materials.

In [1], the main motivation for finding another route than FEMU is that iterative calculations shall be performed with FEMU. An interesting but relatively unnoticed solution has been proposed in [4] to overcome this drawback in the case of plate bending problem. It consists in considering three different bending tests performed on the same plate (only the location of the supports and applied loads changes from configuration to another), and writing the Maxwell-Betti reciprocal work theorem with this set of tests. When considering the identification problem at hand and assuming that full-field measurements are available over the surface of the specimen for each test, applying the Maxwell-Betti theorem leads to a system of linear equations where the bending rigidities of the plate specimen are the unknowns. This linear system is invertible if the three tests are different, which means that compared to FEMU, we have a direct identification technique since no iterative calculation is required in the case of elasticity. This approach has however two major drawbacks. The first one is that several tests are necessary, which is a strong limitation compared to FEMU where only one test is sufficient. The other one is that two experimental fields are involved in each equation. Measurements being noisy, this causes the resulting system of linear equations to be relatively sensitive to noise.

In [1], it is proposed to stick with the idea of considering scalar quantities such as works, but virtual works, by applying the principle of virtual work instead of the Maxwell-Betti reciprocal work theorem. The principle of virtual work can be written as follows:

$$-\underbrace{\int_V \underline{\underline{\sigma}} : \underline{\underline{\varepsilon}}^* dV}_{w_{int}^*} + \underbrace{\int_S (\underline{\underline{\sigma}} \underline{n}) \cdot \underline{u}^* dS}_{w_{ext}^*} = \rho \underbrace{\int_V \underline{\underline{\gamma}} \cdot \underline{u}^* dV}_{w_{acc}^*}, \forall \text{K.A. } \underline{u}^* \quad (2.1)$$

where  $\sigma$  is the actual stress field in the specimen,  $u^*/\varepsilon^{**}$  a kinematically admissible (K.A.) displacement/strain field,  $n$  a unit vector perpendicular to the external surface,  $V$  the volume of the specimen and  $S$  its external surface. Compared to the procedure described above, employing the principle of virtual work leads to two main differences. The first one is that each kinematically admissible virtual field provides a linear equation where the stiffnesses are the unknowns. Since there is an infinite number of K.A. virtual fields, there is also potentially an infinite number of linear equations. In Eq. (2.1), combining these different virtual displacement/strain fields with actual heterogeneous strain fields involving all the unknown parameters leads to a system of linear equations, which provides these unknowns after inversion. One test only instead of several ones is therefore sufficient to identify the unknowns, provided that this test leads to heterogeneous strain fields and that at least as many independent virtual fields as unknown parameters can be defined to get an invertible linear system. The second difference is that the virtual fields can be defined by close-form equations, so these virtual fields are by definition not noisy. Hence, only one measurement field is affected by noise in the principle of virtual work instead of two in the Maxwell-Betti theorem. In the resulting linear equations, the coefficients by which the unknown stiffnesses are multiplied can be regarded as weighted averages of the actual strain measured over the whole specimen, the weights being the virtual strains. This contributes to average out the noise, and thus to regularize the identification problem.

The main results obtained in [1] were published in three different papers, where the principle of the method [5], numerical simulations [6] and experimental results [7] were presented in turn. Compared to FEMU, it can be said that the present approach is direct and not iterative in the case of linear elasticity. Full-fields measurements are however necessary, which is not the case with FEMU since only a limited number of measurements can be processed in this case. Another point is that volume integrals are involved in Eq. (2.1) but measurements are generally obtained only over the external surface. It means that some suitable assumptions are necessary to deduce the actual strain field from the measurements over the surface. This is possible when specimens are thin, which is generally the case.

## **From Bending Plate Problems to Other Applications**

The principle of virtual work being the weak form of equilibrium, it is of general purposes and can therefore be used in other situations than plates subjected to bending tests, as mentioned in [1]. In the early 1990s, fruitful discussions with Fabrice Pierron, who was at that time a PhD student, led to a longstanding collaboration during which various applications of this identification method, as well as its improvement, were investigated. Two main questions were progressively addressed: *i*- how to use this approach in cases different from plate bending, and *ii*- how to define optimal virtual fields, bearing in mind that having potentially an infinite number of K.A. virtual fields means that some combinations are inevitably better than others.

### ***From Elasticity to more Complex Constitutive Equations***

Concerning the first point, the whole set of in-plane stiffnesses of a composite plate was first measured in [8]. Vibrating composite plates were then investigated in [9], paving the way for the identification of complex moduli of polymers or composites [10]. In the meantime, realizing that this procedure was general and could be applied in various situations, it was decided to call it the *Virtual Fields Method* (VFM). This name was employed for the first time in 2000 [11]. Non-linear constitutive equations were also progressively considered. A simple damage model for composites was characterized in [12], but the parameters governing the model were still obtained directly, by inverting a system of linear equations. An important step was to apply the VFM in the case of plasticity [13]. Since the constitutive equations are by essence non-linear in this case, the idea was to minimize a residual defined by the squared left-hand side of Eq. (2.1) (the third integral is null in this case) fed by one or several virtual fields chosen by the user. Minimizing this cost function with respect to the sought parameters leads to an iterative identification procedure. This obviously requires more computational resources than in the linear case, but less than FEMU. Indeed the forward problem, namely finding the displacement/strain fields from a set of parameters chosen a priori, does not have to be solved with VFM. Large strains constitute another cause of non-linearity. This problem has been addressed for the first time in [14], where the parameters governing the hyperelastic response of rubber were identified. Various other types of materials such as wood [15], foams [16] or biological tissues [17] were studied with the VFM during the last few years. The interested reader is referred to [18] for a complete overview.

### ***Virtual Fields Are Smart Filters***

Concerning the use of optimal virtual fields in the identification procedure, we can summarize the conclusions of several studies on this particular point by saying that virtual fields can be regarded as smart filters, in the sense that they enhance or minimize, even nullify, the contribution of zones or parameters in Eq. (2.1) above. They can even minimize the effect of noise in the measurements on the identified parameters. Virtual fields, which can either be defined piecewisely [19] or with functions continuously defined over the whole domain, can therefore be tailored in order to resolve given problems in an optimal way. Some examples are listed below.

### ***Optimizing the Virtual Fields for a Robust Identification***

Measurements are affected by noise, so it is important to try to minimize the propagation of this noise through the identification process. First attempts were proposed in [20] in the case of elasticity, where virtual fields leading to the independent identification of the parameters were proposed. More interestingly, a procedure minimizing the negative effect of noise on the final results is described in [21]. The procedure is iterative, but it is shown that with the fixed-point algorithm used to retrieve the unknowns, only one iteration is generally sufficient to reach converge. In the same spirit, optimized virtual fields were also recently proposed in the case of plasticity [22]. These fields maximize the sensitivity of the sought parameters in the cost function.

### ***Mastering the Boundary Conditions***

In Eq. (2.1), it can be seen that the force distribution applied onto the boundary of the specimen is involved in the second integral. However, the precise distribution remains generally unknown whereas the resulting force can be measured, at least at some points. The virtual fields can therefore be adjusted in such a way that only the resulting force virtually works, as explained in [18], thus avoiding any measurement of, or assumption on the force distribution.

### ***Considering the Specimen Itself as a Load Cell***

In dynamic testing, for instance with Hopkinson's bars, measuring the dynamic force applied to the specimen is challenging because of the transient nature of this force. In [23], it is proposed to remove the need for impact force measurement by processing full-field strain and acceleration measurements with Eq. (2.1). In this case, the virtual fields are chosen in such a way that the second integral in Eq. (2.1) vanishes, for instance by imposing a null virtual field along the boundary of the gauge section. As a result, the first integral in Eq. (2.1), namely the internal virtual work, is balanced with the integral in the right-hand side of Eq. (2.1) only. This can be interpreted by the fact that the specimen itself plays the role of a load cell thanks to a suitable choice of the virtual fields.

### ***Making the Characterization of Heterogeneous Materials Easier***

Heterogeneous materials feature spatially-changing stiffnesses. Identifying the parameters that govern the models describing these spatially-changing stiffnesses is the aim of various papers relying on the VFM. In [24], it is shown that it is possible to detect local stiffness fluctuations in composite plates (for instance caused by a local damage) by relying on piecewise virtual fields. The quality of the results however strongly depends of the choice of the mesh used to define the virtual fields. In [25], it is proposed to describe with a Fourier basis both the virtual fields and the model used to describe the spatially changing stiffnesses. This simplifies the calculations thanks to the orthogonality of the basis functions, and eventually leads to a very fine description of the spatially changing stiffnesses in heterogeneous materials, as illustrated in [25] with paper.

### ***Measuring the Force Distribution Applied on the Specimen***

If the material properties are known, it is possible to focus on the second integral of Eq. (2.1) in order to characterize the load distribution applied on the specimen. This type of problem is especially relevant in vibroacoustics. In [26] for instance, the authors use the VFM in order to measure the load time history in addition to magnitude and location.

### **Current State of Play**

The VFM is spreading slowly but surely in the experimental mechanics community, as illustrated in Fig. 2.1, where the growing number of citations of the VFM in scientific publications is shown. The main reason given by the users for choosing this technique instead of others is the computation time, as in [27] for instance where FEMU and VFM are compared. A commercial code now includes the VFM as an add-on of a Digital Image Correlation program (<https://www.matchid.eu>), which illustrates the versatility of this method.

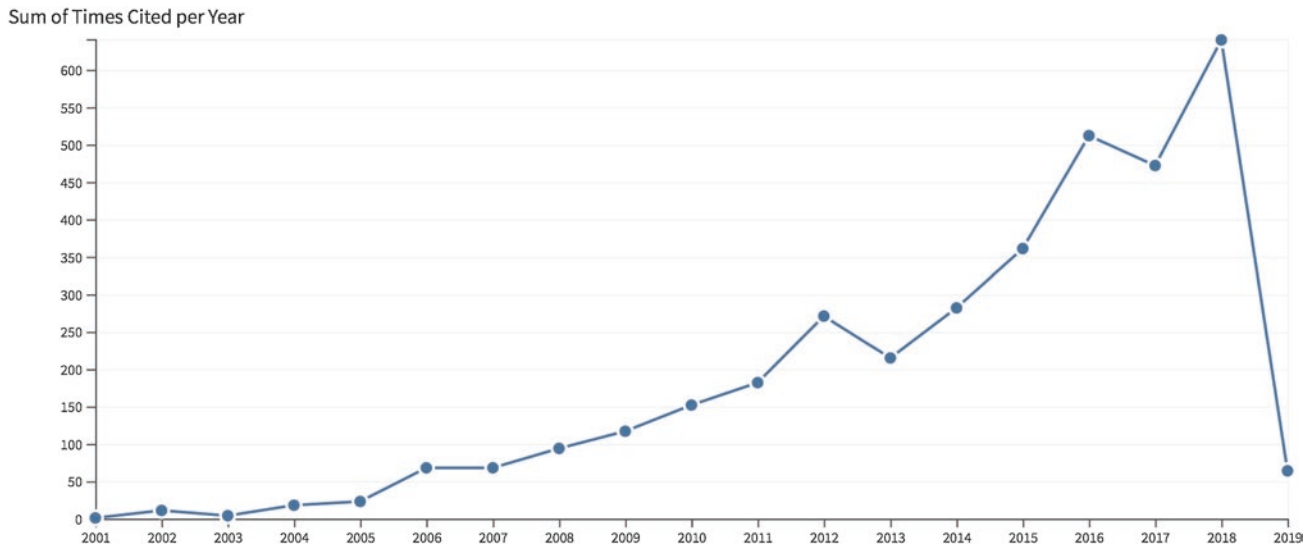


**Fig. 2.1** Number of citations in scientific publications related to the virtual fields method (Web of Science, February 2019)

## Conclusion

A technique initially designed to identify bending stiffnesses of composite plates by using full-field measurements has progressively been developed to become a general and versatile method. It has been applied to an increasing number of identification problems. Various types of constitutive equations and materials were studied in the recent past, and depending on the type of problem to be resolved, different strategies were proposed for the best choice of the virtual fields. The effectiveness of the VFM also depends on the geometry of the specimen as well as on the nature of the loading since these parameters directly influence the heterogeneous nature of the actual strain fields. This problem has been underexplored so far, and this surely constitutes a promising route for improving the quality of material characterization with this type of approach based on the processing of heterogeneous strain fields.

## References

1. M. Grédiac, Mesure des rigidités de flexion de stratifiés minces anisotropes à l'aide d'essais sur plaques, PhD thesis, Université Lyon 1 (1989)
2. Y. Surrel, N. Fournier, M. Grédiac, P.-A. Paris, Phase-stepped deflectometry applied to shape measurement of bent plates. *Exp. Mech.* **39**(1), 66–70 (1999)
3. K.T. Kavanagh, R.W. Clough, Finite element applications in the characterization of elastic solids. *Int. J. Solids Struct.* **7**(1), 11–23 (1971)
4. A. Foudjet, Contribution à l'étude rhéologique du matériau bois, PhD thesis, Université Lyon 1 (1986)
5. M. Grédiac, Principe des travaux virtuels et identification. *C. R. Acad. Sci.* **309-II**, 1–5 (1989)
6. M. Grédiac, A. Vautrin, G. Verchery, A general method for data averaging of anisotropic elastic constants. *J. Appl. Mech.* **60**, 614–618 (1993)
7. M. Grédiac, A. Vautrin, Mechanical characterization of anisotropic plates: experiments and results. *Eur. J. Mech. A Solid.* **12**(6), 819–838 (1993)
8. M. Grédiac, F. Pierron, Y. Surrel, Novel procedure for complete in-plane composite characterization using a T-shaped specimen. *Exp. Mech.* **39**(2), 142–149 (1999)
9. M. Grédiac, P.-A. Paris, Direct identification of elastic constants of anisotropic plates by modal analysis: Theoretical and numerical aspects. *J. Sound Vib.* **195**(3), 401–415 (1996)
10. A. Giraudeau, B. Guo, F. Pierron, Stiffness and damping identification from full field measurements on vibrating plates. *Exp. Mech.* **46**(6), 777–787 (2006)
11. F. Pierron, S. Zhavaronok, M. Grédiac, Identification of the through-thickness properties of thick laminates using the virtual fields method. *Int. J. Solids Struct.* **37**(32), 4437–4453 (2000)
12. M. Grédiac, F. Auslender, F. Pierron, Applying the virtual fields method to determine the through-thickness moduli of thick composites with a nonlinear shear response. *Composites/Part A* **32**(12), 1713–1725 (2001)
13. M. Grédiac, F. Pierron, Applying the virtual fields method to the identification of plastic constitutive equations. *Int. J. Plast.* **26**(4), 602–627 (2006)
14. N. Promma, B. Raka, M. Grédiac, E. Toussaint, J.B. Le Cam, X. Balandraud, F. Hild, Application of the virtual fields method to mechanical characterization of elastomeric materials. *Int. J. Solids Struct.* **46**, 698–715 (2009)

15. J. Xavier, U. Belini, F. Pierron, J. Morais, J. Lousada, M. Tomazello, Characterisation of bending stiffness of MDF from full-field slope measurements. *Wood Sci. Technol.* **47**(2), 423–441 (2013)
16. P. Wang, F. Pierron, M. Rossi, P. Lava, O.T. Thomsen, Optimised experimental characterisation of polymeric foam material using DIC and the virtual fields method. *Strain* **52**(1), 59–79 (2016)
17. S. Avril, P. Badel, A. Duprey, Anisotropic and hyperelastic identification of in vitro human arteries from full-field optical measurements. *J. Biomech.* **16**(43), 2978–2985 (2010)
18. F. Pierron, M. Grédiac, *The virtual fields method* (Springer, New York, 2012), p. 517. ISBN 978-1-4614-1823-8
19. M. Grédiac, E. Toussaint, F. Pierron, Special virtual fields for the direct determination of material parameters with the virtual fields method. 1- principle and definition. *Int. J. Solids Struct.* **39**, 2691–2705 (2002)
20. E. Toussaint, M. Grédiac, F. Pierron, The virtual fields method with piecewise virtual fields. *Int. J. Mech. Sci.* **48**(3), 256–264 (2006)
21. S. Avril, M. Grédiac, F. Pierron, Sensitivity of the virtual fields method to noisy data. *Comput. Mech.* **34**, 439–452 (2004)
22. A. Marek, F.M. Davis, F. Pierron, Sensitivity-based virtual fields for the non-linear virtual fields method. *Comput. Mech.* **60**(3), 409–431 (2017)
23. F. Pierron, H. Zhu, C. Siviour, Beyond Hopkinson's bar. *Philos. Trans. R. Soc. A Math. Phys. Eng. Sci.* **372**(2023), 20130195–20130195 (2014)
24. J.H. Kim, F. Pierron, K.S. Syed Muhammad, M.R. Wisnom, M. Grédiac, E. Toussaint, Identification of the local stiffness reduction of a damaged composite plate using the virtual fields method. In *Comptest 2006, Porto, 2006. Proceedings of the conference.*
25. J.M. Considine, F. Pierron, K.T. Turner, P. Lava, X. Tang, Smoothly varying in-plane stiffness heterogeneity evaluated under uniaxial tensile stress. *Strain* **53**(5), 1–26 (2017)
26. P. O'Donoghue, O. Robin, A. Berry, Time-resolved identification of mechanical loadings on plates using the virtual fields method and deflection measurements. *Strain* **54**(3), e12258 (2017)
27. L. Zhang, S.G. Thakku, M.R. Beotra, M. Baskaran, T. Aung, J.C.H. Goh, N.G. Strouthidis, M.J.A. Girard, Verification of the virtual fields method to extract the mechanical properties of human nerve head tissues un vivo. *Biomech. Model. Mechanobiol.* **16**(3), 871–887 (2017)



## Chapter 3

# Low-Cost Thermoelastic Stress Analysis

Melissa Weihrauch, Ceri Middleton, Richard Greene, and Eann Patterson

**Abstract** The popularity of thermoelastic stress analysis (TSA) has been hampered by the high capital cost of the equipment, the need for a cyclic load and for a surface with uniform emissivity. Current commercially-available TSA systems allow data to be collected when the component of interest is subject to random loading which has broadened the potential applications of TSA. Recent work has shown that matt black paint, which is traditionally applied to achieve uniform emissivity, is not necessary and aerospace primers are adequate for TSA work. At the same time, a number of investigators have explored the use of microbolometers as a lower cost alternative to the staring array cameras that form the core of the commercially available TSA systems and are a major component of the high price tag. However, the cost of microbolometers is still measured in the thousands of dollars; and so, the use of low-cost, chip-mounted infrared sensors has been explored in the EU H2020 project INSTRUCTIVE. The results demonstrate that, using a simple algorithm implemented in MATLAB and a sensor costing a few hundreds of dollars, it is possible to obtain TSA data from a cyclically-loaded test specimen. The quality of the results is proportional to the investment in the sensor but nevertheless the low-cost affordable approach yields useful results and offers the potential for TSA to be used in structural health monitoring to provide early warning of damage to a structure.

**Keywords** Thermoelastic stress analysis · Microbolometer · Damage tracking

## Introduction

Thermoelastic stress analysis (TSA) is a technique well-grounded in theory since its discovery over 160 years ago by Lord Kelvin [1]. In adiabatic conditions and under variable loading, temperature fluctuations observed in a body are proportional to the sum of its principal stresses. This has allowed the distribution of stress to be visualized by monitoring temperatures across a loaded object. Over the past decade, the technique has increased in use through the development and improvement in the resolution of thermal cameras and this has sparked interest in industrial applications [1–3].

The advantages of TSA are that it is a non-contact technique in which no laborious surface preparation is needed, as a result it is suited for *in-situ* applications. Objects can be continuously monitored while results can be obtained in near to real-time. Additionally, changes in stresses and stress concentrations, an indicator of crack initiation, can be detected and their propagation can be monitored [2]. This has led to industries, such as the aviation industry, showing interest in TSA as a method for early damage detection. However, the large capital cost associated with photon detectors that have historically been used for TSA is a major inhibitor of the technique's use in damage detection [3].

More recently, microbolometers have been used as a relatively cheaper alternative to these traditional cameras [3]. Microbolometers have the added advantage of being lighter and smaller in size than photon detectors allowing them to be placed in hard to reach areas. However, these instruments still cost on the order of thousands of dollars, making simultaneous monitoring of large areas expensive. If costs can be reduced even further, using arrays of cameras to monitor objects and detecting damage over larger areas could become feasible. Hence, the use of low cost microbolometers has been explored in the EU H2020 project INSTRUCTIVE.

---

M. Weihrauch (✉) · C. Middleton · E. Patterson  
School of Engineering, University of Liverpool, The Quadrangle, Liverpool, UK  
e-mail: [sgmweih@liverpool.ac.uk](mailto:sgmweih@liverpool.ac.uk)

R. Greene  
Strain Solutions Ltd, Dunston Innovation Centre, Chesterfield, Derbyshire, UK

## Methodology and Results

An uncooled VOx (Vanadium Oxide) microbolometer (*Lepton 3 from FLIR, Wilsonville, OR*) that is capable of capturing images at a resolution of 160 by 120 pixels at a frame rate of 8.7 fps [4] was used. The microbolometer has a fixed lens assembly and can detect wavelengths between 8  $\mu\text{m}$  to 14  $\mu\text{m}$ , making the sensor suitable for operation at room temperature where peak photon emittance occurs at a wavelength of 12  $\mu\text{m}$ . The microbolometer was connected to a Raspberry Pi 3 B+ (*Raspberry Pi, Cambridge, UK*) using a camera-specific break-out board (*Sparkfun, Boulder, CO*) and, hence, could be controlled remotely. The collected raw IR frames were given titles containing a time stamp with millisecond accuracy, which was later used to generate a reference signal for the processing of the TSA data and to more accurately estimate the frame rate of the sensor. A case to hold the Lepton and Raspberry Pi was 3D printed (see Fig. 3.1). The sensor's small size of 11.50  $\times$  12.70  $\times$  7.14 mm means that it can be placed in inaccessible or hard-to-reach areas.

The performance of the microbolometer has been evaluated in a series of fatigue tests, in which TSA data was computed using a short script written in MATLAB that was capable of estimating the test frequency under cyclical loading conditions. A specified number of raw infrared images were accumulated over a time period, during which corrupted frames were discarded, and the frame rate of the camera was estimated. A region of image containing the specimen was identified manually, and the values of the pixels within the region used to estimate the testing frequency. The Fast Fourier Transform (FFT) was computed for each selected pixel and the frequency corresponding to the maximum magnitude of each pixel found. The mode of these frequency results for the selected pixels was then taken to be the test frequency. A sinusoidal reference signal was generated using the obtained frequency and the time stamps associated with each frame. The product of the reference signal and the accumulated raw data was then found and the mean of these results along the time dimension was taken. Lastly, the resulting amplitude data were normalized by the mean value of the data field.

The fatigue test was performed using a servo-hydraulic test machine (*Instron 8501, Instron, Buckinghamshire, UK*) to load a rectangular 200  $\times$  40 mm aluminum 2024-T3 specimen with a 6 mm diameter hole in its center to introduce stress concentrations. The aluminum specimen was covered by a thin Graphit33 coating (*Kontakt Chemie, Iffezheim, Germany*) to increase emissivity. Figure 3.1 shows the experimental setup used in the fatigue tests. The sensor was placed close to the specimen to maximize the amount of relevant information captured and ensured that most of the camera's field of view was the object of interest rather than the surroundings.

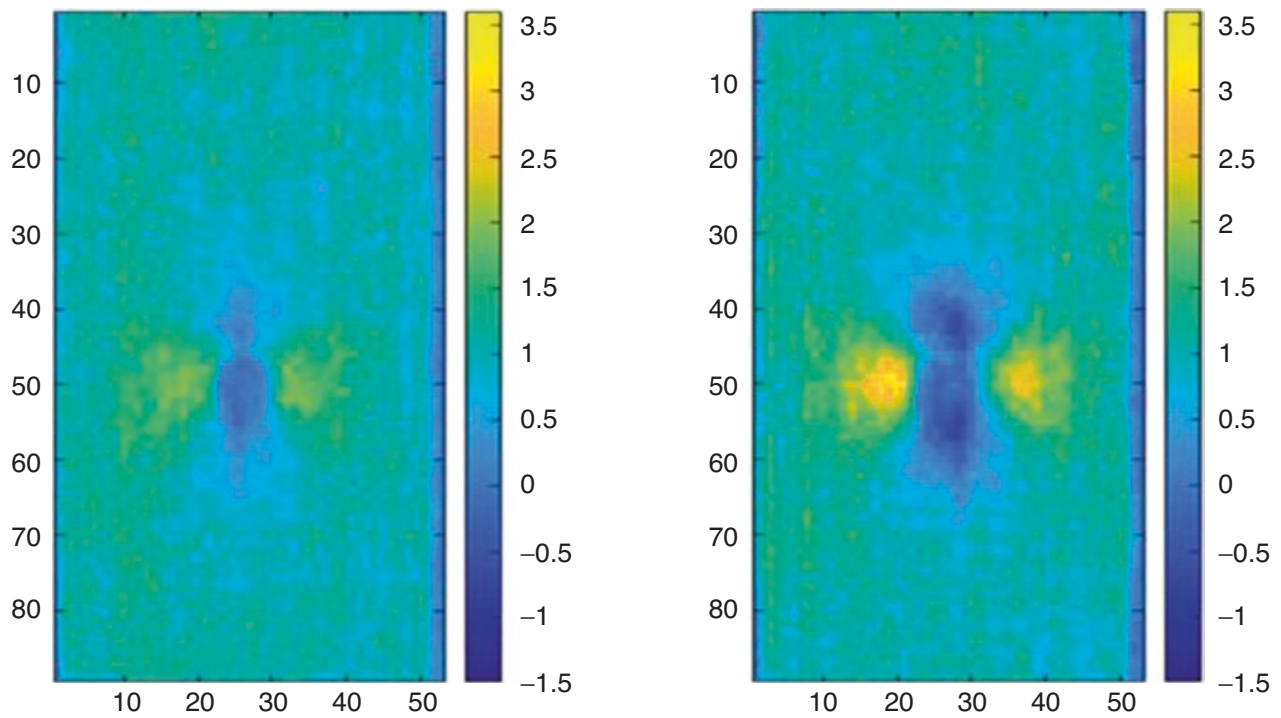
Fatigue tests were performed using cyclic loading at a nominal frequency of 1 Hz with a maximum load of 17.90 kN and a minimum of 1.79 kN. The results in Fig. 3.2 were obtained when the sensor was placed approximately 100 mm from the specimen, whereas for those in Fig. 3.3 the sensor was moved much closer to the specimen.

Figure 3.2 shows a comparison between the stress distributions detected in a sample before and after crack initiation. The color bar shows the values of a normalized TSA signal that is integrated over 128 frames, equivalent to approximately 15 s of collection time. In other words, 128 frames are collected and then processed cumulatively. The axes of the images are in pixels and 1 pixel is equal to 1.325 mm. The images have been cropped to show the test specimen only.

The left image in Fig. 3.2 was taken after approximately 3340 cycles and stress concentrations are visible adjacent to either side of the hole, indicating that a crack has probably not initiated yet. The image on the right shows the same specimen after 8180 cycles; the stress concentrations are higher in magnitude and have begun to move away from the edge of the hole,

**Fig. 3.1** Experimental setup to monitor crack propagation





**Fig. 3.2** TSA normalized signal magnitude from a typical fatigue test acquired with the sensor approximately 100 mm from the specimen (1 pixel = 1.325 mm) at 3340 cycles (left) when no crack is apparent and at 8180 cycles (right) when cracks have initiated

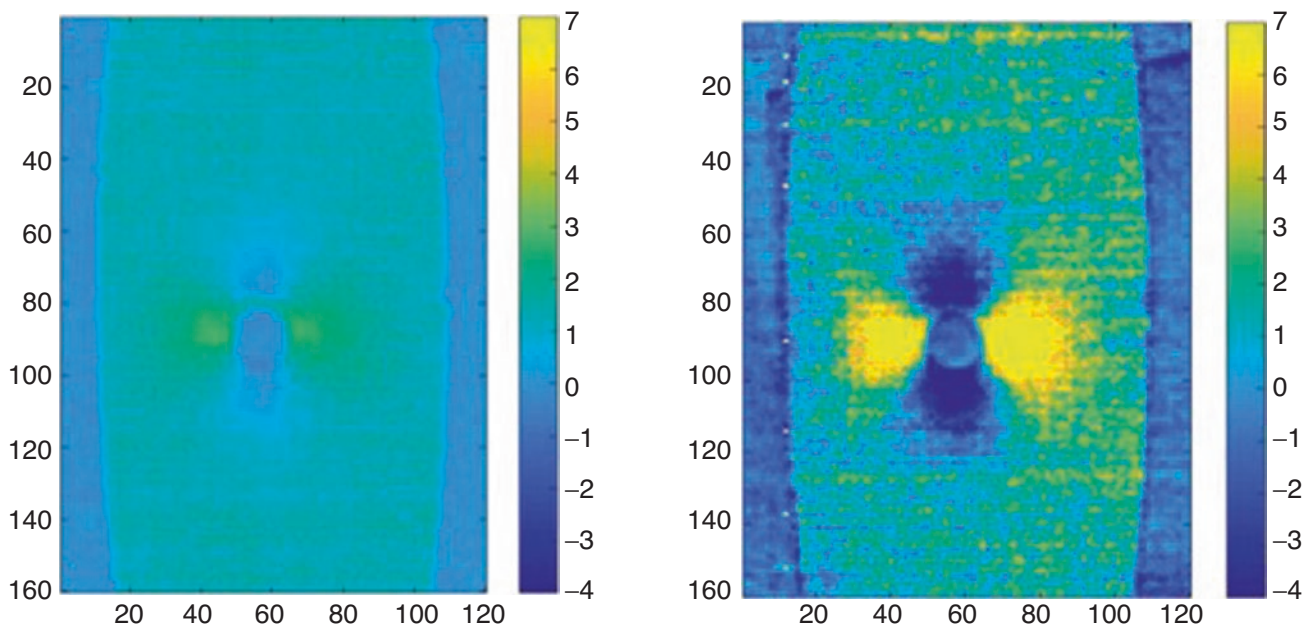


**Fig. 3.3** TSA normalized signal magnitude from a typical fatigue test acquired with the sensor approximately 55 mm from the specimen (1 pixel = 2.425 mm) at 574 cycles (left) when no crack is apparent and at 5600 cycles (right) when cracks have initiated



indicating that cracks have initiated and have started propagating towards the edges of the specimen from the hole. The crack on the right of the hole is possibly longer than the one on the left which causes some eccentricity to the geometry and causes more load to flow through the left ligament.

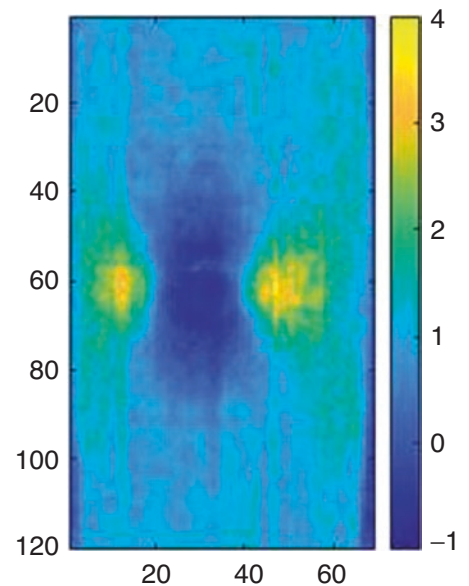
The TSA data in Fig. 3.3 were acquired with the sensor placed closer to the specimen, which increased the magnification to 1 pixel = 2.425 mm, i.e. almost twice the value in the other fatigue test. Similar observations can be made from Fig. 3.3 at high magnification; however, the fixed lens on the microbolometer causes distortion of the image that could be corrected by image processing. As in the previous test (Fig. 3.2), the initial image shows small stress concentrations adjacent to the hole; which are enlarged, more intense and starting to move away from the hole after 5600 cycles, suggesting the presence of two cracks. It would appear that the crack on the left is slightly longer causing eccentricity in the loading, so that more load is transmitted through the more substantial right ligament leading to a higher stress concentration.

## Discussion and Conclusion

Fatigue tests monitored by an uncooled VOx microbolometer bought for a few hundred dollars have shown that useful TSA images can be obtained using a low-cost microbolometer. Tests on undamaged tensile specimens with a central hole initially yielded less severe and, hence, less visible stress concentrations; however, as cracks initiated the stress concentrations became more severe and visible, indicating that the technique could be used to identify crack formation. In a fatigue test performed on a pre-cracked specimen, during loading at 1 Hz at the same R-ratio as previous tests, but with a lower maximum load (11.6 kN), it was possible to capture data showing crack propagation. This is shown in Fig. 3.4, where the stress concentrations associated with the crack tips have moved to the center of the ligaments.

A challenge associated with using the Lepton 3 with its fixed lens is that for relevant data to be obtained, the sensor must be in close proximity to the object being monitored. A comparison of the results in Figs. 3.2 and 3.3 shows that monitoring from relatively large distances is feasible even though it comes at the expense of resolution and sharpness of the image. Future work could attempt to improve results at large separations between camera and specimen using different lens assemblies. The low resolution of the microbolometer can also be compensated for through the use of arrays of sensors while additional information on crack propagation could be obtained by monitoring specimens from both sides.

**Fig. 3.4** TSA data collected during fatigue crack propagation in a pre-cracked specimen, TSA data collected during loading at 1 Hz, with the sensor approximately 90 mm from the specimen



**Acknowledgements** This research forms part of the undergraduate thesis of Melissa Weihrauch and was instigated in support of research carried out as part of the INSTRUCTIVE and DIMES projects. INSTRUCTIVE and DIMES projects have received funding from the Clean Sky 2 Joint Undertaking under the European Union's Horizon 2020 research and innovation programme under grant agreements No. 686777 and No. 820951 respectively.

## References

1. R.J. Greene, E.A. Patterson, R.E. Rowlands, Thermoelastic stress analysis, in *Springer Handbook of Experimental Solid Mechanics*, ed. By W.N. Sharpe (Springer, New York, 2008), pp. 743–767
2. C.A. Middleton, A. Gaio, R.J. Greene, E.A. Patterson, Toward automated tracking of initiation and propagation of cracks in aluminium alloy coupons using thermoelastic stress analysis. *J. Nondestruct. Eval.* **38**, 18 (2019)
3. N. Rajic, D. Rowlands, Thermoelastic stress analysis with a compact low-cost microbolometer system. *Quant. Infr. Therm. J.* **10**(2), 135–158 (2013)
4. <https://www.flir.com/globalassets/imported-assets/document/flir-lepton-engineering-datasheet.pdf>. Accessed 25th Feb 2019



## Chapter 4

# The Effect of Residual Stress on Aluminum Strength Using Thermoelastic Stress Analysis

Wei-Cheng Shen, Shiang-Jiun Lin, Yan-Bing Huang, Xue-Lin Ji, and Wei-Yu Zeng

**Abstract** Residual stress existing in a material can possibly yield the undesired deflection or fracture occurred in an engineering structure. Hence, it would be very helpful for the industry to monitor residual stress and further analyze the influence of residual stress on the strength of a material. Thermoelastic stress analysis is an experimental technique which is able to determine the full-field residual stress by recording temperature changes due to loading. This work analyzes the residual stress distributed over the perforated aluminum plate based on using thermoelastically measured results and further investigate the effect of residual stresses on the material strength.

**Keywords** Thermoelastic stress analysis · Residual stress · Non-destructive experiment · Stress measurement

## Introduction

Thermoelastic stress analysis (TSA) is a non-destructively experimental technique which records the temperature disturbance of a stressed material to provide the stress information throughout the surface. Under adiabatic and reversible conditions, thermoelastic theory indicates the temperature change induced by the dynamic loading will be associated with the sum of principal stresses. Traditional thermoelasticity gives the relation between TSA measured results and the sum of normal stresses remains linearly. Since TSA provides the combination of stresses and individual components of stresses are always necessitated for determining structural failures, many works related to TSA emphasized on separating TSA measurements. Rauch and Rowlands [1] separated TSA results, using finite element method. Lin et al. [2–4] combined Airy stress expression and TSA recorded data to provide individual stresses for symmetrically and un-symmetrically perforated aluminum plates. However, it has to be noticed that while traditional thermoelasticity has been substantiated to provide accurate stress information, the effect on mean stress on TSA measurements is not involved in the traditional TSA theory. When Machin et al. [5] conducted TSA experiment, they found that TSA measured results can be changed as mean stress varies. Later, Wong et al. [6] reviewed thermoelastic theory and gave that as the elastic properties are assumed to be temperature dependence, the thermoelastic response is not only associated with the sum of principal stresses but the mean stress. Since the mean stress is a static stress component and residual stress is mechanically regarded to as static stress, thermoelastic stress analysis is then getting applied to monitor the residual stress existing in a material.

This work employs thermoelastic stress analysis to help determine the residual stress existing in the perforated aluminum plate and analyze the strength variation due to residual stress based on comparing unresidual stressed members.

## Thermoelastic Experiment and Results

The specimens utilized in this work are 2024 aluminum plates having dimensions of 300 mm long, 51 mm wide and 5 mm thick. Each aluminum plate has a hole with the diameter of 25 mm located at the center. Prior to conducting TSA test, all of specimens were coated by a thin and flat paint to enhance the emissivity of the aluminum material. Figure 4.1 shows the TSA experimental setup.

---

W.-C. Shen · S.-J. Lin (✉) · X.-L. Ji · W.-Y. Zeng

Department of Mold and Die Engineering, National Kaohsiung University of Science and Technology, Kaohsiung, Taiwan

Y.-B. Huang

Test Technology Development Section, Metal Industries Research and Development Center, Kaohsiung, Taiwan

**Fig. 4.1** Thermoelastically experimental setup



In order to analyze the residual stress, the present work applied cyclic loading conditions with the mean load of 6 kN and range load of 10 kN as well as the mean load of 7 kN and range load of 10 kN on the specimen. The loading frequency for all of TSA tests is 3 Hz. Once the thermoelastic responses resulting different mean stresses are acquired, the residual stress can be evaluated based on employing revised TSA theoretical expression. Figures 4.2, 4.3, and 4.4 show the TSA-determined residual stress located approximately 1.1R, 1.25R and 1.5R away from the center of the hole. R is the radius of the circular cutout.

## Discussions

Figures 4.2, 4.3, and 4.4 indicate that the residual stress determined by the mean load equal to 6 kN is very close to that provided by the thermoelastic measurement as the mean load selected 7 kN. It supports the accuracy and reliability of the TSA-determined residual stress. Moreover, as can be observed in Figs. 4.2, 4.3, and 4.4, the maximum compressive residual stress appear at  $\theta$  equal to  $0^\circ$  and as  $\theta$  equals  $90^\circ$ , the tensile residual stress will attain maximum.

**Fig. 4.2** Residual stress located 1.1R away from the center of the hole

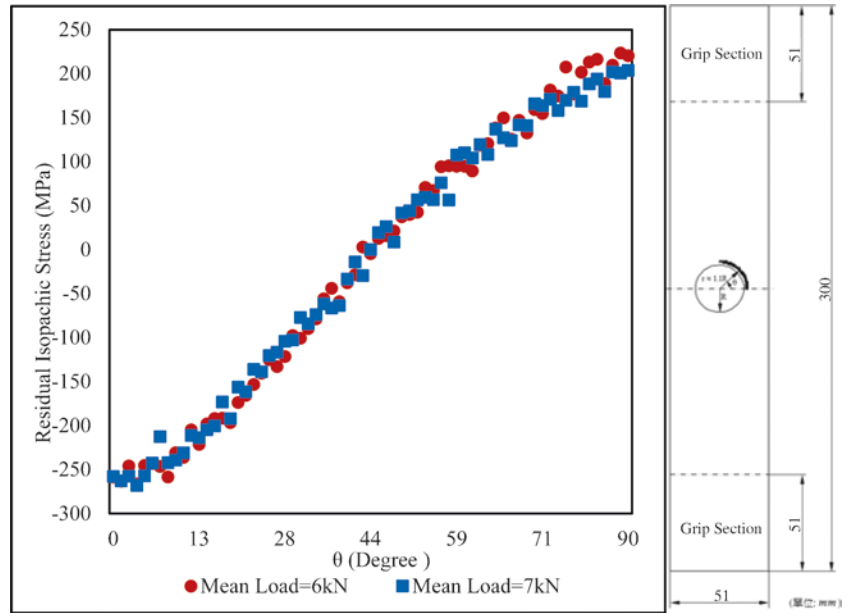


**Fig. 4.3** Residual stress located 1.25R away from the center of the hole

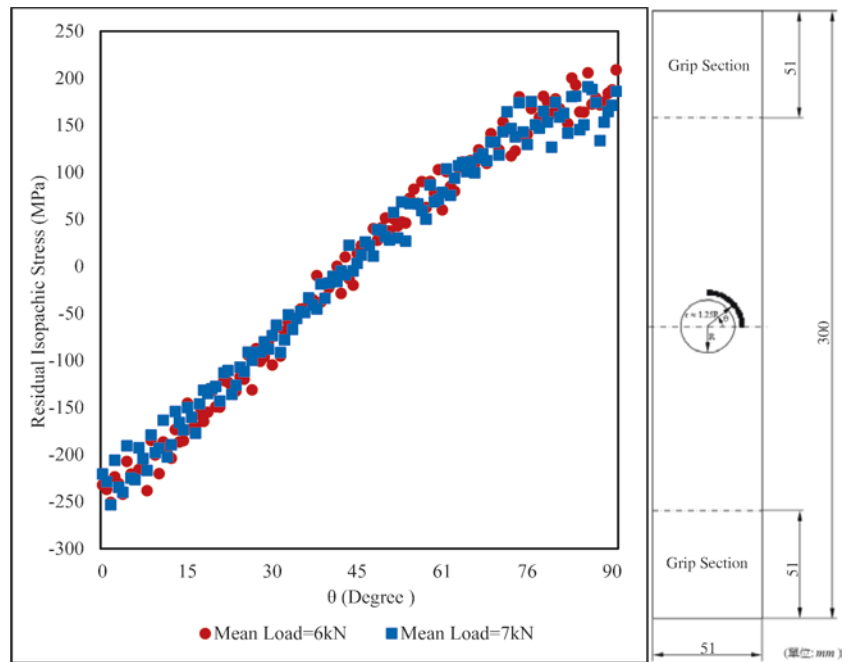
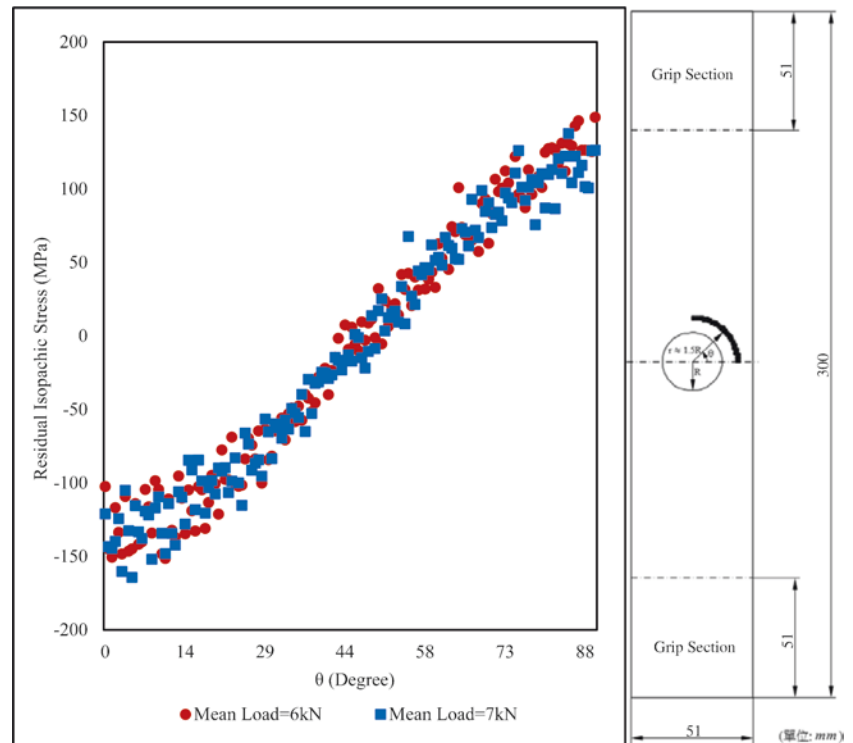


**Fig. 4.4** Residual stress located 1.5R away from the center of the hole



## Conclusion

The present work utilizes thermoelastic stress analysis to investigate the residual stress for the perforated aluminum plate. Based on results acquired in this work, the TSA technique is indeed able to help provide accurate residual stress existing in the material. As specimen is respectively subjected to the mean loads equal to 6 kN and 7 kN and the rage load as well as the loading frequency are fixed, their corresponding thermoelastic responses yield the approximately same residual stresses over the perforated material. It further validates the accuracy of residual stress analyzed by thermoelasticity.

## References

1. B.J. Rauch, R.E. Rowlands, Stress separation of thermoelastically measured isipachics. *Exp. Mech.* **41**(4), 358–367 (2001)
2. S.-J. Lin, D.R. Matthys, R.E. Rowlands, Separating stresses thermoelastically in a central circularly perforated plate using an airy stress function. *Strain* **45**(6), 516–526 (2009)
3. S.-J. Lin, S. Quinn, D.R. Matthys, A.M. New, I.M. Kincaid, B.R. Boyce, A.A. Khaja, R.E. Rowlands, Thermoelastic determination of individual stresses in vicinity of a near-edge hole beneath a concentrated load. *Exp. Mech.* **51**, 797–814 (2011)
4. S.-J. Lin, D.R. Matthys, S. Quinn, J.P. Davidson, B.R. Boyce, A.A. Khaja, R.E. Rowlands, Stresses at and in the neighborhood of a near-edge hole in a plate subjected to an offset load from measured temperatures. *Eur. J. Mech. A Solids* **39**, 209–217 (2013)
5. A.S. Machin, J.G. Sparrow, M.G. Stimson, Mean stress dependence of thermoelastic constant. *Strain* **23**(1), 27–30 (1987)
6. A.K. Wong, S.A. Dunn, J.G. Sparrow, Residual stress measurement by means of the thermoelastic effect. *Natural* **332**, 613–615 (1988)



## Chapter 5

# Calibration of Anisotropic Plasticity Models with an Optimized Heterogeneous Test and the Virtual Fields Method

J. M. P. Martins, S. Thuillier, and A. Andrade-Campos

**Abstract** An accurate calibration of a constitutive model for finite element analysis is as important as an adequate choice of the constitutive model itself. The calibration strategy and the experimental database have determinant roles for the success of this stage. Over recent years, the increasing use of full-field measurement techniques has changed significantly the amount of data that compose the experimental database and suppressed some of the design constraints of the mechanical tests. These techniques enable to capture complete displacement/strain fields during a mechanical test, a feature that has been conveniently used to explore heterogeneous mechanical tests. The use of full-field measurements and heterogeneous tests has proven to be an interesting approach to calibrate complex models with a high number of material parameters, such as the case of anisotropic plasticity models. Usually, the inverse strategies selected to identify the material parameters from heterogeneous fields are based on the so-called finite element model updating (FEMU) method, which is known for being computationally demanding. Nevertheless, novel inverse strategies, such as the virtual fields method, have demonstrated much better results in terms of the computational cost without deterioration of the calibration results. Therefore, the aim of the present study, in the framework of full-field measurements, is to explore the combination of a previously designed heterogeneous test and the virtual fields method (VFM). The heterogeneous test consists of a uniaxial standard test with an optimized specimen shape, called butterfly shape. This specimen was specifically designed to obtain a wide range of strain paths and strain amplitudes and has given promising results when combined with a FEMU-based strategy. A set of virtual fields is developed to combine the butterfly test and the VFM. This set is tested with virtual experimental data generated and the sensitivity of the VFM to the number of virtual fields is confirmed. Moreover, experimentally acquired full-field measurements of butterfly test for a DC04 mild steel are used to assess the performance of this calibration strategy. An anisotropic plasticity model composed by Hill'48 and Swift's law is calibrated.

**Keywords** Calibration of constitutive models · Anisotropic metal plasticity · Heterogeneous test · Full-field measurements · Virtual fields method

## Introduction

The use of numerical simulation tools to support the mechanical design of a manufacturing process or a part has long been employed by the industry. The demands for better accuracy of these tools led to the development of more and more complex constitutive models to mimic the real mechanical behaviour of materials. Nevertheless, before using any of these models, a calibration phase is required, in which the material parameters of the model are adjusted to have a close prediction of the material in hands. The predictive capabilities of constitutive models largely depend on this phase. Moreover, the applicability

---

J. M. P. Martins (✉)

Univ. Bretagne Sud, UMR CNRS 6027, IRDL, Lorient, France

Centre for Mechanical Technology and Automation (TEMA), University of Aveiro, Aveiro, Portugal

e-mail: [joao.martins52@ua.pt](mailto:joao.martins52@ua.pt)

S. Thuillier

Univ. Bretagne Sud, UMR CNRS 6027, IRDL, Lorient, France

e-mail: [sandrine.thuillier@univ-ubs.fr](mailto:sandrine.thuillier@univ-ubs.fr)

A. Andrade-Campos

Centre for Mechanical Technology and Automation (TEMA), University of Aveiro, Aveiro, Portugal

e-mail: [gilac@ua.pt](mailto:gilac@ua.pt)

of the models is also dependent on the experimental effort required for this phase. Frequently, the need for a large and diversified set of experimental tests to calibrate a constitutive model restrains the use of more advanced and accurate constitutive models [1].

The advent of full-field measurement techniques (e.g. Digital Image Correlation, DIC in short [2]) is changing significantly the calibration process of constitutive models. These techniques allow access to dense maps of data (displacements, strains, etc.) from a single mechanical test, which after post-treatment can be used to retrieve the material parameters of a selected constitutive model. Moreover, these techniques enable the use of complex sample geometries to test the mechanical behaviour of materials, which, if correctly designed, produce heterogeneous strain fields with enough information to extract several material parameters from a single test. However, to extract the material parameters from this type of data, it is required to solve an inverse problem that is time-consuming. Therefore, the quest for both efficient inverse methods and appropriate test geometries has been intense in the past few years. Nevertheless, inverse methods and new test geometries for mechanical testing are usually developed and validated separately and consequently, the symbiosis between these two is not fully explored.

In this work, a heterogeneous test specially optimized to calibrate constitutive models [3, 4] for sheet metal plasticity is combined with the Virtual Fields method (VFM) [5]. This heterogeneous test, called butterfly test, is firstly presented as well as the experimental data previously acquired for a DC04 mild steel [4]. This study focuses on the selection of a set of virtual fields suitable for the above-mentioned test, as well as the influence of the number of virtual fields used. Finally, the performance of the VFM combined with the data acquired from a single butterfly test is assessed. An anisotropic model composed by Hill'48 yield criterion and Swift's hardening law is selected to be calibrated.

## The Virtual Fields Method

The virtual fields method is an inverse method which relies on the principle of virtual work and kinematic full-field measurements to retrieve constitutive material parameters. Due to the nature of the principle of virtual work, this method can be applied to any constitutive model. In the case of non-linear models, such as elasto-plastic models, the inverse problem is solved by minimizing the squared difference of the gap between internal and external virtual work, with respect to the sought constitutive parameters and for different time steps. The objective function, in the large strain framework and assuming static equilibrium, can be written as:

$$\varphi(\xi) = \frac{1}{n_v} \sum_{i=1}^{n_v} \frac{1}{n_t} \sum_{j=1}^{n_t} \left( \int_{\Omega_0} \mathbf{P}(\xi, \boldsymbol{\varepsilon}^{\text{exp}}) : \text{Grad} \mathbf{U}^* dV - \int_{\Gamma_0^f} \bar{\mathbf{T}} \cdot \mathbf{U}^* dS \right)^2, \quad (5.1)$$

where  $\mathbf{P}$  is the first Piola-Kirchhoff stress tensor that is a function of the constitutive parameters  $\xi$  and the experimental strain field  $\boldsymbol{\varepsilon}^{\text{exp}}$ .  $\bar{\mathbf{T}}$  is the first Piola-Kirchhoff stress vector calculated on the boundary  $\Gamma_0^f$  where surface forces are applied.  $\mathbf{U}^*$  can be any kinematically admissible virtual field and  $\text{Grad} \mathbf{U}^*$  is the respective gradient calculated with respect to the reference coordinates of the body.  $dV$  and  $dS$  are the infinitesimal volume and area of the body in the reference configuration  $\Omega_0$ .  $n_v$  and  $n_t$  are the number of virtual fields selected and time steps considered, respectively. This large strain formulation is a convenient description to write the principle of virtual work, since for the computation of the internal and external work the geometric quantities are defined on the reference configuration. More details on this formulation can be found in [6].

One of the key parts of this method are the virtual fields selected to build the objective function, which can be any continuous and differentiable function. Nevertheless, these functions are usually selected from a set of kinematically admissible functions, i.e. it is required that the virtual fields vanish on the boundaries of prescribed displacement. In this work, the virtual fields are developed manually, which is addressed in the section Manually Defined Virtual Fields. The other key part of this method is the reconstruction of the stress field from the strain field  $\boldsymbol{\varepsilon}^{\text{exp}}$ , which is derived from the measured displacement field. Usually, the displacement field is acquired on the surface of the specimen and, therefore, to reconstruct the stress field, the plane stress conditions are assumed. Moreover, to reconstruct the stress field, it is necessary to adopt *a priori* a constitutive model to make the link between strains and stresses. In this work, the adopted constitutive model is defined by: (1) linear isotropic elastic behavior (generalized Hooke's law) and; (2) plastic behaviour described by the orthotropic Hill'48 yield criterion and isotropic hardening (Swift's law). The calibration of the plastic part of the model is the focus of the present work, whereas the material parameters that govern elastic part are assumed to be known. Regarding the plastic behaviour, the equivalent Hill'48 yield criterion assumes the following form in plane stress conditions:



$$\bar{\sigma}^2 = F\sigma_{yy}^2 + G\sigma_{xx}^2 + H(\sigma_{xx} - \sigma_{yy})^2 + 2N\sigma_{xy}^2, \quad (5.2)$$

where  $\sigma_{xx}$ ,  $\sigma_{yy}$  and  $\sigma_{xy}$  are the components of the stress tensor with respect to the anisotropic material axes.  $F$ ,  $G$ ,  $H$  and  $N$  are the constitutive parameters that must be calibrated. Nevertheless, the relation  $G + H = 1$  is assumed which leaves only  $F$ ,  $G$  and  $N$  to be identified. The isotropic hardening law (Swift's law) has the following form:

$$\sigma_y(\bar{\varepsilon}^p) = K(\varepsilon_0 + \bar{\varepsilon}^p)^n, \varepsilon_0 = \left(\frac{\sigma_0}{K}\right)^{(1/n)} \quad (5.3)$$

where  $\sigma_0$ ,  $K$  and  $n$  are the material parameters.  $\bar{\varepsilon}^p$  is the equivalent plastic strain. Thus, the adopted model contains 6 material parameters which must be identified according to the studied material.

The methodology presented in this section was implemented in an in-house code using the programming language Fortran. This code contains bilinear shape functions to derive the strain field from the measured displacement field. Due to the non-linearity of the model, the stress reconstruction is performed using an algorithm of the type Backward-Euler return [7]. The minimization of the objective function is conducted by the gradient-based Levenberg-Marquardt optimization method.

## The Butterfly Test

The butterfly test was first proposed by Souto et al. [3]. The geometry of the specimen was numerically designed through a shape optimization procedure which aimed a heterogeneous test to calibrate complex constitutive models for sheet metals. The optimization process was governed by an objective function that rated the information provided by the test in terms of range and diversity of strain states and strain level reached. The final geometry was able to produce a spectrum of strain states ranging from simple shear to plane strain. More recently, this final geometry was adapted by Aquino et al. [4] to facilitate the cutting process of the specimen. This adapted specimen was experimentally validated using special grips (Fig. 5.1a), and an attempt to calibrate a complex anisotropic constitutive model was performed through the inverse method FEMU. The specimen was obtained from 0.7 mm thick sheet metal of a DC04 mild steel. The tests were performed on a common tensile machine. The DIC-system employed to carry out the measurements was the ARAMIS 3D 5M system developed by GOM. Figure 5.1b shows the strain distribution in the principal strain space for a displacement of the tool equal to 7.1 mm. As can be seen, the adapted geometry produces a range of strains from simple shear to plane strain.

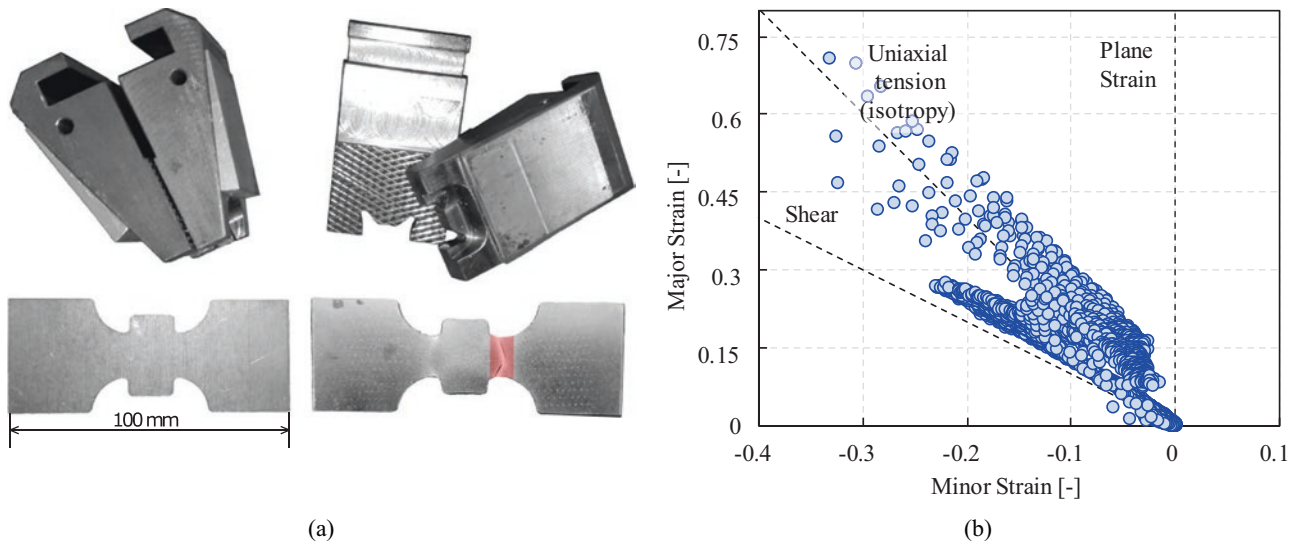


**Fig. 5.1** (a) Grips and specimen used for the adapted butterfly test and (b) principal strains distribution for a tool displacement of 7.1 mm

In this work, the same experimental data used by Aquino et al. [4] is adopted. The displacement fields acquired for the specimen with the rolling direction orientated along the traction axis are used. These displacements fields are projected onto a 2D mesh generated by the Abaqus software (Fig. 5.2a) that represents one-fourth of specimen, in order to be processed by the VFM. A total of 398 steps from the load/displacement history of the grip are considered (Fig. 5.2b). Only the load history between the two red dots is considered, because most of the points in the early stages of the test have a low value of strain and were highly affected by noise. Yet, larger load histories were analysed, and the results were not significantly affected.

## Manually Defined Virtual Fields

In non-linear cases, the VFM relies on the minimization of Eq. (5.1) to retrieve the constitutive parameters. As mentioned before, the virtual fields selected to build the objective function have a fundamental role in the results of the identification. Currently, there are three main approaches to select a suitable set of virtual fields, two of them rely on automatic procedures to select the virtual fields and require a low-level of user's intervention [6, 8]. The other approach, called manually defined virtual fields, depends exclusively on the user's intervention, since it is the user that must develop the suitable set according to the boundary conditions of the test. This last strategy has been the most used and its main advantages are the computational cost and the ease of implementation. For these reasons, this is the strategy adopted in the present work.

Generally, the manually defined virtual fields are developed using polynomial and/or periodic functions. These functions are manipulated to generate kinematically admissible virtual fields [5]. In terms of objective function, the components of the virtual field gradient can be seen as weights for the components of the stress tensor. Specially in anisotropic plasticity, all the components of the stress tensor contain information about the yield criterion, hence must be considered within the identification process. Based on these considerations, a set of 8 virtual fields is developed and the influence of the number of virtual fields on the identification results is assessed. The developed virtual fields can be written as:

$$\mathbf{U}^{*(l)} = \begin{cases} U_x^* = 0 \\ U_y^* = \frac{Y}{L} \end{cases}, \quad (5.4)$$

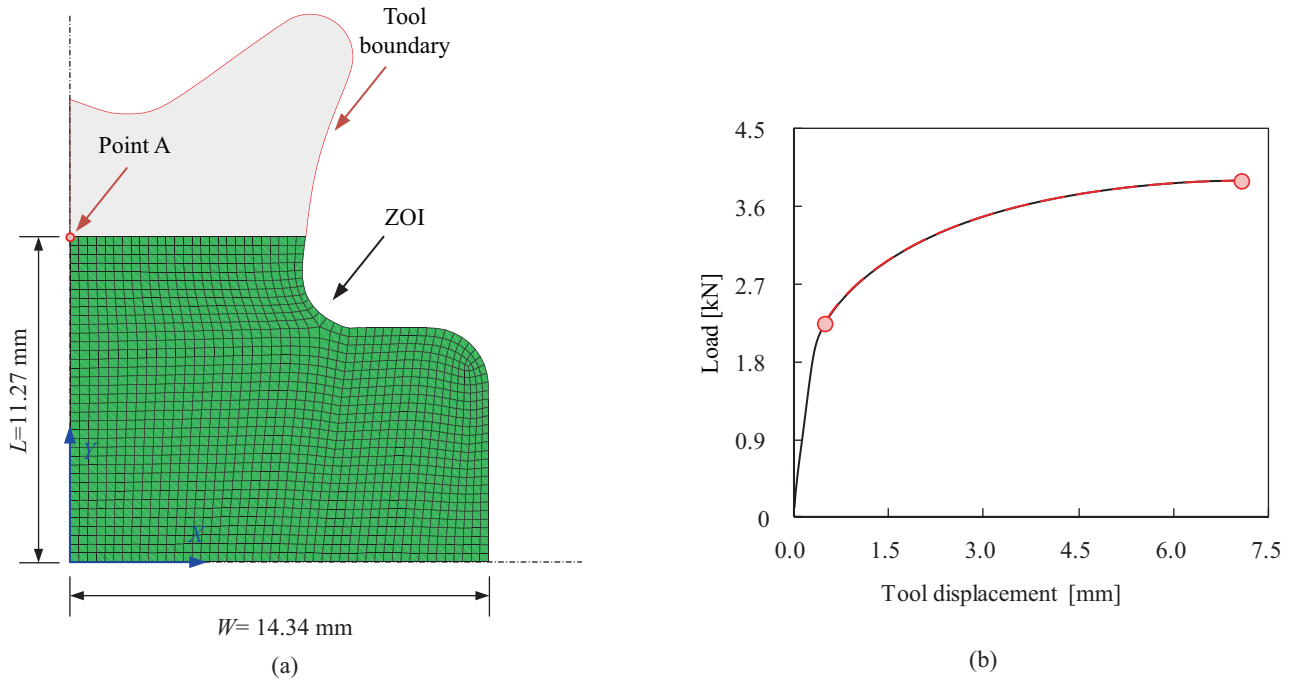


**Fig. 5.2** (a) Zone of interest (ZOI) and regular mesh used for the VFM identification. (b) Load history for the butterfly test

$$\mathbf{U}^{*(2)} = \begin{cases} U_x^* = \frac{X(Y^2 - YL)}{WL^2}, \\ U_y^* = 0 \end{cases}, \quad (5.5)$$

$$\mathbf{U}^{*(3)} = \begin{cases} U_x^* = \sin\left(\frac{X}{W}\pi\right)\sin\left(\frac{Y}{L}\pi\right), \\ U_y^* = 0 \end{cases}, \quad (5.6)$$

$$\mathbf{U}^{*(4)} = \begin{cases} U_x^* = 0 \\ U_y^* = \sin\left(\frac{X}{W}\pi\right)\sin\left(\frac{Y}{L}\pi\right), \end{cases} \quad (5.7)$$

$$\mathbf{U}^{*(5)} = \begin{cases} U_x^* = 0 \\ U_y^* = \frac{XY(Y-L)}{WL^2}, \end{cases} \quad (5.8)$$

$$\mathbf{U}^{*(6)} = \begin{cases} U_x^* = 0 \\ U_y^* = \frac{Y^2(L-Y)}{L^3}\sin\left(\frac{\pi X}{W}\right), \end{cases} \quad (5.9)$$

$$\mathbf{U}^{*(7)} = \begin{cases} U_x^* = \frac{L^3 - Y^3}{L^3}\sin\left(\frac{\pi X}{W}\right), \\ U_y^* = 0 \end{cases}, \quad (5.10)$$

$$\mathbf{U}^{*(8)} = \begin{cases} U_x^* = 0 \\ U_y^* = \frac{YL^2 - Y^3}{L^3}\sin\left(\frac{\pi X}{W}\right), \end{cases} \quad (5.11)$$

where  $W$  and  $L$  are the maximum value of the width and length of the zone of interest (ZOI) of the specimen surface in the reference configuration (see Fig. 5.2a).  $X$  and  $Y$  are the coordinates in the reference configuration. In case of static equilibrium, the first virtual field is the only one that gives a non-zero value of internal virtual work, which should be balanced with the external virtual work. It also gives maximum weight to the normal component of the stress tensor in the  $y$ -direction and neglects the remaining components. The other virtual fields distribute the weight between two components, normal and shear components.

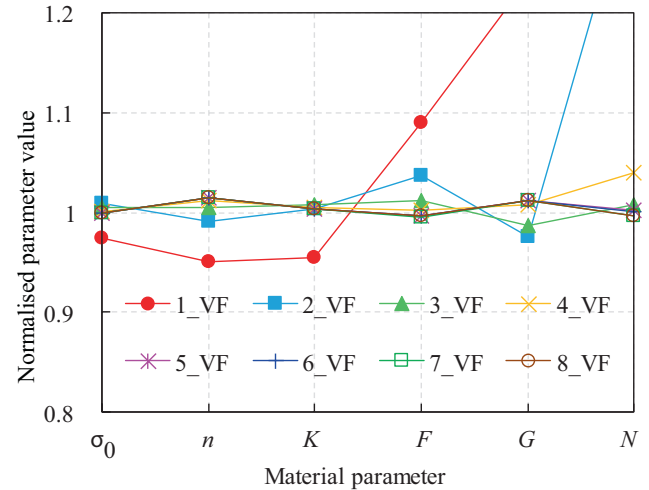
In order to assess the influence of the number of virtual fields in the identification process, virtual experimental data generated by finite element (FE) analysis is used. A two-dimensional FE model representing one-fourth of the butterfly test is built assuming plane stress conditions. A displacement of 1.5 mm is prescribed to a rigid tool, which is modelled assuming tie contact with the irregular boundary on top of the specimen (see Fig. 5.2a). A reference set of material parameters representing a mild steel is adopted and its values are listed in Table 5.1. The test is simulated in Abaqus standard software and the displacement field of a total of 375 load steps is retrieved to build the objective function (Eq. (5.1)).

A total of 8 identifications with an increasing number of virtual fields are performed. The presented virtual fields are added to the objective function in order to enrich the identification process. The results are presented in Fig. 5.3, in which the value of the optimized parameter is normalised by the respective reference value. The results show that for one virtual field (Eq. (5.4)) the errors are the highest, particularly for the yield criterion parameters. Nevertheless, the results are significantly improved when the second virtual field (Eq. (5.5)) is added and tend to stabilize for 5 virtual fields. For a total of 8 virtual fields, the maximum error attained is lower than 1.5% and corresponds to the parameter  $n$ .

This confirms that the number of virtual fields plays an important role in the accuracy of the VFM. Moreover, the set of the developed virtual fields is able to retrieve simultaneously the hardening law and yield criterion parameters using a single virtual butterfly test. This also demonstrates that the butterfly test provides a heterogeneous strain field that contains enough information to identify the present model.

**Table 5.1** Reference material parameters for Swift's hardening law and Hill'48 yield criterion

Swift's hardening law			Hill'48 yield criterion		
$\sigma_0$ (MPa)	$n$	$K$ (MPa)	$F$	$G$	$N$
160	0.26	565	0.2782	0.3731	1.5568

**Fig. 5.3** Influence of the number of virtual fields on the identification results

## Identification of Material Parameters: Results and Analysis

In this section, it is assessed the performance of the VFM combined with the experimental database acquired from the butterfly test to calibrate the constitutive model composed by Hill'48 yield criterion and Swift's hardening law. According to the results of the previous section, the 8 virtual fields presented are used to build the objective function. Moreover, since the optimization method is a gradient-based, the sensitivity to the initial set of parameters given to start the optimization process is also assessed. The initial sets are arbitrarily chosen.

The obtained set of parameters is presented in Table 5.2. Regardless of the initial set of parameters, the results converged always for the same solution set shown in Table 5.2. Moreover, Table 5.2 also shows the yield stress values and plastic anisotropic parameters calculated based on the retrieved parameters. The plastic anisotropic coefficient at 0 degrees (rolling direction) presents a value characteristic of mild steel [9], whereas the other two coefficients present values lower than the characteristic ones of this material.

The evolution of the internal virtual work calculated using the parameters of Table 5.2 and the first virtual field (Eq. (5.4)), and the evolution of the external virtual work calculated based on the measured load are presented in Fig. 5.4a. The evolutions of the internal and external virtual works show a good agreement. Nevertheless, the internal virtual work evolution suffers from minor oscillations, which can result from the presence of noise in the full-field measurements.

In order to check the validity of the retrieved parameters, the butterfly test is simulated with a two-dimensional FE model assuming plane stress conditions and using the retrieved parameters. The results of the force evolution for the FE model are compared with the measured load in Fig. 5.4b. Note that the results are plotted for the displacement of point A (see Fig. 5.4b), in order to minimise the impact of a possible sliding under the grips. Figure 5.4b shows a good agreement between the two load curves and a slight overestimation of the displacement at the end of the test. These results confirm that the material behaviour for the rolling direction is well captured by the constitutive model and its retrieved material parameters.

**Table 5.2** Identification results for Swift's hardening law and Hill'48 yield criterion

Swift's hardening law			Hill'48 yield criterion		
$\sigma_0$ (MPa)	$n$	$K$ (MPa)	$F$	$G$	$N$
166.4	0.31	593.9	0.5503	0.3439	1.4797
Normalised yield stresses $\sigma_\alpha$			Plastic anisotropic coefficients $r_\alpha$		
$\sigma_0$	$\sigma_{45}$	$\sigma_{90}$	$r_0$	$r_{45}$	$r_{90}$
1.0	1.02	0.91	1.90	1.15	1.19

Normalised yield stress values and plastic anisotropic coefficients calculated based on the obtained parameters

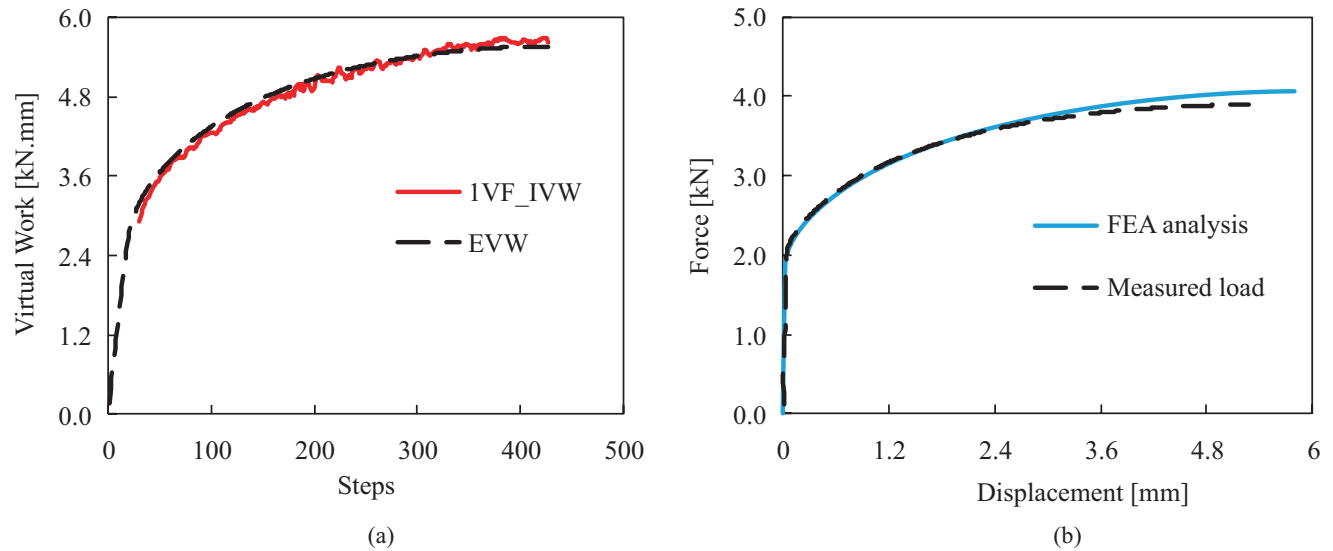


**Fig. 5.4** (a) Evolution of the internal (virtual field of Eq. (5.4)) and external virtual work and (b) comparison of the measured load with the predicted load using FE analysis and the retrieved parameters presented in Table 5.2

## Conclusions

The present work is a first attempt to link an optimized heterogeneous mechanical test with VFM. The aim is to propose a strategy to identify all the parameters of an anisotropic constitutive model using a single test. A set of manually defined virtual fields to link the VFM and the butterfly test is proposed. This set is analysed using virtual experimental data, generated according to the adopted constitutive model. The analysis shows the dependence of the VFM on the number of virtual fields used to build the objective function. In this specific case, for a number superior to 5 virtual fields, there is a reasonable error (maximum error lower than 1.5%) in the identification results. Finally, the constitutive model composed by Hill'48 yield criterion and Swift's hardening law is calibrated using experimental data from a single test on a mild steel. The results revealed insensitivity of the VFM to the initial set of parameters used to start the identification process. Regarding the retrieved parameters, its performance is assessed through the predicted anisotropic plastic coefficients and FE analysis of the test. The predicted anisotropic plastic coefficient for the rolling direction is characteristic of mild steel, but the remaining coefficients suggest that the model was unable to predict them. The FE analysis of the test with the retrieved material parameters confirm this conclusion. The load curve predicted by the FE model shows a good agreement with the experimentally measured load, meaning that the overall behaviour of the material for the rolling direction was well captured. Nevertheless, a thorough study on the influence of the DIC parameters on the acquired data from the butterfly test should be performed.

**Acknowledgements** The authors acknowledge the financial support of FCT under the projects PTDC/EME-APL/29713/2017 (CENTRO-01-0145-FEDER-029713), PTDC/EMS-TEC/6400/2014 (POCI-01-0145-FEDER-016876), PTDC/EME-EME/31243/2017 (POCI-01-0145-FEDER-031243) and PTDC/EME-EME/30592/2017 (POCI-01-0145-FEDER-030592) by UE/FEDER through the programs CENTRO 2020 and COMPETE 2020, and UID/EMS/00481/2013-FCT under CENTRO-01-0145-FEDER-022083. The authors also would like to acknowledge the Région Bretagne (France) for its financial support. J.M.P. Martins is also grateful to the FCT for the PhD grant SFRH/BD/117432/2016.

## References

1. S. Bruschi, T. Altan, D. Banabic, et al., Testing and modelling of material behaviour and formability in sheet metal forming. *CIRP Ann. Manuf. Technol.* **63**, 727–749 (2014)
2. M.A. Sutton, J.-J. Orteu, H. Schreier, *Image Correlation for Shape, Motion and Deformation Measurements* (Springer, Boston, 2009)
3. N. Souto, A. Andrade-Campos, S. Thuillier, Mechanical design of a heterogeneous test for parameters identification. *Int. J. Mater. Form.* **10**(3), 353–367 (2017)
4. J. Aquino, A. Andrade-Campos, S. Thuillier, Design of heterogeneous mechanical tests – numerical methodology and experimental validation. *Strain* **55**, e12313 (2019)
5. F. Pierron, M. Grédiac, *The Virtual Fields Method: Extracting Constitutive Mechanical Parameters from Full-Field Deformation Measurements* (Springer, New York, 2012)
6. A. Marek, F.M. Davis, M. Rossi, F. Pierron, Extension of the sensitivity-based virtual fields to large deformation anisotropic plasticity. *Int. J. Mater. Form.* **12**, 457–476 (2019)
7. M. Crisfield, *Non-Linear Finite Element Analysis of Solids and Structures*, vol 1 (Wiley, Chichester, 1991)
8. F. Pierron, S. Avril, V.T. Tran, Extension of the virtual fields method to elasto-plastic material identification with cyclic loads and kinematic hardening. *Int. J. Solids Struct.* **47**(22), 2993–3010 (2010)
9. S.L. Zang, S. Thuillier, A. Le Port, P.Y. Manach, Prediction of anisotropy and hardening for metallic sheets in tension, simple shear and biaxial tension. *Int. J. Mech. Sci.* **53**, 338–347 (2011)



## Chapter 6

# One-Dimensional Heat Source Reconstruction Applied to Phase Transforming Superelastic Ni-Ti Wire

Antoine Jury, Xavier Balandraud, Luděk Heller, Eduardo Alarcon, and Miroslav Karlik

**Abstract** The study deals with the reconstruction of heat sources originating from deformation processes in metals. A one-dimensional method to be applied on wires or bars is introduced and tested on superelastic NiTi wire subjected to force-controlled loading and unloading. Infrared thermography was used for this purpose. Thermal data were then processed by heat source reconstruction technique using a one-dimensional version of the heat diffusion equation. Attention was paid to the identification of the heat exchanges with the specimen's environment, in particular by convection to the air of ambient temperature. The sensitivity of the method to the degree of spatio-temporal filtering was also tested. Finally, the localization of martensitic transformation in superelastic NiTi was evaluated using the proposed method. It is shown that under force-control regime the phase transformation proceeds in two time-shifted bursts, where each of bursts consists in several displaced and nearly simultaneous transforming zones. This transformation sequence is rationalized by fast latent heat release from the transforming zone upon load control regime, which leads to overheating of surrounding zones thus temporarily suppressing their transformation.

**Keywords** Shape-memory alloy · NiTi · Infrared thermography · Superelasticity · Heat source reconstruction

## Introduction

Among the shape memory alloys (SMAs), near-equiatomic nickel-titanium (NiTi) alloys are the most frequently selected in engineering applications [1]. This is due to their attractive functional properties exhibited by these alloys, such as shape memory effects, superelasticity and high damping capacity. These macroscopic properties originate from a diffusionless

---

A. Jury (✉)

Nuclear Physics Institute of the CAS, Rež, Czech Republic

Institute of Physics of the CAS, Prague, Czech Republic

Czech Technical University in Prague, Faculty of Nuclear Sciences and Physical Engineering, Department of Materials, Prague, Czech Republic

Université Clermont Auvergne, CNRS, SIGMA Clermont, Institut Pascal, Clermont-Ferrand, France  
e-mail: [jury@fzu.cz](mailto:jury@fzu.cz)

X. Balandraud

Université Clermont Auvergne, CNRS, SIGMA Clermont, Institut Pascal, Clermont-Ferrand, France  
e-mail: [xavier.balandraud@sigma-clermont.fr](mailto:xavier.balandraud@sigma-clermont.fr)

L. Heller · E. Alarcon

Nuclear Physics Institute of the CAS, Rež, Czech Republic

Institute of Physics of the CAS, Prague, Czech Republic

e-mail: [heller@fzu.cz](mailto:heller@fzu.cz); [alarcon@fzu.cz](mailto:alarcon@fzu.cz)

M. Karlik

Czech Technical University in Prague, Faculty of Nuclear Sciences and Physical Engineering, Department of Materials, Prague, Czech Republic

Charles University, Faculty of Mathematics and Physics, Department of Physics of Materials, Prague, Czech Republic  
e-mail: [miroslav.karlik@fjfi.cvut.cz](mailto:miroslav.karlik@fjfi.cvut.cz)

solid-solid phase transformation that can be thermally or mechanically induced. According to the thermomechanical heat treatment, environmental conditions (ambient temperature and heat exchange conditions) and mechanical loading (stress level and loading rate), the tensile response of polycrystalline NiTi-based SMAs may exhibit the propagation of phase transformation fronts [2]. The latter were extensively studied in the literature. They were described first in [3] and then investigated in many studies (see for instance [4–7]). The reader is also referred to [8] for details on the origin of these phase transformation fronts.

The stress-induced phase transformation in NiTi wires subjected to tension is usually tracked in-situ by measuring sudden changes of strain and strain rates, both evaluated either integrally using displacement of the testing machine's cross-head, more accurately using clip-on extensometer, or locally using digital image correlation. Thermal Field Measurements (TFM), based on the use of an infrared (IR) camera [4–6, 9–11] are an alternative way of tracking in-situ the phase transformation in NiTi. In general, TFM takes advantage of temperature changes that always accompany material stretching due to thermomechanical couplings and intrinsic dissipation: thermoelastic coupling, latent heat due to solid-solid phase change, self-heating due to plasticity, viscosity or fatigue damage. The reconstruction of heat sources from temperature changes is possible by using the heat diffusion equation, which in the case of wires can be reduced into 1-D considering axial symmetry and seeking for heat sources integrally over the entire wire cross-section. By *heat source*, we mean the heat power density produced or absorbed by the material itself (i.e. not due to conduction, convection and radiation). To the best knowledge of the authors, one dimensional heat source reconstruction has never been carried out on NiTi subjected to force controlled tensile loadings. In fact, the phase transformation in NiTi normally proceeds under a constant plateau-stress but it cannot under the force controlled loading regime as the latent heat of rapidly transformed zones increases the temperature of their surroundings where the phase transformation may be temporarily suppressed. It may lead to sudden bursts and arrests of the phase transformation along the wire axis appear in NiTi wire. Hence, superelastic NiTi subjected to the force controlled regime represents a perfect example case for present work aiming at the development and testing of a method for one-dimensional reconstruction of heat sources evolving dynamically in time and heterogeneously in space.

The paper is divided into three sections as follows. The first section provides the general background on 1D heat source reconstruction. The second section presents the NiTi material experimental set-up. Finally, results are given and discussed in the third section, with a focus on the spatio-temporal features of phase change fronts along the NiTi wire during a load-unload cycle.

## Methodology for Heat Source Reconstruction

Materials produce or absorb heat when subjected to mechanical loadings. As indicated in the introduction, heat sources are defined as the heat power densities (in  $\text{W m}^{-3}$ ) resulting in a temperature changes. In metals, heat is produced or absorbed as a consequence of different deformation and chemical processes. For instance, the thermomechanical coupling upon elastic deformation in metals, called thermoelasticity, results in a heat production inversely proportional to the applied stress rate. On the other hand, phenomena related to energy dissipation such as plasticity, viscosity, fatigue damage always results in irreversible heat production. In NiTi, an additional thermomechanical coupling is involved: a production or absorption of latent heat associated with the austenite-to-martensite or martensite-to-austenite phase changes, respectively. Using the heat diffusion equation, heat sources can be reconstructed from the temperature fields captured by IR thermography at the specimen surface [10–17]. In the present study, we used the so-called 1D approach [10, 13, 14] for reconstructing the heat sources of NiTi wires subjected to force-controlled tensile loadings.

Let us consider a straight NiTi wire whose axial coordinate is denoted  $z$ . The simplified local form of the heat equation (6.1) provides the relationship between the temperature change  $\Theta(z, t)$  and the heat source  $s(z, t)$  (here expressed in  $^{\circ}\text{K s}^{-1}$  resulting from its reduction by the product of the density  $\rho$  and the specific heat  $C$ ). The latter quantity is defined with respect to a reference configuration, considered in practice as the unloaded state in thermal equilibrium. The parameter  $D$  is the thermal diffusivity of the material (in  $\text{m}^2 \text{s}^{-1}$ ) and  $\tau$  is a characteristic time (in s) characterizing the heat exchanges between the wire lateral surface and its surroundings. The calculation of heat source from the right-hand side of Eq. (6.1) was implemented using derivative Gaussian filters, as detailed in [16].

$$s(z, t) = \frac{d\Theta(z, t)}{dt} + \frac{\Theta(z, t)}{\tau} - D \frac{d^2\Theta(z, t)}{dz^2} \quad (6.1)$$

The characteristic time  $\tau$  was evaluated from a natural cooling of the sample to ambient temperature after its homogeneous heating without any contact with the jaws of the testing machine. In practice, the specimen was suspended in air with a piece of tape. Figure 6.1a shows the temperature change  $\theta(t)$  during a homogeneous natural return to ambient temperature



after homogeneous heating using a hot air gun. In this way, we consider only the heat exchange of the lateral surface of the specimen with its surroundings. As the heat source is equal to zero (the specimen did not produce heat), Eq. (6.1) becomes:

$$0 = \frac{d\Theta}{dt} + \frac{\Theta}{\tau} \quad (6.2)$$

If  $\tau$  is a constant, the solution of Eq. (6.2) is a decreasing exponential function of the cooling duration. Assuming that  $\tau$  may potentially depend on the temperature change  $\Theta$ , it was proposed to identify the value of  $\tau(\Theta)$  for different portions of the curve  $\Theta(t)$  as illustrated in Fig. 6.1a. A minimization algorithm was employed with a correlation index equal to 0.995 as stopping criteria. Results are presented in Fig. 6.1b, each point corresponding to the value of  $\tau$  for a given portion of the curve. A linear equation was identified for the function  $\tau(\Theta)$ . Figure 6.1c shows the residual heat sources obtained using experimental data. The latter corresponds to the right-hand side of Eq. (6.2) as calculated using the linear fit of  $\tau(\Theta)$  (Fig. 6.1b). In fact, the residual heat source values should be equal to zero during this natural return to ambient temperature. The curve in Fig. 6.1c thus provides an estimation of the measurement resolution of the heat source in the case of homogeneous temperature fields: a few tenth of one  $\text{K s}^{-1}$  at the maximum.

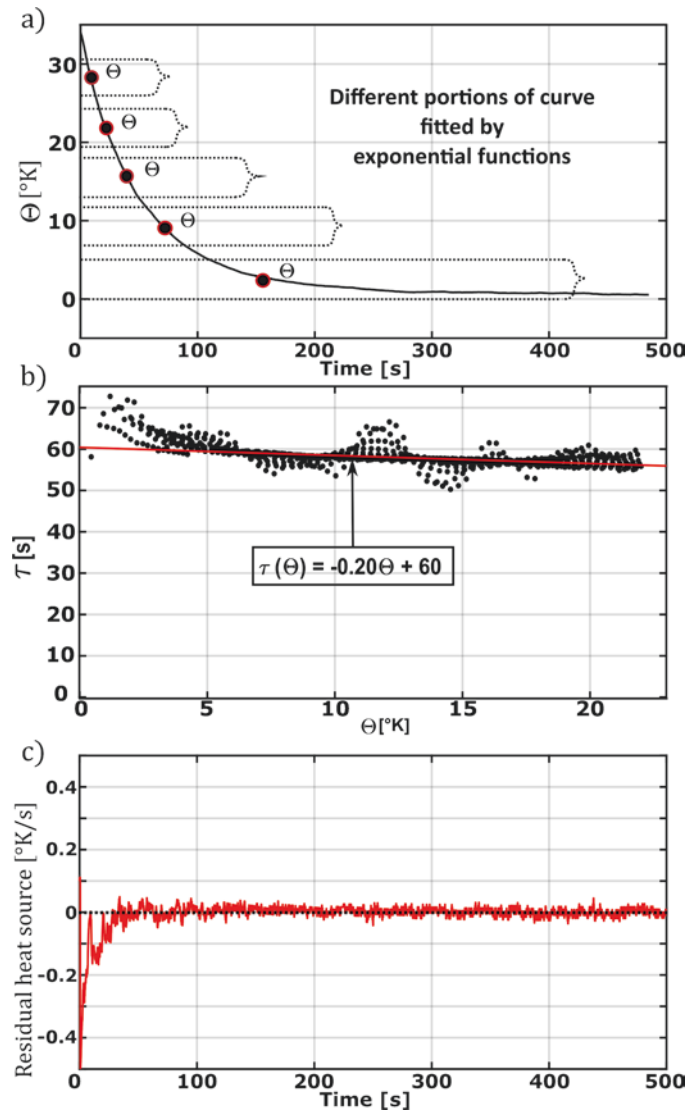


**Fig. 6.1** Identification of the characteristic time  $\tau$ : (a) temperature change  $\Theta$  during a homogeneous natural return to ambient temperature, (b) values of  $\tau$  as a function of  $\Theta$ , (c) residual heat sources obtained after heat source reconstruction

The thermal diffusivity  $D$  was measured using a similar approach. We calculated Eq. (6.1) during the natural cooling after a local heating. This time, the specimen was clamped in the jaws of the machine, then heated locally by gently applying a pressure in the middle of the specimen with the fingers. A unique value of  $D$  was identified at room temperature equal to  $2.7 \times 10^{-6} \text{ m}^2 \text{ s}^{-1}$ , which is in agreement with [15].

## Experimental Set-Up

A Cedip Jade III-MWIR infrared camera was employed to capture the temperature fields after calibration in the range [268 K; 333 K]. The mechanical loading was applied with an MTS uniaxial machine equipped with a 15 kN load cell. Figure 6.2a presents a schematic view of the NiTi wire during heat treatment by Joule effect. Figure 6.2b, c show the wire placed in the mechanical test configuration. It can be noticed that two reference elements made of the same material were added on both sides of the mechanically tested specimen: each reference was clamped in a jaw of the testing machine. This experimental device was introduced in [11]. Effects of changes in the specimen's environment during a test can be tracked thanks to these reference elements: change in temperature of the jaws of the testing machine, in temperature and flow of the ambient air, and more generally any change of the testing room conditions (machines, persons, walls, etc.). The NiTi wire and its two reference elements were painted in black to maximize the thermal emissivity, as well as the close environment to limit parasitic reflections: see Fig. 6.2c.

The specimen was a Ni-Ti SMA wire of 1.78 mm of diameter, supplied by Fort Wayne Metals. It was preliminary heat treated by Joule effect using a 50 A current for a period of 3.5 s as presented in [18]. It was then subjected to mechanical training at ambient temperature ( $\approx 300 \text{ K}$ ) for 20 cycles at  $\pm 392 \text{ N s}^{-1}$  between 20 N and 1984 N. Lengths  $L1$  and  $L2$  in Fig. 6.1a were equal 40 mm and 80 mm, respectively. These lengths were used for both the annealing treatment and the mechanical loadings. The wire is fully austenitic at ambient temperature in the stress-free state.

A tensile test was carried out on the specimen in a force-controlled mode with a rate of  $\pm 20 \text{ N s}^{-1}$ , and same minimum and maximum forces as for the preliminary mechanical training. The room temperature was 300 K. The spatial resolution of the full-field thermal measurement was equal to  $148.5 \mu\text{m}$  (will be referred to as  $dz$  in the following). Recording frequency was set to 162 Hz, leading to a temporal resolution of 6.17 ms (will be referred to as  $dt$ ). As we are interested in localized phase transformation phenomena (both in time and in space), there is a compromise to be found between measurement resolution (improved by filtering) and spatial/temporal resolution (penalized by filtering and derivation) for the calculation of the heat sources from Eq. (6.1).

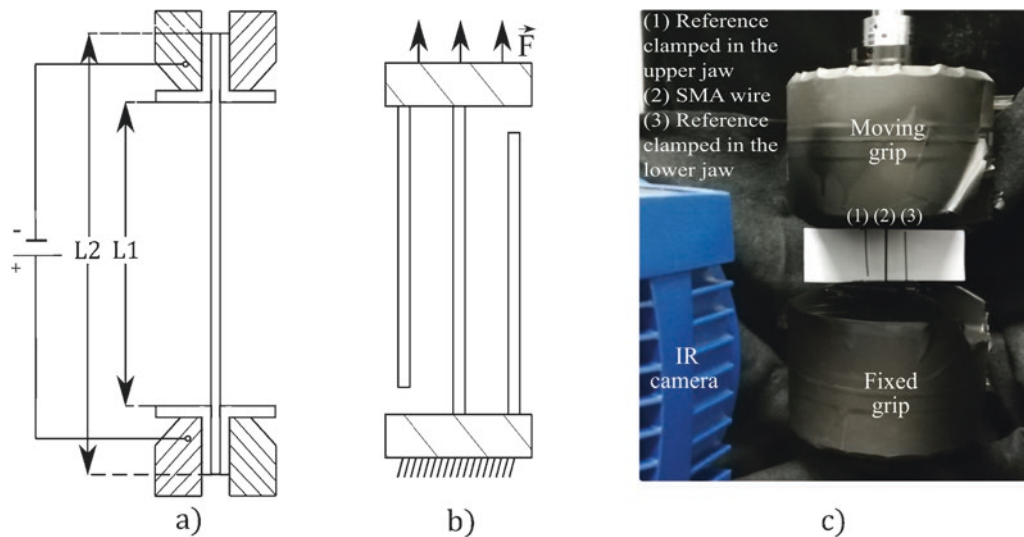


**Fig. 6.2** (a) Schematic view of the NiTi wire during heat treatment by Joule effect, (b) schematic view of the specimen with two reference elements for thermomechanical analysis, (c) photo of the specimen and reference elements placed in the jaws of the testing machine

## Analysis

Heat source reconstruction was implemented using first-derivative (in time) Gaussian filter in time for the term  $d\theta/dt$  and second-derivative (in space) Gaussian filter in space for the term  $d^2\theta/dz^2$ . No filter was applied to the term  $\theta/\tau$ . Figure 6.3 shows the influence of the standard deviations  $\sigma_{space}$  (in mm) and  $\sigma_{time}$  (in s) of the two Gaussian functions on the spatio-temporal heat source distribution around a short and localized event (see Fig. 6.4 for a global view along the whole duration of the test and the whole length of the wire). The kernel sizes of the convolution windows were set to  $\pm 4.5\sigma_{space}$  in space and  $\pm 3\sigma_{time}$  in time, i.e. 9 and 6 times the standard deviations respectively. In practice,  $\sigma_{space}$  and  $\sigma_{time}$  were expressed in terms of multiple of the spatial and temporal resolutions of the thermal fields:

$$\sigma_{space} = k_{space} dz \text{ and } \sigma_{time} = k_{time} dt \quad (6.3)$$

where  $k_{space}$  and  $k_{time}$  are integers.

Figure 6.3a presents the temperature change  $\theta(z, t)$  of a strong calorific event that we used to investigate appropriate filter parameters. Figure 6.3b shows the heat sources that were reconstructed using only a finite difference (FD) scheme

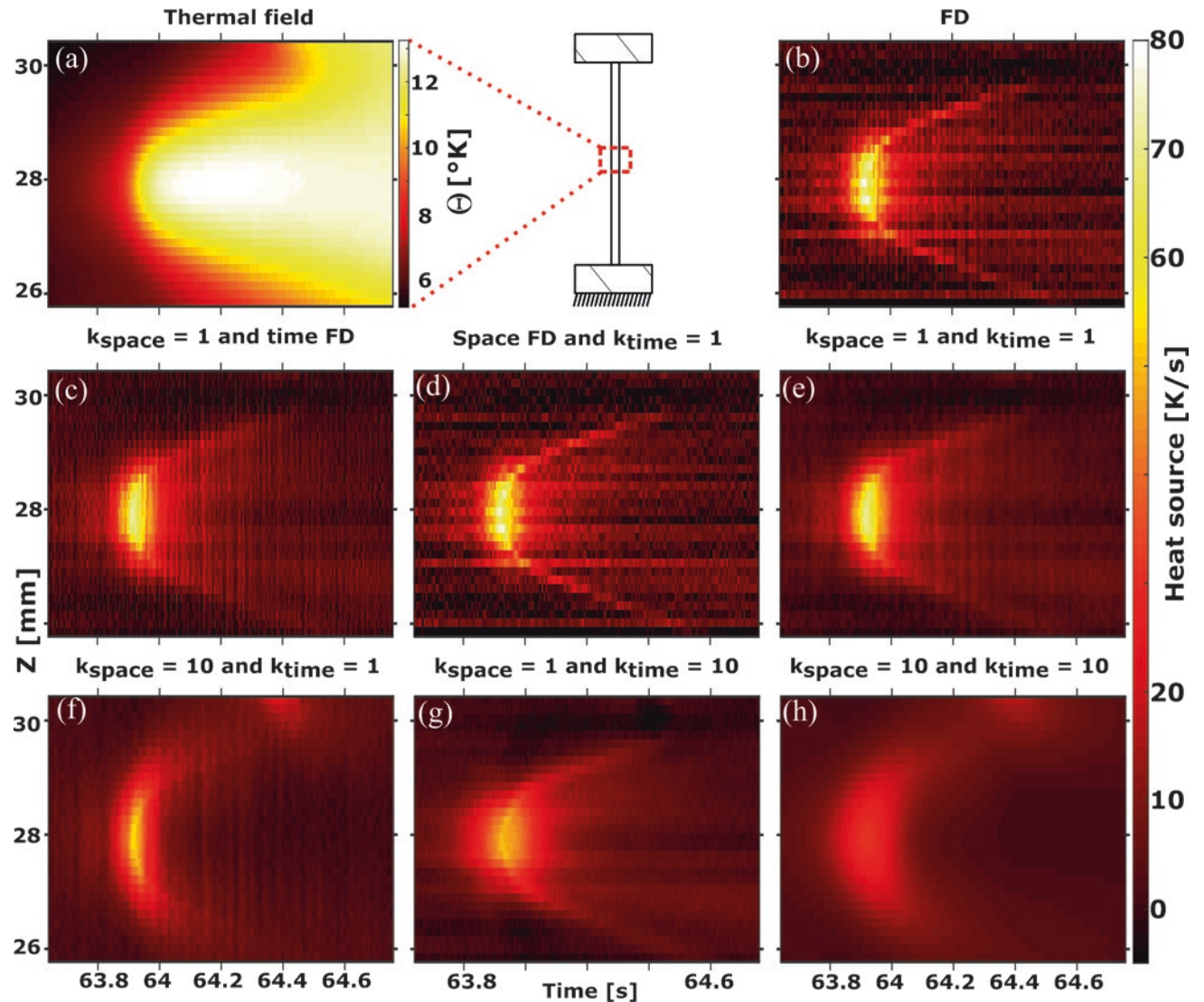


**Fig. 6.3** (a) Temperature change  $\theta$  around a short and localized calorific event, (c–h) influence of the standard deviations in terms of multiples of spatial ( $k_{space}$ ) and temporal ( $k_{time}$ ) resolutions  $\sigma_{space}$  and  $\sigma_{time}$  of the Gaussian derivative filters on the reconstructed heat sources as compared with the solution via Finite differences (FD) method (b)

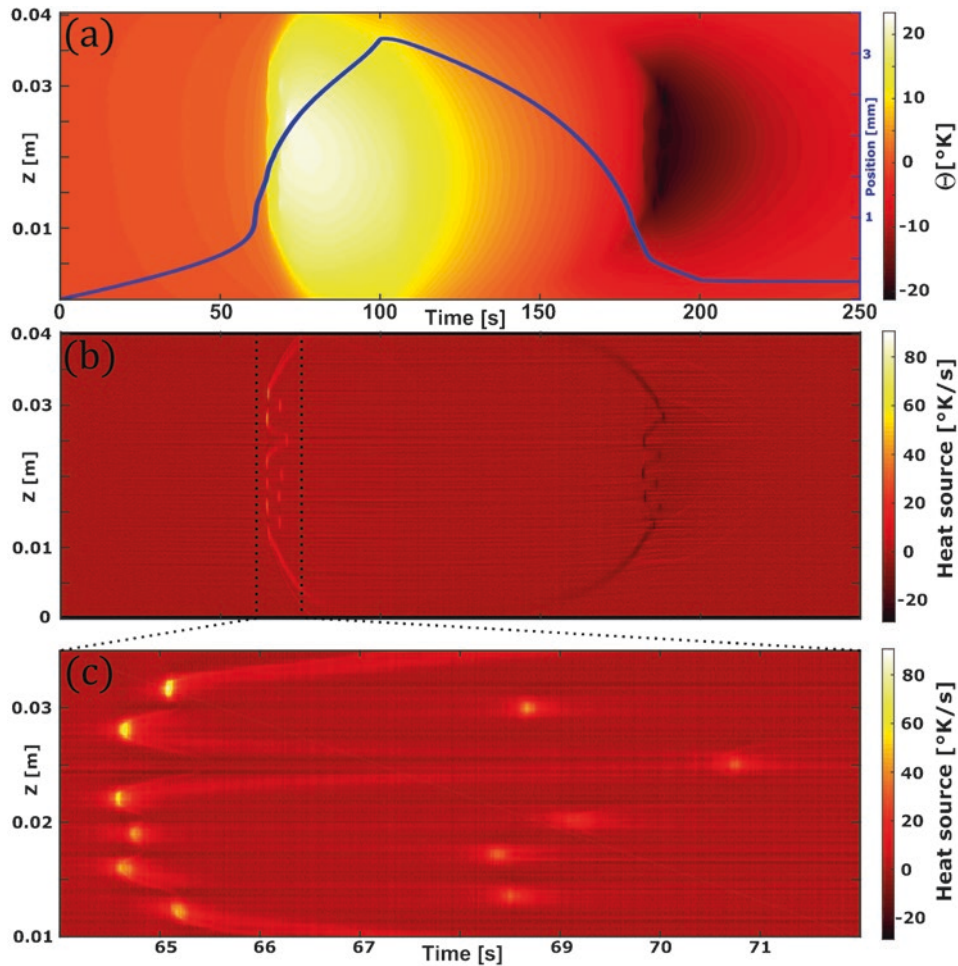


**Fig. 6.4** Load-unload cycle: (a) temperature change  $\Theta$  as a function of time and space. The displacement of the actuator is also plotted as a function of time; (b) heat source reconstructed from the temperature changes, mapped over the whole duration of the test, (c) zoom on the heat source map over the short period revealing strong heat source activity

named forward time centered space of the right-hand side of Eq. (6.1), without filtering. Figure 6.3c–h show the heat sources reconstructed using Gaussian derivation filters for the two derivative terms. It is worth noting that, by construction, heat sources are much more localized in time and in space than the temperatures. Indeed, heat source reconstruction is a physics-based data processing that removes heat exchanges with the specimen surroundings and the heat conduction through the axis of the specimen. It can be also noted that filtering tends to smooth the calorific phenomena. The case for which  $\sigma_{space} = dz$  and  $\sigma_{time} = dt$  appears to be a good compromise: see Fig. 6.3e. In other words, the advantageous signal-to-noise ratio of the thermal data allows us to apply a “soft” filtering without strongly penalizing the spatial and temporal resolutions of the reconstructed heat sources. The chosen spatial and temporal resolutions of the reconstructed heat sources are then equal to 1.04 mm and 43.4 ms respectively.

Figure 6.4a presents the temperature change  $\Theta(z, t)$ , as well as the position of the actuator, as a function of time during the load-unload cycle. Figure 6.4b shows the map of the reconstructed heat source, and Fig. 6.4c shows a zoom over the forward phase transformation (delimited between dotted lines in Fig. 6.4b). The following comments can be made with respect to these graphs.

- Up to approximately 64 s, the actuator moved quasi-linearly, exhibiting an elastic response of the NiTi wire. Although unseen in Fig. 6.4, the temperature slightly decreased during the first seconds as expected due to thermoelastic coupling: decrease of about 0.02 K in 3.5 s. Then the temperature kept rising continuously and homogeneously up to reach a value of 2 K above the ambient temperature. This increase might be related to premartensitic R-phase transformation, although further investigations are needed to confirm it. It can be noted that the corresponding heat sources of these two phenomena

are not detectable because of the chosen filtering parameters (broader filtering windows would enhance the information about this quasi-homogeneous phenomenon, similar to the so-called zero-dimensional approach [14]).

- From 64 s to 68 s approximatively, the actuator position rate rapidly increased due to the large transformation strain of the stress-induced martensitic transformation. It is accompanied by a strong temperature increase of the wire. This is attributed to the production of latent heat of the phase transformation. Six transformation zones separated by non-transforming zones appeared in less than one second (at around 65 s). Four of the non-transforming zones transformed almost 4 s later, and the last one did it 6 s later. The length of individual transformation zones is  $\sim 1.5$  mm. Figure 6.3 reveals that the duration of individual transformation zones is shorter than 0.1 s. The burst of an individual transformation zone was followed by two transformation fronts propagating upwards and downwards indicated by inclined heat source traces (covering a total distance of less than 1.5 mm in less than 0.1 s).
- The intensity of the heat sources at the first six transformation zones is two higher than the intensity of the following five.
- It can be noted that continuous propagation of phase transformation fronts also occurred at the two ends of the wire, just after the appearance of the first six martensitic zones (see Fig. 6.4b).
- The reverse transformation, starting at  $\sim 150$  s, is characterized by heat absorption. The intensity of the heat sources upon the reverse transformation is, however, three times lower than the one observed upon the forward transformation. The differences might be related to other material processes occurring simultaneously upon phase transformations such as plasticity.
- Unlike the forward phase transformation, the reverse transformation initiates inside the clamping jaws. There is not an evident correspondence between the order of activation of the transformation zones upon loading and unloading. The number of localized transformation zones upon the reverse transformation is even lower than upon the forward transformation.

## Conclusion

We apply the 1D heat source reconstruction to track the heterogeneous distribution of stress-induced phase transformation in superelastic NiTi upon a force controlled tensile loading-unloading test. Significant temperature changes were observed, as a result of the strong thermomechanical coupling associated supposedly with phase transformations (production and absorption of latent heat). Recorded temperature fields were successfully converted into spatio-temporal evolutions of heat sources associated with forward and reverse martensitic transformation. Attention was paid to the choice of processing parameters with respect to the spatial and temporal resolutions required for a suitable identification of the spatial and temporal kinetics of transformation: rapid nucleation of small martensitic zones and propagation of phase transformation fronts. The method allowed to identify sudden bursts and arrests of phase transformation due to heat effects. In fact, the force controlled loading regime leads to a burst of several phase transformation zones that are displaced due to increasing temperature of their surroundings where the phase transformation is suppressed. These zones can transform only after a sufficient stress increase and/or temperature decrease as a consequence of transformation stress-temperature coupling in NiTi. Consequently, the phase transformation proceeds in two bursts of several displaced transformation zones, where the second burst is shifted in time and related transformation zones fill the non-transformed volume left after the first one.

**Acknowledgements** This publication was supported by OP RDE, MEYS, under the project “European Spallation Source—participation of the Czech Republic—OP”, “Reg. No. CZ.02.1.01/0.0/0.0/16\_013/0001794”. A.J. acknowledges the support received from the Agence Nationale de Recherche of the French government through the program “Investissements d’Avenir” (16-IDEX-0001 CAP 20-25). M.K. would like to acknowledge financial support of the ERDF in the frame of the Project No. CZ.02.1.01/0.0/0.0/15\_003/0000485.

## References

1. C. Otsuka, K. Wayman, *Shape Memory Materials* (Cambridge University Press, Cambridge, 1999)
2. H. Yin, Y. He, Q. Sun, Effect of deformation frequency on temperature and stress oscillations in cyclic phase transition of NiTi shape memory alloy. *J. Mech. Phys. Solids* **67**, 100–128 (2014)
3. S. Miyazaki, T. Imai, K. Otsuka, Y. Suzuki, Lüders-like deformation observed in the transformation pseudoelasticity of a Ti-Ni alloy. *Scr. Metall.* **15**, 853–856 (1981)
4. H. Louche, P. Schlosser, D. Favier, L. Orgéas, Heat source processing for localized deformation with non-constant thermal conductivity. Application to superelastic tensile tests of NiTi shape memory alloys. *Exp. Mech.* **52**(9), 1313–1328 (2012)
5. J.A. Shaw, S. Kyriakides, Thermomechanical aspects of NiTi. *J. Mech. Phys. Solids* **43**(8), 1243–1281 (1995)

6. J.A. Shaw, S. Kyriakides, Initiation and propagation of localized deformation in elasto-plastic strips under uniaxial tension. *Int. J. Plast.* **13**(10), 837–871 (1997)
7. J.A. Shaw, S. Kyriakides, On the nucleation and propagation of phase transformation fronts in a NiTi alloy. *Acta Mater.* **45**(2), 683–700 (1997)
8. P. Sittner, Y. Liu, V. Novak, On the origin of Lüders-like deformation of NiTi shape memory alloys. *J. Mech. Phys. Solids* **53**, 1719–1746 (2005)
9. X. Balandraud, E. Ernst, E. Soós, Rheological phenomena in shape memory alloys. *C.R. Acad. Sci., Ser. IIb: Mec., Phys., Chim., Astron.* **327**(1), 33–39 (1999)
10. X. Balandraud, A. Chrysochoos, S. Leclercq, R. Peyroux, Influence of the thermomechanical coupling on the propagation of a phase change front. *C.R. Acad. Sci., Ser. IIb: Mec.* **329**, 621–626 (2001)
11. D. Delpueyo, X. Balandraud, M. Grédiac, S. Stanciu, N. Cimpoesu, A specific device for enhanced measurement of mechanical dissipation in specimens subjected to long-term tensile tests in fatigue. *Strain* **54**, e1225 (2018)
12. A. Chrysochoos, H. Louche, An infrared image processing to analyse the calorific effects accompanying strain localisation. *Int. J. Eng. Sci.* **38**(16), 1759–1788 (2000)
13. V. Delobelle, D. Favier, H. Louche, N. Connesson, Determination of local thermophysical properties and heat of transition from thermal fields measurement during drop calorimetric experiment. *Exp. Mech.* **55**, 711–725 (2015)
14. P. Jongchansitto, C. Douellou, I. Preechawuttipong, X. Balandraud, Comparison between 0D and 1D approaches for mechanical dissipation measurement during fatigue tests. *Strain* **55**, e12307 (2019)
15. C. Zanotti, P. Giuliani, A. Chrysanthou, Martensitic-austenitic phase transformation of Ni-Ti SMAs: Thermal properties. *Intermetallics* **24**, 106–114 (2012)
16. D. Delpueyo, X. Balandraud, M. Grédiac, Heat source reconstruction from noisy temperature fields using an optimised derivative Gaussian filter. *Infrared Phys. Technol.* **60**, 312–322 (2013)
17. H. Louche, Analyse par thermographie infrarouge des effets dissipatifs de la localisation dans des aciers. *Mécanique [physics.med-ph]*, Université Montpellier II - Sciences et Techniques du Languedoc, 1999 (in French)
18. J. Pilch, L. Heller, P. Sittner, Final thermomechanical treatment of thin NiTi filaments for textile applications by electric current, in *ESOMAT 2009 - 8th European Symposium on Martensitic Transformations Prague*, EDP Sciences, vol 05024 (2009). <https://doi.org/10.1051/esomat/200905024>



# Chapter 7

## Coupled NIRT/3D-DIC for a FEMU Identification of the Thermo-Mechanical Behavior of Zr-4 Claddings Under Simulated Reactivity Initiated Accident

T. Jailin, N. Tardif, J. Desquines, M. Coret, M.-C. Baidetto, T. Breville, P. Chaudet, and V. Georghentum

**Abstract** Nowadays, full field measurements techniques enable heterogeneous experiments to be performed without the need of averaging assumptions. The richness and the quantity of recording data obtained by these techniques led to the development of robust identification methods, such as the finite element model updating (FEMU) technique. However, it is still difficult to measure both kinematic and thermal full fields at the same location and time since the methods and the devices used to compute them are radically different. Furthermore, it may be complicated to calibrate the temperature measurement system without interfering with the metallurgical state of the sample. The present paper proposes a low-cost procedure that uses the same two CMOS cameras to compute both the 3D-surface kinematic field and the associated thermal field, by stereo-correlation and near infrared thermography, respectively. No interpolation or smoothing operation were finally necessary.

**Keywords** 3D-DIC · NIRT · Full field measurements · High temperatures

### Introduction

The Reactivity Initiated Accident (RIA) is a design basis accident that can potentially occur in pressurized water reactors. During such accident, the fuel claddings can be subjected to intense thermo-mechanical loading conditions. Heating rates above 1000 °C/s can be observed up to more than 1000 °C while claddings are internally pressurized (5–100 bar). Such thermal conditions may have a strong impact on the mechanical properties of the material, especially above 800 °C from which an allotropic phase transformation (hcp → bcc) is expected in Zirconium alloys. The present work aims at characterizing the thermo-mechanical behavior of as-fabricated stress relieved annealed Zircaloy-4 claddings under simulated RIA conditions.

Full field measurements in experimental mechanics have been more and more used these last years for constitutive laws identification purposes. Local measurements — like strain gages or thermocouples — show their weaknesses when experiments do not enable averaging assumptions, for instance in case of localization, complex loading conditions or anisotropic behavior. The use of full field measurements techniques gives access to a large amount of data during the tests. Hence, averaging

---

T. Jailin (✉)

Institut de Radioprotection et de Sûreté Nucléaire (IRSN), PSN-RES, Cadarache, Saint Paul lez Durance, France

Université de Lyon, CNRS, INSA-LYON, LaMCoS (UMR 5259), Villeurbanne, France

e-mail: [thomas.jailin@insa-lyon.fr](mailto:thomas.jailin@insa-lyon.fr)

N. Tardif · M.-C. Baidetto · P. Chaudet

Université de Lyon, CNRS, INSA-LYON, LaMCoS (UMR 5259), Villeurbanne, France

e-mail: [nicolas.tardif@insa-lyon.fr](mailto:nicolas.tardif@insa-lyon.fr); [marie-christine.baidetto@insa-lyon.fr](mailto:marie-christine.baidetto@insa-lyon.fr); [philippe.chaudet@insa-lyon.fr](mailto:philippe.chaudet@insa-lyon.fr)

J. Desquines · V. Georghentum

Institut de Radioprotection et de Sûreté Nucléaire (IRSN), PSN-RES, Cadarache, Saint Paul lez Durance, France

e-mail: [jean.desquines@irsn.fr](mailto:jean.desquines@irsn.fr); [vincent.georghentum@irsn.fr](mailto:vincent.georghentum@irsn.fr)

M. Coret

GeM (UMR 6183), École Centrale de Nantes, Nantes, France

e-mail: [michel.coret@ec-nantes.fr](mailto:michel.coret@ec-nantes.fr)

T. Breville

ATYS Consulting Group, Herbeys, France

assumptions do not remain necessary anymore. It goes even further since heterogeneities in tests are now sought after to obtain richer data useful for identification purposes [1].

However, it is still difficult to measure both kinematic and thermal full fields at the same location and time since the techniques used to compute them are radically different. Digital images correlation (DIC) technique for instance requires a high random gradient in the images. Thermal full field methods, like infrared (IR) or near-infrared thermography (NIRT), need on the contrary a well-known and homogenous emissivity of the sample surface. Some authors [2, 3] used two different optical systems to compute the thermal and the kinematic fields but time and spatial interpolations remained necessary at the end to link the two types of field. Other authors proposed to extend the DIC technique to infrared cameras [4]. However, this method needs a prior calibration step and IR cameras have often a poor spatial resolution and are relatively costly compared to standard CMOS or CCD cameras.

An additional difficulty come in case of fast thermal transients where the temperature may be difficult to measure. On the one hand, thermocouples are subjected to a potential high inertia effect under fast thermal transients. On the other hand, the speckle pattern leads to an unknown emissivity of the sample surface. Using a pyrometer is therefore complicated.

This paper proposes a low-cost procedure that uses the same two CMOS cameras to compute both 3D-surface kinematic and thermal full fields under fast thermal transients. The global stereo-correlation software Ufreckles [5] was first used to compute the 3D-surface kinematic field. Then, a simple and robust procedure was developed to identify the radiometric model, used to perform the NIRT. A weak coupling between the two kinds of fields was finally achieved so that no interpolation or smoothing operation were finally required. The first section deals with the experimental setup used to perform fast thermal transient experiments. The thermal calibration procedure and the weak coupling with the 3D-DIC are detailed in the second section.

## Creep Ballooning Tests Under Fast Thermal Transients

### Experimental Setup

The experimental device ELLIE was used to perform creep ballooning tests on fuel rods samples with very high thermal transients. A scheme of the setup is depicted in Fig. 7.1. The device is presented in more details in [6]. Some reminders are given in the following. The test specimens were cut from as-fabricated stress relieved annealed Zircaloy-4 claddings. They were 90 mm long with an external diameter of 9.5 mm and a wall-thickness of 0.57 mm. In order to perform stereo-correlation measurements a black undercoating and a white speckle pattern were applied onto the samples with high-temperature paintings. Three thermocouples (type K, diameter of 79  $\mu\text{m}$ ) were spot-welded in the region of interest (ROI) of the specimens.

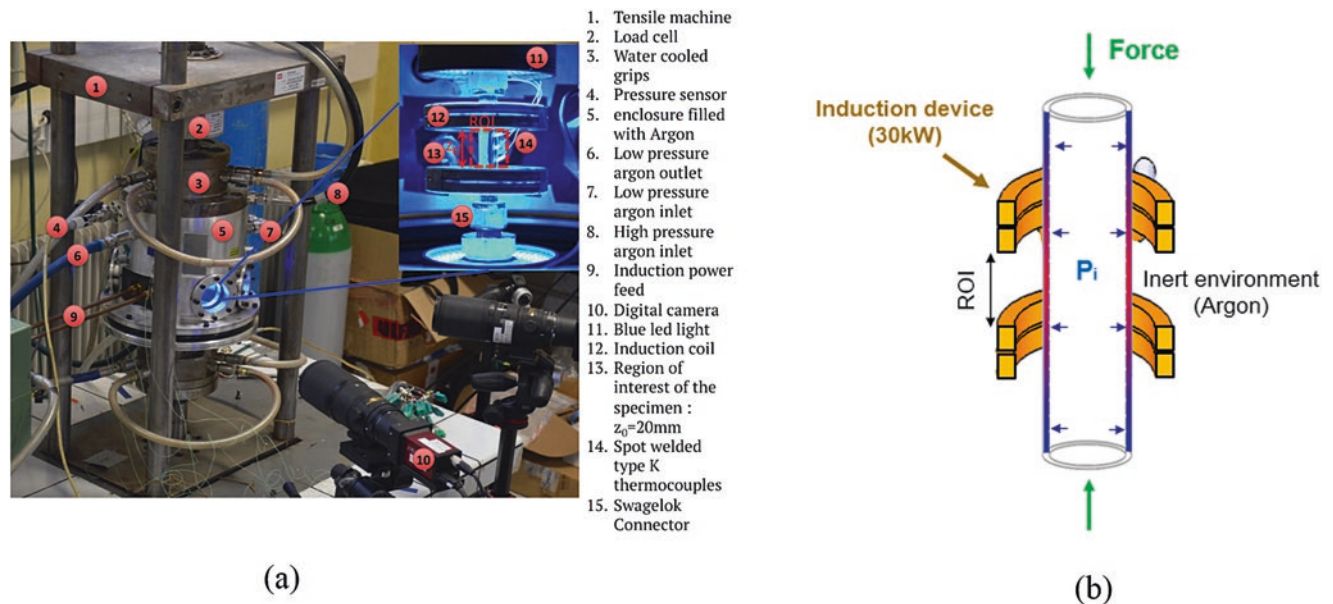
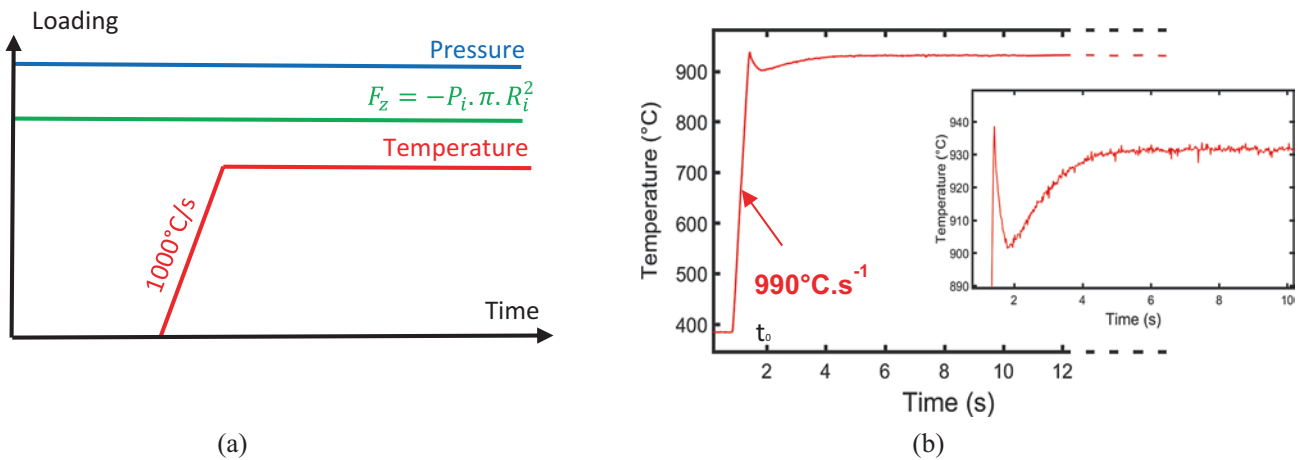


Fig. 7.1 Description of ELLIE device (a) Picture of the device [6]. (b) Scheme of the setup





**Fig. 7.2** (a) Loading sequence; (b) example of a thermal transient obtained [7]

The test bench was composed of a 10 kN servo-hydraulic tensile machine connected to a pressurization system. Internal pressure up to 70 bar could be applied and controlled within the claddings during the whole experiments using Argon gas. An induction heating device enabled samples heating rates up to  $1500^\circ\text{C/s}$  up to more than  $1000^\circ\text{C}$  [7]. The temperature regulation was achieved using a Metis 322 pyrometer at a wavelength of  $\lambda = [1.45\text{--}1.65] \mu\text{m}$ . In order to avoid the oxidation of the samples at high temperatures all the experiments were performed within an enclosure where an Argon flush was setup during the tests.

## Experimental Procedure

The experimental procedure is depicted in Fig. 7.2a. The mechanical loading was first applied by a combination of an internal pressure  $P_i$  and a compressive force  $F_z$ . The compressive force was calculated to compensate the pressure-induced effect as described in Fig. 7.2a (with  $R_i$  the inner radius of the cladding). Once the mechanical loading was stabilized, the thermal loading was applied with heating rate around  $1000^\circ\text{C/s}$  up to the set point. The PID optimization led to overshoots ranging between  $-6$  and  $+25^\circ\text{C}$  around the target temperature. The temperature was then stabilized until the specimen burst. An example of thermal transient is shown in Fig. 7.2b. 3D surface kinematic and thermal fields were obtained during the whole experiment using the same two CMOS cameras by 3D-DIC and NIRT, respectively.

## Optical Full Field Acquisition

The application of fast thermal transients led to non-axisymmetric temperature distributions in the samples. Full field measurements techniques were used to record these loading heterogeneities. Two 12 Mpx CMOS cameras recorded images of the ROI during the tests at a frequency up to 55 Hz. A scheme of the setup is presented in Fig. 7.3. The two CMOS cameras were equipped of 200 mm macro optics and near infrared pass-band filters ( $\lambda = 860 \pm 10\text{nm}$ ) were mounted on the optics. The exposure time of the cameras was setup to obtain non-saturated images between  $-100$  and  $+50^\circ\text{C}$  around the test regulation temperature.

## Kinematic Full Field Measurements by Stereo-Correlation

The global stereo-correlation software UFreckles [5, 8], developed by J. Réthoré was used to compute the 3D-surface kinematic field. A finite element basis of Q4 elements with an element size of  $35 \times 35 \text{px}^2$  was used to perform the images analysis ( $1 \text{px} \approx 9 \mu\text{m}$ ). In order to avoid chromatic aberrations at high temperature the optical system calibration was performed at low temperature before the test. This step was achieved by lighting the sample in the near infrared domain using a LED ring

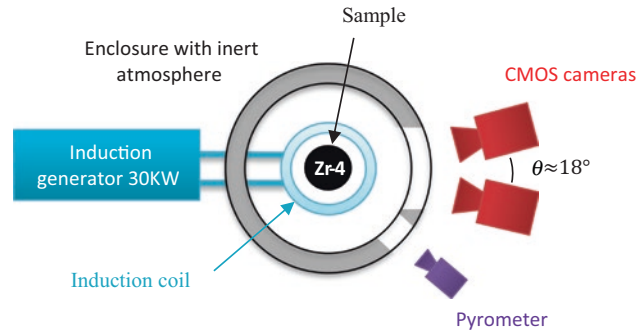


**Fig. 7.3** Scheme of a top view of the setup

at the wavelength  $\lambda = 860$  nm. The near infrared band-pass filters mounted on the optics enabled the calibration procedure to be carried out at ambient temperature while remaining valid at high temperature.

A standard calibration, using calibration grids, could not be performed because of the device geometry and the presence of the induction coil. This step was then achieved using the well-known geometry of the claddings. Finally, the noise was estimated to be around  $1 \mu\text{m}$  for the in-plane displacements and about  $5 \mu\text{m}$  for the out-of-plane displacements.

### *Thermal Full Field Measurements by Near Infrared Thermography (NIRT)*

The NIRT technique [9] was used to compute the thermal field on the sample outer surface. This method, based on Planck's law, links the digital level intensity  $I$  of an image (i.e. the gray level of the pixels) to the temperature  $T$  using a radiometric model that can be written as:

$$T = \frac{K_1}{\ln\left(\frac{K_2}{I} + 1\right)} \quad (7.1)$$

Two unknown constants  $K_1$  and  $K_2$  had to be identified in this model.

A large range of temperatures had to be used in order to identify accurately this model. Only the pyrometer data could be used since the thermocouples are potentially subjected to high inertia effects under fast thermal transients. As mentioned above the speckle pattern led to an unknown emissivity onto the specimen surface. A prior emissivity identification could not be performed without interfering with the metallurgical state of the material. The pyrometer emissivity was then setup to an arbitrary value — close to its expected value — during the experiments. This emissivity value had to be corrected after the test to obtain correct pyrometer data. A third unknown to identify was then defined to be the true emissivity at the pyrometer pointing location.

On the other hand, the speckle pattern led to a heterogeneous emissivity onto the claddings. We recall that the radiometric model is based on a homogeneous and constant emissivity assumption. In order to use a single emissivity value in the radiometric model it was chosen to use only the black painting since it is the more stable to a potential oxidation of the sample. A parameter  $P$  was then defined as the percentage of pixels corresponding to the black painting. Only the black pixels identified by this parameter were used to identify the radiometric model and compute the thermal field. A too low value of  $P$  would result in a high impact of the noise. A too important value would lead to the use of multiple emissivities; the thermal field would then be very noisy.

Four parameters had finally to be identified to compute the thermal field: the two constants  $K_1$  and  $K_2$ , the emissivity  $\epsilon_{pyro}$  at the pyrometer pointing location and the parameter  $P$  that can be seen as a percentage threshold value defining the black painting.

### **Identification Procedure**

The pyrometer emissivity could not be identified directly using the thermocouples data since the pyrometer and the thermocouples were not located at the same position. The NIRT was then used to link the pyrometer with the thermocouples. An identification procedure of the four parameters  $\{K_1, K_2, \epsilon_{pyro}, P\}$  is proposed below. Two objective functions are first defined:

$$er_1^2 = (T_{TC}^{NIRT} - T_{TC})^2, \quad (7.2)$$

$$er_2^2 = (T_{Pyro}^{NIRT} - T_{Pyro})^2, \quad (7.3)$$

With:

- $T_{TC}$ : The temperature measured by the thermocouples,
- $T_{Pyro}$ : The temperature measured by the pyrometer,
- $T_{TC}^{NIRT}$ : The temperature obtained by NIRT at the thermocouples areas (green circles in Fig. 7.4b),
- $T_{Pyro}^{NIRT}$ : The temperature obtained by NIRT at the pyrometer area (red circle in Fig. 7.4b).

The parameter  $\epsilon_{pyro}$  was identified by minimizing the error  $er_1^2$  using the plateau temperature data, once the thermocouples were stabilized. The temperature  $T_{TC}^{NIRT}$  was obtained by identifying the three others parameters ( $K_1$ ,  $K_2$  and  $P$ ) using a Newton-Gauss algorithm where the error  $er_2^2$  was minimized. The data obtained during the thermal transient were used to minimize  $er_2^2$ . This crisscrossed procedure enabled characterizing properly the “emissivity of the pyrometer” while identifying the radiometric model with a large range of temperature. The authors recall that only the  $P$  percentage of the brightest pixels were used to compute  $T_{TC}^{NIRT}$  and  $T_{Pyro}^{NIRT}$ . The Fig. 7.5 depicted the results obtained for a test performed at a regulation temperature of 970 °C with a thermal transient of 1260 °C/s. A “delay” of around 30 °C is observed during the thermal transient for the thermocouples because of their intrusive nature.

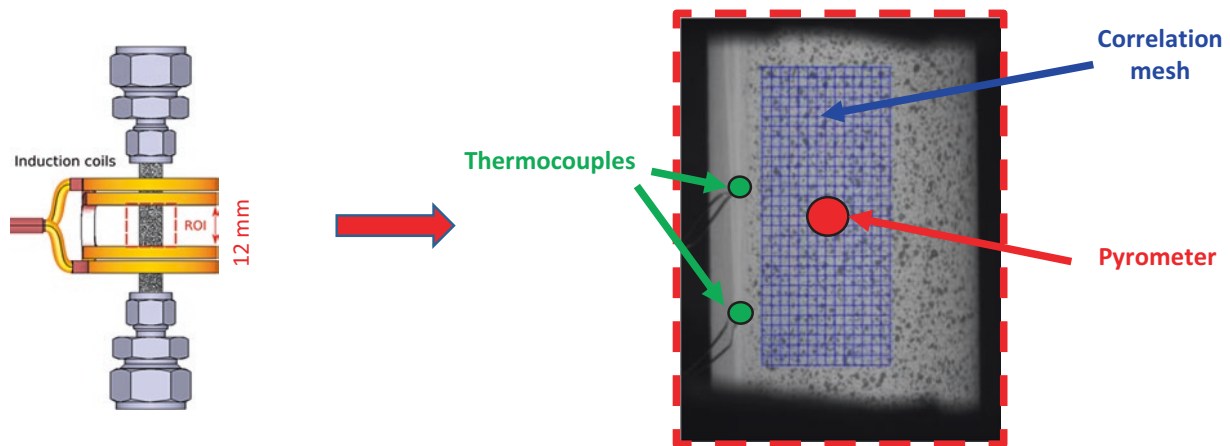


Fig. 7.4 (a) Scheme of the sample with the induction coil and (b) example of an image obtained with the DIC mesh

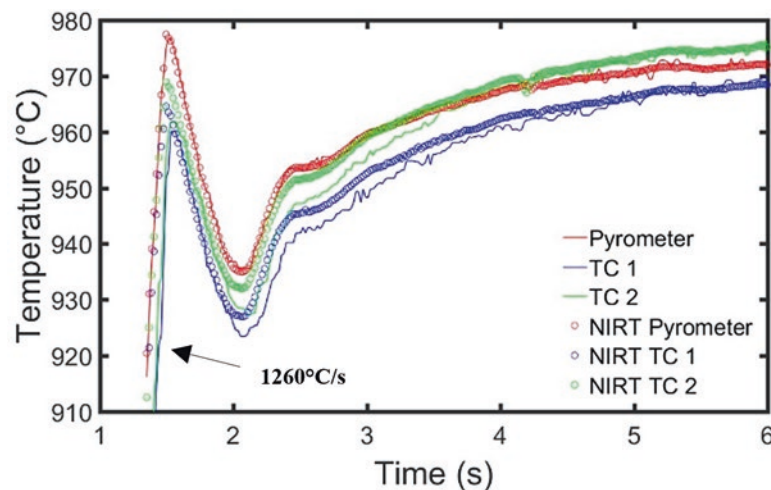
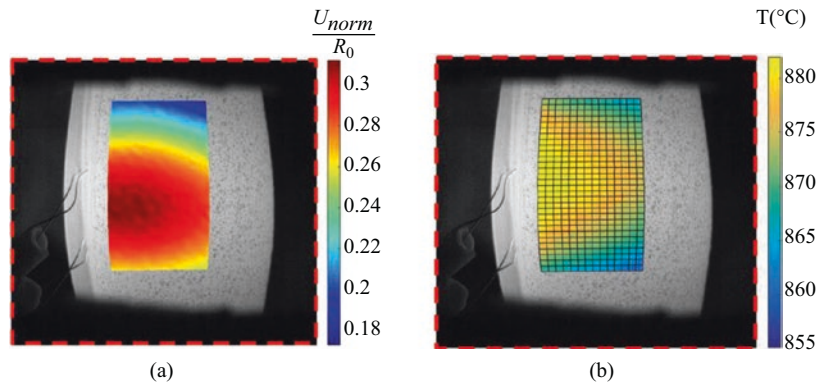


Fig. 7.5 Example of results obtained after the identification procedure for a test carried out at a regulation temperature of 970 °C. Two thermocouples (TC) were visible on the ROI



**Fig. 7.6** Example of “coupled fields”: (a) Magnitude of displacement obtained by stereo-correlation normalized by the initial outer radius of the sample  $R_0$ ; (b) thermal field obtained by NIRT using the deformed correlation mesh obtained by 3D-DIC

### Weak Coupling with the 3D-DIC

The same images were used to compute both the thermal field and the kinematic field. A weak coupling between the 3D-DIC and the NIRT was then developed to obtain the two kinds of data at the exact same location without need of interpolations. To do so, the correlation mesh used to perform the 3D-DIC (see in Fig. 7.4b) was reused to compute the thermal field. Two assumptions were first formulated:

- The temperature is averaged within each element of the correlation mesh (an element has a size of  $315 \times 315 \mu\text{m}^2$ )
- The  $P$  percentage of the brightest pixels within an element correspond to the black painting (only these pixels will be used to compute the thermal field).

Since the correlation mesh “follows” the deformation, the pattern within an element remains constant in all images. The black pixels identified in the reference images remain then unchanged in all images, excepting noise effect.

These two assumptions enabled computing the thermal field at each time step on the deformed correlation mesh. This thermal field is smooth, because non-affected by the speckle pattern. No interpolation or smoothing operation were finally necessary. An example of “coupled fields” is presented in Fig. 7.6. The uncertainty of the thermal field mainly results from the devices that are used to identify the radiometric model [6]. The thermal uncertainty is then estimated to 0.7% of the measured temperature.

### Conclusion

A low-cost procedure that uses only two CMOS cameras has been presented to compute in the same time the 3D-surface displacement field by stereo-correlation and the associated thermal field by NIRT. No interpolation or smoothing operation were necessary at the end. The thermal calibration was performed after-experiment in order to enable experiments to be performed without unexpected changes of the metallurgical state of the samples. This “coupled” full fields method will enable identifying constitutive laws by a finite elements method updating algorithm (FEMU).

**Acknowledgments** The authors acknowledge with thanks financial support of this work from EdF. The authors want also to express their thanks to J. Réthoré for allowing access to UFreckles software.

### References

1. D. Campello, N. Tardif, M. Marwa, et al., Identification of the steady state creep behavior of Zircaloy-4 claddings under simulated Loss-Of-Coolant Accident conditions based on a coupled experimental/numerical approach. *Int. J. Solids Struct.* **115**, 190–199 (2017)
2. L. Bodelot, L. Sabatier, E. Charkaluk, et al., Experimental setup for fully coupled kinematic and thermal measurements at the microstructure scale of an AISI 316L steel. *Mater. Sci. Eng. A* **501**(1-2), 52–60 (2009)

3. A. Chrysochoos, B. Berthel, F. Latourte, A. Galtier, et al., Local energy analysis of high-cycle fatigue using digital image correlation and infrared thermography. *J. Strain Anal. Eng. Des.* **43**(6), 411–422 (2008)
4. A. Maynadier, M. Poncelet, K. Lavernhe-Taillard, et al., One-shot measurement of thermal and kinematic fields: infrared image correlation (IRIC). *Exp. Mech.* **52**(3), 241–255 (2012)
5. J. Réthoré, Ufreckles (Version v 2.0). Zenodo (2018). <https://doi.org/10.5281/zenodo.1433776>
6. D. Campello, N. Tardif, J. Desquines, et al., Validation of a multi-modal setup for the study of Zirconium alloys claddings' behavior under simulated LOCA conditions. *Strain* **54**, e12279 (2018). <https://doi.org/10.1111/str.12279>
7. T. Jailin, N. Tardif, J. Desquines et al. Mechanical behavior of as-fabricated Zircaloy-4 claddings under the simulated thermo-mechanical post-DNB conditions of a Reactivity Initiated Accident (RIA). In *Top Fuel* (2018)
8. J. Réthoré, T. Elguedj, P. Simon, et al., On the use of NURBS functions for displacement derivatives measurement by digital image correlation. *Exp. Mech.* **50**(7), 1099–1116 (2010)
9. Y. Rotrou, T. Sentenac, Y. Le Maout, et al., Near infrared thermography with silicon FPA-comparison to MWIR and LWIR thermography. *Quant Infrared Thermography J* **3**(1), 93–115 (2006)



## Chapter 8

# Residual Stresses at Critical Locations in Additively-Manufactured Components

Christopher R. D'Elia, Michael R. Hill, Michael E. Stender, and Christopher W. San Marchi

**Abstract** Adopting additively-manufactured components in conventional supply chains requires an understanding of residual stress effects on typical component quality: dimensional accuracy, mechanical strength, and fatigue performance. Residual stresses are central to these elements of component quality; however, they vary significantly at different locations in additively-manufactured parts. Multiple methods are used to assess residual stresses at critical locations including the build/baseplate interface, the near surface layers, between layers, and typical planes of interest. Exploratory measurements on laser engineering net shaping (LENS) and powder bed fusion (PBF) bosses are performed using the contour method and slitting method. Steep stress gradients and high stresses with limits approaching the material yield strength are reported. These stresses are often compressive at the component interior and tensile near the outer surfaces. Future work is planned to investigate repeatability of both the measurement methods and the ADDITIVE manufacturing processes.

**Keywords** Residual stress · Additive manufacturing

## Introduction

The opportunity to build complex and highly optimized geometries in a multitude of materials has brought significant attention to additive manufacturing. Numerous additive manufacturing techniques are in development including powder bed fusion (PBF) and directed energy deposition (DED), which are the focus of the present work. The significant thermal cycles in most additive manufacturing processes result in substantial residual stress fields. In many instances, the literature shows residual stresses can greatly influence component manufacturing and performance. Controlling and designing with residual stresses in mind has been shown to reduce component distortion and increase part performance, making manufacturing and operation more reliable. Achieving the full benefits of metal additive manufacturing will require characterization and control of residual stress fields. The objective of the present work is to characterize residual stress fields in example metal additive manufactured parts.

## Background

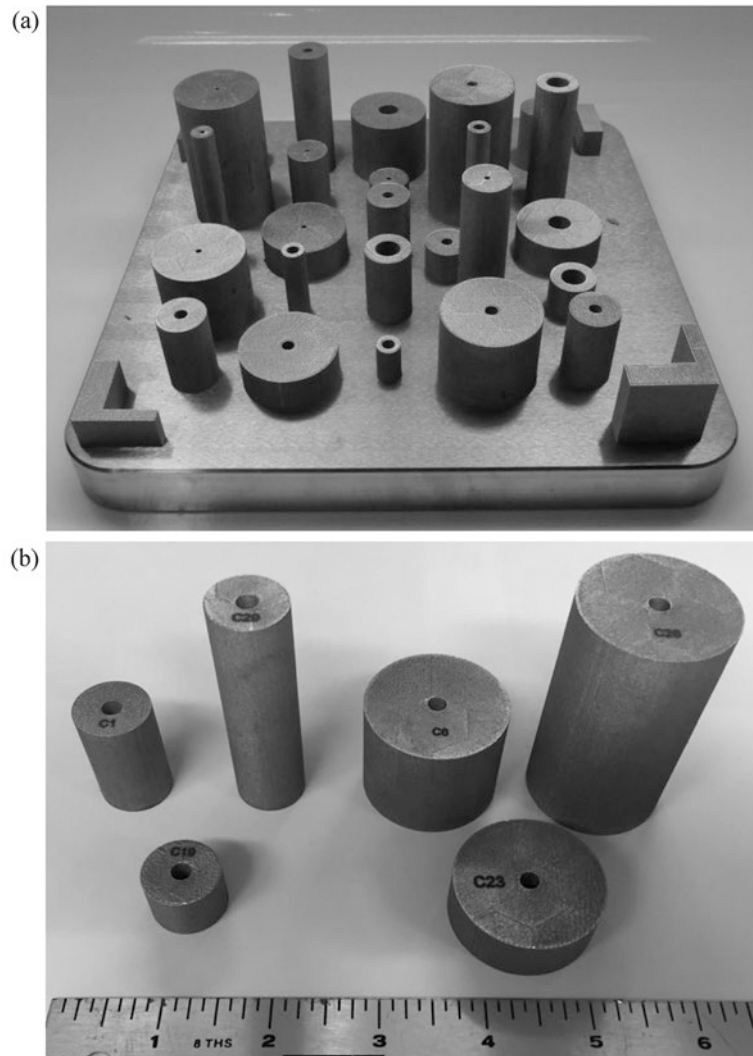
**Materials** Available components manufactured using laser powder bed fusion (L-PBF) and powder fed directed energy deposition (DED) were used to develop an understanding of the typical residual stress fields. Figure 8.1 shows a L-PBF build with various cylindrical features.

Figure 8.1 shows 316L stainless steel cylindrical build features that were removed from the baseplate and used for residual stress measurements. All cylinders used for measurements have a 0.19 in. (4.8 mm) nominal inside diameter. Outside

---

C. R. D'Elia (✉) · M. R. Hill  
Mechanical and Aerospace Engineering, University of California, Davis, Davis, CA, USA  
e-mail: [crdelia@ucdavis.edu](mailto:crdelia@ucdavis.edu); [mrhill@ucdavis.edu](mailto:mrhill@ucdavis.edu)

M. E. Stender · C. W. San Marchi  
Sandia National Laboratories, Livermore, CA, USA  
e-mail: [mstende@sandia.gov](mailto:mstende@sandia.gov); [cwsanma@sandia.gov](mailto:cwsanma@sandia.gov)



**Fig. 8.1** (a) L-PBF build in 316L used for exploratory residual stress measurements and (b) cylinders removed from the build as provided for measurements

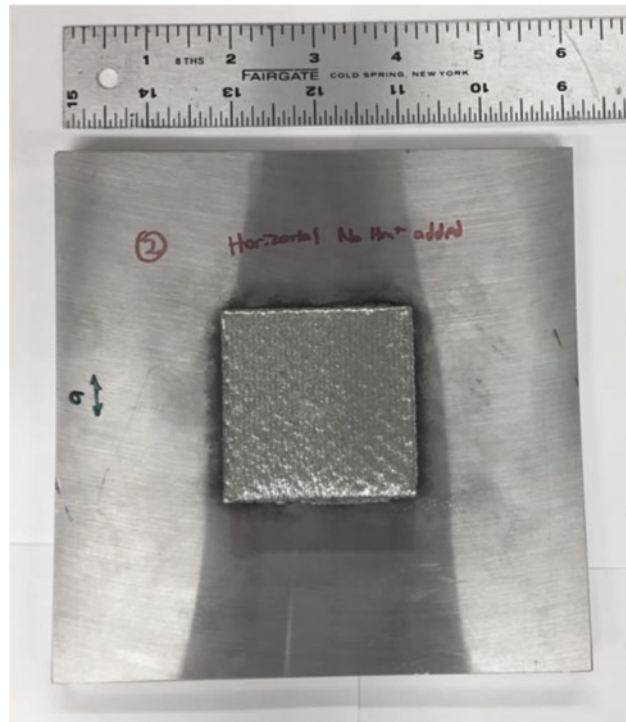
diameters are 0.75 in. (19.1 mm) or 1.50 in. (38.1 mm). Cylinder lengths are 0.55 in. (14.0 mm), 1.20 in. (30.5 mm), and 2.50 in. (63.5 mm), with the length corresponding to build height.

Figure 8.2 shows rectangular boss AM2 built by DED in 304L stainless steel. The baseplate is nominally 6.0 in. (152 mm) square and 0.25 in. (6.4 mm) thick; the boss build is 2.00 in. (50.8 mm) square and 0.50 in. (12.7 mm) tall along the build direction.

Figure 8.3 shows rectangular wall W1 built by DED in 304L stainless steel. The baseplate is nominally 6.0 in. (152 mm) square and 0.25 in. (6.4 mm) thick; the wall build is 2.00 in. (50.8 mm) long, 0.38 in. (9.5 mm) wide, and 0.75 in. (19.1 mm) tall along the build direction.

**Techniques** Mechanical residual stress measurement techniques, including the contour and slitting method, are the focus of the present work. Typical measurements are described herein; however, a more complete description of each method can be found in the literature [1].

The contour method develops a map of normal residual stress in a plane on interest. Typical components are symmetric about the plane of interest identified for contour measurement. The component is then sectioned by wire EDM, which results in redistribution of the residual stress in the component. Distortions, normal to the plane of interest, can be measured using typical profilometry equipment. A smooth fit can be developed from these distortion measurements, and applied to a finite element model of one half of the sectioned component. The normal stress computed on the plane of interest is representative of the original stress in the component prior to sectioning.



**Fig. 8.2** DED boss AM2 in SS304L used for exploratory residual stress measurements

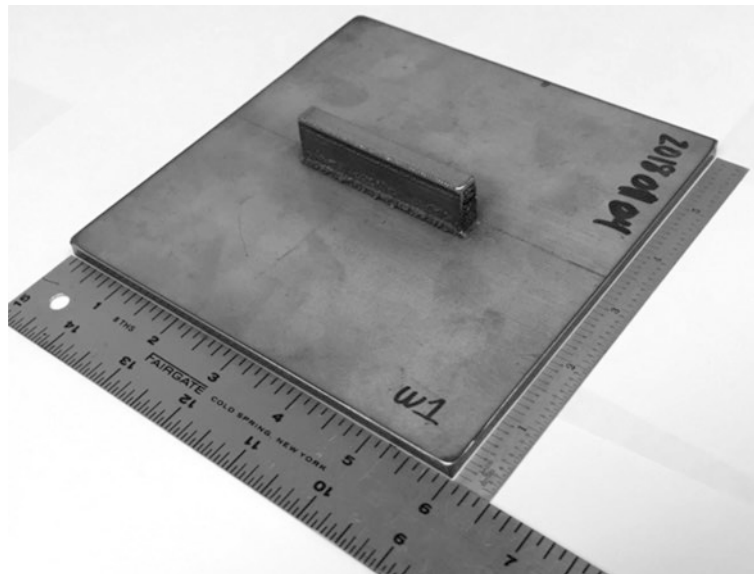


**Fig. 8.3** DED wall W1 in SS304L used for exploratory residual stress measurements

The slitting method produces a one dimensional through thickness average of residual stress along a plane of interest. Typical components are symmetric about the plane of interest identified for slitting measurement. The component is incrementally slit by wire EDM, which results in incremental redistribution of the residual stress in the component. At each increment, the redistribution of residual stress is observed by a strain gauge. An inverse problem is then solved for the residual stress at each depth using the measured strains.

**Methods** In L-PBF SS316L cylinders residual stress measurements were made in two builds: one 1.20 in. (30.5 mm) high, C1, and one 2.50 in. (63.5 mm) high, C29. In cylinder C1, a contour measurement, providing a two-dimensional map of build



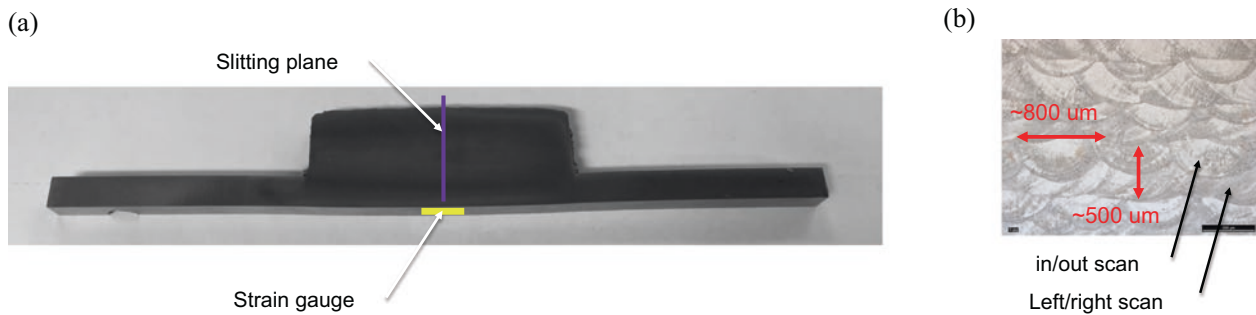


**Fig. 8.4** (a) Slice removed near the center of the DED boss AM2 of Fig. 8.2 with schematic of slitting measurement, and (b) etched area of slice showing alternating DED layers that may cause residual stress variation

direction (axial) residual stress, was made at the mid-height. A subsequent contour measurement in the remaining upper half of the cylinder C1 measured build plane stress (hoop). In cylinder C29, a contour measurement was made 1.00 in. (25.4 mm) from the top of the build to map build direction (axial) residual stress.

In DED SS304L boss AM2, residual stress was measured at the bulk and mesoscale levels. For bulk stress, a contour measurement was made at mid width of the build to provide a map of build plane stress. Subsequently, a slice was removed parallel to the contour plane and slitting measurements made to assess variation of build plane stress along the build direction. The setup of the slitting measurements is shown in Fig. 8.4a. In an effort to measure variation of residual stress at the scale of the DED layer thickness, approximately 0.008 in. (0.20 mm) by 0.016 in. (0.50 mm), as shown in Fig. 8.4b, slitting was performed in small increments of cut depth, approximately 0.002 in. (0.05 mm).

In DED SS304L wall W1, a two dimensional map of the build direction residual stress 0.03 in. (0.7 mm) above the baseplate was measured using the contour method.

## Results

L-PBF cylinder C1 is pictured in Fig. 8.5 following two contour measurements, a first measuring build-direction (axial) stress at the cylinder mid-length and a second measuring build plane stress (hoop) in the remaining half. The figure shows: a cut surface from the measurement in the upper right, where the cut is perpendicular to the build direction; the two cut surfaces from the second measurement in the upper left, where the cut surfaces are perpendicular to the hoop orientation; and a thin wafer of material at the lower center that was used to assess cutting quality. Wire fiducials were glued to the part to mark the orientation of each section after cutting the cylinder, and these are visible in the figure.

Results of the first contour measurement of build direction stress (axial) in L-PBF cylinder C1 are shown in Fig. 8.6. The pattern of stress is nearly axisymmetric with tensile stress at the OD and compression near the ID with tensile stress magnitude near the expected yield strength. Neglecting the edges, the results display approximately symmetric bending stress through the cylinder wall thickness. These symmetric, bending-type stresses counteract one another at the various clock positions and are consistent with the commonly cited “hour glassing” in metal AM cylinders (particularly in cylinders with thinner walls than C1) [2]. Minor asymmetry in the residual stress is observed, with some correlation to the direction of the EDM cutting shown by the annotation. Such asymmetries tend to appear near the wire entrance and exit (i.e., left and right side of the figure), where the cross-section height changes most rapidly.

Hoop stresses in the top half of L-PBF cylinder C1 determined by the second contour measurement are shown in Fig. 8.7. The hoop stress is significantly lower than the axial stress but the pattern is similar, with tension on the OD and compression at the ID. The localized tensile stress at the bottom of Fig. 8.7 is at the location of the prior axial stress measurement plane and should be considered an artifact of the prior measurement.

L-PBF cylinder C29 is pictured in Fig. 8.8 following an axial contour measurement. In an initial step, the rough outer skin was removed using a lathe to enable reliable strain gauge application for subsequent residual stress measurement using the slitting method (to be completed later, pending available effort); the amount of material removed was small (OD was 0.754 in. (19.15 mm) before machining and 0.748 in. (19.00 mm) after).

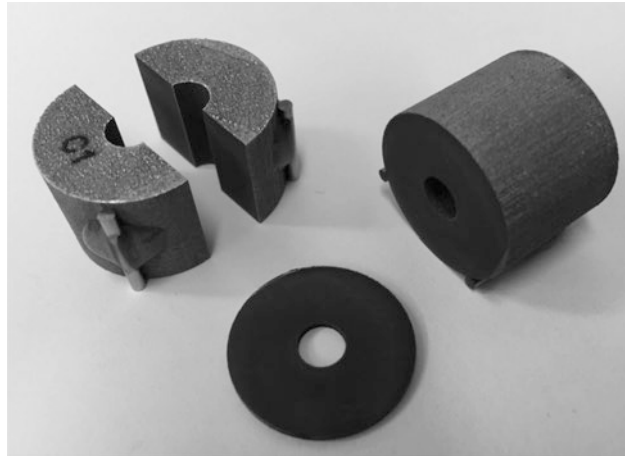


Fig. 8.5 L-PBF cylinder C1 in 316L following exploratory residual stress measurements

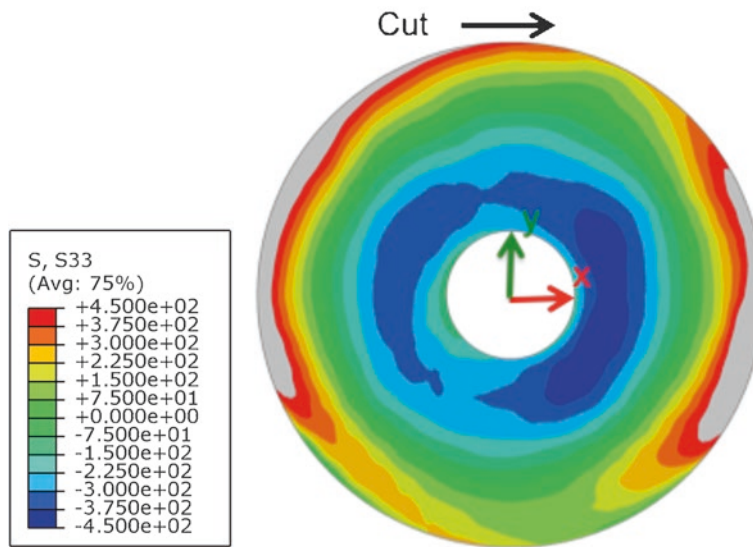


Fig. 8.6 Contour results for L-PBF cylinder C1 axial stress measurement

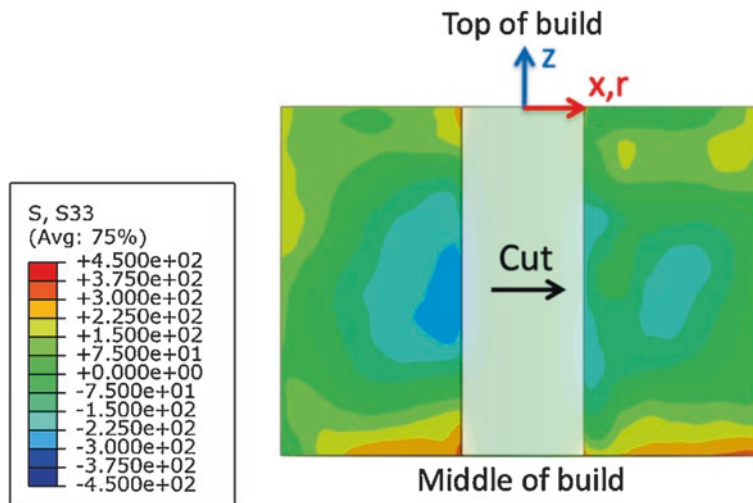
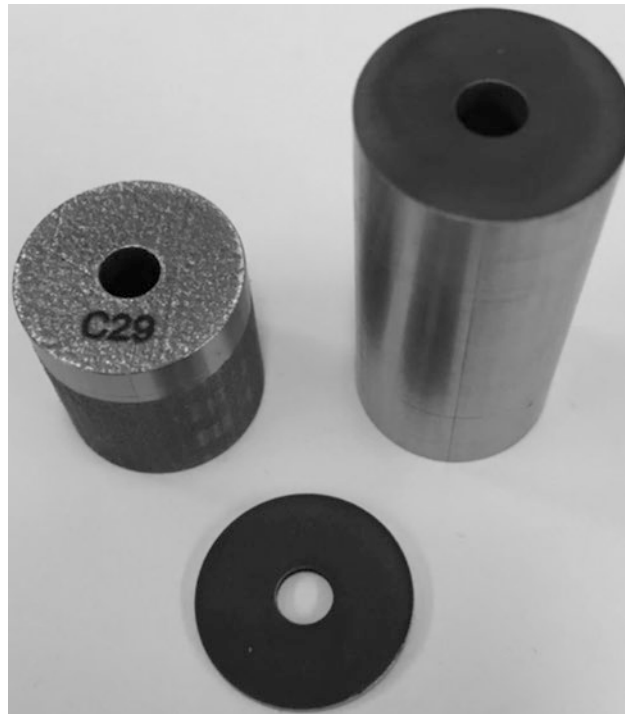
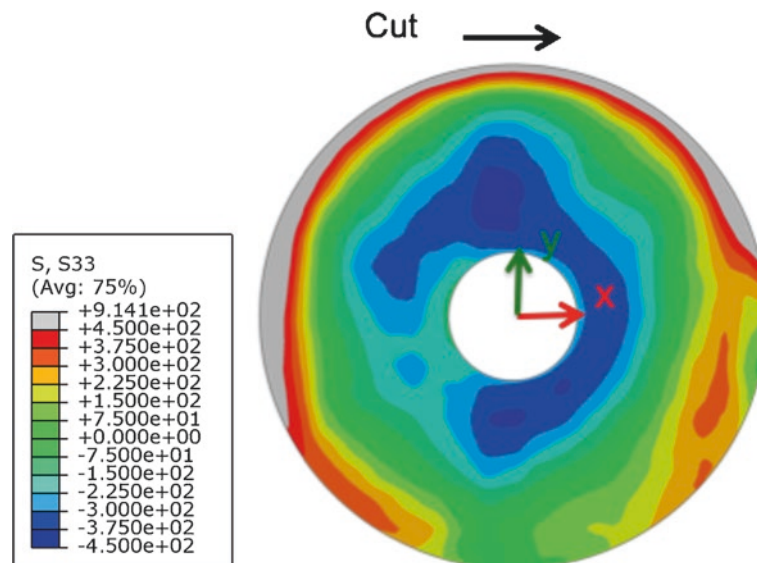


Fig. 8.7 Contour results for L-PBF cylinder C1 hoop stress measurement



**Fig. 8.8** L-PBF cylinder C29 in 316L following exploratory residual stress measurement



**Fig. 8.9** Contour results for L-PBF cylinder C29 axial stress measurement

Contour measurement results for the axial (build direction) residual stress in L-PBF cylinder C29 are reported in Fig. 8.9. The axial stress in C29 (Fig. 8.9) is similar to that found in cylinder C1 (Fig. 8.6) including tensile residual stress near the OD and compression near the ID.

DED boss AM2 is pictured in Fig. 8.10 following the contour measurement at the mid-width of the boss. Visible at the right side of the figure is a small hole (0.16 in. (4.0 mm)) that was drilled in the baseplate far from the build (0.50 in. (12.7 mm) from the edge of the baseplate) and prior to the contour measurement. Referred to as a self-restraint hole, this hole was used to initiate the EDM cut. The EDM contour cut was then performed in two segments, a first from the hole across the build and out of the baseplate (to the left in Fig. 8.10), and a second to sever the small remaining ligament (at the right in Fig. 8.10).



Fig. 8.10 DED build AM 2 following contour measurement with self-constraint

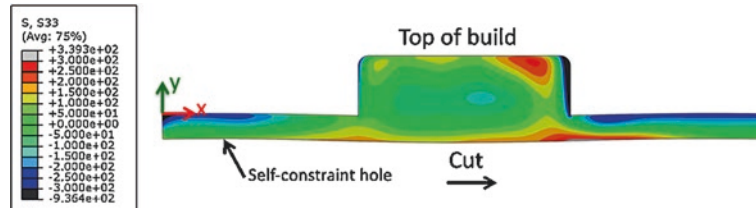


Fig. 8.11 Residual stress in DED build AM 2; stress component perpendicular to the plane of the page

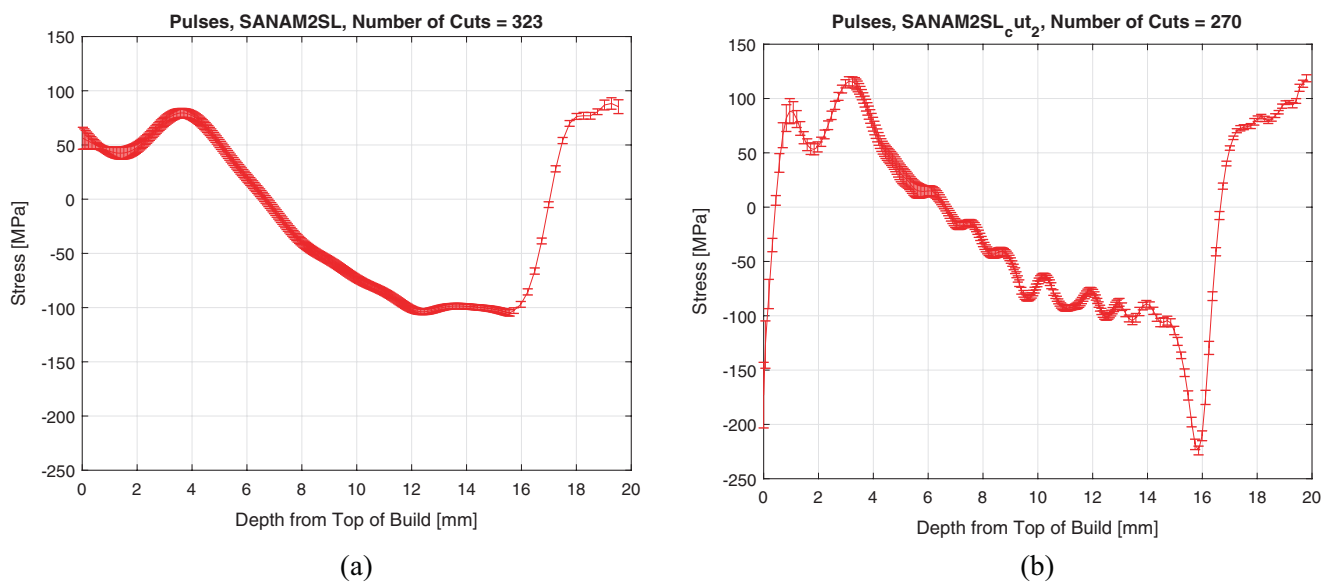


Fig. 8.12 Residual stress in slice extracted from DED build AM2; stress component acts left to right in plane of Fig. 8.11; two results obtained with different strain measurement precision: (a)  $1 \mu\epsilon$  and (b)  $0.1 \mu\epsilon$  (inset shows layer thickness from etched cross-section)

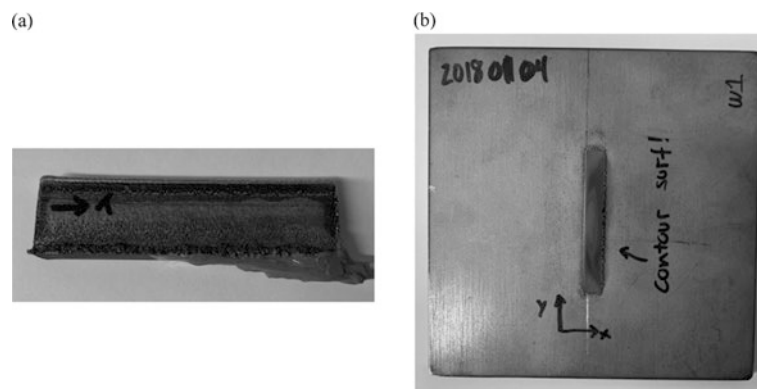
During cutting of the first segment, the small ligament acts to restrain opening of the cut and thereby reduces potential for errors due to plasticity [3].

The contour measurement result in DED build AM2, shown in Fig. 8.11, provided residual stress in the build plane, perpendicular to the build direction ( $\sigma_{zz}$ ) at the build mid-width. The magnitude of residual stress is lower than the build direction stress in the L-PBF cylinders and similar in magnitude to the hoop stress in L-PBF cylinder C1 (Fig. 8.7). There is tension at the upper surface of the build and compression at the bottom of the build. The baseplate has balancing stress that is tensile at the baseplate lower surface and compressive at the build-baseplate interface. The highly compressive region near the right edge of the build is likely a measurement error resulting from a cutting artifact where the cut exits the build (and there is an abrupt change of cross-section) and/or from difficulties associated with measuring the cut surface contour near the rough build surface.

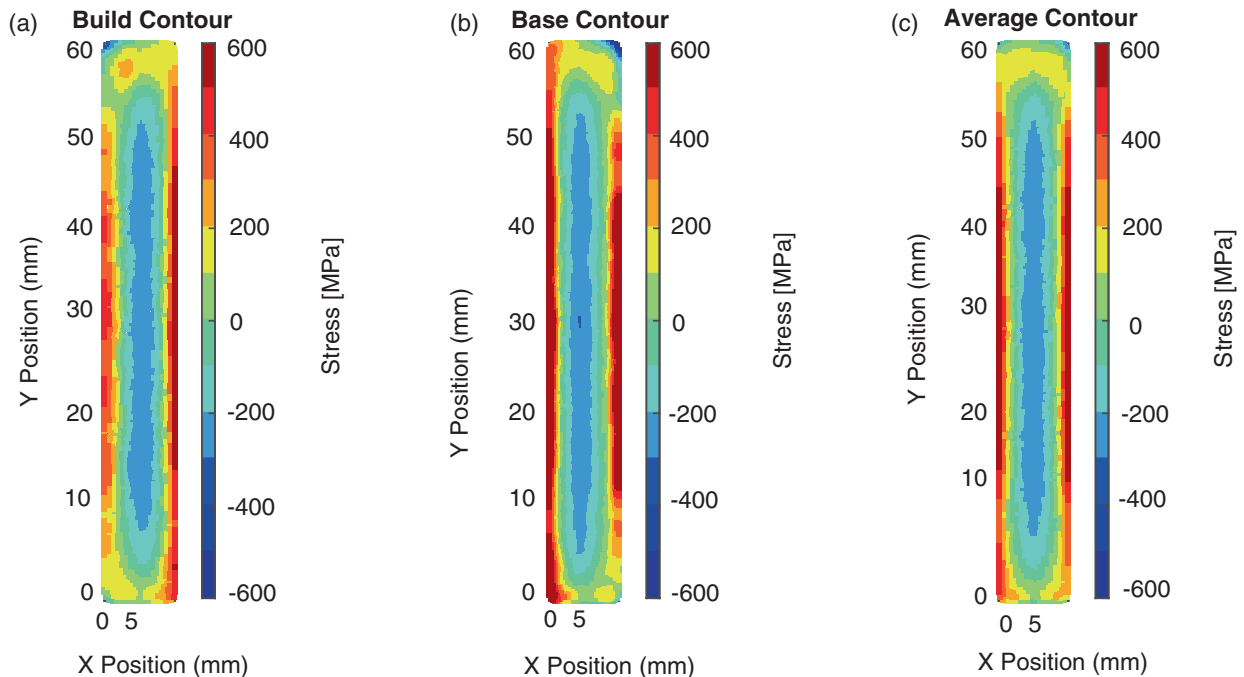
Two slitting measurements were made following the contour measurement on a 0.20 in. (5.0 mm) thick slice extracted from build AM2 parallel to the contour plane and shown in Fig. 8.4. Each measurement determined residual stress acting in the build plane, perpendicular to the build direction and in the plane of Fig. 8.11, defined as  $\sigma_{xx}$  (stress component orthogonal to both stress in the build direction ( $\sigma_{yy}$ ) and the stress measured in the prior contour measurement ( $\sigma_{zz}$ )). Line profiles of residual stress are reported in Fig. 8.12. The first measurement (Fig. 8.12a) shows tensile stress near the top of the build and the bottom of the baseplate, with compression at intermediate depths; this trend is consistent the prior contour results in

Fig. 8.11 (of an orthogonal stress component). The second result, shown in Fig. 8.12b, was obtained using a 10× higher resolution in strain measurement ( $0.1 \mu\epsilon$ ). The higher resolution revealed small-scale oscillations in residual stress on top of the bulk residual stress trend shown in the prior measurement (Fig. 8.12a); the oscillation wavelength is somewhat larger than the 0.020 in. (0.50 mm) DED build layer thickness shown in the figure inset. Similar small-scale stress oscillations, with wavelength very close to the DED build layer thickness, were recently found by Strantza et al., in titanium alloy DED builds [4]; they used “mesoscale” to describe these oscillatory features of the residual stress field to reflect that they are larger than the scale of the microstructure (e.g., grain-to-grain) and smaller the scale of the bulk (e.g., part geometry).

DED wall W1 is pictured in Fig. 8.13 following a contour measurement that removed the wall from the baseplate. Build direction residual stress for DED wall W1 is shown in Fig. 8.14 as a function of in-plane position. The first two parts of the figure, (a) and (b), show intermediate results obtained from stress analysis using geometry for each half of the asymmetric cut and the last part, (c), shows the final estimate of residual stress, which is an average of the two. The similarity of Fig. 8.14a, b indicates that the effect of cut asymmetry is small. The build direction residual stress is tensile around the perimeter and compressive in the interior. Overall, the magnitude and spatial distribution of build direction residual stress in the DED wall is consistent with that in the L-PBF cylinders.



**Fig. 8.13** DED wall W1 following contour measurement showing (a) removed build and (b) baseplate (strain gage and sealant visible in (a) on the part lower edge were applied after completion of the contour measurement and prior to a slitting experiment that is planned)



**Fig. 8.14** Build direction residual stress in DED wall W1 from stress analysis of the (a) build, (b) baseplate, and (c) their average

## Conclusion

Residual stresses in metal AM components can lead to distortion and affect part performance. This work shows that typical residual stress measurement techniques are useful in assessing residual stress in metal AM builds. In metal AM builds by both L-PBF and DED, build direction residual stress generally has a spatial residual stress variation that is the inverse of typical quenched residual stress states. The build direction stress has tension near the surface with peak magnitude near the yield strength that is balanced by a compressive core. Residual stresses in the build plane, perpendicular to the build direction, appear more variable. The build plane residual stresses appear lower in magnitude than the build direction residual stress. Additionally, the build plane stress appears to be more affected by AM process.

**Acknowledgements** Sandia National Laboratories is a multimission laboratory managed and operated by National Technology and Engineering Solutions of Sandia, LLC., a wholly owned subsidiary of Honeywell International, Inc., for the U.S. Department of Energy's National Nuclear Security Administration under contract DE-NA-0003525.

## References

1. G.S. Schajer, *Practical Residual Stress Measurement Methods* (Wiley, Chichester, 2013)
2. A. Dunbar, E. Delinger, M. Gouge, P. Michaleris, Experimental validation of finite element modeling of laser powder bed fusion. *Addi. Manuf.* **12**, 108–120 (2016). <https://doi.org/10.1016/j.addma.2016.08.003>
3. F. Hosseinzadeh, J. Kowal, P.J. Bouchard, Towards good practice guidelines for the contour method of residual stress measurement. *J. Eng.* **2014**(8), 453–468 (2014). <https://doi.org/10.1049/joe.2014.0134>
4. M. Strantza, B. Vrancken, M.B. Prime, C. Truman, M. Rombouts, D.W. Brown, P. Guillaume, D. Van Hemelrijck, Directional and oscillating residual stress on the mesoscale in additively manufactured Ti-6Al-4V. *Acta Mater.* **168**, 299 (2018)



## Chapter 9

# Identification of Constitutive Parameters Governing the Hyperelastic Response of Rubber by Using Full-Field Measurement and the Virtual Fields Method

A. Tayeb, J.-B. Le Cam, M. Grédiac, E. Toussaint, F. Canévet, E. Robin, and X. Balandraud

**Abstract** In this study, the Virtual Fields Method (VFM) is applied to identify constitutive parameters of hyperelastic models from a heterogeneous test. Digital image correlation (DIC) was used to estimate the displacement and strain fields required by the identification procedure. Two different hyperelastic models were considered: the Mooney model and the Ogden model. Applying the VFM to the Mooney model leads to a linear system that involves the hyperelastic parameters thanks to the linearity of the stress with respect to these parameters. In the case of the Ogden model, the stress is a nonlinear function of the hyperelastic parameters and a suitable procedure should be used to determine virtual fields leading to the best identification. This complicates the identification and affects its robustness. This is the reason why the sensitivity-based virtual field approach recently proposed in case of anisotropic plasticity by Marek et al. (Comput Mech 60(3):409–431, 2017) has been successfully implemented to be applied in case of hyperelasticity. Results obtained clearly highlight the benefits of such an inverse identification approach in case of non-linear systems.

**Keywords** Inverse identification · Virtual fields method · Sensitivity-based virtual fields · Hyperelasticity · Digital image correlation

## Introduction

The constitutive parameters of hyperelastic models are generally identified from several homogeneous tests, typically uniaxial tension (UT), pure shear (PS) and equibiaxial tension (EQT). An alternative methodology consists in performing only one heterogeneous test [1–4] that induces a large number of mechanical states at the specimen's surface. The resulting heterogeneous strain fields are generally measured by the Digital Image Correlation (DIC) technique during the loading. Among the different identification methodologies available, the Virtual Field Method (VFM) has been successfully applied to hyperelasticity in [2]. In this work, linear systems are obtained due to the linearity of the stress with respect to the constitutive parameters (see the models in [5, 6]). When the system becomes non-linear, typically for the Ogden model [7], a statistical analysis can be carried out for optimizing the choice of the virtual fields. This complicates the identification procedure and affects its robustness. This is the reason why we also applied here to hyperelasticity the sensitivity-based virtual field approach recently proposed in case of anisotropic plasticity by [8].

---

A. Tayeb (✉) · J.-B. Le Cam · E. Robin  
Univ Rennes, CNRS, IPR (Institut de Physique de Rennes) - UMR 6251, Rennes, France

LC-DRIME, Joint Research Laboratory, Cooper Standard - Institut de Physique UMR 6251, Rennes Cedex, France  
e-mail: [adel.tayeb@univ-rennes1.fr](mailto:adel.tayeb@univ-rennes1.fr); [jean-benoit.lecam@univ-rennes1.fr](mailto:jean-benoit.lecam@univ-rennes1.fr); [eric.robin@univ-rennes1.fr](mailto:eric.robin@univ-rennes1.fr)

M. Grédiac · E. Toussaint · X. Balandraud  
Université Clermont Auvergne, CNRS, Sigma Clermont, Institut Pascal, Clermont-Ferrand, France  
e-mail: [michel.grediac@uca.fr](mailto:michel.grediac@uca.fr); [evelyne.toussaint@uca.fr](mailto:evelyne.toussaint@uca.fr); [xavier.balandraud@sigma-clermont.fr](mailto:xavier.balandraud@sigma-clermont.fr)

F. Canévet  
Cooper Standard France, Rennes, France  
e-mail: [Frederic.Canevet@cooperstandard.com](mailto:Frederic.Canevet@cooperstandard.com)

## Theoretical Background

Assuming a plane stress state and large strains, the principle of virtual work can be expressed as follows in the Lagrangian configuration:

$$-e_0 \int_{S_0} \Pi(X,t) : \frac{\partial U^*}{\partial X}(X,t) dS_0 + e_0 \int_{\partial S_0} (\Pi \cdot N) \cdot U^*(X,t) dL_0 = 0, \quad (9.1)$$

where  $\Pi$  is the first Piola-Kirchhoff stress tensor,  $e_0$  is thickness of the solid,  $S_0$  is the surface of the solid in the normal direction to the thin dimension and  $\partial S_0$  its boundary. They are measured in the reference configuration chosen here as the undeformed state.  $X$  are the coordinates and  $N$  denotes the normal vector to the edge.

## Hyperelasticity

For hyperelastic materials, the mechanical behavior is described by the strain energy density  $W$  relating the stress to the strain through the principle stretches  $(\lambda_1, \lambda_2, \lambda_3)$  or the first two principal invariants of the left Cauchy-Green strain tensor ( $I_1$  and  $I_2$ ). Assuming that the material is incompressible, the first Piola-Kirchhoff stress tensor for such material reads:

$$\Pi = -pF^{-t} + \frac{\partial W}{\partial F}, \quad (9.2)$$

where  $p$  is an indeterminate coefficient due to incompressibility,  $F$  is the deformation gradient tensor and  $\bullet^t$  designates the transpose of a second-order tensor. For the Mooney model [5], the strain energy density writes:

$$W = c_1 (I_1 - 3) + c_2 (I_2 - 3), \quad (9.3)$$

where  $c_1$  and  $c_2$  are the constitutive parameters to be identified. Combining Eqs. (9.2) and (9.3) and replacing  $\Pi$  by its expression in Eq. (9.1) leads to the expression of the principle of virtual work:

$$c_1 \int_{S_0} \Theta : \frac{\partial U^*}{\partial X} dS_0 + c_2 \int_{S_0} \Lambda : \frac{\partial U^*}{\partial X} dS_0 = \int_{\partial S_0} (\Pi \cdot N) \cdot U^* dL_0, \quad (9.4)$$

where  $\Theta$  and  $\Lambda$  are two functions of the principle stretches. Using Eq. (9.4) with two independent displacement virtual fields leads to the following linear system

$$\mathbf{A}\mathbf{c} = \mathbf{B}$$

with

$$\mathbf{A} : \begin{bmatrix} \int_{S_0} \Theta : \frac{\partial \mathbf{U}^{*(1)}}{\partial \mathbf{X}} dS_0 & \int_{S_0} \Lambda : \frac{\partial \mathbf{U}^{*(1)}}{\partial \mathbf{X}} dS_0 \\ \int_{S_0} \Theta : \frac{\partial \mathbf{U}^{*(2)}}{\partial \mathbf{X}} dS_0 & \int_{S_0} \Lambda : \frac{\partial \mathbf{U}^{*(2)}}{\partial \mathbf{X}} dS_0 \end{bmatrix} \quad (9.5)$$

and

$$\mathbf{c} = \begin{Bmatrix} c_1 \\ c_2 \end{Bmatrix}, \mathbf{B} = \begin{Bmatrix} \int_{\partial S_0} (\Pi \cdot \mathbf{N}) \cdot \mathbf{U}^{*(1)} dL_0 \\ \int_{\partial S_0} (\Pi \cdot \mathbf{N}) \cdot \mathbf{U}^{*(2)} dL_0 \end{Bmatrix}$$

After inversion, this system gives the two constitutive parameters  $c_1$  and  $c_2$ . The second model considered in the present study is due to [7]. In this case, the strain energy density reads

$$W = \sum_{i=1}^N \frac{2\mu_i}{\alpha_i^2} (\lambda_1^{\alpha_i} + \lambda_2^{\alpha_i} + \lambda_3^{\alpha_i} - 3), \quad (9.6)$$



where  $\mu_i, \alpha_i; i = 1..N$  are the constitutive parameters. From Eqs. (9.2) and (9.6), the eigenvalues of the Piola-Kirchhoff stress tensor are defined by

$$\Pi_i = \frac{\partial W}{\partial \lambda_i} - \lambda_i^{-1} p. \quad (9.7)$$

The principle of virtual work of Eq. (9.1) becomes in this case

$$-\int_{S_0} (\Pi_1 \cdot U_{u,u}^* + \Pi_2 \cdot U_{v,v}^*) dS_0 + \int_{\partial S_0} (\Pi \cdot \mathbf{N}) \cdot \mathbf{U}^*(\mathbf{X}, t) dL_0 = 0, \quad (9.8)$$

where  $(u, v)$  is the principle basis of the strain tensor. In this basis, the cost function to be minimized to find the constitutive parameters can be written as follows

$$\mathbf{f}(\boldsymbol{\chi}) = \sum_{j=1}^{nVF} \left[ \sum_{t=1}^{nTime} \left( \sum_{i=1}^{nPts} (\Pi_1(\boldsymbol{\chi}) \cdot U_{u,u}^{*i(j)} + \Pi_2(\boldsymbol{\chi}) \cdot U_{v,v}^{*i(j)}) S^i - W_{ext}^* \right)^2 \right] \quad (9.9)$$

$nVF$ ,  $nTime$  and  $nPts$  denote respectively the number of independent virtual fields, the time steps and the number of Zones of Interest (ZOIs).

In this paper, only the first order ( $N = 1$ ) of this model is considered. The identification of the constitutive parameters is carried out by minimizing the cost function  $\mathbf{f}$ .

## Choice of the Virtual Displacement Fields

Since an infinite number of kinematically admissible virtual fields  $\mathbf{U}^*$  satisfies the principle of virtual work in Eq. (9.1), the choice of a set of independent virtual fields remains a typical issue. The case of linear elasticity is discussed in [9]. We address here the most challenging case of hyperelasticity.

### *Random Virtual Displacement Fields*

To deal with hyperelastic materials, different approaches in the generation of independent virtual displacement fields should be applied. To the authors' knowledge, the virtual fields method was first applied to hyperelastic materials in [2]. Motivated by a noise-sensitivity study, a set of random virtual displacement fields was generated. The procedure relies on the division of the region of interest in the sample into 12 quadrangular sub-domains over which piecewise virtual fields are defined. Random values for the displacement at the nodes are then generated and the set of virtual fields leading to the best identification is chosen. The displacement is approximated in each sub-domain by using four-noded quadrangular finite elements formulations [10]. In [2], these random virtual displacement fields were used for two hyperelastic models for which the application of the virtual fields method led to a linear system. In this case, to ensure the independence of the virtual fields generated, the criterion was a good conditioning of the system defined in Eq. (9.5). However, for models for which the virtual field method does not lead to a linear system, such as the Ogden model, a statistical study should have been done to generate independent virtual fields, which makes identification more complicated and less robust and thus requires the development of alternative strategies.

### *Sensitivity-Based Virtual Displacement Fields*

In a recent work [8], a new procedure for generating independent virtual displacement fields was employed for the identification of the constitutive parameters in the case of an anisotropic plastic material in the small strain domain. The method is based on the sensitivity of the stress to small changes of the constitutive parameters. The virtual displacement fields are then generated proportionally to the stress sensitivity fields through a finite element-like approach. The method was then extended to finite strain for anisotropic plasticity in [11]. For finite strains, the stress sensitivity field is defined by

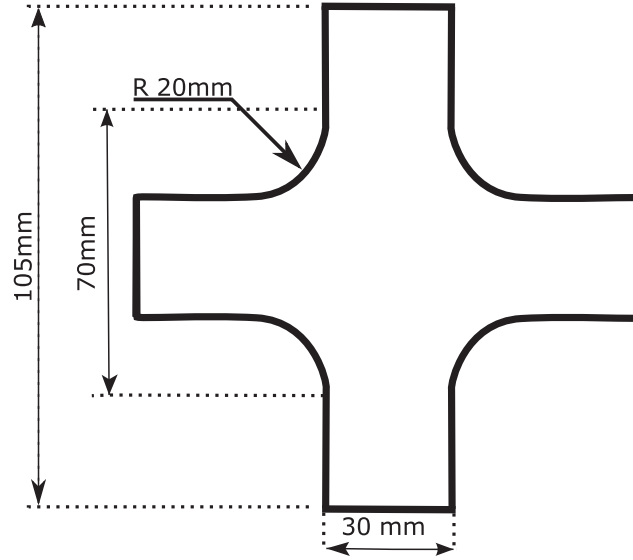


**Fig. 9.1** Sample geometry

$$\delta\Pi^{(i)}(\boldsymbol{\chi}, t) = \Pi(\boldsymbol{\chi} + \delta\boldsymbol{\chi}_i, t) - \Pi(\boldsymbol{\chi}, t), \quad (9.10)$$

where  $0.1\chi_i \leq \delta\chi_i \leq 0.2\chi_i$  is the sensitivity of the  $i^{\text{th}}$  parameter, which numerical values for the parameter picked in the literature. Note that the stress sensitivity field in Eq. (9.10) gives the influence of each constitutive parameter in the global response of the material at each point since the experiment used is heterogeneous. Therefore, the virtual displacement fields were generated proportionally by setting the stress sensitivity fields with the following expression:

$$\delta\Pi^{(i)}(\boldsymbol{\chi}, t) = \mathbf{B}_{glob} \mathbf{U}^{*(i)}, \quad (9.11)$$

where  $\mathbf{B}_{glob}$  is the global strain-displacement matrix from a virtual mesh generated *a priori*. This matrix is obtained by assembling of the elementary strain-displacement matrix obtained directly from the derivation of the shape functions with respect to the coordinates.  $\mathbf{U}^{*(i)}$  in Eq. (9.11) designates the virtual displacement field corresponding to the  $i^{\text{th}}$  constitutive parameter. Note that this virtual displacement field is a *test function* and has no physical meaning. In practice, matrix  $\mathbf{B}_{glob}$  should be modified to account for the boundary conditions of the region of interest (ROI). Typically, for edges where external loading is unknown, a null displacement should be imposed. Therefore, a new matrix  $\bar{\mathbf{B}}_{glob}$  is obtained from the original matrix  $\mathbf{B}_{glob}$ . The virtual displacement field is then given by

$$\mathbf{U}^{*(i)} = \text{pinv}(\bar{\mathbf{B}}_{glob}) \delta^{(i)}(\boldsymbol{\chi}, t), \quad (9.12)$$

where *pinv* designates the pseudo inverse operator. Once the virtual displacement field is obtained, its gradient needed in the principle of virtual work is computed using the classic equation obtained with the finite elements method

$$\frac{\partial \mathbf{U}^{*(i)}}{\partial \mathbf{X}} = \mathbf{B}_{glob} \mathbf{U}^{*(i)}. \quad (9.13)$$

The contribution of each constitutive parameter to the response of the material is very different and unique. Therefore, a scaling in the cost function should be added (see [8, 11]).

## Experiments

The material used in this study is a carbon black filled natural rubber. The sample is shown in Fig. 9.1. It is 105 mm in length and 2 mm in thickness. The experimental setup is presented in Fig. 9.2. It is composed by a home-made biaxial testing machine and a digital camera. The four independent actuators were linked to have the same movement such that the

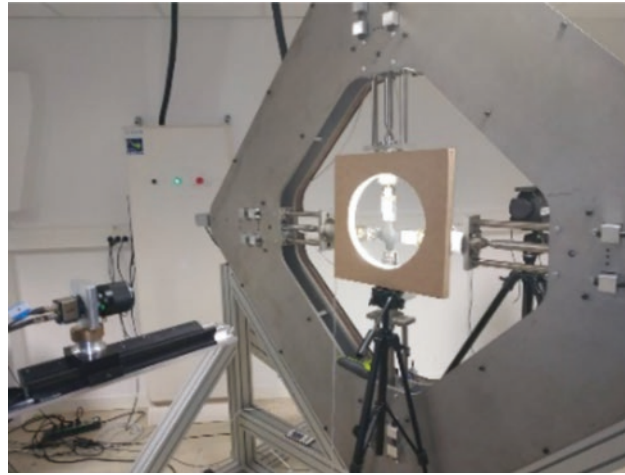


**Fig. 9.2** Experimental setup

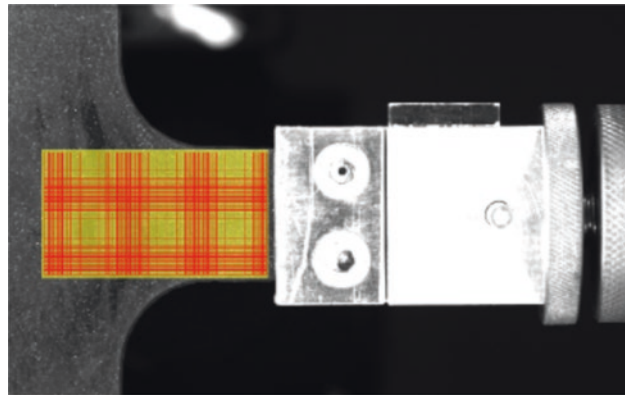


**Fig. 9.3** ROI with ZOIs of 10 by 10 px

specimen center was motionless during the test. Hence, a reference point is obtained in the center of the sample with respect to the correlation procedure. A displacement of 70 mm was applied to each branch at a loading rate of 150 mm/min which corresponds to a value of  $\lambda_{max}$  of around 3.4. During the mechanical test, images of the specimen surface were stored at a frequency of 5 Hz using an IDS camera equipped with a 55 mm telecentric objective. The charge-coupled device (CCD) sensor of the camera has  $1920 \times 1200$  joined pixels. The displacement field at the surface of the specimen was determined using the digital image correlation (DIC) technique. The correlation process is achieved thanks to the SeptD software [12]. The spatial resolution, defined as the smallest distance between two independent points, was equal to 10 pixels. A rectangular region on one branch of the specimen and including the specimen centre is sufficient to apply the identification procedure described above. The rectangular region of interest (*R.O.I.*) is represented in Fig. 9.3.

## Results

### *Experimental Kinematic Fields*

The displacement field obtained from the SeptD software is smoothed using a mean centered filter. The values in the zones of interest (*ZOIs*) where the correlation could not be achieved were interpolated. The displacement gradient fields are presented in Fig. 9.4 for the rectangular *ROI*. These data were smoothed using the same filter. The data obtained experimentally were used in the identification of the constitutive parameters for random and sensitivity-based virtual displacement fields.

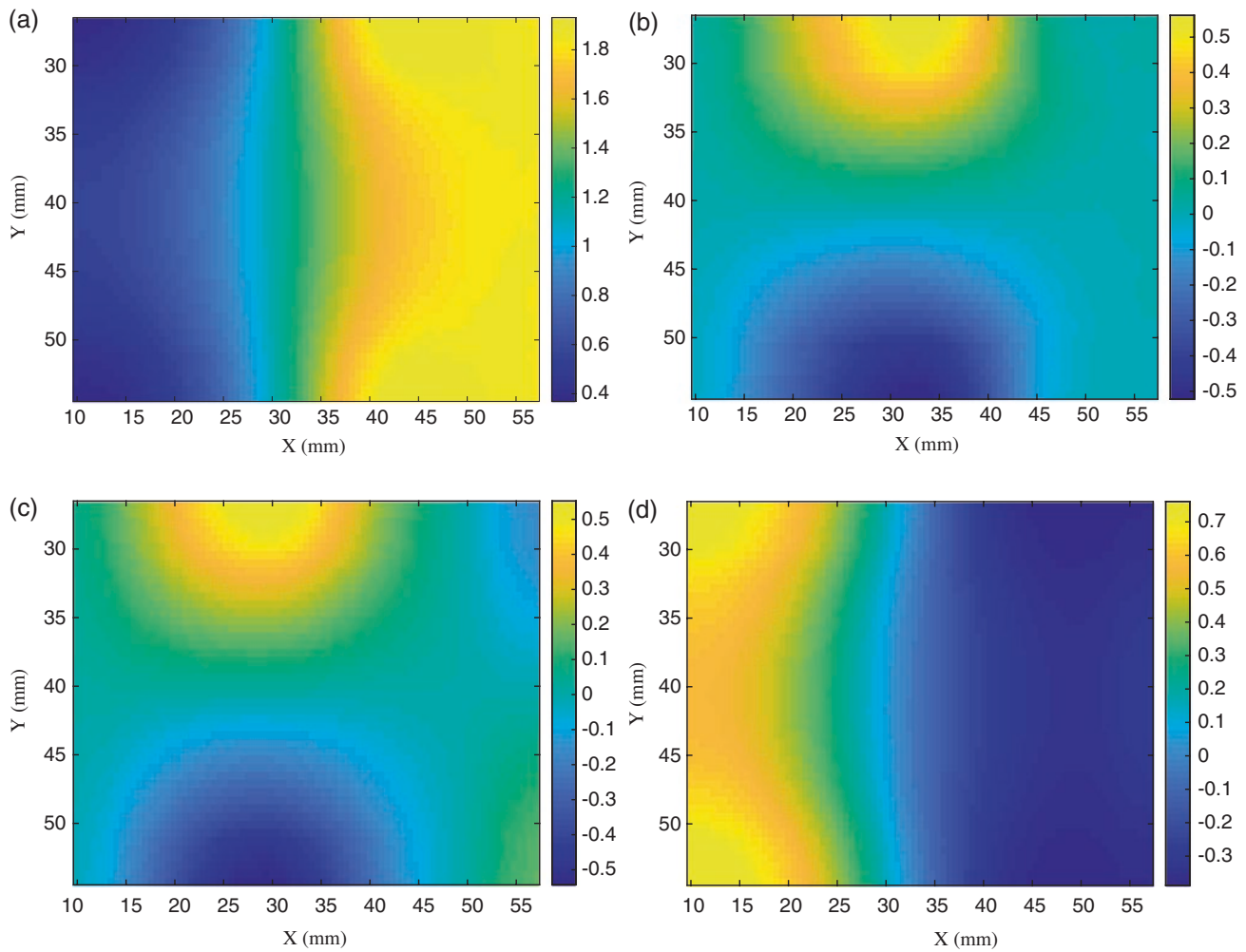


**Fig. 9.4** Experimental displacement gradient fields

**Table 9.1** Identified hyperelastic constitutive parameters using random virtual displacement fields

Model	Parameters	Value
Mooney [5]	$c_1$	0.229 MPa
–	$c_2$	$9.4 \times 10^{-4}$ MPa
Ogden [7]	$\mu_1$	0.68 MPa
–	$\alpha_1$	1.4

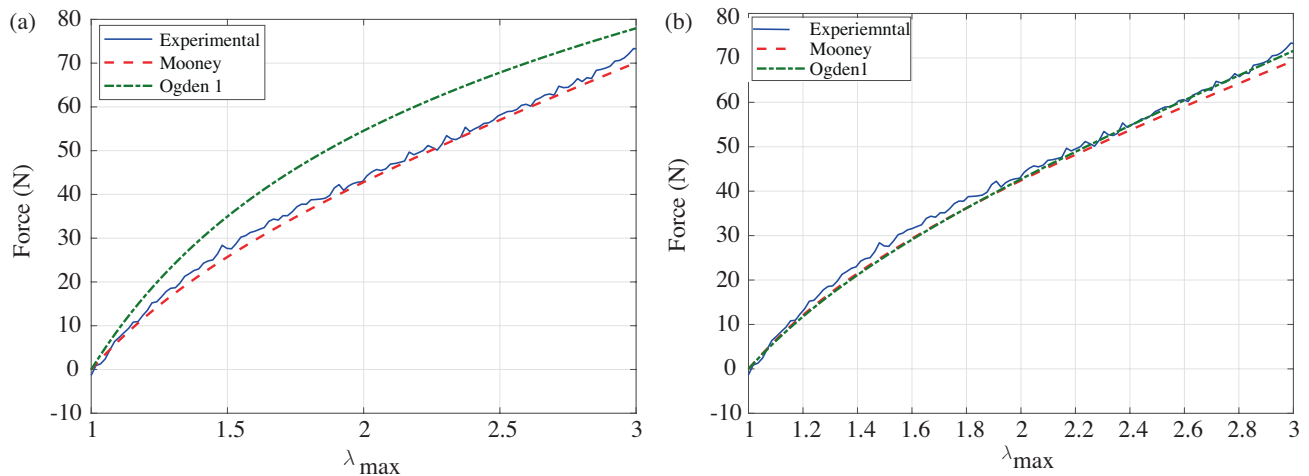
### Identification Results and Comparison

For the randomly generated virtual fields, the virtual displacement fields for the Mooney model were chosen in such a way that the conditioning of the matrix  $\mathbf{A}$  of Eq. (9.5) is greater than 0.3. For the Ogden model, no criterion is available for the choice of the virtual displacement fields. Hence, a wide number of virtual fields were generated and used in the identification procedure. The parameters identified using this approach are reported in Table 9.1.

For the sensitivity based virtual fields, first, a virtual mesh is generated. It can be different from the correlation grid. Then, the virtual fields are generated proportionally to the stress sensitivity fields. The values of the parameters identified are reported in Table 9.2. Unlike for random virtual fields, the parameters for all the models considered are in the range of those reported in the literature. Note that the parameters of Table 9.2 are obtained for several simulations with different sensitivity

**Table 9.2** Parameters identified using sensitivity based virtual fields

Model	Parameters	Value
Mooney [5]	$c_1$	0.22 MPa
–	$c_2$	$1.9 \times 10^{-2}$ MPa
Ogden [7]	$\mu_1$	0.46 MPa
–	$\alpha_1$	2.11

**Fig. 9.5** Force obtained from finite element simulations compared to experimental force

parameters, i.e., for different virtual fields. Furthermore, the mean values for the parameters did not affect the final result of the identification. In fact, the mean values for each parameter could change within a given range without affecting the final result of the identification. For the Ogden model, the least square error (the value of the objective function at the end of the identification) is about  $1.5 \times 10^{-5}$ .

To evaluate the accuracy of the parameters identified, the biaxial experiment used in this work was simulated using Abaqus software for a plane stress problem with the parameters of Tables 9.1 and 9.2. For each set of parameters, the resulting force predicted in every branch of the sample was compared to the experimental force measured. The results of the comparison are shown in Fig. 9.5 in which *SBVF* and *RVF* refer to sensitivity-based virtual fields and random virtual fields, respectively. For the *RVF* method, the Mooney model appears to have a good result for a maximum stretch up to 2.7, which is the usual range for this model. However, the Ogden model overestimates the force in the branch for the whole experiment. This is due to the choice of the virtual displacement fields, which was done randomly and no criterion was found in its selection for this model. For the *SBVF* method, the Mooney model has a good prediction for the experimental force for a principal stretch up to 2.6. The Ogden model has a better result for wider strain range corresponding to a principle stretch up to 3. The results of these two models are very satisfactory given that they do not take into account the stress-hardening phenomenon. Hence, the capacity of the *SBVF* method in the generation of the virtual displacement fields is illustrated here in the case of hyperelastic behavior.

## Conclusions

In this study, the Virtual Fields Method (VFM) was applied to identify constitutive parameters of hyperelastic models from a heterogeneous test in the cases of linear and non-linear relationships between the stress and the constitutive parameters to be identified. In the former case, the Mooney model was considered and the virtual field were randomly generated. For the latter case, the Ogden model was used and a sensitivity-based virtual fields approach inspired from a recent work due to [8] for anisotropic plasticity was applied to choose the virtual fields. Results obtained with the two approaches clearly highlight the benefits of using the sensitivity based virtual fields approach for identifying the constitutive parameters in case of non-linear systems.

## References

1. T. Guélon, E. Toussaint, J.-B. Le Cam, N. Promma, M. Grédiac, A new characterization method for rubbers. *Polym. Test.* **28**, 715–723 (2009)
2. N. Promma, B. Raka, M. Grédiac, E. Toussaint, J.-B. Le Cam, X. Balandraud, F. Hild, Application of the virtual fields method to mechanical characterization of elastomeric materials. *Int. J. Solids Struct.* **46**(3-4), 687–715 (2009)
3. M. Johlitz, S. Diebels, Characterisation of a polymer using biaxial tension tests. part I: hyperelasticity. *Arch. Appl. Mech.* **81**, 1333–1349 (2011)
4. H. Seibert, T. Scheffer, S. Diebels, Biaxial testing of elastomers - experimental setup, measurement and experimental optimisation of specimen's shape. *Tech. Mech.* **81**, 72–89 (2014)
5. M. Mooney, A theory of large elastic deformation. *J. Appl. Phys.* **11**(9), 582–592 (1940)
6. O.H. Yeoh, Some forms of the strain energy function for rubber. *Rubber Chem. Technol.* **66**, 754–771 (1993)
7. R.W. Ogden, Large deformation isotropic elasticity - on the correlation of theory and experiment for incompressible rubberlike solids. *Proc. R. Soc. Lond. A* **326**(1567), 565–584 (1972)
8. A. Marek, F.M. Davis, F. Pierron, Sensitivity-based virtual fields for the non-linear virtual fields method. *Comput. Mech.* **60**(3), 409–431 (2017)
9. S. Avril, M. Grédiac, F. Pierron, Sensitivity of virtual fields to noisy data. *Comput. Mech.* **34**, 439–452 (2004)
10. O.C. Zienkiewicz, R.L. Taylor, *The Finite Element Method* (McGraw-hill, London, 1977)
11. A. Marek, F.M. Davis, M. Rossi, F. Pierron, Extension of the sensitivity-based virtual fields to large deformation anisotropic plasticity. *Int. J. Mater. Form.* **12**, 457 (2019)
12. P. Vacher, S. Dumoulin, F. Morestin, S. Mguil-Touchal, Bidimensional strain measurement using digital images. *Proc. Inst. Mech. Eng. C J. Mech. Eng. Sci.* **213**, 811 (1999)



## Chapter 10

# Intermethod Comparison and Evaluation of Near Surface Residual Stress in Aluminum Parts Subject to Various Milling Parameters

Christopher R. Chighizola, Christopher R. D'Elia, and Michael R. Hill

**Abstract** Near surface residual stress (NSRS) induced by machining (e.g., milling) is known to drive distortion in machined aluminum, particularly in thin complex geometries with tight tolerance requirements where large distortion is undesirable. The understanding and characterization of NSRS in milled aluminum parts is important and should be included in the design and manufacturing process. There exists a variety of experimental tests for characterizing these stresses. The objective of this paper is to assess the quality of three experimental methods for evaluating NSRS versus depth from the surface in prismatic aluminum parts subject to various milling parameters. The three methods are: hole-drilling, slotting, and X-ray diffraction. The aluminum parts are cut from stress-relieved plate, AA7050-T7451. A combination of milling table and tool speeds are used to machine a flat surface in the parts. Measurements are made at specified locations and depths on each part. NSRS data from the hole drilling and slotting measurements were comparable; NSRS data from X-ray diffraction differed and was less repeatable. NSRS data for different milling parameters shows that the depth of NSRS increases with feed per tooth but is unaffected by different cutting speeds.

**Keywords** Residual stress measurement, Machining, Slotting, Hole-drilling, X-ray diffraction

## Introduction

The measurement and characterization of near surface residual stress (NSRS) in machined workpieces is important for understanding the driving factors of in situ and post process distortion. This understanding is particularly critical for thin walled components such as those often found in aerospace applications. It is in these types of components that the potential for deformation from initial and machine induced residual stress is greater due to geometrical limitations [1, 2]. The focus of this study is to investigate three techniques for measuring NSRS in milled aluminum workpieces. The techniques discussed herein are hole drilling, slotting, and X-ray diffraction. All three involve the incremental removal of material at the surface resulting in a profile of measured NSRS as a function of depth. Several measurements are performed in order to examine the repeatability of each method and develop satisfactory understanding of the proficiency and reliability of each technique in determining NSRS. An examination of the average of repeated measurements helps to discern how results from the methods compare to one another.

The measurements are made on milled stress relieved, or low stress (LS), AA7050-T7451. The LS state was achieved prior to the milling of the workpieces. Tang and Liu showed that cutting speed and feed per tooth influenced both the magnitude and depth of stress in milled 7050-T7451 [3]. Here, the workpieces are milled using two cutting speeds of 200 and 450 m/min and three feed per tooth lengths of 0.04, 0.1, and 0.2 mm. Measurements of NSRS in workpieces machined with a combination of these parameters is performed in an attempt to determine the impact of different milling parameters on NSRS. NSRS is compared at fixed cutting speeds with variable feed per tooth lengths and vice versa.

---

C. R. Chighizola (✉) · C. R. D'Elia · M. R. Hill

Department of Mechanical and Aerospace Engineering, University of California, Davis, CA, USA  
e-mail: [crchighizola@ucdavis.edu](mailto:crchighizola@ucdavis.edu); [crdelia@ucdavis.edu](mailto:crdelia@ucdavis.edu); [mrhill@ucdavis.edu](mailto:mrhill@ucdavis.edu)

## Methods

### Sample Description

The aluminum workpieces used in this study were approximately 200 mm long by 100 mm wide and 25.4 mm thick. Each was cut length-wise from larger blocks. All machining was performed with a three flute 12 mm diameter end mill. The workpieces were milled on the 200 × 100 mm face, using passes along the 200 mm length. The cut depth and step over lengths per tool pass were fixed at 3 and 4 mm, respectively. Table 10.1 summarizes the combination of machining parameters including the sample identifiers.

### Measurement Layout

The 200 × 100 mm machined face was subdivided into a grid consisting of 34 × 25.4 mm areas, as shown in Fig. 10.1. The milling tool passes were made along the x-direction and the tool step over along the y-direction. Surface residual stress measurements were made near the center of the grids, as shown, and the labels X#Y# used to denote each measurement location.

### Residual Stress Measurement Technique

#### Hole Drilling

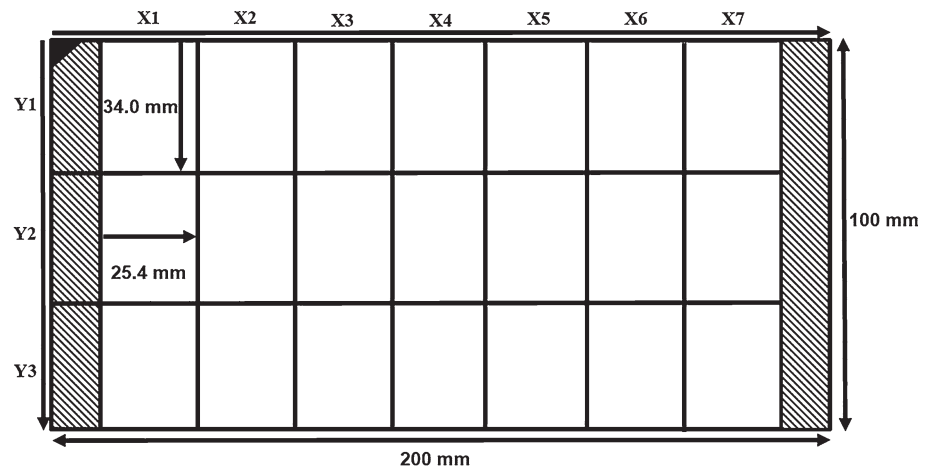
The hole drilling technique used follows the procedures outlined by ASTM standard E837-13a where a strain gage rosette is used to measure three components ( $\sigma_{xx}$ ,  $\sigma_{yy}$ ,  $\tau_{xy}$ ) of residual stress as functions of depth in a flat workpiece by incrementally removing a minimum of 0.025 mm (0.001 inch) of material [4]. The stresses of interest in this study lie just below the machined surface. Therefore very fine increments are necessary to capture the NSRS just below the surface.

Table 10.2 shows a summary of these increments and indexes over which they are applied. For the first 10 indexes increments of 0.0127 mm (0.0005 inch) are used up to a depth of 0.127 mm (0.005 inch). The next 6 indexes are graduated to

**Table 10.1** Summary of parameters used to machine 200 × 100 × 25.4 mm 7050-T7451 aluminum samples

Cutting speed, $v_c$ (m/min)	Feed per tooth, $f_z$ (mm)	Low stress samples
200	0.04	A12, B18
200	0.10	B15, B23
200	0.20	B4, A20
450	0.04	B5, A22

**Fig. 10.1** Sample measurement grid layout where X#Y# indicates a grid location and the measurement is performed near the center of each subdivision





0.0254 mm (0.001 inch). The decision to graduate the depth increment is informed by work done by Tang and Liu in measuring very shallow residual stress in milled 7050-T7451. Where it is shown that the maximum compressive value of NSRS occurs at depths of 0.015–0.020 mm (0.0006–0.0008 inch) and trends towards the steady stress state at depths greater than 0.020 mm [3]. The increment spacing is graduated a second time to 0.0508 mm (0.002 inch) for the remaining 6 indexes up to a maximum depth of 0.5842 mm (0.023 inch).

The strain gage used is a CEA-13-062UL-120 made by Vishay Micro Measurements. This gage is a 5.13 mm (0.0625 inch) Type A rosette and is bonded directly over the measurement location. The standard states that for a 5.13 mm diameter gage the recommended maximum and minimum hole diameters to achieve the best results for non-uniform stresses are 2.12 mm (0.085 inch) and 1.88 mm (0.075 inch) respectively [4]. The hole is approximately 2 mm (0.080 inch) in diameter and is cut using an orbital path with a 1.5875 mm (0.0625 inch) diameter end mill using an electric spindle. The incremental cutting is achieved automatically using computer controlled precision actuators.

During the measurement deformation occurs at the boundary of the hole with each incremental removal of material. This deformation is the result of the redistribution, or ‘relaxation’, of stresses at the hole [5]. These incremental deformations are detected as strains. The recorded strains are reduced following the procedure outlined by ASTM E837-13a for non-uniform stresses as a function of depth. This involves regularizing the data [4].

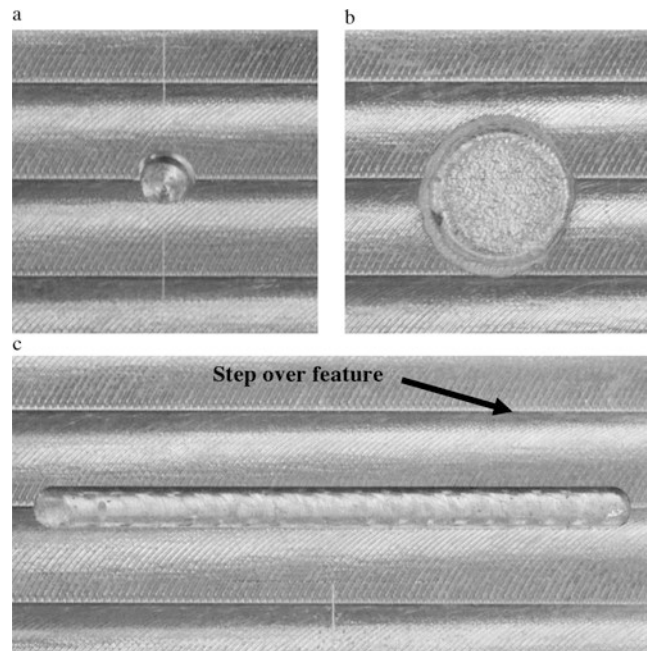
### Slotting

The slotting technique is like one-dimensional hole drilling in the sense that a single component of residual stress is measured per machined slot. Similar to hole drilling incremental cuts are made in the work piece and strain is measured. However, rather than a rosette, the slotting technique adopts a uniaxial gage. The slotting technique used the same depth schedule as shown in Table 10.2. The slot is shown in Fig. 10.2, and compared to the hole used for hole drilling.

**Table 10.2** Summary of the depth schedule used for slotting and hole drilling techniques

Index	Increment (mm)	Depth (mm)
0	0	0
1–10	0.0127	0.0127–0.127
11–16	0.0254	0.1524–0.2794
17–22	0.0508	0.3302–0.5842

**Fig. 10.2** Images of a (a) hole drilling measurement, (b) X-ray diffraction etch pit, and (c) slotting measurement. The distance between step over features is 4 mm. The diameter of the (a) hole is approximately 2 mm and the diameter of the (b) etch pit is approximately 5 mm. The length of the (c) slot is 24 mm and its width is 1.8 mm



## X-ray Diffraction

The application of X-ray diffraction in this study was facilitated by a Pulstec  $\mu$ -X360s X-ray residual stress measurement system. The experimental setup measures stress in one direction using a chromium tube producing X-rays at a wavelength of 2.29093 Å. The source output is 30 kV with a current of 1 mA and an exposure time between 15 and 30 s [6]. The X-rays are projected through a 1 mm (0.040 inch) diameter collimator at an incident angle of  $25^\circ \pm 1^\circ$  relative to the surface. This results in a scan area of approximately 2 mm (0.080 inch) diameter at the measurement location on the surface of the sample.

To measure NSRS as a function of depth an electrolytic polishing technique was used to incrementally remove layers of material. This process included the application of an adhesive strip and sealant with a 5 mm diameter hole over the measurement location. A plastic tube was placed over the measurement location and filled with an electrolytic solution. A current of 4 amps was passed through a metallic wand submerged in this solution for 15 s. These etch parameters removed layers of material of  $0.01 \pm 0.0025$  mm to  $0.02 \pm 0.0025$  mm over 12–15 increments and provided an approximately flat etch pit. These increments gave a total depth of 0.120–0.150 mm resulting in a depth profile similar to that used in the two mechanical techniques discussed above. Since the  $\mu$ -X360s only measures one component of stress per exposure the workpiece was rotated at each depth increment to measure both  $\sigma_{xx}$  and  $\sigma_{yy}$ .

Measuring the stress as a function of depth at multiple locations on a workpiece provides data that can be used to draw conclusion about the repeatability of NSRS from each technique. Averaging and overlaying these data from all techniques allows for intermethod comparison of the NSRS data. Additionally, measuring the NSRS with each technique on workpieces machined using a combination of cutting speed and feed per tooth lengths revealed correlations between these parameters and the magnitude and depth of NSRS. It is assumed that NSRS due to milling does not vary over the surface area of the plate (note that all measurements are in areas of steady-state milling, away from edges and areas of lead-in).

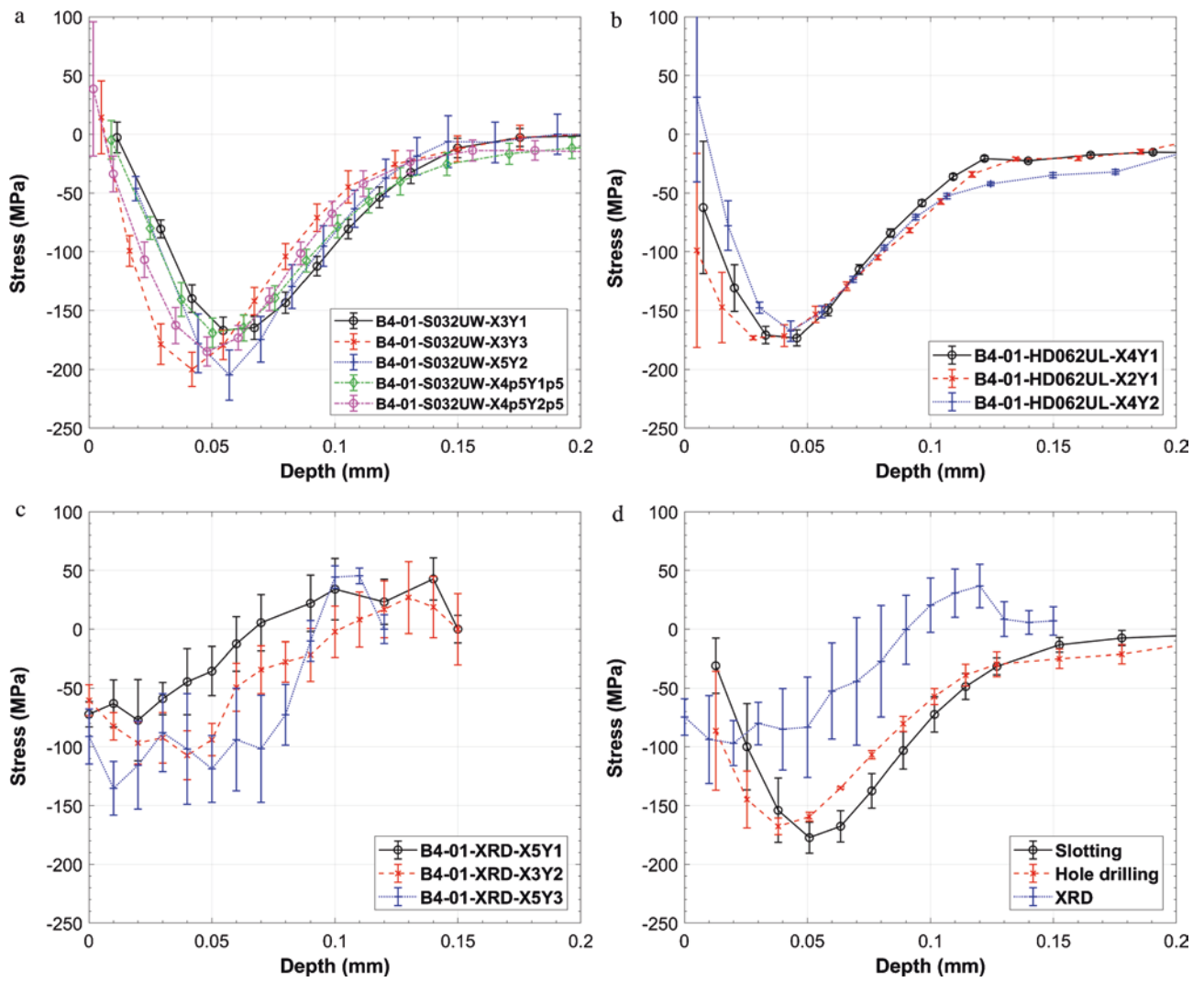
## Results

Figure 10.3 shows repeated stress measurements of the transverse component ( $\sigma_{yy}$ ) of NSRS (orthogonal to the machining path) using each method on the same part at various locations over the milled surface (location code defined in Fig. 10.1). Across all methods there is a clear trend of increasing compressive stress from the surface up to a depth of 0.05–0.06 mm (0.002–0.0024 inch) with a gradual climb to a steady stress of nearly 0 MPa at a depth of 0.12–0.15 mm. Data from the hole drilling and slotting techniques have maximum compressive value of stress of  $-175 \pm 10$  MPa at a depth of  $0.05 \pm 0.01$  mm. The X-ray diffraction data have maximum compressive stress of approximately  $-100$  MPa.

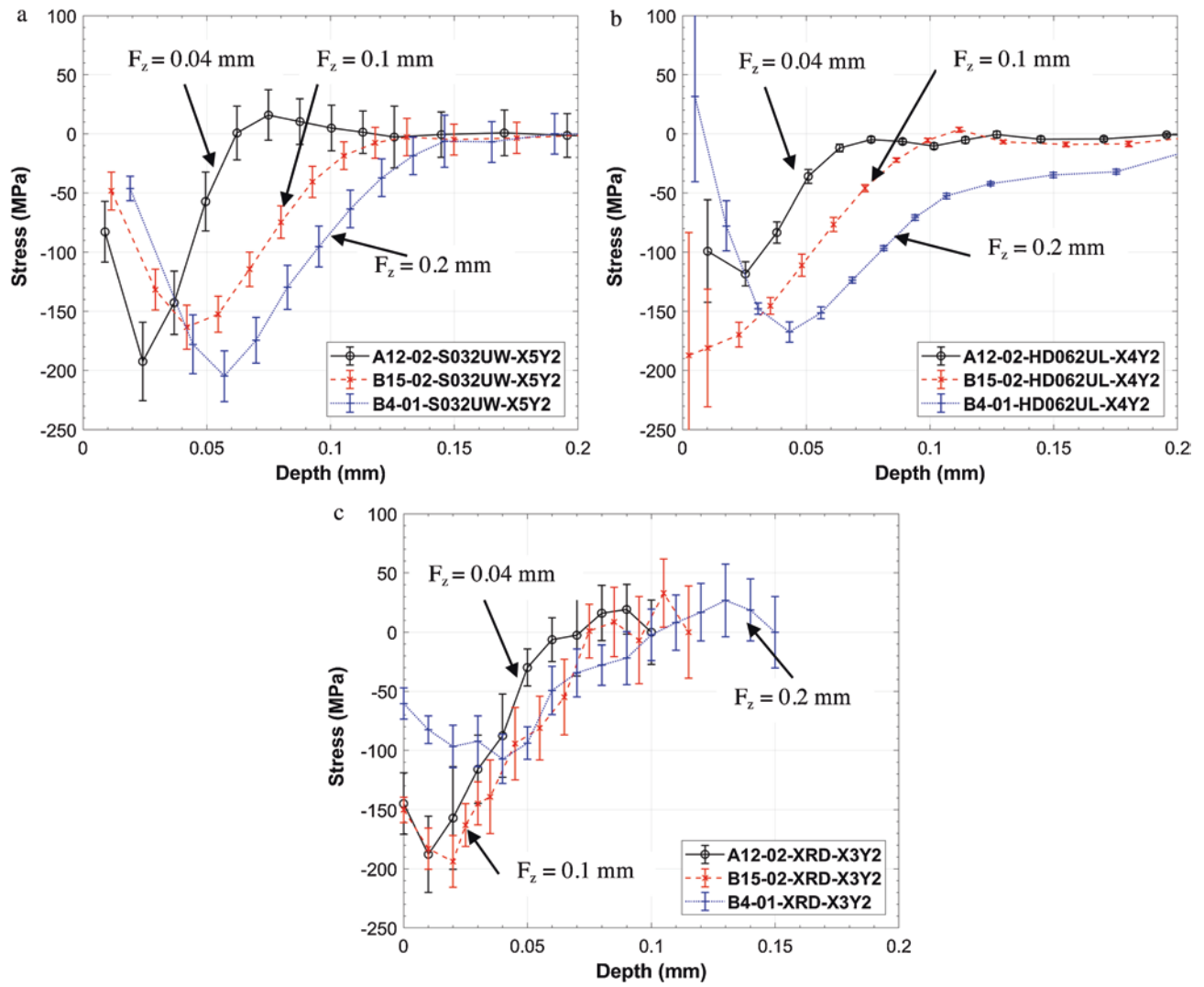
Figure 10.3d shows averaged data for each technique calculated by interpolating independent measurements to the depth schedule in Table 10.2 and calculating the average stress at each depth; the standard deviation at each depth is shown by the error bars in Fig. 10.3d. The hole drilling and slotting techniques compare well with a small difference in the depth of stress. The X-ray diffraction technique shows the same trend in stress but differs greatly in magnitude.

Figure 10.4 shows the transverse component ( $\sigma_{yy}$ ) of NSRS in samples A12, B15, and B4 which share the same cutting speed and vary in feed per tooth. There is a clear increase in the depth of residual stress with increasing feed per tooth. Across all techniques the maximum value of compressive stress ranges between  $-125$  and  $-200$  MPa with the depth of stress shifting by approximately 0.05 mm over the range in feed per tooth. The measurements on sample A12 appear consistent for all three techniques. On samples B15 and B4, data from the slotting and hole drilling measurements agree but the X-ray diffraction data does not.

Figure 10.5 shows the transverse component ( $\sigma_{yy}$ ) NSRS in samples A12 and B5 where the feed per tooth was fixed and the cutting speeds are 200 and 450 m/min, respectively. The data show that the two cutting speeds produce nearly the same residual stress. All three techniques provide consistent results. The slotting and X-ray techniques both show a maximum compressive value of stress of  $-190 \pm 30$  MPa, but they slightly disagree on the depth where this stress occurs. The slotting and hole drilling techniques show that the maximum compressive value of stress occurs at the same depth, 0.025 mm, but the magnitude from hole drilling is considerably less than that from slotting.



**Fig. 10.3** Repeat measurements of transverse residual stress ( $\sigma_{yy}$ ) on sample B4 for (a) slotting, (b) hole drilling, (c) X-ray diffraction, and (d) intermethod comparison of data from all techniques. The sample is machined with a cutting speed of 200 m/min and a feed per tooth length of 0.2 mm



**Fig. 10.4** Comparison of transverse ( $\sigma_{yy}$ ) residual stress in samples A12, B15, and B4 machined at a fixed cutting speed of 200 m/min and variable feed per tooth lengths for (a) slotting, (b) hole drilling, and (c) X-ray diffraction

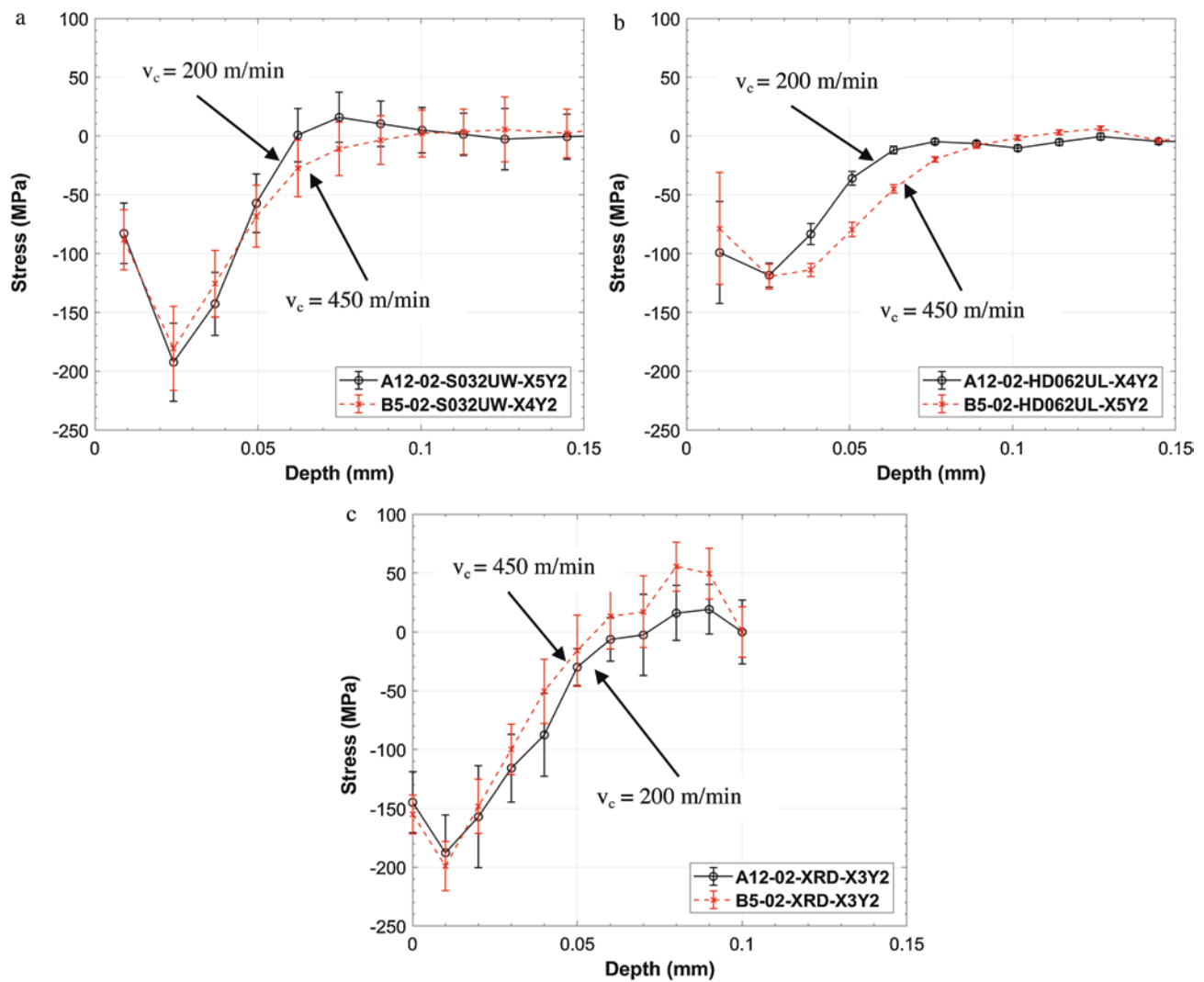


**Fig. 10.5** Comparison of transverse ( $\sigma_{yy}$ ) residual stress in low stress material machined at a fixed feed per tooth of 0.04 mm and variable cutting speed for (a) slotting, (b) hole drilling, and (c) X-ray diffraction

## Conclusion

The capability to measure near surface residual stress in aluminum work pieces machined with various milling parameters using hole drilling, slotting, and X-ray diffraction techniques has been considered through the above study. The repeatability data in Fig. 10.3 show that the hole drilling and slotting techniques provide more reliable NSRS data than X-ray diffraction in this alloy. Additionally, the intermethod comparison in Fig. 10.3d shows that the mechanical methods are consistent with one another, but not with X-ray diffraction.

This study was able to show, across all three techniques, that changes in the feed per tooth length (0.04, 0.1, and 0.2 mm) affects NSRS. The hole drilling and slotting data in Fig. 10.4 clearly show that the depth of NSRS increases with feed per tooth. The X-ray diffraction technique shows this trend weakly; however the X-ray results are not consistent with the other two techniques. The comparison of variable cutting speed (200 and 450 m/min) and fixed feed per tooth (0.04 mm) in Fig. 10.5 suggests that cutting speed did not significantly affect the depth or magnitude of NSRS. This trend is consistent across all of the techniques.

**Acknowledgements** The authors would like to thank Toshikazu Suzuki and his company, Pulstec, for the loan and instruction on the use of the  $\mu$ -X360s X-ray residual stress measurement system. Additional thanks to Dr. Benjamin Kirsch and Daniel Weber of the Institute for Manufacturing Technology and Production Systems, University of Kaiserslautern for their planning and manufacture of the machined workpieces used in this study. Thank you to Deutsche Forschungsgemeinschaft (DFG) for their cooperation and support. UC Davis received funding from the National Science Foundation under Award No. 1663341 (Division of Civil, Mechanical and Manufacturing Innovation, Manufacturing Machines and Equipment (MME)). Any opinions, findings, and conclusions or recommendations expressed in this material are those of the authors and do not necessarily reflect the views of the National Science Foundation.

## References

1. S. Masoudi, S. Amini, E. Saeidi, H. Eslami-Chalander, Effect of machining-induced residual stress on the distortion of thin-walled parts. *Int. J. Adv. Manuf. Technol.* **76**, 597–608 (2015). <https://doi.org/10.1007/s00170-014-6281-x>
2. B. Li, X. Jiang, J. Yang, S.Y. Liang, Effects of depth of cut on the redistribution of residual stress and distortion during the milling of thin-walled part. *J. Mater. Process. Technol.* **216**, 223–233 (2015). <https://doi.org/10.1016/j.jmatprotec.2014.09.016>
3. Z.T. Tang, Z.Q. Liu, X.A. Wan, Study on residual stresses in milling aluminum alloy 7050-T7451, in *Advanced Design and Manufacture to Gain a Competitive Edge: New Manufacturing Techniques and their Role in Improving Enterprise Performance*, ed. By X.T. Yan, C. Jiang, B. Eynard (Springer, London, 2008), pp. 169–178
4. STM International, *Standard Test Method for Determining Residual Stresses by the Hole-Drilling Strain-Gage Method* (ASTM International, West Conshohocken, 2013). <https://doi.org/10.1520/E0837-13A>
5. G.S. Schajer, P.S. Whitehead, *Hole-Drilling Method for Measuring Residual Stresses* (Morgan & Claypool Publishers, San Rafael, 2017)
6. T. Suzuki, interview by Christopher Chighizola. Pulstec Equipment Orientation and Training (2018)



# Chapter 11

## Inversion of Residual Stresses in Silicon Wafer from Surface Deflection Measurements

Yuri Obata and Satoru Yoneyama

**Abstract** This paper describes the evaluation method of residual stress of thin plate from deflection distribution. Using the deflection distribution calculated from the FEM and the deflection distribution of the actual silicon wafer, coefficients used for the principle of superposition are calculated from the least squares method. Residual stress is estimated from the principle of superposition using the stress obtained from FEM and the calculated coefficient. In order to evaluate the validity of the proposed method, residual stress distributions of those obtained by the finite element method and those obtained by the propose method are compared. Also from actual deflection distribution of silicon wafers, Residual stresses are estimated by the proposed method. Results show that the residual stress in silicon wafers can be obtained by the proposed method.

**Keywords** FEM · Deflection distribution · Residual stress · Principle of superposition

### Introduction

The higher precision and dimension accuracy of a silicon wafer are demanded due to the miniaturization and the complication of electronic substrates. A silicon wafer is a material formed of a pure silicon, and made of a single crystal of silicon into a thin disc shape. Residual stresses are generated from the temperature difference between the front and back surfaces of the silicon wafer during a manufacturing process [1–6]. Residual stress causes warping and peeling, so that the product is defective. From such a problem, it is important to consider how much residual stress will occur beforehand. Currently, deflection measurement using a laser displacement meter or an interferometer is used for quality inspection of silicon wafers. However, for the measurement of residual stress, it is necessary to use a hole drilling method or a X-ray diffraction method. If the residual stress can be obtained from the deflection measurements, it can be evaluated simply, and it is expected to be able to provide useful information for the manufacturing process.

In the past research, stress distribution was estimated from the displacement distribution of the linear elastic body [7, 8]. A hybrid method that using experiments and numerical analysis is proposed to obtain accurate stress and strain.

In this research, we propose a method for estimating the residual stress by inverse problem analysis from the deflection distribution measurement value of silicon wafers. The deflection distribution of a silicon wafer is measured using a laser displacement sensor. Then, the residual stresses are estimated from the measured and simulated deflections that considering orthotropic anisotropy based on the principle of superposition [4]. The effectiveness of the proposed method is demonstrated by evaluating the residual stresses of a silicon wafer. Results show that the proposed method can be applied to the evaluation of the residual stresses of the silicon wafer.

### Residual Stress Evaluation Method

As a prerequisite, linear elastic body is the target. This deformation is by thermal stress. Bending of a thin plate is assumed. In this research, we consider the case where the out-of-plane direction displacement distribution of the measurement object is obtained by using the laser displacement meter. We prepare the model of the measurement by finite element method. We calculate the out-of-plane direction displacement by FEM when the  $x$  and  $y$  direction unit normal stresses are applied to one

---

Y. Obata (✉) · S. Yoneyama

Department of Mechanical Engineering, Aoyama Gakuin University, Sagamihara, Kanagawa, Japan  
e-mail: c5618129@aoyama.jp; yoneyama@me.aoyama.ac.jp

element and behind it. Then, initial stress of positive value is given to surface. And initial stress of negative value is given to reverse side. By this condition, we consider the case of bending plate. The out-of-plane direction displacement by calculating FEM is assumed to be the displacement components  $w'_{ij}$ . In this case,  $i$  and  $j$  are subscripts for identifying the measurement points of the respective data and those number that given as initial stress to the elements, and  $i = 1 \sim M$  and  $j = 1 \sim N$ . Also, the out-of-plane direction displacement distribution of the actual measurement target is defined as  $w_i$ . Using the measured displacement value of the out-of-plane direction of the measurement object and the displacement component  $w'_{ij}$  calculated using the finite element method model, the following from the principle of superposition.

$$w_i = \alpha_j w'_{ij} \quad (11.1)$$

Here,  $\alpha_j$  is coefficients. The displacement component  $w'_{ij}$  is obtained by the finite element method, and the actual displacement  $w_i$  is obtained by measurement. Therefore, when the number of the data measurement point  $M$  is larger than the number  $N$  of elements giving the unit stress, the coefficient  $\alpha_j$  can be obtained by the least squares method of the following equation.

$$\alpha = (\mathbf{A}^T \mathbf{A})^{-1} \mathbf{A}^T \mathbf{U} \quad (11.2)$$

where  $\alpha$ ,  $\mathbf{A}$ , and  $\mathbf{U}$  are the coefficients, the displacements obtained by the unit initial stress, and the measured values of the out-of-plane displacement, respectively. These can be expressed as follows.

$$\alpha = \begin{Bmatrix} \alpha_1 \\ \alpha_2 \\ \vdots \\ \alpha_N \end{Bmatrix} \quad \mathbf{A} = \begin{Bmatrix} w'_{11} & w'_{12} & \cdots & w'_{1N} \\ w'_{21} & \cdots & \cdots & \vdots \\ \vdots & \ddots & \ddots & \vdots \\ w'_{M1} & \cdots & \cdots & w'_{MN} \end{Bmatrix} \quad \mathbf{U} = \begin{Bmatrix} u_1 \\ u_2 \\ \vdots \\ u_N \end{Bmatrix} \quad (11.3)$$

From the above equations, we can determine  $\alpha_j$ , so that it is possible to calculate the residual stress distribution. The principle of superposition principle can also be applied to stress. Therefore, the following equation holds.

$$\sigma_i = \alpha_j \sigma'_{ij} \quad (11.4)$$

Based on the above equation, residual stress can be estimated. In proposed method, the least squares method is applied in consideration of measurement error. Therefore, it can be expected to improve the reliability of the calculated result.

## Verification of Proposed Method

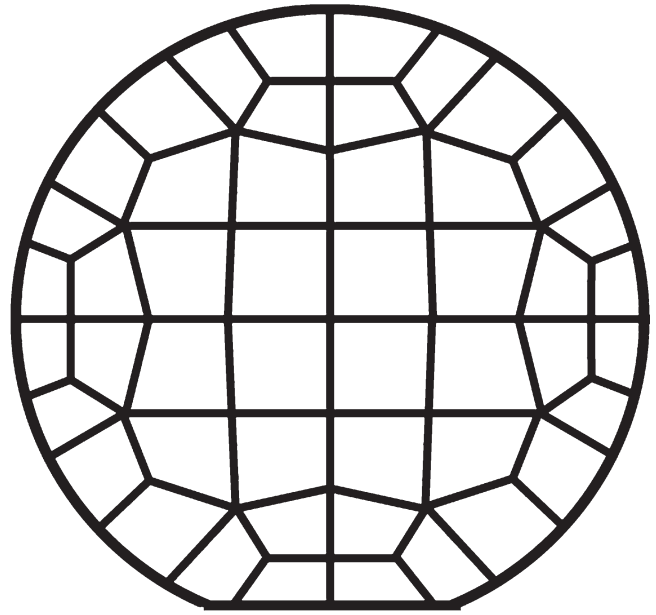
We assess the validity of the residual stress estimation method. As verification, the actual measurement is not used. By using the finite element method, the out-of-plane directional displacement of actual measurement is simulated. It is treated as the measured value and correct value. The residual stress distribution obtained by the finite element method is compared with the residual stress distribution calculated by the proposed method. The model is shown in Fig. 11.1. The model to be used is a silicon wafer with  $\phi 200$  mm and a thickness of 725  $\mu\text{m}$ , consisting of 96 elements in total, 48 elements on the front side and 48 elements on the back side. For the setting of the finite element method, the solid element used is an isoparametric element, the material property is an orthotropic property, the elastic constants are  $c_{11} = 165.77\text{GPa}$ ,  $c_{12} = 63.93\text{GPa}$ ,  $c_{44} = 79.62\text{GPa}$  [9].

The measurement point to use is 169 points on the surface node of the model. Moreover, by constraint the  $x$ ,  $y$ ,  $z$  direction of the model with 2 points, rotation of the object is prevented. The unit stress is given to each element of the model to obtain deflection distribution,  $x$  direction stress, and  $y$  direction stress. Figure 11.2 shows the deflection distribution results when initial stress is applied to the model simulating the actual measurement object.

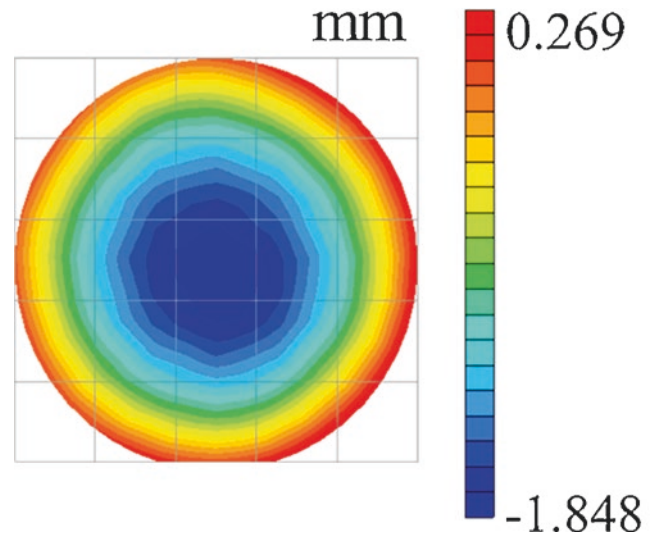
Using the displacement components and the stress components and the distribution deflection of measurement, residual stresses evaluation is performed by the least squares method and the principle of superposition. Figure 11.3 shows the deflection results by proposed method. From Fig. 11.4, the deflection calculated by the proposed method concordant correct value. From the result, it is shown that  $\alpha_j$  is accurately calculated using the least squares method and the deflection is also calculated



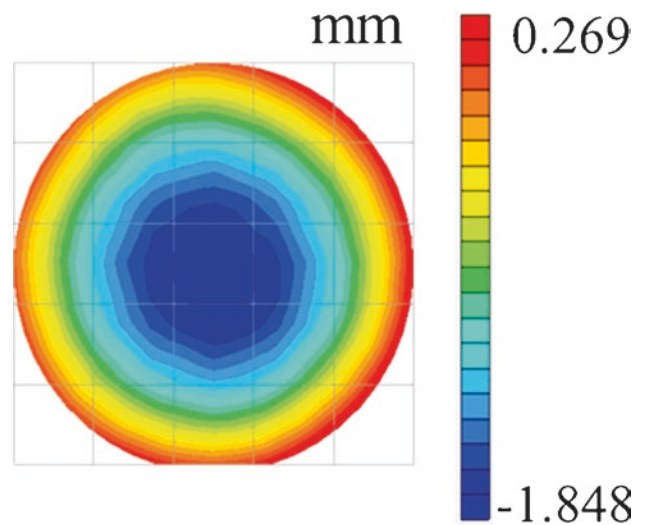
**Fig. 11.1** Silicon wafers model



**Fig. 11.2** Distribution deflection of measuring object



**Fig. 11.3** Deflection by proposed method



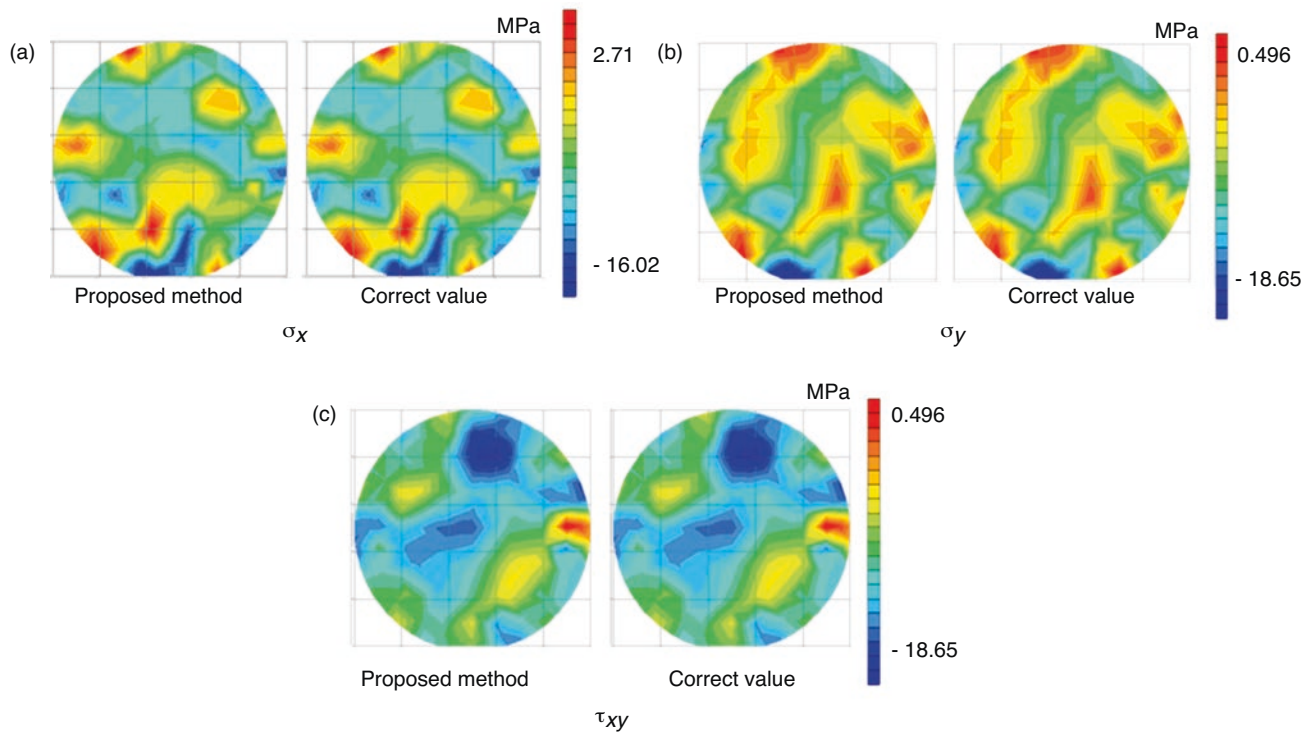


Fig. 11.4 Stress by proposed method and correct value(FEM)

using the principle of superposition. When applying the principle of superposition to stress, it is considered that the residual stress can be estimated by using the  $\alpha_j$  obtained from the deflection. Figure 11.4 show the result of the stress distribution by using the proposed method and the correct value.

Figure 11.4 shows that the normal stress in the  $x$  direction and the  $y$  direction and the shear stress both coincide with the correct value. Therefore, the  $\alpha_j$  calculated from the deflection distribution by the least squares method can also be applied to the principle of stress superposition. From the above results, it is possible to show the validity of the proposed method of residual stress estimation using the principle of superposition.

## Residual Stress by Proposed Method

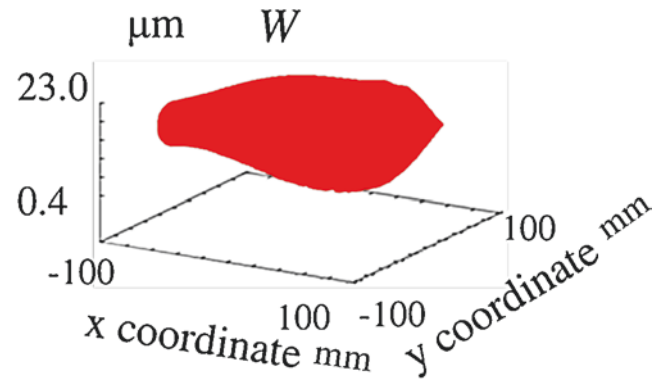
From the third chapter, the validity of the proposed method was examined. In this chapter, residual stress is estimated by the proposed method from using actual measured deflection distribution of silicon wafer. Figure 11.5 shows actual measured deflection distribution of a silicon wafer by a laser displacement sensor. The measured silicon wafer size is 200 mm in diameter and 725  $\mu\text{m}$  in thickness. Minimum resolution of testing machine is 0.1  $\mu\text{m}$ . The measurement pitch is 0.5 mm.

The coordinates of measured deflection distribution is different from the node coordinates of the finite element method. And displacement components calculated by FEM are zero displacement at two point. So we must match the coordinates of the FEM with the coordinates of the measured deflection distribution. Figure 11.6 shows the deflection distribution used for the proposed method, which coincides the measured coordinates with the coordinates of FEM.

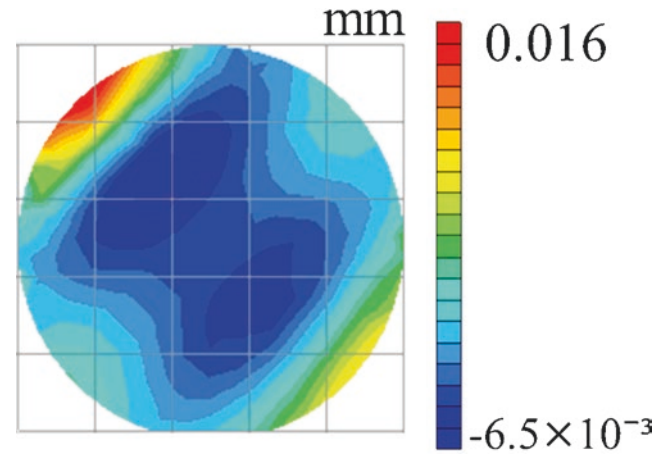
Residual stress of measured deflection distribution is estimated from the deflection of Fig. 11.6 and component of displacement and stress by FEM. First, Fig. 11.7 shows the calculated deflection distribution using the measured deflection distribution and displacement components by the least squares method.

From this result, the calculated deflection distribution is almost correspond with the measured deflection distribution and  $\alpha_j$  is calculated by the least squares method. According to the principle of superposition, residual stress is estimated using calculated  $\alpha_j$  and the stress component. Figure 11.8 shows residual stresses of  $x$  and  $y$  normal stress and shear stress.

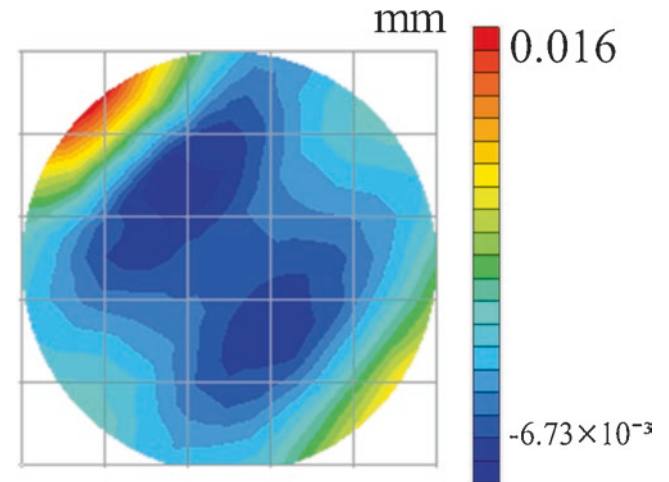
**Fig. 11.5** The measured deflection of silicon wafers



**Fig. 11.6** The measured deflection distribution after smoothing



**Fig. 11.7** Calculated deflection distribution by proposed method



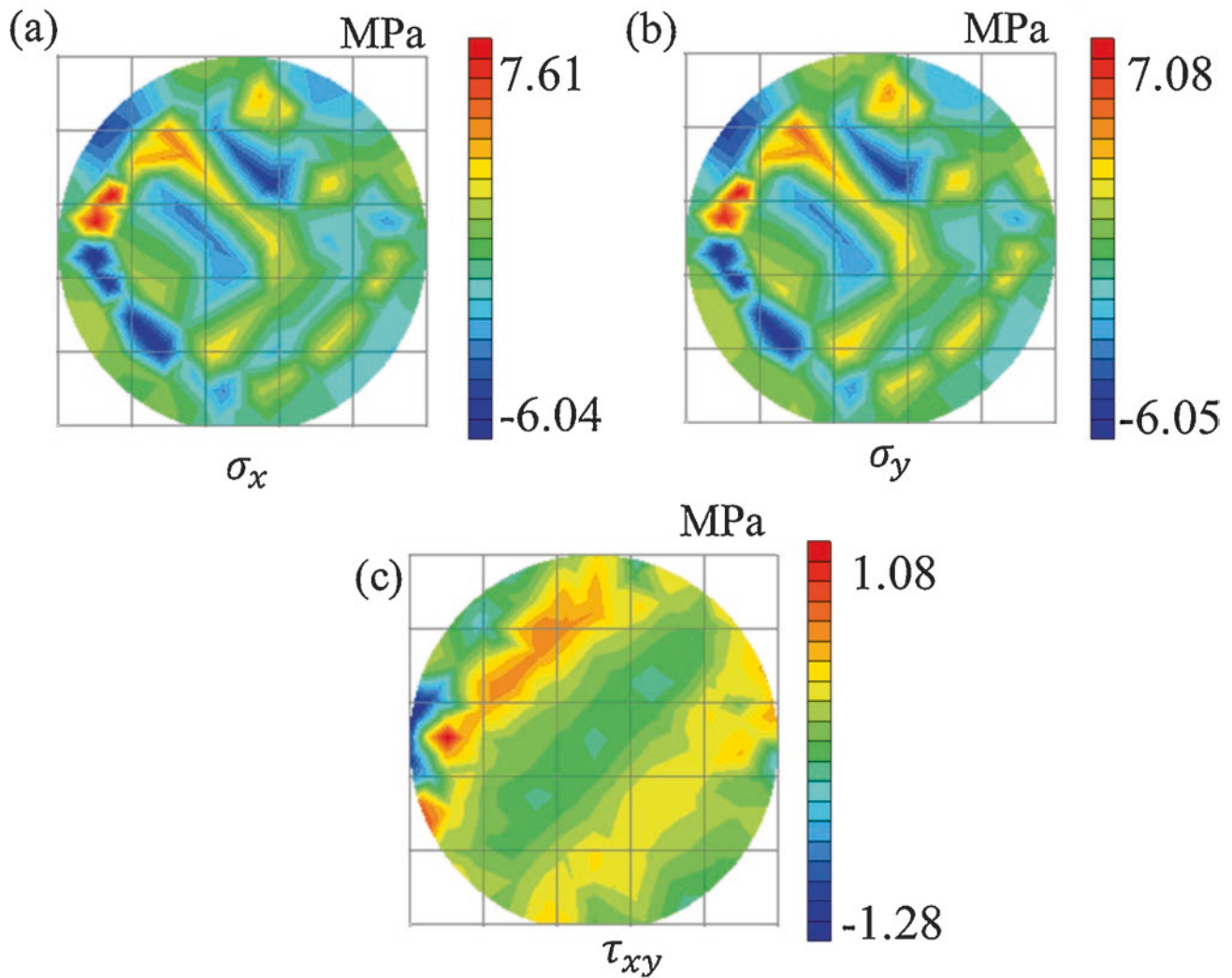


**Fig. 11.8** Calculated residual stresses of silicon wafer when deflection occurred by proposed method

The result of estimating the residual stress of an actual silicon wafer by the proposed method is shown. Section “Verification of Proposed Method” shows the validity of the proposed method. From Fig. 11.8, we show the possibility that residual stress can be estimated by the proposed method.

## Discussion

In this study, a method of residual stress estimation based on the principle of superposition and the least squares method using the FEM and actual deflection distribution is proposed. A model considering material properties of silicon wafers was made using the FEM. Also, displacement components and stress components are calculated using the model.  $\alpha_j$  is calculated by the least squares method using the deflection distribution and the displacement component of the measurement object. Using the obtained  $\alpha_j$ , the results of the deflection distribution and the stress calculated by the superposition principle were compared with the results of FEM with correct values. From the comparison result, the validity of the proposed method for estimating the residual stress is shown. Also, residual stresses of actual measured deflection distribution is estimated by proposed method. This result show the possibility that residual stress can be estimated by the proposed method.

## References

1. K. Masanori, Semiconductor no Kihon. Softbank Creat. **6**, 124–136 (2011)
2. Y.B. Tian, Finite element analysis of deflection and residual stress on machined ultra-thin silicon wafers. *Semicond. Sci. Technol.* **36**, 105002 (2011)
3. H. Sudou, Residual stresses and distorted. *Uchida Rokakuhou.* **7**, 85–97 (2003)
4. Y.B. Tian et al., Finite element analysis of deflection and residual stress on machined ultra-thin silicon wafers. *Semicond. Sci. Technol.* **26**(10), 1–7 (2011)
5. S. Arimura, Silicon crystal and wafer processing. *Precis. Eng. J.* **51**(7), 1296–1302 (1985)
6. K. Tanaka, *Evaluation of Residual Stresses by X-Ray Diffraction –Fundamental and Applications* (Yokendo, Tokyo, 2006), pp. 25–32
7. S. Yoneyama, S. Akikawa, Identification of boundary condition from measured displacement for linear elastic deformation fields. *Proc. IUTAM* **4**, 215–216 (2011)
8. S. Yoneyama, Determination of boundary conditions and stress distribution using measured values of displacement distribution. *Mater. Syst.* **29**, 40–45 (2011)
9. N. Suzuki et al., *Ultrasonic Handbook* (Ultrasonic Handbook Editing Committee, New York, 2001), pp. 281–284



## Chapter 12

# Evaluating the Coefficient of Thermal Expansion of Electronic Board Using the Virtual Fields Method

Yohei Kanai, Shuichi Arikawa, Satoru Yoneyama, and Yasuhisa Fujimoto

**Abstract** This paper proposes a method for identifying the coefficient of thermal expansion of dissimilar materials. Dissimilar materials are simulating on an electronic packaging. Displacement data used for inverse analysis are obtained by digital image correlation which is a method for measuring displacement in the full field of view without contact. The virtual fields method based on the principle of virtual work is employed as a method for inverse analysis. Each coefficient of thermal expansion that is unknown parameters is determined by preparing virtual displacements as many as the number of unknowns. The effectiveness of the inverse analysis method is demonstrated by identifying the coefficients of thermal expansion of dissimilar materials. Results show that the coefficient of thermal expansion can be obtained by the proposed method.

**Keywords** Coefficient of thermal expansion · Inverse analysis · Virtual fields method · DIC · Electronic board

## Introduction

Electronic circuit boards are a mechanical component of electronics used in railway vehicles, automobiles, elevator control devices, etc. They are made of various materials such as metal, resin and ceramics having different mechanical properties. A difference in the coefficient of thermal expansion of the materials can lead to large thermal stress and strain from heat generation in device and changes in ambient temperature, leading to device failure. Therefore, repeated thermal stress and strain occur on the mounting board due to repeated application of heat on elements and parts on the board due to turning on and off of the electronic equipment under harsh environments of high voltage and large current [1]. Due to this repeated thermal stress, peeling and cracking are caused in solder of parts and bonded parts such as resin, which is considered as one of causes of failure. For designing various products and structures, it is important to understand the material characteristics constituting those devices and structures. In recent years, along with high performance, compactness, weight reduction, and cost reduction of electronic devices and products, the miniaturization and the densification of mounting boards are progressing. Material properties in device may be different from the values obtained from the conventional tensile tests with bulk specimens. Therefore it is necessary to accurately ascertain the coefficient of thermal expansion of the minute parts and structures contained in electric substrate.

As a method for identifying the material properties, it is effective to apply a load to the actual equipment structure and perform inverse problem analysis with the measurement results of displacement and strain obtained as input data. The Virtual Fields Method (VFM) proposed by Grediac et al. [2] is based on the principle of virtual work. It is a method for identifying material properties in a constitutive equation, and the research has been actively conducted in recent years [3, 4]. As a past study, Sato et al. [5] identified elastic material characteristic distribution of dissimilar materials using VFM. This method is effective for identifying material properties of heterogeneous materials.

---

Y. Kanai (✉) · S. Yoneyama

Department of Mechanical Engineering, Aoyama Gakuin University, Sagami-hara-shi, Kanagawa, Japan  
e-mail: [c5618132@aoyama.jp](mailto:c5618132@aoyama.jp); [yoneyama@me.aoyama.ac.jp](mailto:yoneyama@me.aoyama.ac.jp)

S. Arikawa

Department of Mechanical Engineering Informatics, Meiji University, Tama-ku, Kawasaki-shi, Kanagawa, Japan  
e-mail: [arikawa@meiji.ac.jp](mailto:arikawa@meiji.ac.jp)

Y. Fujimoto

Mitsubishi Electric Corporation Advanced Technology Research and Development Center, Amagasaki-shi, Hyogo, Japan  
e-mail: [fujimoto.yasuhisa@db.MitsubishiElectric.co.jp](mailto:fujimoto.yasuhisa@db.MitsubishiElectric.co.jp)

This research aims to identify the coefficient of thermal expansion of dissimilar materials from displacement distribution. Here, the dissimilar materials simulate a mounting structure of soldered joints and the laminates of electric mounting boards. Displacement distribution measured using digital image correlation (DIC) [6] is used as the input and the virtual fields method is used as an inverse analysis method. Results of a uniform thermal loading test show the effectiveness of the proposed method.

## Methods

### *Basic Principle of the Virtual Fields Method*

VFM is used for identification of the coefficient of thermal expansion of a test specimen. This method is based on the principle of virtual work. When an arbitrary virtual displacement is given to an object in equilibrium state, external virtual work and internal virtual work are equal. The principle of virtual work is expressed as

$$\int_{\Omega} \sigma_{ij} \varepsilon_{ij}^* d\Omega = \int_{\Gamma} T_i u_i^* d\Gamma \quad (12.1)$$

In this equation,  $\sigma_{ij}$  is the stress component,  $\varepsilon_{ij}^*$  is the virtual strain component,  $T_i$  is the traction,  $u_i^*$  is the virtual displacement,  $\Omega$  is the analysis area and  $\Gamma$  is the boundary surface of  $\Omega$  that is subjected to external loading. The subscripts  $i$  and  $j$  indicate the  $x$  and  $y$  directions in the Cartesian coordinate system.

Considering an elastic body as a test specimen, the stress-strain relationship can be expressed as follows with the stiffness matrix.

$$\begin{Bmatrix} \sigma_1 \\ \sigma_2 \\ \sigma_6 \end{Bmatrix} = \begin{bmatrix} C_{11} & C_{12} & 0 \\ C_{12} & C_{22} & 0 \\ 0 & 0 & C_{66} \end{bmatrix} \begin{Bmatrix} \varepsilon_1 \\ \varepsilon_2 \\ \varepsilon_6 \end{Bmatrix} \quad (12.2)$$

where  $\sigma_1$  and  $\sigma_2$  are the normal stresses,  $\sigma_6$  is the shear stress,  $\varepsilon_1$  and  $\varepsilon_2$  the normal strains, and  $\varepsilon_6$  is the shear strain, respectively. In Eq. (12.2),  $C_{11}$ ,  $C_{12}$ ,  $C_{22}$  and  $C_{66}$  are the elastic constants, and relate the elastic modulus and Poisson's ratio. The following equation is obtained from Eqs. (12.1) and (12.2).

$$C_{11} \int_{\Omega} \left( \varepsilon_1 \varepsilon_1^* + \varepsilon_2 \varepsilon_2^* + \frac{1}{2} \varepsilon_6 \varepsilon_6^* \right) d\Omega + C_{12} \int_{\Omega} \left( \varepsilon_2 \varepsilon_1^* + \varepsilon_1 \varepsilon_2^* - \frac{1}{2} \varepsilon_6 \varepsilon_6^* \right) d\Omega = \int_{\Gamma} (T_1 u_1^* + T_2 u_2^*) d\Gamma \quad (12.3)$$

In Eq. (12.3),  $\varepsilon_1$ ,  $\varepsilon_2$  and  $\varepsilon_6$  are the strain components in the target object and can be obtained by differentiating the measured displacement. Also,  $u_1^*$  and  $u_2^*$  are the virtual displacement components, and  $\varepsilon_1^*$ ,  $\varepsilon_2^*$  and  $\varepsilon_6^*$  are the virtual strain components that can be obtained by differentiating the virtual displacements. Unknown parameters  $C_{11}$  and  $C_{12}$  can be obtained by substituting two kinds of virtual displacement into Eq. (12.3) and solving it.

### *Identification of the Coefficient of Thermal Expansion*

In order to apply the virtual fields method to the identification of the coefficient of thermal expansion, considering the thermal load. Since the test specimen is not bounded in this test, it is assumed that  $T_i = 0$ , and Eq. (12.1) can be expressed as

$$\int_{\Omega} \sigma_{ij} \varepsilon_{ij}^* d\Omega = 0 \quad (12.4)$$

As the temperature changes, the size and shape of the object change and displacement, strain and stress are generated. The generated displacement, strain and stress due to temperature change, are referred to as thermal displacement, thermal strain and thermal stress, respectively. Since the total strain is the sum of the thermal strain and the elastic strain, it is expressed by the following equation.

$$\varepsilon^{\text{all}} = \varepsilon + \varepsilon^{\text{th}} \quad (12.5)$$

where  $\varepsilon^{\text{all}}$  is the total strain,  $\varepsilon$  is the elastic strain,  $\varepsilon^{\text{th}}$  is the thermal strain. The following equation is obtained from Eqs. (12.2) and (12.5). At this time, since deformation due to heat is not related to shear stress and shear strain,  $\sigma_6$  and  $\varepsilon_6$  do not change.

$$\begin{Bmatrix} \sigma_1 \\ \sigma_2 \\ \sigma_6 \end{Bmatrix} = \begin{bmatrix} C_{11} & C_{12} & 0 \\ C_{12} & C_{22} & 0 \\ 0 & 0 & C_{66} \end{bmatrix} \begin{Bmatrix} \varepsilon_1 - \varepsilon_x^{\text{th}} \\ \varepsilon_2 - \varepsilon_y^{\text{th}} \\ \varepsilon_6 \end{Bmatrix} \quad (12.6)$$

where  $\varepsilon_x^{\text{th}}$  and  $\varepsilon_y^{\text{th}}$  can be expressed as  $\alpha T$ .  $\alpha$  is the coefficient of thermal expansion and  $T$  is the temperature change. The following equation is obtained from Eqs. (12.3) and (12.6).

$$C_{11} \int_{\Omega} \left( \varepsilon_1 \varepsilon_1^* + \varepsilon_2 \varepsilon_2^* + \frac{1}{2} \varepsilon_6 \varepsilon_6^* \right) d\Omega + C_{12} \int_{\Omega} \left( \varepsilon_2 \varepsilon_1^* + \varepsilon_1 \varepsilon_2^* - \frac{1}{2} \varepsilon_6 \varepsilon_6^* \right) d\Omega = \alpha T \int_{\Omega} (C_{11} + C_{12}) (\varepsilon_1^* + \varepsilon_2^*) d\Omega \quad (12.7)$$

The inverse analysis can be carried out by giving virtual displacements corresponding to the number of materials when only the coefficient of thermal expansion is unknown parameter.

In the case of identifying the material properties of the dissimilar materials composed of three different metals, the following equation can be obtained from the Eq. (12.7) when the three kinds of materials are A, B and C, respectively.

$$\begin{aligned} & C_{11}^A \int_{\Omega^A} \left( \varepsilon_1^A \varepsilon_1^* + \varepsilon_2^A \varepsilon_2^* + \frac{1}{2} \varepsilon_6^A \varepsilon_6^* \right) d\Omega + C_{12}^A \int_{\Omega^A} \left( \varepsilon_2^A \varepsilon_1^* + \varepsilon_1^A \varepsilon_2^* - \frac{1}{2} \varepsilon_6^A \varepsilon_6^* \right) d\Omega \\ & + C_{11}^B \int_{\Omega^B} \left( \varepsilon_1^B \varepsilon_1^* + \varepsilon_2^B \varepsilon_2^* + \frac{1}{2} \varepsilon_6^B \varepsilon_6^* \right) d\Omega + C_{12}^B \int_{\Omega^B} \left( \varepsilon_2^B \varepsilon_1^* + \varepsilon_1^B \varepsilon_2^* - \frac{1}{2} \varepsilon_6^B \varepsilon_6^* \right) d\Omega \\ & + C_{11}^C \int_{\Omega^C} \left( \varepsilon_1^C \varepsilon_1^* + \varepsilon_2^C \varepsilon_2^* + \frac{1}{2} \varepsilon_6^C \varepsilon_6^* \right) d\Omega + C_{12}^C \int_{\Omega^C} \left( \varepsilon_2^C \varepsilon_1^* + \varepsilon_1^C \varepsilon_2^* - \frac{1}{2} \varepsilon_6^C \varepsilon_6^* \right) d\Omega \\ & = C_{11}^A \alpha^A T^A \int_{\Omega^A} (\varepsilon_1^* + \varepsilon_2^*) d\Omega + C_{12}^A \alpha^A T^A \int_{\Omega^A} (\varepsilon_1^* + \varepsilon_2^*) d\Omega \\ & + C_{11}^B \alpha^B T^B \int_{\Omega^B} (\varepsilon_1^* + \varepsilon_2^*) d\Omega + C_{12}^B \alpha^B T^B \int_{\Omega^B} (\varepsilon_1^* + \varepsilon_2^*) d\Omega \\ & + C_{11}^C \alpha^C T^C \int_{\Omega^C} (\varepsilon_1^* + \varepsilon_2^*) d\Omega + C_{12}^C \alpha^C T^C \int_{\Omega^C} (\varepsilon_1^* + \varepsilon_2^*) d\Omega \end{aligned} \quad (12.8)$$

Following equation is obtained by giving three types of virtual displacements for unknowns.

$$\begin{pmatrix} P^{(1)} \\ P^{(2)} \\ P^{(3)} \end{pmatrix} = T \begin{bmatrix} Q^{A(1)} & Q^{B(1)} & Q^{C(1)} \\ Q^{A(2)} & Q^{B(2)} & Q^{C(2)} \\ Q^{A(3)} & Q^{B(3)} & Q^{C(3)} \end{bmatrix} \begin{pmatrix} \alpha^A \\ \alpha^B \\ \alpha^C \end{pmatrix} \quad (12.9)$$

where

$$\begin{aligned} P^{(1)} &= C_{11}^A \int_{\Omega^A} \left( \varepsilon_1^A \varepsilon_1^{*(1)} + \varepsilon_2^A \varepsilon_2^{*(1)} + \frac{1}{2} \varepsilon_6^A \varepsilon_6^{*(1)} \right) d\Omega + C_{12}^A \int_{\Omega^A} \left( \varepsilon_2^A \varepsilon_1^{*(1)} + \varepsilon_1^A \varepsilon_2^{*(1)} - \frac{1}{2} \varepsilon_6^A \varepsilon_6^{*(1)} \right) d\Omega \\ & + C_{11}^B \int_{\Omega^B} \left( \varepsilon_1^B \varepsilon_1^{*(1)} + \varepsilon_2^B \varepsilon_2^{*(1)} + \frac{1}{2} \varepsilon_6^B \varepsilon_6^{*(1)} \right) d\Omega + C_{12}^B \int_{\Omega^B} \left( \varepsilon_2^B \varepsilon_1^{*(1)} + \varepsilon_1^B \varepsilon_2^{*(1)} - \frac{1}{2} \varepsilon_6^B \varepsilon_6^{*(1)} \right) d\Omega \\ & + C_{11}^C \int_{\Omega^C} \left( \varepsilon_1^C \varepsilon_1^{*(1)} + \varepsilon_2^C \varepsilon_2^{*(1)} + \frac{1}{2} \varepsilon_6^C \varepsilon_6^{*(1)} \right) d\Omega + C_{12}^C \int_{\Omega^C} \left( \varepsilon_2^C \varepsilon_1^{*(1)} + \varepsilon_1^C \varepsilon_2^{*(1)} - \frac{1}{2} \varepsilon_6^C \varepsilon_6^{*(1)} \right) d\Omega \\ Q^{A(1)} &= C_{11}^A \int_{\Omega^A} (\varepsilon_1^* + \varepsilon_2^*) d\Omega + C_{12}^A \int_{\Omega^A} (\varepsilon_1^* + \varepsilon_2^*) d\Omega \end{aligned} \quad (12.10)$$

The superscript of  $P$  and  $Q$  describes the index of virtual displacement. Equation (12.9) can be expressed as following equation.

$$\mathbf{P} = \mathbf{Q}\mathbf{R} \quad (12.11)$$

Equation (12.11) is simultaneous equations relating to unknown parameters  $\alpha^A$ ,  $\alpha^B$  and  $\alpha^C$ . Therefore, the coefficient of thermal expansion can be obtained from multiplying the left side of both sides of equation by the inverse matrix  $\mathbf{Q}^{-1}$ .



## Experiment

### Specimen

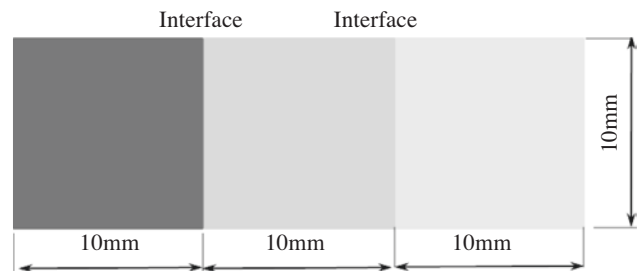
To verify the effectiveness of the proposed method, a thermal load test is carried out with dissimilar materials composed three kinds of metal with the coefficient of thermal expansion mismatch. Figure 12.1 shows the dimensions and shape of an example test specimen schematically. Silver solder is used for adhesion and the joining method is torch brazing. For the specimen, heterojointed body consisting of a low coefficient of thermal expansion and a high coefficient of thermal expansion simulating the substrate structure is used. Most of the laminate has three layers or more and a structure including an intermediate layer. Therefore, to observe the influence by the dimension of the width, four kinds of test specimen with different widths of the intermediate layer are used. The size of the test specimen is  $10 \times 10 \times 3$  mm at both ends, and the intermediate layer has 4 types of length and thickness of  $10 \times 3$  mm, width of 2, 4, 7 and 10 mm. Combination of the test piece used for the heat load test is C2801-C1020-SUS430. Table 12.1 shows the material properties of each material.

### Experimental and Analysis Procedure

A test specimen is placed in a heat spreader in a thermostatic chamber. A CCD camera is placed above the thermostat to capture the deformation behavior of the test specimen. The temperature in the chamber can be controlled in the increments of  $1^\circ\text{C}$ . The test specimen is heated from the room temperature ( $25^\circ\text{C}$ ) to  $75^\circ\text{C}$  ( $\Delta 50^\circ\text{C}$ ),  $100^\circ\text{C}$  ( $\Delta 75^\circ\text{C}$ ),  $125^\circ\text{C}$  ( $\Delta 100^\circ\text{C}$ ),  $150^\circ\text{C}$  ( $\Delta 125^\circ\text{C}$ ) and  $175^\circ\text{C}$  ( $\Delta 150^\circ\text{C}$ ) and a uniform heat load is applied to the test piece. The displacement distribution of the surface of the test specimen is measured from the photographed images. DIC is used for the displacement measurement. DIC is performed from images obtained before and after the uniform thermal load test. A telecentric lens is attached to a CCD camera whose resolution is  $2048 \times 2048$  pixels and its bit depth is 8 bits. The subset size for analysis is  $31 \times 31$  pixels. A test specimen is coated with a random pattern of the surface with a black and white lacquer spray.

Figure 12.2 shows the mesh models used for inverse analysis in this experiment, which are constructed using 8 node isoparametric elements. A similar analysis is carried out using mesh model which is 75 elements model. The displacement data is allocated to each node point of the mesh model and the inverse analysis is performed. The integral calculation included in Eq. (12.7) is executed by piecewise virtual fields [7, 8] with the mesh model [9].

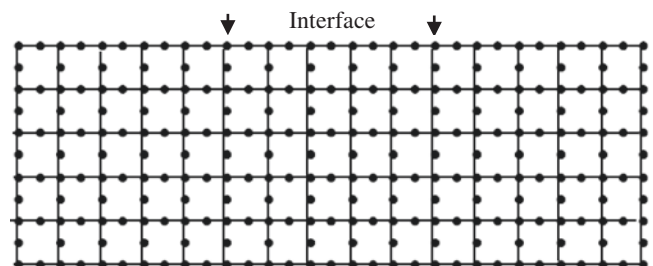
**Fig. 12.1** Test specimen



**Table 12.1** Material properties

Material	Elastic modulus (GPa)	Poisson's ratio	Coefficient of thermal expansion (ppm/ $^\circ\text{C}$ )
C2801 (brass)	103	0.35	19.5
C1020 (copper)	118	0.33	17.4
SUS430 (stainless steel)	206	0.30	10.3

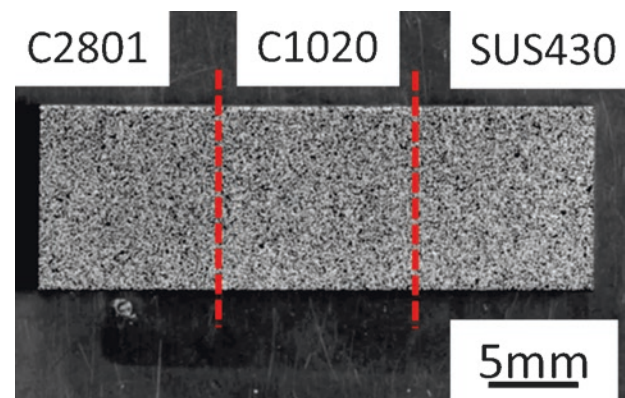
**Fig. 12.2** Mesh model  
(nodes: 266, elements:75)



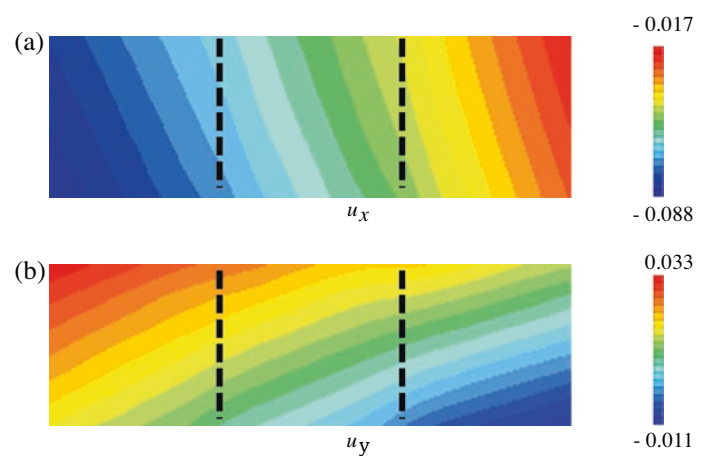
## Results

Figure 12.3 shows the surface image of the test specimen at the reference temperature (25 °C) before thermal loading. The red dash line indicates the interface. Displacement distribution data are obtained from DIC, taking the image of specimens before uniform thermal loading as the reference image. A displacement fields measured by DIC for a uniform thermal loading test are shown in Fig. 12.4. The results of displacement distribution is not uniform and increase as the temperature increase, and results show that  $u_x$  and  $u_y$  of the brass on the left side of the test specimen are large, respectively. Each of the three virtual displacements is prepared by performing a finite element analysis of the mesh model shown in Fig. 12.2. Using the proposed method the coefficient of the thermal expansion is identified from the input value of the displacement distribution. The identified results for the coefficient of thermal expansion are presented in Table 12.2. The results of each material are close to the reference value. Moreover, even if the width of C1020 (Copper) which is the intermediate layer changed, results are close to the reference. Influence due to the difference in width of the intermediate layer of the test specimen is not observed.

**Fig. 12.3** Image of test specimen



**Fig. 12.4** Displacement distribution ( $\Delta T = 150$  °C, unit: mm)



**Table 12.2** Inverse analysis result ( $\Delta T = 150$  °C)

	Coefficient of thermal expansion (ppm/°C)		
	C2801 (brass)	C1020 (copper)	SUS430 (stainless steel)
Reference	19.5	17.4	10.3
2 mm	19.7	17.6	10.3
4 mm	19.8	17.6	10.4
7 mm	19.7	17.6	10.5
10 mm	19.7	17.2	10.4

## Conclusions

This study proposes a method for identifying the coefficient of thermal expansion of dissimilar materials composed of three kinds of materials simulating a substrate. A uniform thermal load test is carried out to verify the effectiveness of the proposed method. The identification result is close to the reference value. In addition, the difference in width of the intermediate layer of the test specimen does not affect.

## References

1. A. Khalilollahi, W. Russell, L.O. Onipede, *Thermal Reliability Design and Optimization for Multilayer Composite Electronic Boards* (ASME, International Mechanical Engineering Congress and Exposition, New York, 2005), pp. 845–851
2. M. Grédiac, F. Pierron, A. Vautrin, The iosipescu in-plane shear test applied to composites: a new approach based on displacement field processing. *Compos. Sci. Technol.* **51**(3), 409–417 (1994)
3. M.A. Sutton, J.H. Yan, S. Avril, F. Pierron, S.M. Adeb, Identification of heterogeneous constitutive parameters in a welded specimen: uniform stress and virtual fields methods for material property estimation. *Exp. Mech.* **48**(4), 451–464 (2008)
4. M. Grédiac, F. Pierron, Identifying constitutive parameters from heterogeneous strain fields using the virtual fields method. *Proc. IUTAM* **4**, 48–53 (2012)
5. Y. Sato, S. Arikawa, S. Yoneyama, Identification of elastic material characteristics of dissimilar materials by virtual fields method (in Japanese). *J. JSEM* **14**, 250–256 (2014)
6. S. Yoneyama, Basic principle of digital image correlation for inplane displacement and strain measurement. *Adv. Compos. Mater.* **25**, 105–123 (2015)
7. M. Grédiac, F. Pierron, S. Avril, E. Toussaint, The virtual fields method for extracting constitutive parameters from full-field measurements: a review. *Strain* **42**, 233–253 (2006)
8. S. Yoneyama, P.G. Ifju, S.E. Rohde, Identifying through-thickness material properties of carbon-fiber-reinforced plastics using the virtual fields method combined with moiré interferometry. *Adv. Compos. Mater.* **27**, 1–17 (2018)
9. D.J. Segalman, D.B. Woyak, R.E. Rowlands, Smooth spline-like finite element differentiation of full-field experimental data over arbitrary geometry. *Exp. Mech.* **19**, 429–437 (1979)



# Chapter 13

## Identification of Constitutive Parameters from Full Thermal and Kinematic Fields: Application to Hyperelasticity

S. Charlès and J.-B. Le Cam

**Abstract** In this paper, a new inverse identification method is developed from full kinematic and thermal field measurements. It consists in reconstructing the heat source from two approaches, a first one that requires the measurement of the temperature field and the value of the thermophysical parameters, and a second one based on the measurement of the kinematics field and a thermo-hyperelastic model that contains the parameters to be identified. The identification does not require any boundary conditions since it is carried out at the local scale. In the present work, the method is applied to the identification of hyperelastic parameters from a heterogeneous heat source field. Due to large deformation undergone by the rubber specimen tested, a motion compensation technique is developed to plot the kinematic and thermal fields at the same points before reconstructing the heat source.

**Keywords** Inverse identification · heat source reconstruction · infrared thermography · digital image correlation · hyperelasticity

### Introduction

Several methods have been recently developed for identifying parameters from field measurements. They are reviewed in [1]. In many of these approaches, the boundary conditions are necessary to solve the identification problem. The present study aims at developing a methodology for inverse identification using only local quantities. This means that constitutive parameters would be identified from a zone at the surface of the specimen, whatever the loading conditions applied to it. This implies that local quantities explicitly depend on the strain-stress relationship. In this work, we propose to identify the constitutive parameters by reconstructing the heat source field according to two different ways: a first one that requires the kinematic field and a given thermomechanical model that contains the parameters to be identified, and a second one that needs the temperature field and the thermophysical parameters. This inverse identification method has been applied to a hyperelastic material, which involves several difficulties. Indeed, hyperelasticity is generally used as a first approximation to predict the mechanical response of rubbery materials while several phenomena come into play in the deformation process. Numerous constitutive relations are available in the literature and reviewed in [2]. Due to the fact that hyperelastic models do not account for the above-mentioned phenomena, the values of the hyperelastic constitutive parameters depend on the strain state. This is the reason why constitutive parameters are classically identified from several homogeneous tests, namely uniaxial tensile (UT), pure shear (PS) and equibiaxial tensile (EQT). These three tests completely describe the domain of possible loading paths. A trade-off between the sets of values obtained with the different tests has therefore to be found to obtain parameters that can reasonably be considered as intrinsic to the mechanical behaviour of the material. Such identification approach exhibits several disadvantages, such as the necessity of making different geometry for the different tests, and the comparison between the constitutive parameters identified from the different loadings. An alternative approach has been proposed, based on the fact that the identification of constitutive parameters can be done from only one heterogeneous test, as soon as it induces at least the three tests mentioned above. In fact, a wide range of loading is also induced [3, 4]. In the present study, such heterogeneous test is used to identify the hyperelastic constitutive parameters from a heat source approach.

---

S. Charlès · J.-B. Le Cam (✉)

University of Rennes, CNRS, IPR (Institut de Physique de Rennes) - UMR 6251, Rennes, France  
e-mail: [sylvain.charles@univ-rennes1.fr](mailto:sylvain.charles@univ-rennes1.fr); [jean-benoit.lecam@univ-rennes1.fr](mailto:jean-benoit.lecam@univ-rennes1.fr)

## Heat Source Approach

In this approach, the heat source field is reconstructed from two different ways. A first one is based on the kinematic field and a given thermomechanical model that contains the parameters to be identified, and a second one is based on the temperature field and the thermophysical parameters. Considering that the constitutive state equations derive from the Helmholtz free energy function and that heat conduction follows the Fourier's law, the local diffusion equation writes:

$$\rho_0 C T - \text{Div}(\mathbf{K}_0 \text{Grad} T) - R = S$$

where

- $\rho_0$  is the density in the reference configuration,
- $C$  is the heat capacity,
- $\mathbf{K}_0$  is the thermal conductivity tensor,
- $T$  is the absolute temperature,
- $R$  is the external heat source (from radiation for instance),
- $S$  is the heat source in the Lagrangian configuration.

IR thermography provides in-plane full temperature fields. Therefore, the specimen under study has to be thin and a two-dimensional version of the heat equation is required to reconstruct the heat source field. For that purpose, several assumptions are used. First, the heat conduction is considered as isotropic. Second, the temperature is considered to be homogeneous through the specimen thickness. Third, the external radiations  $R$  are assumed to remain constants over time. These assumptions lead to the two-dimensional formulation of the heat diffusion equation:

$$\rho_0 C \left( \dot{\theta} + \frac{\theta}{\tau} - k_0 \Delta_{2D} \theta \right) = S$$

where

- $k_0$  is the coefficient of thermal conductivity,
- $\theta$  is the temperature variation  $\theta = T - T_0$ ,
- $\tau$  is a time characterizing the heat exchanges along the Z-direction by convection with the air at the specimen's surface,
- $\Delta_{2D}$  is the Laplacian operator in the specimen plane in the Lagrangian configuration.

The prediction of the heat sources produced during the deformation process requires the choice of a free energy. Here, the material is assumed to behave as a hyperelastic material that is mechanically incompressible and isotropic. At low strain levels, typically inferior to 250%, the Neo-Hookean model can be chosen to predict the mechanical behaviour [5]. The free energy function is then given by the following strain energy density:

$$W(\mathbf{F}, T) = \frac{1}{2} N k T (I_1 - 3)$$

where

- $\mathbf{F}$  is the deformation gradient tensor,
- $N$  is the number of network chains per unit volume
- $k$  is the Boltzmann's constant,
- $I_1$  is the first invariant of the right Cauchy-green deformation tensor  $\mathbf{C}$ .

While the material is supposed to be incompressible, the deformation gradient tensor for a biaxial loading is given by:

$$\mathbf{F} = \lambda \mathbf{e}_1 \otimes \mathbf{e}_1 + \lambda^B \mathbf{e}_2 \otimes \mathbf{e}_2 + \lambda^{-(B+1)} \mathbf{e}_3 \otimes \mathbf{e}_3$$

where:

- $e_1, e_2$  and  $e_3$  are three orthonormal vectors of the 3D Euclidian space,
- $\lambda$  is the stretch ratio in the  $e_1$  direction,
- the operator  $\otimes$  between two vectors is such that  $[a \otimes b]_{ij} = a_i b_j$ ,
- $B$  is the biaxiality ratio. It is equal to  $-0.5, 0$  and  $1$  for uniaxial tension, pure shear and equibiaxial tension, respectively.

In the case where the material does not produce intrinsic dissipation and no other thermomechanical couplings come into play, the heat source is given by:

$$S = NkT \left( \lambda + B\lambda^{2B-1} - (B+1)\lambda^{-2B-3} \right) \frac{d\lambda}{dt}$$

It should be noted that for temperature variations that do not exceed a few degrees, the quantity  $NkT$  remains nearly equal to  $NkT_0$ .

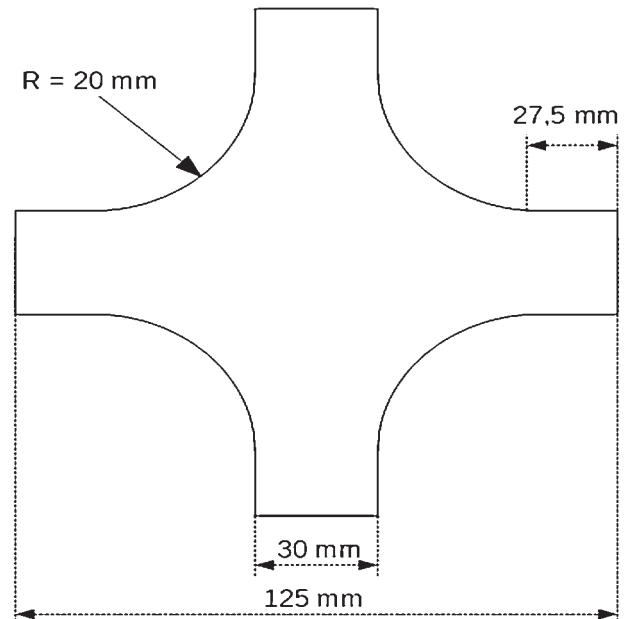
### Experimental Setup

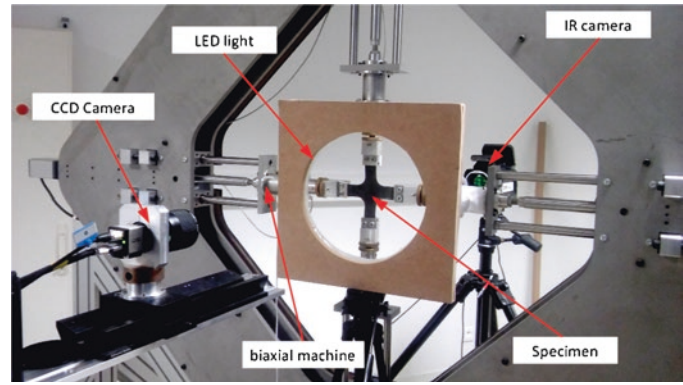
In the present study, the material chosen is an unfilled nitrile rubber. Its thermomechanical behaviour is driven by the coupling between strain and temperature only, i.e. it does not produce intrinsic dissipation and no other thermomechanical couplings come into play. Therefore, only the contribution of the thermo-elastic coupling is considered in the heat source description. The specimen geometry is shown in Fig. 13.1.

Figure 13.2 presents an overview of the experimental setup composed of an optical camera and an infrared one, on both side of the home-made biaxial testing machine. In the present study, an equibiaxial loading was applied, by controlling the four actuators. For each of them, the displacement and the loading rate was set to 70 mm and 150 mm/min, respectively. It should be noted that the two cameras are triggered for storing images at the same time, at the rate of 5 Hz. Displacement field at the specimen surface is determined by using the digital image correlation (DIC) technique. In order to improve the image contrast, a white paint is sprayed on the surface. The software used for the correlation process was SeptD [6]. The spatial resolution, defined as the smallest distance between two independent points, was equal to 10 pixels, which corresponds to 0.97 mm. The components of the deformation gradient tensor are determined at the centre of each square elements defined by the DIC grid. Within an element, the displacement is supposed to be a bilinear function of the Eulerian coordinates and can be obtain using the following equations:

$$\begin{cases} U_x(X_1, X_2) = a + bX_1 + cX_2 + dX_1X_2 \\ U_y(X_1, X_2) = e + fX_1 + gX_2 + hX_1X_2 \end{cases}$$

**Fig. 13.1** Specimen geometry



**Fig. 13.2** Experimental setup

where  $U$  is the displacement, are the Eulerian coordinates and  $a, b, c, d, e, f, g$  and  $h$  are constants that can be identified from the values at the four nodes. Finally, the components of deformation gradient tensor  $F$  are defined by  $F_{ij} = \frac{\partial x_i}{\partial X_j}$ , where  $x$  are the Lagrangian coordinates. The three principal stretches ( $\lambda_1 > \lambda_2 > \lambda_3$ ) are defined as the square roots of the eigenvalues of the right Cauchy-Green tensor  $C$  ( $C = F^T F$ ). Since in-plane displacement is measured, only  $\lambda_1$  and  $\lambda_2$  are determined,  $\lambda_3$  is deduced by assuming the material to be incompressible. The biaxiality coefficient  $B$ , defined as  $\log(\lambda_2/\lambda_1)$ , is then computed. The two invariants  $I_1$  and  $I_2$  of  $C$  are used to characterize the heterogeneity of the stretch states and the distribution in the maximum principal stretch value.

Temperature measurements were performed by using a FLIR infrared camera. The calibration of camera detectors was carried out with a black body using a one-point Non-Uniformity Correction (NUC) procedure at the acquisition frequency. The noise equivalent temperature difference (NETD) is equal to 20 mK for a range between 5 and 40 °C. The spatial resolution of the thermal field was equal to 300  $\mu\text{m}/\text{pixel}$ . In order to stabilize its internal temperature, the camera was switched on several hours before the test. Due to large deformation undergone by the material, material points observed by the IR camera move from pixel to pixel in the IR images. The temperature variation at a given material point has therefore to be processed by compensating its movement and to track its temperature in the IR images [7–10]. This requires first describing the kinematic and thermal fields in the same coordinate system. For that purpose, a calibration test pattern is positioned in place of the specimen. It is a plate with two sets of four holes, one that forms a large rectangle and a second one that forms a small rectangle. This is illustrated in Fig. 13.3. The set of holes used depends on the spatial resolution of the kinematic and thermal fields. Mark tracking algorithm is used to determine coordinates of these holes for both optical and IR camera. After that, a shared coordinate system is defined by choosing one of these marks as the reference. Thanks to this shared coordinate system, each point where the deformation gradient tensor is computed can be plotted in the infrared camera. As the two cameras do not have the same resolution, the temperature of each point is interpolated from the four nearby IR pixels.

## Results and Discussions

The heterogeneous test presented in the previous section is performed. Figure 13.4 presents the displacement field along the  $x$  and  $y$  axis. Then, the deformation gradient tensor components are determined by using the methodology described in the previous section. The heterogeneity of the test can be evaluated by mapping the stretch states over the area of study. A color scale is defined in such a way that EQT, PS and UT states appear in blue, green and red colors, respectively. Figure 13.5 highlights the spatial distribution of the strain states: EQT at the specimen center, UT in the branches and PS between these two states.

Motion compensation technique has been then applied to track the temperature of each point of the DIC grid. In order to reconstruct the heat source field from IR thermography measurements, the time constant  $\tau$  has to be determined experimentally. The method used consists in heating the specimen and in measuring the temperature field during the return to thermal equilibrium, then in fitting the curve by an exponential function. Since heat source field can now be obtained both by the heat equation and the Neo-Hookean model, the constitutive parameter can be determined. Two different approaches can be considered, a global one considering an unique Neo-Hookean parameter for the whole specimen; a local one considering a different constitutive parameter for each ZOI studied. The results obtained will be precisely detailed and discussed in the presentation.

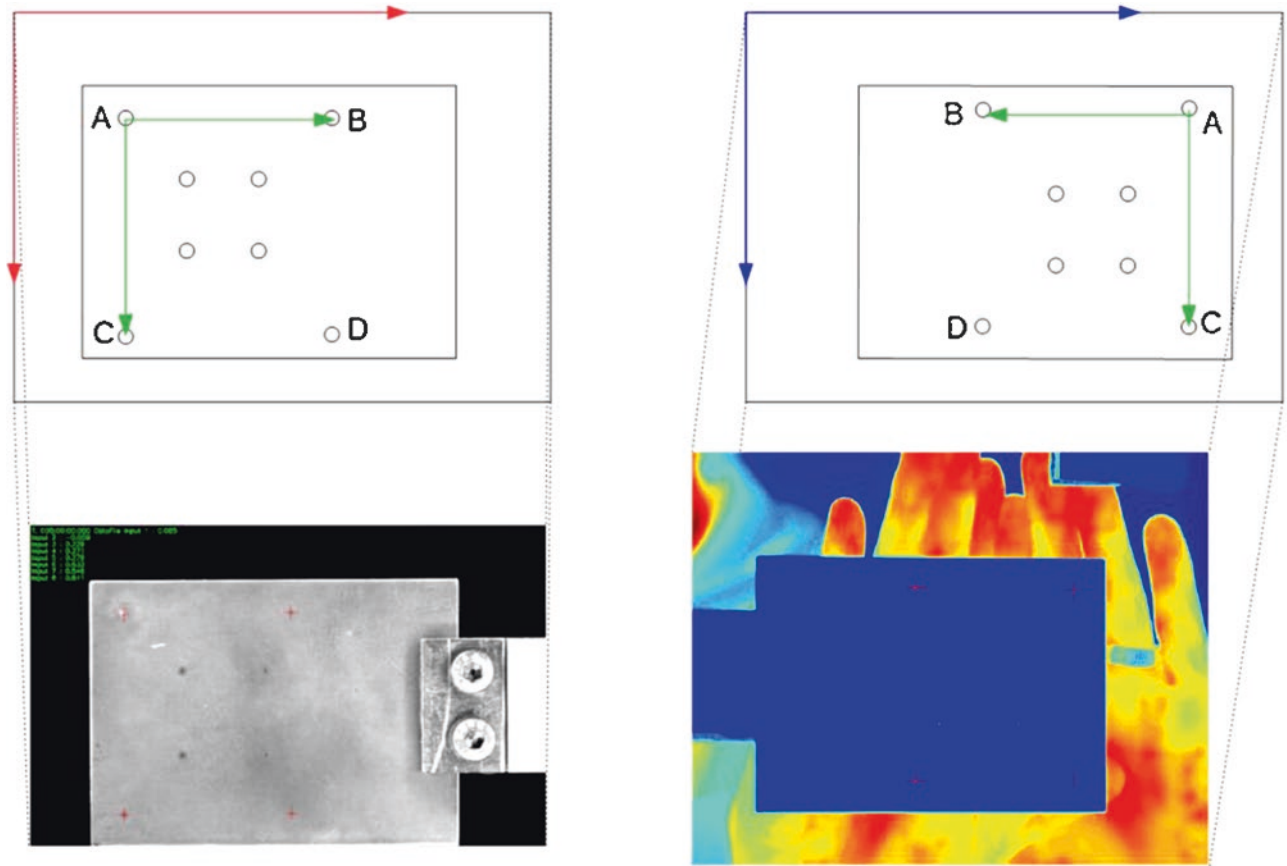


**Fig. 13.3** Scheme and image of the calibration pattern with the optical camera (on the left hand side) and with the IR camera (on the right hand side)

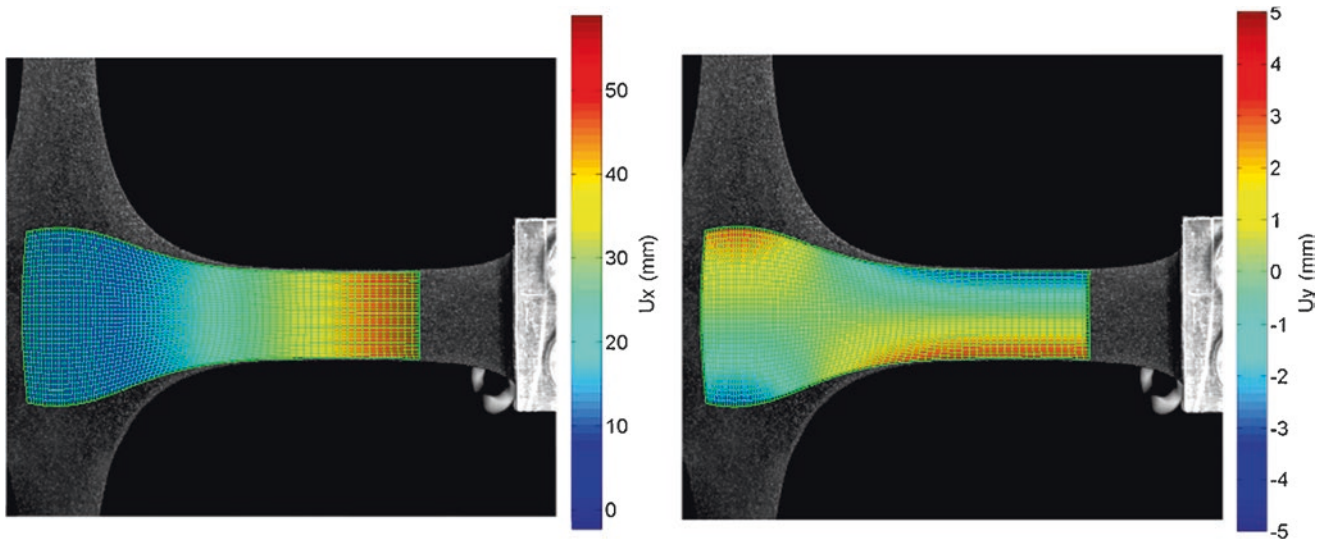
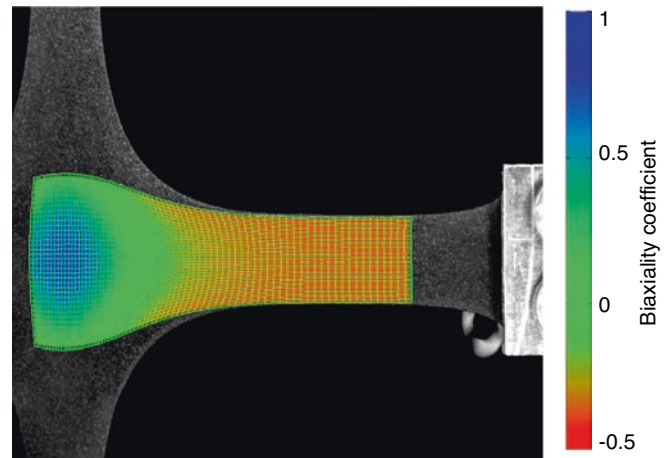


**Fig. 13.4** Displacement field along the x and y axis



**Fig. 13.5** Biaxiality coefficient field



## Conclusion

In this paper, a new inverse identification is developed from the reconstruction of the heat source field from two approaches. The first one requires the measurement of the temperature field and the value of the thermophysical parameters. The second one requires the measurement of the kinematics field and the choice of a thermo-hyperelastic model that contains the parameters to be identified. Since it is a local approach, the boundary conditions are not needed. In the present work, the method is applied to large deformations of rubber, where the movement of the observed points has to be compensated. A motion compensation technique has been developed and validated. Finally, the identification is performed at the local scale (the scale of the pixel itself) and at the scale of the Region of Interest. A very good agreement in the force-displacement response measured during the test and predicted by a finite element simulation with the parameters identified illustrates the relevancy of this new inverse identification method from heat source field.

**Acknowledgements** The authors thank the National Center for Scientific Research (MRCT-CNRS and MI-CNRS), Rennes Metropole and Region Bretagne for financially supporting this work and the PCM Technologies S.A.S. Company for providing the specimens. Authors also thank Dr. Mathieu Miroir, M. Vincent Burgaud and M. Mickaël Lefur for having designed the biaxial tensile machine. Dr. Eric Robin is acknowledged for providing the mark tracking algorithm.

## References

1. S. Avril, M. Bonnet, A. Bretelle, M. Grédiac, F. Hild, P. Ienny, F. Latourte, D. Lemosse, S. Pagano, F. Pierron, Overview of identification methods of mechanical parameters based on full-field measurements. *Exp. Mech.* **4**, 381–402 (2008)
2. G. Marckmann, E. Verron, Comparison of hyperelastic models for rubber-like materials. *Rubber Chem. Technol.* **79**, 835–858 (2007)
3. R. Promma, B. Raka, M. Grédiac, E. Toussaint, J.B. Le Cam, X. Balandraud, F. Hild, Application of the virtual field method to mechanical characterization of elastomeric materials. *Int. J. Solids Struct.* **46**, 698–715 (2009)
4. T. Guélon, E. Toussaint, J.B. Le Cam, N. Promma, M. Grédiac, A new characterisation method for rubber. *Polym. Test.* **28**, 715–723 (2009)
5. L.R.G. Treloar, The elasticity of a network of long chain molecules I and II. *Trans. Faraday Soc.* **39**, 241–246 (1943)
6. P. Vacher, S. Dumoulin, F. Morestin, S. Mguil-Touchal, Bidimensional strain measurement using digital images. *Proc. Inst. Mech. Eng. Pt. C J. Mech. Eng. Sci.* **213**, 811–817 (1999)
7. T. Pottier, M.P. Moutrille, J.B. Le Cam, X. Balandraud, M. Grédiac, Study on the use of motion compensation techniques to determine heat sources. Application to large deformations on cracked rubber specimens. *Exp. Mech.* **49**, 561–574 (2009)
8. E. Toussaint, X. Balandraud, J.B. Le Cam, M. Grédiac, Combining displacement, strain, temperature and heat source fields to investigate the thermomechanical response of an elastomeric specimen subjected to large deformations. *Polym. Test.* **31**, 916–925 (2012)
9. J.R. Samaca Martinez, X. Balandraud, E. Toussaint, J.B. Le Cam, D. Berghezan, Thermomechanical analysis of the crack tip zone in stretched crystallizable natural rubber by using infrared thermography and digital image correlation. *Polymer* **55**, 6345–6353 (2014)
10. J.R. Samaca Martinez, E. Toussaint, X. Balandraud, D. Berghezan, Heat and strain measurements at the crack tip of filled rubber under cyclic loadings using full field techniques. *Mech. Mater.* **81**, 62–71 (2015)



## Chapter 14

# Calorific Analysis of a Granular System Made in Shape Memory Alloy

Tanapon Yachai, Rym Boufayed, Pawarut Jongchansitto, Itthichai Preechawuttipong, and Xavier Balandraud

**Abstract** The study deals with the calorific response of a granular system made of Ni-Ti shape-memory-alloy (SMA) cylinders. SMAs belong to the family of active materials. Depending on their operating temperature, they feature unusual thermomechanical properties for metals: super-elasticity, one-way and two-way memory effects, as well as strong damping capacities. These properties take their origin from a solid-solid phase transformation accompanied by production or absorption of latent heat, which opens perspectives for the development of new heating/cooling systems. A “porous” material was built by placing SMA wires in parallel. It was subjected to confined compression with a uniaxial testing machine. Thermal measurements were performed by infrared thermography. Production and absorption of latent heat were observed in the contact zones between cylinders. Results enable us to envisage the circulation of a fluid through the SMA granular material for heat transfer.

**Keywords** Shape-memory alloy · Granular material · Infrared thermography · Elastocaloric effect

## Introduction

Shape-memory alloys (SMAs) belong to the family of smart and active materials as they are temperature- and mechanical-responsive. Depending on the temperature, they feature unusual mechanical properties for metals: super-elasticity, one-way and two-way memory effects, as well as some strong damping capacities. These macroscopic properties have their origin in a diffusionless solid-solid phase transformation triggered by stress and temperature. The austenite-to-martensite phase transition in SMAs is accompanied by large reversible strains (several per-cents) as well as a production of latent heat. Since the 1990s, scientific studies on these materials have been very numerous. After an intense academic research phase, application development is now in full swing. For example, the review by Jani et al. [1] cites more than 400 articles and 100 patents in four major fields of application: automotive, aerospace, robotics and biomedical. In parallel, thousands of patents involving SMA components have been proposed. SMAs are used as mechanical actuators or thermal sensors in a multitude of devices. Recently, applications to cooling and/or heating systems have been developed: see for instance [2–4]. Some studies also concern the analysis of the elastocaloric effect of superelastic SMAs for potential use in heating and cooling devices: see for instance [5–8]. The aim of the present study is to build an elastocaloric “granular” material by placing superelastic SMA cylinders in parallel (forming thus a so-called Schneebeli material [9]). Each cylinder corresponds thus to a particle of a two-dimensional (2D) discrete medium. This configuration allows us to envisage the circulation of a fluid through the “porous” material thus created, for heat transfer from the superelastic SMA wires to the fluid.

Granular materials are generally composed of grains with various sizes and shapes of particles, as well as different constitutive materials: sands, soils, rocks (civil engineering), cereals, sugar and rice (agro-food processing industry), raw particles (pharmaceutical industry). They exhibit mechanical behaviors that differ from common solids, liquids, and gases [10] because the mechanical response is governed by the contact forces between particles. Under macroscopic mechanical loading, a granular material is characterized by a heterogeneous network of interparticle forces [11]. Numerous numerical investigations have been presented in the literature to analyze the influence of parameters such as particle size and shape [12–14],

---

T. Yachai · P. Jongchansitto · I. Preechawuttipong  
Faculty of Engineering, Department of Mechanical Engineering, Chiang Mai University, Chiang Mai, Thailand  
e-mail: [pawarut.j@cmu.ac.th](mailto:pawarut.j@cmu.ac.th); [itthichai.p@cmu.ac.th](mailto:itthichai.p@cmu.ac.th)

R. Boufayed · X. Balandraud (✉)  
Université Clermont Auvergne, CNRS, SIGMA Clermont, Institut Pascal, Clermont-Ferrand, France  
e-mail: [rym.boufayed@sigma-clermont.fr](mailto:rym.boufayed@sigma-clermont.fr); [xavier.balandraud@sigma-clermont.fr](mailto:xavier.balandraud@sigma-clermont.fr)

friction [15], surface energy [16] and base materials [17]. Experimental approaches are also available, involving in particular full-field measurement techniques. To the best knowledge of the authors, granular materials made in SMA have never been studied in the literature. The objective of the present study is to perform experimental and numerical validation of a SMA Schneebeli material to be used for heat transfer to a fluid.

The paper is divided in four parts as follows. The first section presents the experimental setup used to analyze the thermo-mechanical response of a SMA Schneebeli material under confined compression. The second section is devoted to preliminary 2D finite element (FE) simulations to visualize the distribution of austenite and martensite phases inside the SMA cylinders under load. The third section presents the experimental results in terms of temperature change in the SMA cylinders. The last section proposes a demonstrator employing air as a fluid circulating in the elastocaloric material system.

## Experimental Setup

Figure 14.1 presents the experimental setup for the thermomechanical analysis of a SMA Schneebeli material under confined compression. A long bar in nickel-titanium (Ni-Ti) SMA, 2 m in length and 3.81 mm in mm, was supplied by Fort Wayne Metals. This alloy featured an austenite-finish ( $A_f$ ) temperature around 14 °C. At ambient temperature, the austenite-to-martensite stress plateau upon loading in tension was at around 480 MPa. The stress plateau for the reverse transformation (martensite-to-austenite) upon unloading was at around 140 MPa. Small cylinders, 25 mm in length, were cut and slightly polished to obtain smooth surfaces. Once placed in the rectangular frame, black paint was applied on the ends of the cylinders to maximize the thermal emissivity. Close environment was covered by thick black fabric to limit parasitic reflection in the infrared range.

The mechanical loading was applied with a Schenck uniaxial machine equipped with a  $\pm 250$  kN load cell. The test consisted of a displacement-controlled compression phase applied with a rate of  $-1$  mm  $s^{-1}$  until a maximum force of  $F_{\max} = -150$  kN, followed by an immediate unloading phase (in about 40 ms) after reaching the maximum compression force. The maximum force of  $-150$  kN was defined from preliminary FE simulations (see the next section). Before starting the test, several load-unload cycles were applied to pack the granular system, followed by a waiting time of 30 min in order to start the loading from a thermal equilibrium state.

Tests were performed as ambient temperature  $T_{\text{amb}} = 24.5$  °C, so the SMA cylinders were purely austenite in the stress-free state ( $T_{\text{amb}} > A_f$ ). A Cedip Jade III-MWIR infrared camera was employed to capture the temperature fields. The spatial resolution of the thermal measurement was equal to 88.6  $\mu\text{m}$ . Recording frequency was set to 147 Hz, leading to a temporal resolution of 6.80 ms. Temperature changes during a mechanical test were obtained by subtracting the initial temperature field captured before starting the test.

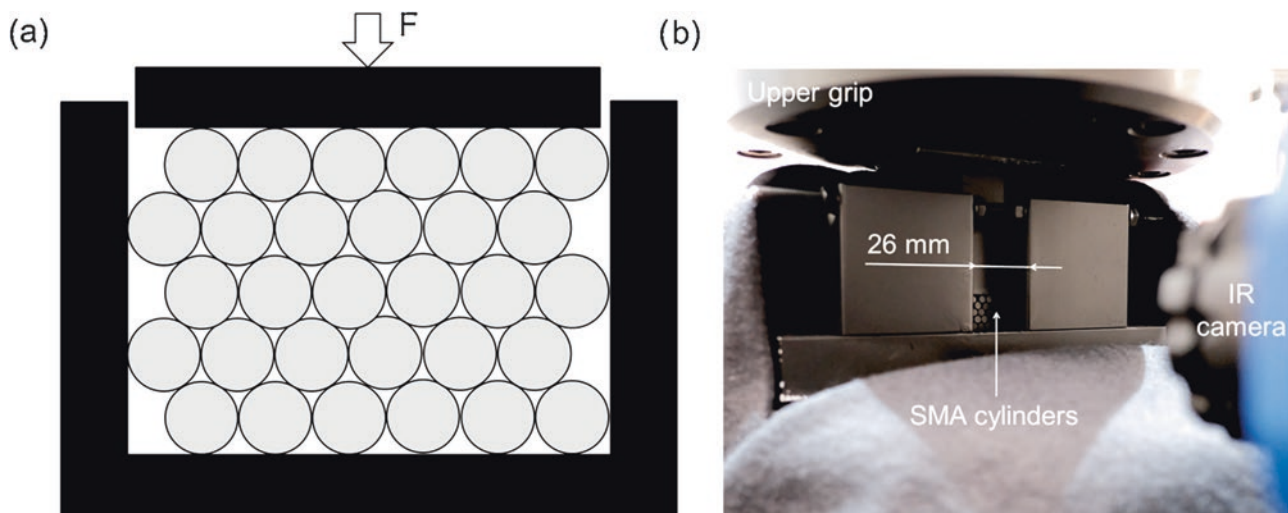


**Fig. 14.1** Experimental setup for thermal analysis by IR thermography: (a) schematic view of the 2D granular system made of SMA wires, (b) photo of the experiment

## Finite Element Simulations

FE simulations were performed to model the force transfer in a periodic granular system made in superelastic SMA. Ansys package was employed for this purpose. The Auricchio's SMA model is implemented in the software [18]. A 2D calculation with a hypothesis of plane stresses was considered, which can be accepted for comparisons with experimental results. Indeed, thermal measurements by IR thermography were done on free surfaces, i.e. surfaces in a plane-stress state. Element PLANE182 of Ansys was used to mesh the cylinders. Periodic organization of the cylinder network was assumed in the simulations.

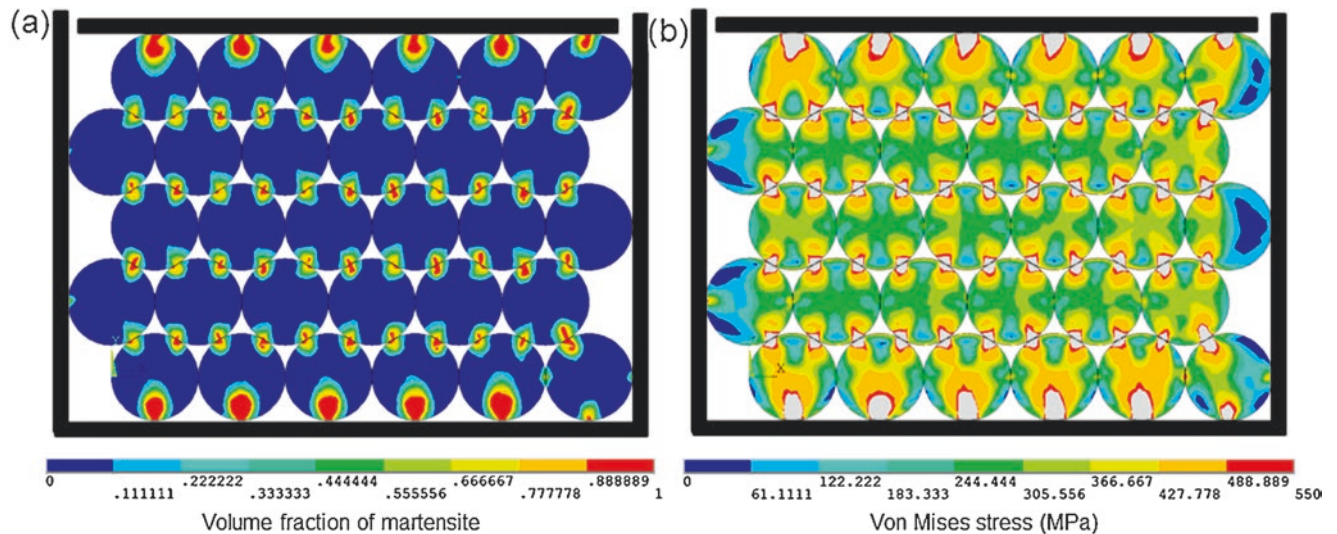
Figure 14.2a shows the field of martensite volume fraction  $x$  in the granular medium under a vertical compression force of  $-150$  kN. Pure austenite and pure martensite correspond to  $x = 0$  and  $x = 1$  respectively, whereas  $x \in ]0; 1[$  corresponds to a mix of the two phases. Figure 14.2a shows that martensite is present only in the contact zones, which is logical because these zones are subjected to higher stresses. It can be noted also that martensite is more present in the bottom and upper rows of cylinders. This result can be justified by the fact that these cylinders have fewer contacts than the others, so they are potentially subjected to higher contact forces. Figure 14.2b shows the field of Von Mises stress in the austenitic zones. It appears that the cylinders in contact with the two vertical walls feature lowest Von Mises stresses. This is why less martensite is produced in these boundary cylinders.

Martensite volume fraction  $x$  can be considered as proportional to the latent heat produced. In the case of an adiabatic transformation, the same property is true for the temperature change  $\theta$ , i.e.  $x$  should be in theory proportional to  $\theta$ . Compression force of  $-150$  kN was considered as relevant to exhibit detectable heterogeneous temperature changes in the granular system. Next section analyzes the experimental temperature changes obtained by IR thermography.

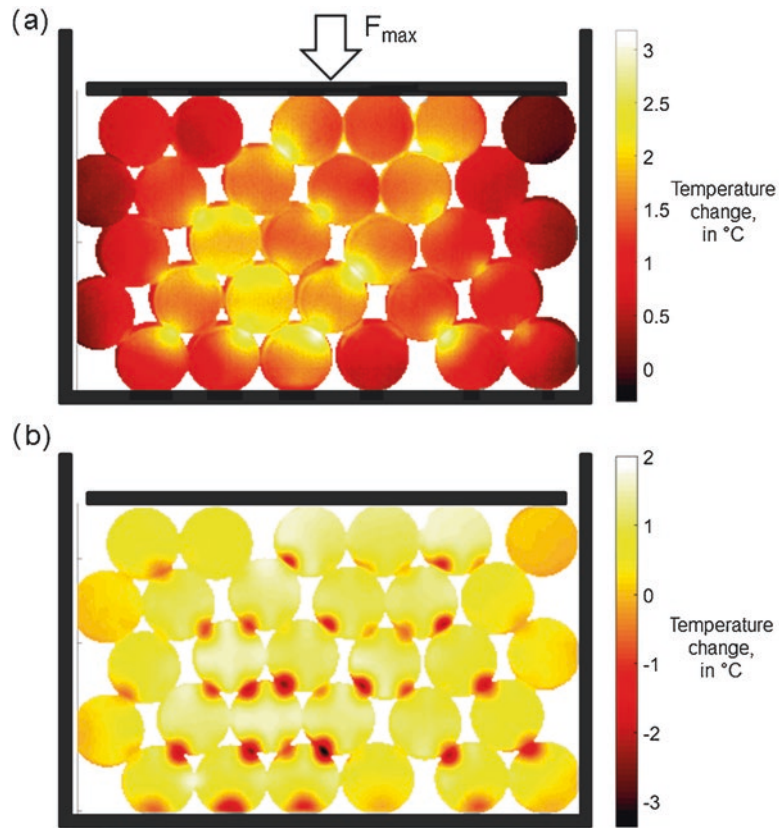
## Experimental Results

Figure 14.3a shows the field of temperature change  $\theta$  for the maximum compression force  $F_{\max} = -150$  kN. It can be seen that the cylinder network is not perfectly periodic. As a consequence, the field of temperature change due to contact forces is not periodic either. Strong temperature increases are visible in certain cylinders. Temperature rises of more than  $3$  °C are detected in the contact zones between cylinders. They can be attributed to an austenite-to-martensite transformation. They can be also attributed to thermoelastic couplings as well as mechanical dissipation due to friction. Lowest temperature changes are on the right side of the granular system. This can be explained by the fact that the cylinder at the top right was not subjected to mechanical loading. Indeed, no temperature change is detected in this cylinder.

Figure 14.3b shows the field of temperature change  $\theta$  at the end of the unloading phase. Strong temperature decreases are detected at the contacts between cylinders:  $\theta$  reached around  $-3$  °C in certain zones. These temperature drops can be attributed to the reverse phase transformation, i.e. to the martensite-to-austenite transformation. It can be noted that the



**Fig. 14.2** Result of a FE simulation for a periodic SMA granular system under a compression force of  $-150$  kN: (a) field of martensite volume fraction, (b) field of Von Mises stress in the austenitic zones



**Fig. 14.3** Field of temperature change  $\theta$  measured by IR thermography: (a) for the maximum compression force  $F_{\max} = -150$  kN, (b) at the end of the unloading phase

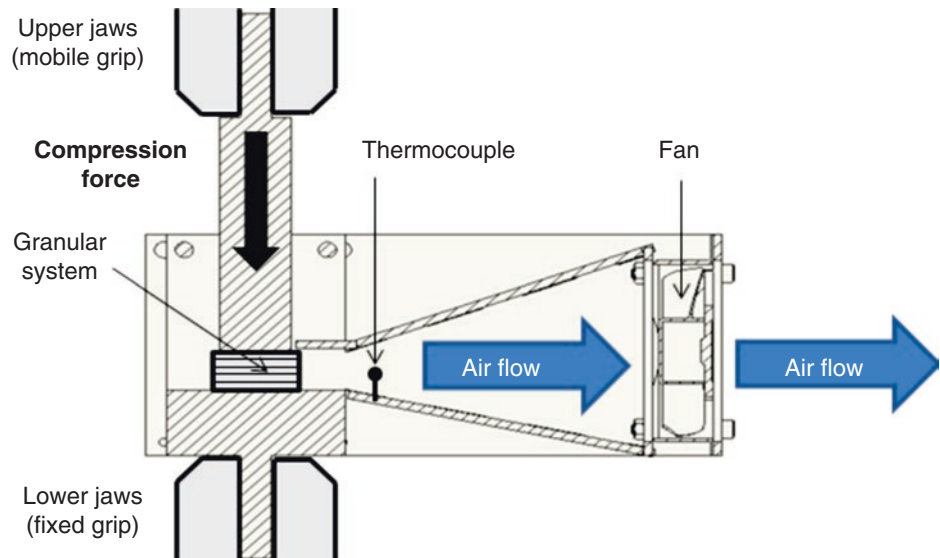
temperature gradients are more concentrated for the unloading phase than for during the loading phase. This can be explained by the rapid unloading phase, leading to better adiabaticity than for the loading phase. Identification of strong temperature drops during the unloading phase could be advantageously used to reveal contact force networks in such a granular medium.

Differences between the (experimental) field of temperature change  $\theta$  in Fig. 14.3a and the (simulated) field of martensite volume fraction  $x$  in Fig. 14.2a can be explained by several reasons: (1) experimental loading is not fast enough to achieve adiabaticity; (2) thermoelastic coupling is not taken into account in the simulation; (3) the placement of the cylinders in the experiment is not perfectly periodic. This latter reason is probably the most important. Indeed, the force network is strongly impacted by the actual locations of the cylinders. Any slight fluctuations from the perfectly periodic configuration lead to major changes in the interparticle force network.

## Demonstrator of Elastocaloric Device

A demonstrator was designed to show that an elastocaloric granular system made of SMA cylinders can be used for heating or cooling a fluid: see Fig. 14.4. Air was chosen for the first validation tests. The mechanical loading applied to the granular system was cyclic: force-controlled at a frequency of 0.17 Hz, minimum and maximum vertical force of  $-18$  kN and  $-180$  kN respectively. The rotation speed of the fan was set to 3200 rpm. Air thus circulated between the cylinders during the cyclic confined compression loading. A type-K thermocouple was used to measure the output temperature. A cyclic oscillation of the air temperature at the same frequency of the mechanical loading was evidenced. The amplitude of the oscillation was of nearly  $0.2$   $^{\circ}\text{C}$ . A maximum temperature rise of  $0.5$   $^{\circ}\text{C}$  was measured at the beginning of the loading. These temperature levels are small because of the fluid used. However, the demonstrator opens perspectives for the design of efficient elastocaloric granular systems made of SMA wires by using a real heat transfer fluid and another mechanical solicitation mode.

**Fig. 14.4** Demonstrator of elastocaloric granular system made of SMA cylinders



## Conclusion

The calorific response of a granular system made of superelastic Ni-Ti SMA wires subjected to confined compression was analyzed by IR thermography. Strong heat production was observed at some contacts, revealing localized austenite-to-martensite transformation due to the contact forces. Results allow us to envisage the circulation of a fluid through the SMA granular system for heat transfer. A first demonstrator was developed, opening perspectives for the design of new elastocaloric systems made of SMA wires.

**Acknowledgements** The authors gratefully acknowledge the Ministère de l'Europe et des Affaires Etrangères (MEAE) and the Ministère de l'Enseignement supérieur, de la Recherche et de l'Innovation (MESRI) in France, as well as the Office of the Higher Education Commission (OHEC) of the Ministry of Education in Thailand. The authors also gratefully thank the French Embassy in Thailand and Campus France for their support during this research (PHC SIAM 2018, Project 40710SE). The authors would also like to acknowledge the financial support through the Research Grant for New Scholar (MRG6080251) from the Thailand Research Fund (TRF) and Thailand's Office of the Higher Education Commission (OHEC). Finally, the authors gratefully thank Mr. Axel Cariat, Sigma-Clermont Engineering School, for the preliminary finite element models, as well as Mr. Alexis Gravier and Mr. Clément Weigel, Sigma-Clermont Engineering School, for the manufacturing of the mechanical devices.

## References

1. J.M. Jani, M. Leary, A. Subic, M.A. Gibson, A review of shape memory alloy research, applications and opportunities. *Mater. Des.* **56**, 1078–1113 (2014)
2. H. Ossmer, C. Chluba, S. Kauffmann-Weiss, E. Quandt, M. Kohl, TiNi-based films for elastocaloric microcooling-Fatigue life and device performance. *APL Mater.* **4**, 064102 (2016)
3. F. Bruederlin, H. Ossmer, F. Wendler, S. Miyazaki, M. Kohl, SMA foil-based elastocaloric cooling: from material behavior to device engineering. *J. Phys. D Appl. Phys.* **50**, 424003 (2017)
4. D. Luo, Y.S. Feng, P. Verma, Modeling and analysis of an integrated solid state elastocaloric heat pumping system. *Energy* **130**, 500–514 (2017)
5. J. Tusek, K. Engelbrecht, L.P. Mikkelsen, N. Pryds, Elastocaloric effect of Ni-Ti wire for application in a cooling device. *J. Appl. Phys.* **117**, 124901 (2015)
6. K. Engelbrecht, J. Tusek, S. Sanna, D. Eriksen, O.V. Mishin, C.R.H. Bahl, N. Pryds, Effects of surface finish and mechanical training on Ni-Ti sheets for elastocaloric cooling. *APL Mater.* **4**, 064110 (2016)
7. J. Tusek, A. Zerovnik, M. Cebren, M. Brojan, B. Zuzek, K. Engelbrecht, A. Cadelli, Elastocaloric effect vs fatigue life: exploring the durability limits of Ni-Ti plates under pre-strain conditions for elastocaloric cooling. *Acta Mater.* **150**, 295–307 (2018)
8. M. Zhou, Y.S. Li, C. Zhang, L.F. Li, Elastocaloric effect and mechanical behavior for NiTi shape memory alloys. *Chin. Phys. B* **27**, 106501 (2018)
9. G. Schneebeli, Une analogie mécanique pour les terres sans cohésion. *C. R. Hebd. Acad. Sci.* **243**, 125–126 (1956)

10. H.M. Jaeger, S.R. Nagel, Granular solids, liquids, and gases. *Rev. Mod. Phys.* **68**, 1259–1272 (1996)
11. S. Ostojsic, E. Somfai, B. Nienhuis, Scale invariance and universality of force networks in static granular matter. *Nature* **439**, 828–830 (2006)
12. D.H. Nguyen, E. Azéma, F. Radjai, P. Sornay, Effect of size polydispersity versus particle shape in dense granular media. *Phys. Rev. E* **90**, 012202 (2014)
13. A.A. Peña, R. García-Rojo, H.J. Herrmann, Influence of particle shape on sheared dense granular media. *Granul. Matter* **9**, 279–291 (2007)
14. C. Nouguier-Lehon, B. Cambou, E. Vincens, Influence of particle shape and angularity on the behaviour of granular materials: a numerical analysis. *Int. J. Numer. Anal. Methods Geomech.* **27**, 1207–1226 (2003)
15. S.G. Bardenhagen, J.U. Brackbill, D. Sulsky, Numerical study of stress distribution in sheared granular material in two dimensions. *Phys. Rev. E* **62**, 3882–3890 (2000)
16. I. Preechawuttipong, R. Peyroux, F. Radjai, W. Rangsri, Static states of cohesive granular media. *J. Mech. Sci. Technol.* **21**, 1957–1963 (2007)
17. P. Jongchansitto, I. Preechawuttipong, X. Balandraud, M. Grédiac, Numerical investigation of the influence of particle size and particle number ratios on texture and force transmission in binary granular composites. *Powder Technol.* **308**, 324–333 (2017)
18. F. Auricchio, A robust integration-algorithm for a finite-strain shape-memory-alloy. *Int. J. Plast.* **17**, 971–990 (2001)



# Chapter 15

## Dynamic VFM to Identify Viscoplastic Parameters. Analysis of Impact Tests on Titanium Alloy

Thomas Fourest, Pascal Bouda, Bertrand Langrand, Delphine Notta-Cuvier,  
Éric Markiewicz, Lloyd Fletcher, and Fabrice Pierron

**Abstract** The present work aims at identifying an elastic-viscoplastic material behavior over a wide plastic strain and plastic strain-rate range (up to 0.1 and 1000 s<sup>-1</sup> respectively), using the Virtual Fields Method. Image-Based Inertial Impact tests have been performed on the Ti6Al4V titanium alloy. The strain-rate dependency of the material has been identified with the results provided by these tests and compared to references.

**Keywords** Titanium alloy · Johnson-Cook · Virtual fields method · Full-field measurement · Viscoplasticity

### Introduction

Normalized tensile tests performed at different constant strain rates are regularly used to study the strain-rate dependency of the mechanical behavior of metallic materials. The strain-stress responses are successfully used to identify parameters of hardening and viscoplastic models. However, the method is costly due to the large number of specimens to be tested to investigate a wide range of strain rates, mostly because of the required hypothesis of constant strain rate during loading. In addition, a very limited number of loading directions are usually studied with the method. The present work aims at identifying viscoplastic model parameters over a large plastic strain and strain-rate range using the dynamic Virtual Fields Method (dynamic VFM). The dynamic VFM is a very promising method to identify material model parameters based on an inverse approach and full-field measurements of displacements only (no contact measurement). It can be based on a limited number of impact tests thanks to the full exploitation of non-homogeneous strain, strain-rate and stress state generated in the specimen. The complete experimental setup was designed using simulated image-based numerical process (e.g., specimen shape, impact conditions, spatial and temporal regularization parameters). In the present work, the experimental set-up is presented, the impact tests performed on a titanium alloy are described, the results are discussed, and an identification of a viscoplastic model is proposed with the dynamic VFM.

---

T. Fourest (✉) · P. Bouda · B. Langrand  
DMAS, ONERA, Lille, France  
e-mail: [thomas.fourest@onera.fr](mailto:thomas.fourest@onera.fr); [pascal.bouda@onera.fr](mailto:pascal.bouda@onera.fr); [bertrand.langrand@onera.fr](mailto:bertrand.langrand@onera.fr)

D. Notta-Cuvier · É. Markiewicz  
Polytechnic University Hauts-de-France, LAMIH UMR CNRS 8201, Valenciennes, France  
e-mail: [Delphine.Notta@univ-valenciennes.fr](mailto:Delphine.Notta@univ-valenciennes.fr); [Eric.Markiewicz@uphf.fr](mailto:Eric.Markiewicz@uphf.fr)

L. Fletcher · F. Pierron  
Faculty of Engineering and the Physical Sciences, University of Southampton, Southampton, UK  
e-mail: [l.c.fletcher@soton.ac.uk](mailto:l.c.fletcher@soton.ac.uk); [F.Pierron@soton.ac.uk](mailto:F.Pierron@soton.ac.uk)



## Image-Based Inertial Impact Tests

Image-Based Inertial Impact (IBII) method has been recently proposed [1, 2] to take advantage of the dynamic VFM. Among existing inverse methods, the dynamic VFM enables the identification of material parameters with the sole knowledge of the strain and acceleration fields (Eq. 15.1). In particular, the dynamic VFM does not require the knowledge of any external loads, thus avoiding the use of an intrusive sensor (e.g., accelerometer, strain gauge, ...) which was proven to be problematic for high strain rate tests.

$$\underbrace{\int_V \underline{\underline{\sigma}}[\underline{\underline{X}}] : \underline{\underline{\varepsilon}}^* dV}_{W_{int}^*} + \underbrace{\int_V \rho \underline{\underline{\gamma}} \cdot \underline{\underline{u}}^* dV}_{W_{acc}^*} = 0 \quad (15.1)$$

The design of the tests has been performed using finite element analysis (FEA) to generate virtual images that were processed with the same toolchain that will be used to analyse the tests results. This work has been presented in [3]. As non-linear viscoplastic behavior might need a lot of material parameters to be described, it is necessary to explore more extensively the design space in order to optimize the procedure of identification, in particular for a high yield stress material such as Ti6Al4V (973 MPa [4]). From this process three different kinds of specimen geometry (i.e., rectangular, with notches, and with a hole) have been selected. The full-field measurements are obtained over the specimen surface using the grid method and pictures recorded with an ultra-high speed camera. The strain rate dependency has been identified. Figure 15.1 shows an example of the plastic strain computed for the last stage recorded during an IBII test on a rectangular specimen.

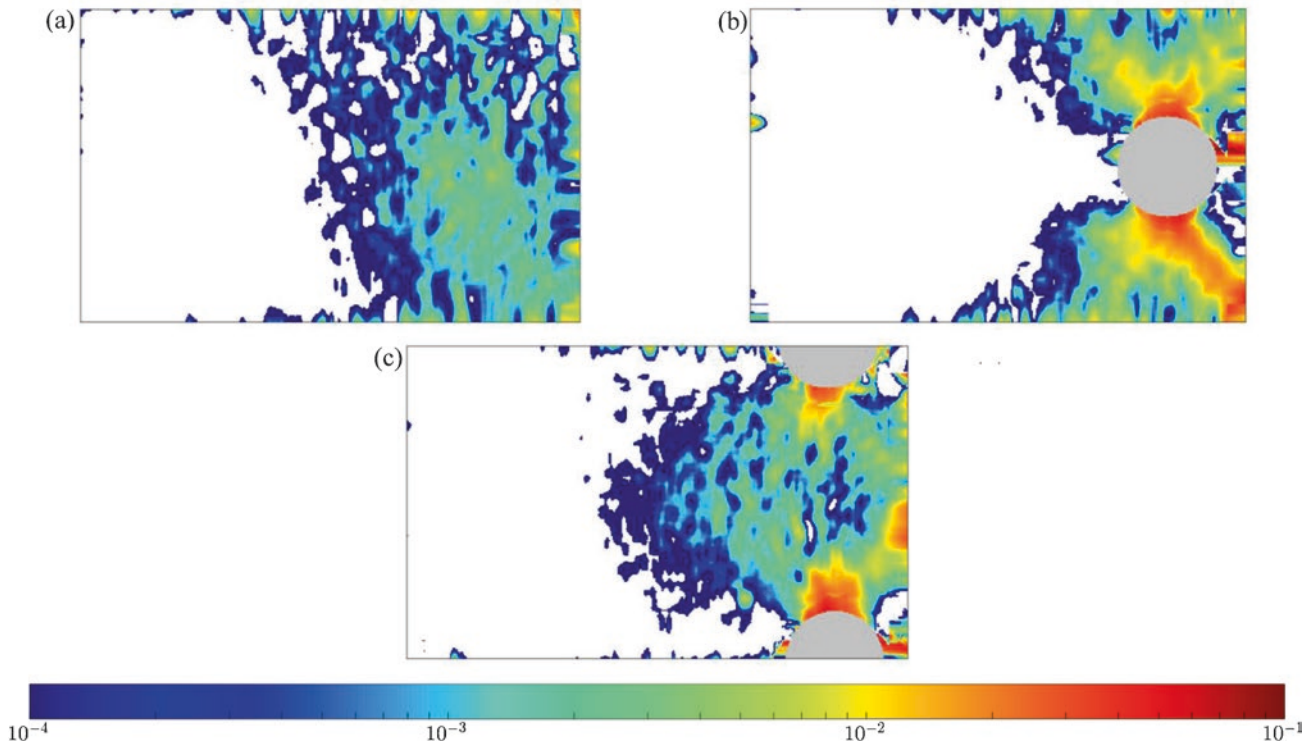


**Fig. 15.1** Typical longitudinal plastic strain at the last stage recorded during the IBII test (a) rectangular specimen, (b) specimen with a hole, (c) specimen with two notches

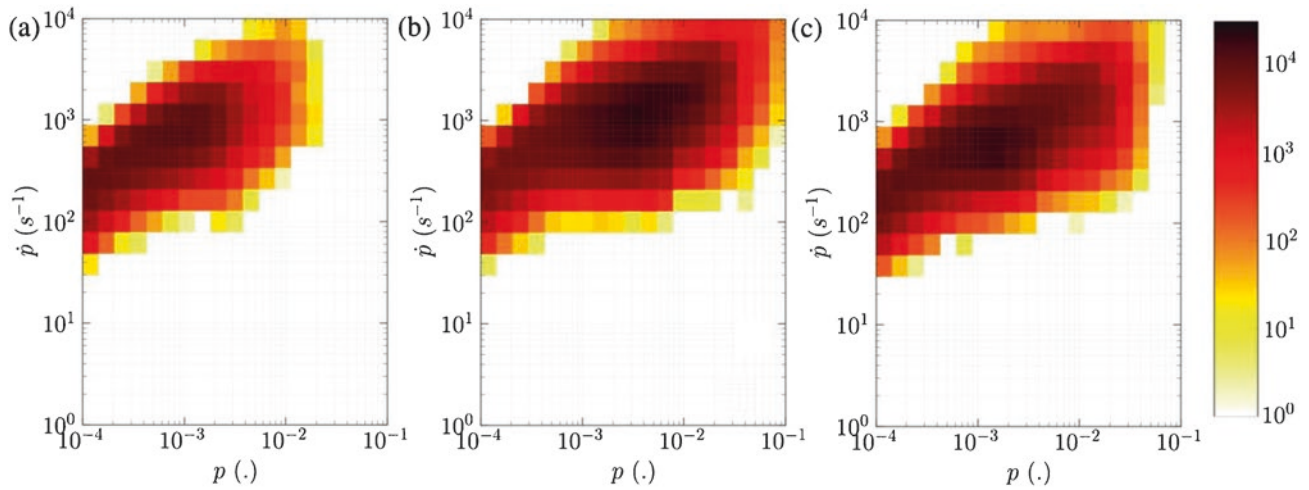


**Fig. 15.2** Viscoplasticity histogram contour at the last step recorded in the IBII experiments. (a) Rectangular specimen, (b) holed specimen, (c) notched specimen

## Viscoplastic Spectra Covered By the IBII Tests

One advantage in inverse methods such as the Virtual Fields Method is that inhomogeneous tests can be performed to generate a wider range of experimental data than the one that could be obtained from “standard” tests. Figure 15.2 illustrates spectra in terms of plastic strain/plastic strain rate typically recorded for each specimen geometry. It can be seen that a large spectrum is covered using only one IBII test. In terms of plastic strain rate it is mainly between  $30 \text{ s}^{-1}$  to  $2 \times 10^3 \text{ s}^{-1}$  for the rectangular specimen. Also, for the same impact speed the specimens including stress concentrating geometries enable to cover a larger spectrum (between  $30 \text{ s}^{-1}$  to over  $10^4 \text{ s}^{-1}$  for the specimen geometry including a hole for instance).

## Conclusion

In this study the strain rate dependency of Ti6Al4V has been successfully identified using the dynamic VFM. Very high strain rate (over  $10^4 \text{ s}^{-1}$ ) have been reached in the IBII tests. The next step is to compare the experimental results with those predicted by the numerical approach to better understand the sources of possible differences in the toolchain used.

## References

1. F. Pierron, H. Zhu, C. Siviour, Beyond Hopkinson’s bar. *Philos. Trans. R. Soc. London, Ser. A* **372**, 2023 (2014)
2. S. Dreuilhe, Ph.D. thesis, University of Southampton (2017)
3. P. Bouda, D. Notta-Cuvier, B. Langrand, E. Markiewicz, F. Pierron, in *SEM 2018 Annual Conference*, June 4–7 2018, Greenville SC, USA (2018)
4. D. Notta-Cuvier, B. Langrand, E. Markiewicz, F. Lauro, G. Portemont, Identification of Johnson–Cook’s viscoplastic model parameters using the virtual fields method: application to titanium alloy Ti6Al4V. *Strain* **49**, 22 (2013)



# Chapter 16

## Test Design for Identification from Full-Field Measurements: A Concise Review

Fabrice Pierron

**Abstract** Full-field optical measurements like Digital Image Correlation or the Grid Method have brought a paradigm shift in the experimental mechanics community. While inverse identification techniques like Finite Element Model Updating (FEMU) or the Virtual Fields Method (VFM) have been the object of significant developments, current test methods, inherited from the age of strain gauges or LVDTs, are not generally well adapted to the rich information provided by these new measurement tools. This paper provides a short review of the research dealing with the design and optimization of heterogeneous mechanical tests for identification of material parameters from full-field measurements.

**Keywords** Virtual fields method · Finite element updating · Full-field measurements · Test design

### Introduction

In the last decade, optical full-field measurements like Digital Image Correlation (DIC, [1]) or the Grid Method (GM, [2]) have provided in-depth transformations to the way researchers and engineers perform mechanical experiments on materials and structures. These measurement technologies have become mature, after intensive international research effort, as reflected by the recently published guide of good practice for DIC [3]. Such measurements make it possible to move from simple statically determinate tests to more complex ones, with a view to get more data from a single test, thus reducing the testing effort and increasing the quality of the material models. However, in this case, inverse solutions have to be employed to go from heterogeneous kinematic fields to material parameters (and/or unknown loading distributions). This has also been the object of extensive research, with two main techniques having emerged, Finite Element Model Updating (FEMU, [4]) and the Virtual Fields Method (VFM, [5]).

However, there is a third element to this new paradigm in materials testing: the test configuration itself. Most of our mechanical testing toolkit was developed at a time when only strain gauges or other point sensors were available. As a consequence, they are generally strongly inspired from traditional tests developed for a different type of metrological information.

There has been some research effort to look at the problem of designing heterogeneous tests that would be better adapted to full-field measurements and inverse identification for a given type of constitutive model, and this is the object of this short review. However, this is still an underexplored area of research that requires sustained effort to realise the full potential of this new paradigm in materials testing.

### The Early Attempts

In the late 1980s and early 1990s, two pioneering research groups started to work on new testing procedures based on full-field measurements and inverse identification. The first one was at the School of Mines in St-Etienne, France, with the PhD of Michel Grédiac under the supervision of Alain Vautrin. They combined a deflectometry set-up and the Virtual Fields Method, first proposed by M. Grédiac in his PhD, to the identification of elastic anisotropic stiffness components of thin composite plates [6, 7]. The test configuration was a series of three bending tests realised on the same plate but moving the

---

F. Pierron (✉)

Faculty of Engineering and Physical Sciences, University of Southampton, Southampton, UK  
e-mail: [F.Pierron@soton.ac.uk](mailto:F.Pierron@soton.ac.uk)

loading point, to create a database with enough information to identify the six anisotropic bending stiffness components. The second one was the group of Cees Oomens at TU Eindhoven, with a motivation to test biological membranes like skin [8], and later, metals [9]. In the latter, a double asymmetrical notch configuration was selected to create heterogeneity, though little justification was provided for this choice.

Research in this area expanded in the 1990s and 2000s, for anisotropic elasticity [10–13], elasto-plasticity [14–18], hyper-elasticity [19–23], high strain rate behaviour [24–30] and heterogeneous materials [31–35], to cite but a few references.

## Test Design and Optimization

### *Designs Based on the Strain State*

Attempts to optimize test configurations were only scarce initially. To the best knowledge of the present author, the first paper on this was published in 1998 [36]. To identify the full set of in-plane elastic parameters for an orthotropic composite material, a tension/bending test on a unidirectional composite specimen in the shape of a ‘T’ was imagined (Fig. 16.1). The ends of the horizontal bar of the ‘T’ rest on rollers while the vertical bar is gripped and pulled down. The vertical bar is where the vertical modulus is activated, while the horizontal bar sees bending and shear, activating the horizontal and the shear moduli. The aspect ratio of the specimen was optimized using the native ANSYS APDL language so that the average horizontal strain in area 1, the average vertical strain in area 2 and the average shear strain in area 3 were identical. This was then validated experimentally in [10]. The results were rather good except for major’s Poisson’s ratio but this is likely to come from the manually-defined virtual fields used in that study.

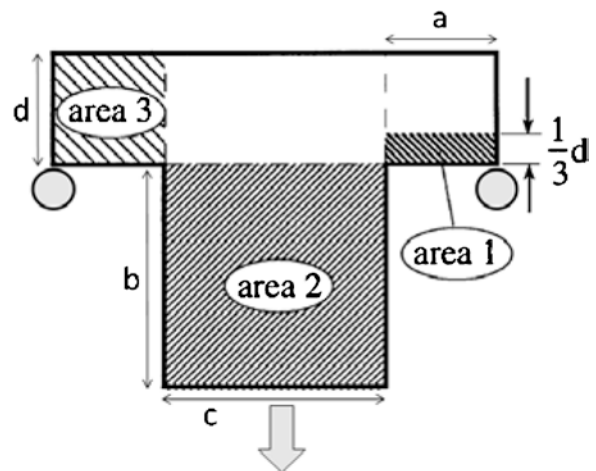
In [37], a number of indicators based on strain metrics were developed for elasto-plastic identification. These indicators were then used in a shape optimization problem by the same group [38]. Starting from a circular shape parameterized by cubic splines, the control points of the splines were adjusted with respect to a cost function that combined the indicators from [37]. The result was a ‘butterfly-shaped specimen and experimental validations was published in [39]. Another interesting shape was devised using similar criteria but including the strain rate for visco-plasticity identification [40].

### *Designs Based on Identification Quality*

Strain metrics, while easy to compute, are several steps away from the actual identification results and therefore, may lead to non-optimal configurations in practice. A step forward consists in considering the identification uncertainty as the cost function to optimize test configurations. To the best knowledge of the present author, the first attempt was published in 2007 [41]. A rectangular unidirectional composite test specimen was loaded in a combination of bending and shear using a Iosipescu fixture.

The specimen free length (between supports) and off-axis fibre angle were used as design variables and a cost function established at balancing the four sensitivity-to-noise coefficients from the noise-optimized VFM [43], one for each individual

**Fig. 16.1** T-shaped specimen, inspired from [36]



orthotropic stiffness component. It should be noted that these coefficients scale down with the signal to noise ratio and therefore, a normalizing procedure had to be established to limit the allowable deformation in the purely elastic simulations. This is an essential step that has to be controlled carefully as it can significantly affect the end result. The other issue is that the length had to be constrained to a maximum value as the algorithm has a tendency to converge towards much longer specimens that would have been physically impractical because of the loss of spatial resolution. This was one of the motivations for moving to the full identification chain as reported in the next subsection. The problem was solved by driving ANSYS® through Matlab using a text input file for the FE model. An optimal configuration was found and successfully validated experimentally using ESPI [41]. Compared to the standard configuration used in [44] for instance, the improvement was significant. A very similar study was conducted using an Arcan test configuration and DIC to identify the orthotropic stiffness components of a PVC foams [45].

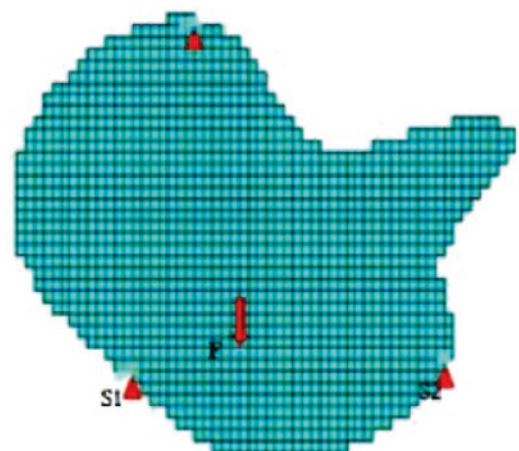
The same approach was used by Michel Grédiac's group [42] to optimize the shape of thin plates in bending, to identify the full set of orthotropic bending stiffness components for a unidirectional composite. The only difference is that the design variables were much wider: shape, support and loading points, and fibre angle. The shape was parameterized using splines, as in [38]. The final result for the shape and loading points is non-intuitive (Fig. 16.2) but again, it may not be practical because of potential strain concentrations not well reconstructed by the measurement technique, and the loss of pixels as the shape moves further away from the camera aspect ratio. No experimental validation was attempted on this shape.

### *Designs Based on Full Identification Chain Simulation*

The main limitation of the use of strains directly from finite element simulations to optimize test configurations based on identification quality is the fact that experimental constraints are not taken into account. All experimentalists familiar with DIC or the GM know that spatial resolution and camera noise play an important role in the quality of the results. Moreover, many processing and post-processing parameters have to be selected (DIC subset, step size, shape functions, strain window to cite a few in the case of DIC) and this choice does impact the quality of the identification. For instance, a particular test configuration may provide excellent heterogeneities but the strain gradients are too large to be faithfully rendered for a given imaging set-up and this will lead to a large systematic error that the procedures described above will miss.

To circumvent this issue, a programme was developed to simulate the full measurement and identification chain, so that complete uncertainty and error propagation could be studied. This was developed for the VFM, first with the grid method [46] and later extended to DIC [47]. The initial motivation was to evaluate random and systematic errors with a view to providing accurate uncertainty limits. This is an essential point for such tests to be used as standard tools in industry. The work in [45] on PVC foams was refined by optimizing the configuration based on the total identification error and a different optimal configuration was found [48]. Since the DIC parameters also affect the results, they were optimized in a second step, after a first configuration was found with pre-set DIC parameters. Finally, not only were the four orthotropic stiffness components identified successfully from a single test, but the standard deviations were predicted within less than a factor of 2. This was thought very satisfactory as a starting point as many experimental issues like variations in light (amplified by reflective hotspots), machine vibrations, specimen alignment and geometrical defects were not taken into account. A similar study

**Fig. 16.2** Optimized bending test, from [42]. Red triangles indicate supports, arrow indicates applied force



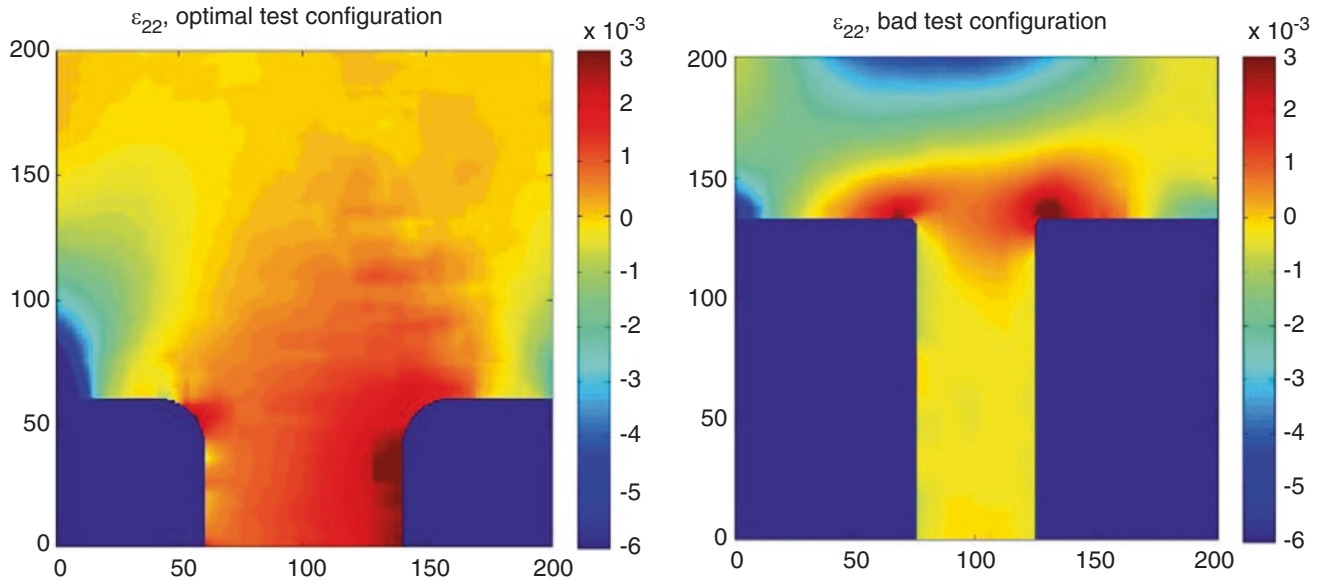


**Fig. 16.3** Optimal (left) and non-optimal (right) configurations for the T-shaped specimen [50]. Strain transverse to the fibres represented. For optimal configuration: fibre direction  $27^\circ$  from horizontal axis, subset 36, step 1, quadratic shape functions and strain window of 8

was performed on three different test configurations to identify the orthotropic stiffness components of composites with a single test. Each configuration was optimized for geometry and fibre angle, and then for DIC parameters. Interestingly, all cases converged to quadratic shape functions and steps of 1 pixel [49].

Clearly, the ultimate stage is to combine geometry and measurement parameters simultaneously into a single optimization problem. This was attempted on the T-shaped specimen problem from [36]. Eight design variables were used: three geometrical parameters ( $b$  and  $c$  as defined in Fig. 16.1, plus the radius of a fillet joining the two bars of the ‘T’, total height and width were fixed to correspond to the camera sensor aspect ratio), the orthotropy angle, and DIC subset, step size, shape functions (linear or quadratic) and the strain window [50]. A genetic algorithm was used to solve the problem. The cost function was total error (systematic  $\pm$  twice the standard deviation, whichever was the further away from the reference). This converged to the configuration shown in Fig. 16.3. It is very interesting to notice how the optimization always tries to minimize the number of lost pixels, which strongly affects the systematic error. Also worth noting that again, quadratic shape functions and step of 1 are obtained at convergence. It has not yet been attempted to experimentally validate this work but experimental difficulties may arise from the very thick vertical bar which may lead to instabilities. This suggests that a buckling load constraint may have to be added to the optimization problem.

## Conclusion and Future Work

This short review has shown that although some research effort has been dedicated to the design and/or optimization of new heterogeneous tests for inverse identification from full-field measurements, there is still a long way to go. Most of the examples are on anisotropic elasticity, with a few on anisotropic plasticity and/or visco-plasticity. Also, the vast majority of these efforts have risen from the VFM community. This is not a surprise considering the large difference of computational efficiency between the VFM and FEMU (VFM quoted to be 125 times faster than FEMU in [23]). Since test optimization has to rely on many resolutions of subsequent identification problems, the use of FEMU for this makes it quickly computationally prohibitive.

The next stage is now to extend the optimization based on the full measurement and identification simulator to anisotropic plasticity, to progress the interesting work by Andrade-Campos and Thuillier further. The recent development of the sensitivity-based virtual fields [51, 52] provide the perfect tool for this. Extension to hyperelastic models would also be interesting, though additional constraints may be needed to prevent wrinkling. Finally, once promising tests have been designed that seem fit for purpose, experimental validation of uncertainty bounds, coupled with round-robin testing will be needed to establish them as the next generation of test standards.

## References

1. M.A. Sutton, J.J. Orteu, H.W. Schreier, *Image Correlation for Shape, Motion and Deformation Measurements: Basic Concepts, Theory and Applications* (Springer, New York, 2009), pp. 1–321
2. M. Grédiac, F. Sur, B. Blaysat, The Grid Method for in-plane displacement and strain measurement: a review and analysis. *Strain* **52**(3), 205–243 (2016)
3. E.M.C. Jones, M.A. Iadicola, *A Good Practices Guide for Digital Image Correlation* (International Digital Image Correlation Society, Portland, 2018)
4. S. Avril et al., Overview of identification methods of mechanical parameters based on full-field measurements. *Exp. Mech.* **48**(4), 381–402 (2008)
5. F. Pierron, M. Grédiac, *The Virtual Fields Method. Extracting Constitutive Mechanical Parameters from Full-Field Deformation Measurements* (Springer, New-York, 2012), p. 517
6. M. Grédiac, A. Vautrin, A new method for determination of bending rigidities of thin anisotropic plates. *J. Appl. Mech.* **57**(4), 964–968 (1990)
7. M. Grédiac, Principle of virtual work and identification. *C. R. Acad. Sci. Sér. II* **309**(1), 1–5 (1989)
8. C.W.J. Oomens et al., A numerical-experimental method for a mechanical characterization of biological materials. *J. Biomech.* **26**(4–5), 617–621 (1993)
9. M.H.H. Meuwissen et al., Determination of the elasto-plastic properties of aluminium using a mixed numerical–experimental method. *J. Mater. Process. Technol.* **75**(1–3), 204–211 (1998)
10. M. Grédiac, F. Pierron, Y. Surrel, Novel procedure for complete in-plane composite characterization using a single T-shaped specimen. *Exp. Mech.* **39**(2), 142–149 (1999)
11. R. Moulart, S. Avril, F. Pierron, Identification of the through-thickness rigidities of a thick laminated composite tube. *Compos. Pt A Appl. Sci. Manuf.* **37**(2), 326–336 (2006)
12. C. Gogu et al., Bayesian identification of elastic constants in multi-directional laminate from moiré interferometry displacement fields. *Exp. Mech.* **53**(4), 635–648 (2013)
13. R. Gras et al., Identification of a set of macroscopic elastic parameters in a 3D woven composite: uncertainty analysis and regularization. *Int. J. Solids Struct.* **55**, 2–16 (2015)
14. J. Kajberg, G. Lindkvist, Characterisation of materials subjected to large strains by inverse modelling based on in-plane displacement fields. *Int. J. Solids Struct.* **41**(13), 3439–3459 (2004)
15. L. Robert et al., Identification of hardening parameters using finite element models and full-field measurements: some case studies. *J. Strain Anal. Eng. Des.* **47**(1), 3–17 (2012)
16. M. Grédiac, F. Pierron, Applying the virtual fields method to the identification of elasto-plastic constitutive parameters. *Int. J. Plast.* **22**(4), 602–627 (2006)
17. M. Bertin et al., Integrated digital image correlation applied to elastoplastic identification in a biaxial experiment. *J. Strain Anal. Eng. Des.* **51**(2), 118–131 (2016)
18. J.M.P. Martins, A. Andrade-Campos, S. Thuillier, Comparison of inverse identification strategies for constitutive mechanical models using full-field measurements. *Int. J. Mech. Sci.* **145**, 330–345 (2018)
19. N. Prouma et al., Application of the virtual fields method to mechanical characterization of elastomeric materials. *Int. J. Solids Struct.* **46**(3–4), 698–715 (2009)
20. S. Avril, P. Badel, A. Duprey, Anisotropic and hyperelastic identification of in vitro human arteries from full-field optical measurements. *J. Biomech.* **43**(15), 2978–2985 (2010)
21. G. Palmieri et al., Virtual fields method on planar tension tests for hyperelastic materials characterisation. *Strain* **47**(suppl. 2), 196–209 (2011)
22. L.E. Perotti et al., Method for the unique identification of hyperelastic material properties using full-field measures. Application to the passive myocardium material response. *Int. J. Numer. Methods Biomed. Eng.* **33**(11), e2866 (2017)
23. L. Zhang et al., Verification of a virtual fields method to extract the mechanical properties of human optic nerve head tissues in vivo. *Biomech. Model. Mechanobiol.* **16**(3), 871–887 (2017)
24. J. Kajberg, B. Wikman, Viscoplastic parameter estimation by high strain-rate experiments and inverse modelling - speckle measurements and high-speed photography. *Int. J. Solids Struct.* **44**(1), 145–164 (2007)
25. J. Kajberg et al., High strain-rate tensile testing and viscoplastic parameter identification using microscopic high-speed photography. *Int. J. Plast.* **20**(4–5), 561–575 (2004)
26. D. Notta-Cuvier et al., Identification of Johnson-Cook’s viscoplastic model parameters using the virtual fields method: application to titanium alloy Ti6Al4V. *Strain* **49**(1), 22–45 (2013)
27. S.-h. Yoon, I. Giannakopoulos, C.R. Siviour, Application of the Virtual Fields Method to the uniaxial behavior of rubbers at medium strain rates. *Int. J. Solids Struct.* **69**, 553–568 (2015)
28. B. Koohbor, A. Kidane, W.-Y. Lu, Effect of specimen size, compressibility and inertia on the response of rigid polymer foams subjected to high velocity direct impact loading. *Int. J. Impact Eng.* **98**, 62–74 (2016)
29. F. Pierron, H. Zhu, C. Siviour, Beyond Hopkinson’s bar. *Philos. Trans. R. Soc. London, Ser. A* **372**(2023), 20130195 (2014)
30. L. Fletcher, F. Pierron, An image-based inertial impact (IBII) test for tungsten carbide cermets. *J. Dyn. Behav. Mater.* **4**(4), 481–504 (2018)
31. Y. Sato, S. Arikawa, S. Yoneyama, Identification of heterogeneous elastic material characteristics by virtual fields method, in *International Conference on Experimental Mechanics*, (SPIE, Bellingham, 2014)
32. S. Huang, P. Feissel, P. Villon, Modified constitutive relation error: an identification framework dealing with the reliability of information. *Comput. Methods Appl. Mech. Eng.* **311**, 1–17 (2016)
33. J.M. Considine et al., Smoothly varying in-plane stiffness heterogeneity evaluated under uniaxial tensile stress. *Strain* **53**(5), e12237 (2017)
34. M.A. Sutton et al., Identification of heterogeneous constitutive parameters in a welded specimen: uniform stress and virtual fields methods for material property estimation. *Exp. Mech.* **48**(4), 451–464 (2008)

35. G.L. Louëdec et al., Identification of the local elasto-plastic behavior of FSW welds using the virtual fields method. *Exp. Mech.* **53**(5), 849–859 (2013)
36. M. Grédiac, F. Pierron, A T-shaped specimen for the direct characterization of orthotropic materials. *Int. J. Numer. Methods Eng.* **41**(2), 293–309 (1998)
37. N. Souto, S. Thuillier, A. Andrade-Campos, Design of an indicator to characterize and classify mechanical tests for sheet metals. *Int. J. Mech. Sci.* **101**, 252–271 (2015)
38. N. Souto, A. Andrade-Campos, S. Thuillier, Mechanical design of a heterogeneous test for material parameters identification. *Int. J. Mater. Form.* **10**(3), 353–367 (2016)
39. J. Aquino et al., Experimental validation of a new heterogeneous mechanical test design. *AIP Conf. Proc.* **1960**, 090002 (2018)
40. E.M.C. Jones et al., Parameter covariance and non-uniqueness in material model calibration using the virtual fields method. *Comput. Mater. Sci.* **152**, 268–290 (2018)
41. F. Pierron et al., Identification of the orthotropic elastic stiffnesses of composites with the virtual fields method: sensitivity study and experimental validation. *Strain* **43**(3), 250–259 (2007)
42. K. Syed-Muhammad, E. Toussaint, M. Grédiac, Optimization of a mechanical test on composite plates with the virtual fields method. *Struct. Multidiscip. Optim.* **38**(1), 71–82 (2009)
43. S. Avril, M. Grédiac, F. Pierron, Sensitivity of the virtual fields method to noisy data. *Comput. Mech.* **34**(6), 439–452 (2004)
44. H. Chalal et al., Experimental identification of a nonlinear model for composites using the grid technique coupled to the virtual fields method. *Compos. Pt. A Appl. Sci. Manuf.* **37**(2), 315–325 (2006)
45. P. Wang, F. Pierron, O.T. Thomsen, Identification of material parameters of PVC foams using digital image correlation and the virtual fields method. *Exp. Mech.* **53**(6), 1001–1015 (2013)
46. M. Rossi, F. Pierron, On the use of simulated experiments in designing tests for material characterization from full-field measurements. *Int. J. Solids Struct.* **49**(3-4), 420–435 (2012)
47. M. Rossi et al., Effect of DIC spatial resolution, noise and interpolation error on identification results with the VFM. *Strain* **51**(3), 206–222 (2015)
48. P. Wang et al., Optimised experimental characterisation of polymeric foam material using DIC and the virtual fields method. *Strain* **52**(1), 59–79 (2016)
49. X. Gu, F. Pierron, Towards the design of a new standard for composite stiffness identification. *Compos. Pt. A Appl. Sci. Manuf.* **91**, 448–460 (2016)
50. X. Gu, F. Pierron, *Full Optimization of the T-Shaped Tensile Test Using Genetic Algorithm* (University of Southampton/Shanghai Jiaotong University, Southampton/Shanghai, 2016)
51. A. Marek, F.M. Davis, F. Pierron, Sensitivity-based virtual fields for the non-linear virtual fields method. *Comput. Mech.* **60**(3), 409–431 (2017)
52. A. Marek, F.M. Davis, F. Pierron, Sheet metals characterization using the virtual fields method. *AIP Conf. Proc.* **1960**, 170011 (2018)





## Chapter 17

# Stress Determination for Granular Materials Using TSA: An Inverse Approach

Mohammad Yousefi, Xavier Balandraud, and Wael A. Samad

**Abstract** Granular materials are among the materials which do not fall within the traditional definition of matter. The behavior of granular materials is of great importance in fields such as chemical and agronomical industries, since many of the materials used are prepared from powders or grains, or in geotechnical engineering due to discrete nature of soils. Extensive research has been done to study and quantify the contact force network on various granular systems, specifically the contact force distribution in terms of magnitudes and orientations. However, the stress magnitudes in the contact zones have always been a challenge, regardless of the full-field method used in the analysis. The objective of the work presented here is to determine the stresses in two-dimensional granular materials from a thermoelastic stress analysis (TSA) test using an inverse approach. The inverse approach relies on both the TSA values in the vicinity of the interparticle contacts, an extension of superposed Flamant solutions for concentrated forces on surfaces, as well as static equilibrium equations. Preliminary results on a periodic stacking of cylinders show promising perspectives for granular materials.

**Keywords** Infrared thermography · Granular material · TSA · Hybrid-TSA · Flamant solution · Inverse technique

## Introduction

Granular materials are composed of grains with various sizes, shapes and constitutive materials. They are widely used in many industrial fields. Sands, soils and rocks are involved in civil engineering for instance. Cereals, sugar and rice are used in the agro-food processing industry. Pharmaceutical industry employs raw granular materials for preparing medical drugs. Discrete matters have mechanical behaviors differing from those of solids, liquids and gases [1]. Their global mechanical response is governed by the interparticle contact forces [2]. Different approaches by simulation have been employed to study the influence of various parameters: size and shape of the particles [3–5], friction properties [6], surface energy [7] and properties of the base materials [8]. Different experimental approaches are also available, in particular full-field measurement techniques, to identify the contact force network of granular systems subjected to macroscopic mechanical loadings.

Non-contact full-field measurement techniques have also been employed for various types of material, but applications to granular media are relatively rare compared with continuous media. This can be explained by the three-dimensional nature of media such as sands, requiring measurements in the volume and thus limiting the number of techniques available such as X-ray tomography combined with volumetric digital image correlation [9, 10]. Two-dimensional (2D) granular systems have been also analyzed using suitable 2D full-field measurement techniques. Many applications concern cylinders placed in parallel, forming so-called Schneebeli materials [11]. Optical imaging was combined with digital image correlation (DIC) to perform the particle image velocimetry (PIV) technique and then measure the rigid-body displacements of the particles and the strains of the granular system [12–14]. DIC was also used to measure strains in the particles themselves [15–18]. Finally,

---

M. Yousefi · W. A. Samad (✉)  
Rochester Institute of Technology, Dubai, UAE  
e-mail: [mmy3147@g.rit.edu](mailto:mmy3147@g.rit.edu); [wascad@rit.edu](mailto:wascad@rit.edu)

X. Balandraud  
Université Clermont Auvergne, CNRS, SIGMA Clermont, Institut Pascal, Clermont-Ferrand, France  
e-mail: [xavier.balandraud@sigma-clermont.fr](mailto:xavier.balandraud@sigma-clermont.fr)

two full-field measurement techniques are available to measure stresses in the particles. Photoelasticity was employed to measure shear stresses in birefringent particles [19–21]. Infrared (IR) thermography was also carried out to measure fields of hydrostatic stress in granular systems by thermoelastic stress analysis (TSA) [8, 22, 23].

Extensive research has been done to study and quantify the contact force networks on granular systems, specifically the contact force distribution in terms of magnitudes and orientations. Photoelastic data and DIC data combined with Granular Element Method or Finite Element Method were used to identify these force networks [16–18, 24]. However, the stress magnitudes in the contact zones have always been a challenge, regardless of the full-field method used in the analysis. The objective of the present work is to identify stresses in a 2D granular material from TSA data and using an inverse approach. The latter relies on the TSA values in the vicinity of the interparticle contacts, an extension of superposed Flamant solutions for concentrated forces on surfaces, as well as static equilibrium equations. Previous work has shown the possibility of reconstructing stress contours on simpler loading scenarios (e.g. Brazilian test) [25], but has not been extended to more complicated periodic stacking scenarios.

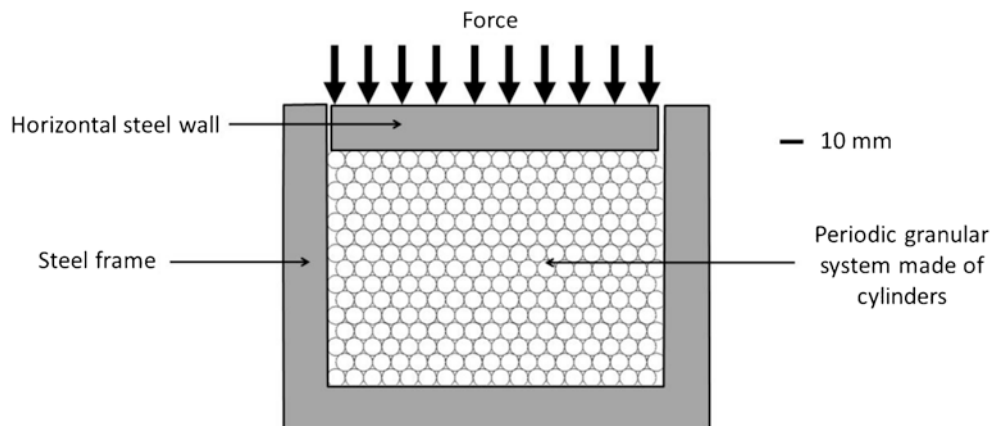
It is worth mentioning that the analytical-Flamant and experimental-TSA coupling presented here was made possible thanks to the prior successes in hybridizing TSA measurements. Most of the research came out of the Experimental Mechanics Group at the University of Wisconsin—Madison where over the years, coupled isopachic stresses (in the form of  $\sigma_x + \sigma_y$ ) were separated and reconstructed using a hybrid experimental-analytical formulations. Hybrid-TSA method was applied to various geometries and loading scenarios such as: circular holes [26], elliptical holes [27], irregularly shaped cutouts [28], pinned-connections and bolted structures [29] and diametrically loaded disks [30]. For more information on Hybrid-TSA, comprehensive review papers can be found in [31].

The paper is divided in three sections as follows. The first section presents the experimental test providing TSA data in a 2D periodic granular system under confined compression. The second section provides the background about Flamant solutions. The third section presents the results obtained.

## Experimental Test

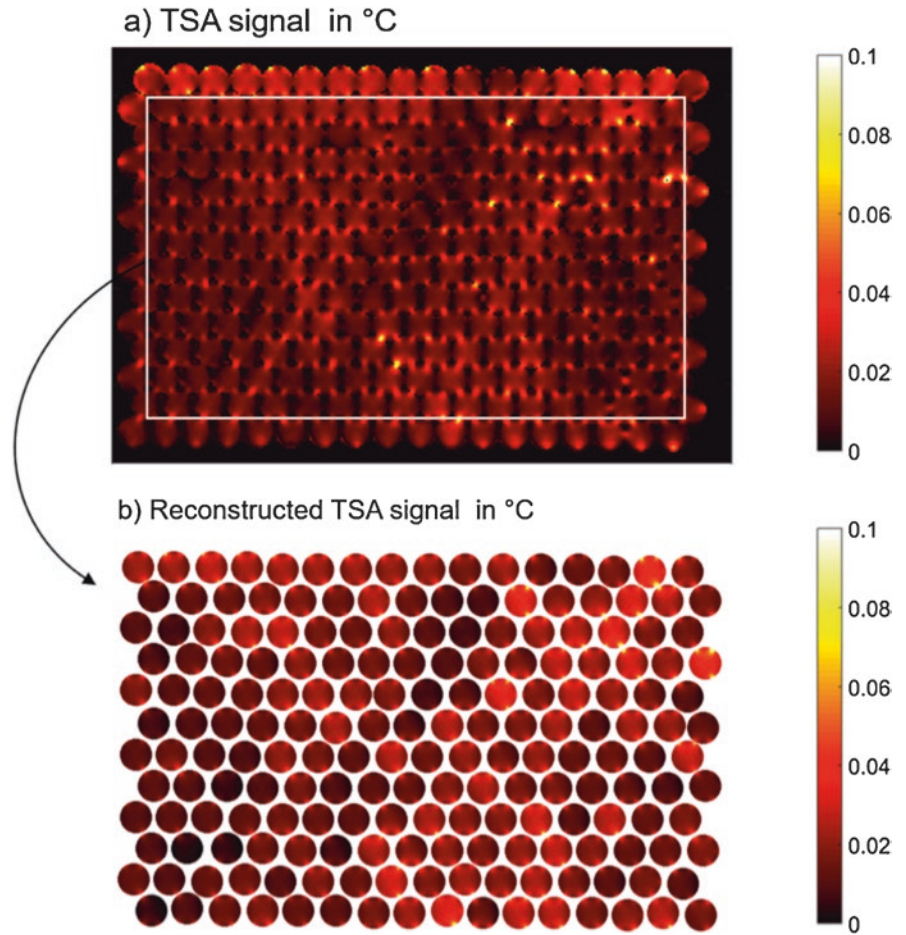
Figure 17.1 presents a schematic view of the experimental device used for the mechanical test under study. The granular system is composed of cylinders made in POM polymer with the same diameter (8 mm), forming thus a 2D quasi-periodic monodisperse organization. The frame and the top horizontal wall are made of steel and can be considered non-deformable compared to the granular material subjected to confined compression. The mechanical loading was performed using a  $\pm 15$  kN MTS uniaxial testing machine. A force-controlled sinusoidal signal was applied at a frequency of 3 Hz. The maximum compression force was fixed to  $-5$  kN for a load ratio of 0.1. A Cedip Jade III-MWIR camera was employed for temperature measurements. It features a wavelength range of  $3.5\text{--}5$   $\mu\text{m}$ , a sensor size of  $320 \times 240$  pixels and a Noise Equivalent Temperature Difference (NETD) of  $0.02$   $^{\circ}\text{C}$ . The granular system was preliminary painted in black to maximize the thermal emissivity of the observed surfaces. The acquisition frequency was set to 147 Hz.

Figure 17.2a presents the TSA data (in  $^{\circ}\text{C}$ ), namely the amplitudes of temperature oscillation at the frequency of the mechanical loading. Assuming an adiabatic response, these data can be considered as proportional to the hydrostatic stress. It can be noted that the observed surface are “free” by definition, meaning that they are in a plane stress state. As a consequence, the TSA data can be considered as proportional to the sum of the two principal stresses. Following comments can be done from



**Fig. 17.1** Schematic view of the experimental system used for the mechanical test. An IR camera was employed to measure the temperature changes on the end of the cylinders during cyclic confined compression

**Fig. 17.2** (a) Data obtained by TSA approach, (b) reconstructed TSA image. Boundary cylinders have been removed in the reconstructed image



this figure. First, the field of TSA data is not periodic. This result is not surprising because the geometric periodicity cannot be achieved in an actual monodisperse granular material (actual ratio between frame's width and particle diameter different from the theoretical one). Moreover it is well known that the contact force network is impacted by slight local fluctuations in the base material and the particle shapes. In the present experiment, large triangular patterns can be visualized in Fig. 17.2a. Second, although each cylinder is in theory in contact with six surrounding particles (except at the contact with the frame and the top horizontal wall), only four contact generally transfer force. This result is typical of periodic monodisperse systems. Third, they are cylinders with three and five contacts transferring forces. Last, it can be noted that the weak spatial resolution of the field of TSA data prevents clear analysis. Flamant solutions can be advantageously employed to improve the raw data, as shown in Fig. 17.2b and explained in the next sections. Note that Fig. 17.2b shows small gaps between the different cylinders. This is due to the fact that the Flamant solution goes to infinity right at the contact location, and was as such avoided.

## Background About Flamant Solutions

Flamant's problem aims to identify the stress fields caused by a force acting normal to the surface of a half plane. Apply thing to this analytical formulation to the case of a diametrically loaded disk is shown in Fig. 17.3.

Notice that this case involves the summation of two Flamant solutions, each in its own coordinate system, and then adding a radial tension component so that traction free boundary conditions on the outer surface of the disk is maintained.

The three individual components of stress for Flamant's problem are shown below, where  $F$  is the magnitude of the contact force and the Cartesian system origin is centered about the point of application of the force,  $F$ :

$$\sigma_x = \sigma_r \cos^2 \theta = -\frac{2Fx^2y}{\pi(x^2 + y^2)^2} \quad (17.1)$$

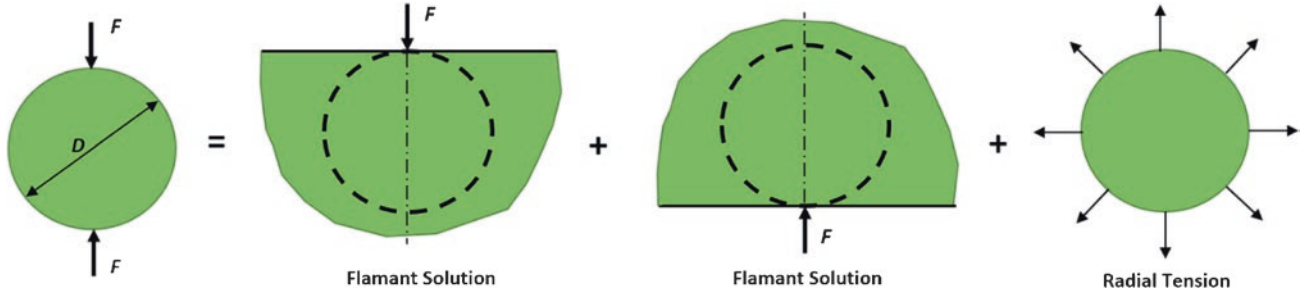


Fig. 17.3 Flamant's case: half-plane subjected to a normal force at the surface for the case of a diametrically loaded disk

$$\sigma_y = \sigma_r \sin^2 \theta = -\frac{2Fy^3}{\pi(x^2 + y^2)^2} \quad (17.2)$$

$$\tau_{xy} = \sigma_r \sin \theta \cos \theta = -\frac{2Fxy^2}{\pi(x^2 + y^2)^2} \quad (17.3)$$

With the additional radial tension stress shown below:

$$\sigma_{radial} = \frac{2F}{\pi D} \quad (17.4)$$

For the case of a stacking of disks involving several contacts, the individual Flamant solutions for each contact location would have its own force magnitude;  $F$  in Eqs. (17.1)–(17.3). With this being an inverse approach, where the TSA full-field stresses are used to retrieve the contact forces,  $F$ 's, the thermoelastic quantities ( $\sigma_x + \sigma_y$ ) are expressed in terms of the Flamant solution as shown in the equation below:

$$\sigma_x + \sigma_y = -\left[ \left[ \frac{2Fx^2y}{\pi(x^2 + y^2)^2} \times \sin\left(\theta + \frac{\pi}{2}\right) \right] + \left[ \frac{2Fx^2y}{\pi(x^2 + y^2)^2} \times \cos\left(\theta + \frac{\pi}{2}\right) \right] + \left[ \frac{2Fy^3}{\pi(x^2 + y^2)^2} \times \cos(\theta) \right] + \left[ \frac{2Fy^3}{\pi(x^2 + y^2)^2} \times \sin(\theta) \right] \right] \quad (17.5)$$

Equation (17.5) can be then factored and written in the following simplified form below:

$$K_{i,k} = F_i \times \left[ \frac{(-2x_k^2y_k \left( \sin\left(\theta_k + \frac{\pi}{2}\right) + \cos\left(\theta_k + \frac{\pi}{2}\right) \right) + (-2y_k^3 (\cos(\theta_k) + \sin(\theta_k))))}{\pi(x_k^2 + y_k^2)^2} \right] \quad (17.6)$$

where  $i$  is the increment representing the contact force number index, and  $k$  is the increment describing the location relative to the force application. Both  $i$  and  $k$  start from 1 and terminate at  $n$ , the total number of contact forces for a given disk, resulting in a square matrix,  $K_{n \times n}$ .

Note that for this generalized case, Eq. (17.4) of the radial component of stress does not exactly apply. As such, the resultant component of the radial stress is expressed in terms of the contact forces,  $F_1$  through  $F_n$ , and set to zero as shown in the equation below so that the determined contact forces conform to the traction-free conditions.

$$R_n = \sigma_{rn} = F_n \times \left[ -\frac{2x_n^2y_n}{\cos^2\left(\tan^{-1}\left(\frac{y_n}{x_n}\right)\right)\pi(x_n^2 + y_n^2)^2} \right] = 0 \quad (17.7)$$

Moreover, and to add validity to the inversely determined contact forces, static equilibrium conditions are expressed again in terms of all the present contact forces.

$$\sum_1^n F_x = 0 \quad (17.8)$$

$$\sum_1^n F_y = 0 \quad (17.9)$$

with that Eqs. (17.6)–(17.9) are compiled together in the matrix equation below, where all the contact forces can be solved for using a linear-least squares approach:

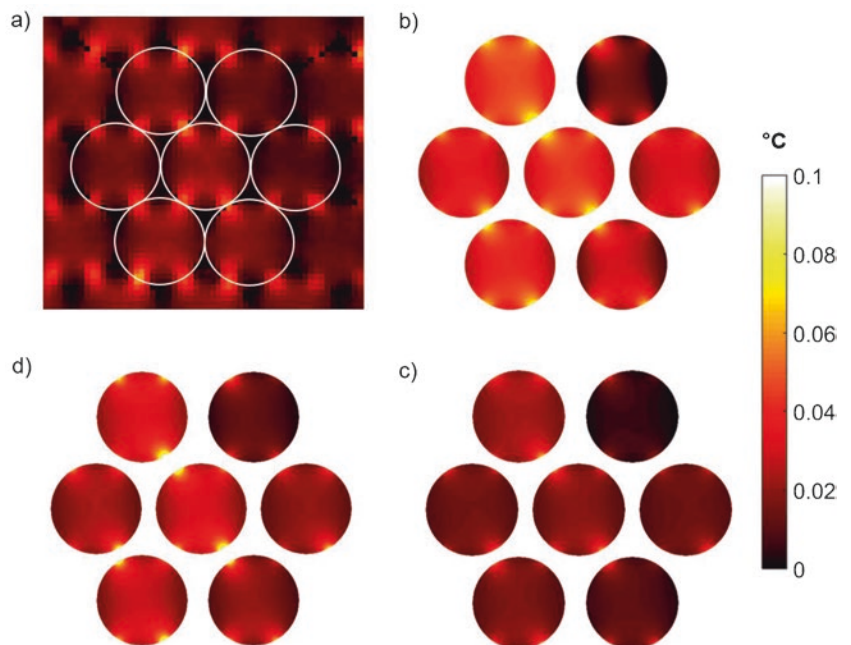
$$\begin{bmatrix} K_{1,1} & \cdots & K_{1,n} \\ \vdots & K_{i,k} & \vdots \\ K_{1,n} & \cdots & K_{n,n} \\ -\cos(\theta_1) & \cdots & -\cos(\theta_n) \\ -\sin(\theta_1) & \cdots & -\sin(\theta_n) \\ R_1 & \cdots & R_n \end{bmatrix} \begin{bmatrix} F_1 \\ \vdots \\ F_n \end{bmatrix} = \begin{bmatrix} (\sigma_x + \sigma_y)_1 \\ \vdots \\ (\sigma_x + \sigma_y)_n \\ 0 \\ 0 \\ 0 \end{bmatrix} \quad (17.10)$$

Having determined the contact forces, those can now be substituted back in the analytical expressions of stresses from the superposed Flamant solutions discussed earlier.

## Application to the 2D Periodic Granular System

Figure 17.4a shows a snapshot of Fig. 17.2 in the bottom right-hand side of the granular material. The processing is focused on seven cylinders, indicated with white circles in the image. The TSA data at the six contacts of each cylinder were extracted to reconstruct the TSA signal: see Fig. 17.4b. Additionally, TSA stresses are now separated and made available full-field in the x and y directions as shown in Fig. 17.4c, d respectively. This is of great importance as now high magnitude stress networks can be identified in the both directions.

**Fig. 17.4** Full-field stresses: (a) raw TSA data, and the reconstructed stress fields via Flamant solutions of (b) TSA, (c)  $\sigma_x$  and (d)  $\sigma_y$



## Conclusion

Granular materials exhibit contact force networks when they are submitted to macroscopic mechanical loading. Identification of such networks is of prime interest to understand the mechanical response of these materials. In the present study, a quasi-periodic granular media was built from cylinders placed in parallel and then submitted to cyclic confined compression. IR thermography was employed to extract data related to the thermoelastic coupling featured by the base material (TSA approach). Then an inverse approach based on an extension of superposed Flamant solutions for concentrated forces on surfaces, as well as static equilibrium equations, was performed to reconstruct the TSA signal. Preliminary results show promising perspective for various stacking scenarios of granular materials.

**Acknowledgements** The authors gratefully acknowledge Dr. Chanwit Chaiamarit, Dr. Pawarut Jongchansitto and Prof. Itthichai Preechawuttipong from Chiang Mai University, Thailand for the discussions about the mechanical response of granular materials. Ms. Rym Boufayed, Université Clermont-Auvergne, France is also acknowledged for the help in image processing.

## References

1. H.M. Jaeger, S.R. Nagel, Granular solids, liquids, and gases. *Rev. Mod. Phys.* **68**, 1259–1272 (1996)
2. S. Ostojic, E. Somfai, B. Nienhuis, Scale invariance and universality of force networks in static granular matter. *Nature* **439**, 828–830 (2006)
3. D.H. Nguyen, E. Azéma, F. Radjai, P. Sornay, Effect of size polydispersity versus particle shape in dense granular media. *Phys. Rev. E* **90**, 012202 (2014)
4. A.A. Peña, R. García-Rojo, H.J. Herrmann, Influence of particle shape on sheared dense granular media. *Granul. Matter* **9**, 279–291 (2007)
5. C. Nouguier-Lehon, B. Cambou, E. Vincens, Influence of particle shape and angularity on the behaviour of granular materials: a numerical analysis. *Int. J. Numer. Anal. Methods Geomech.* **27**, 1207–1226 (2003)
6. S.G. Bardenhagen, J.U. Brackbill, D. Sulsky, Numerical study of stress distribution in sheared granular material in two dimensions. *Phys. Rev. E* **62**, 3882–3890 (2000)
7. I. Preechawuttipong, R. Peyroux, F. Radjai, W. Rangsri, Static states of cohesive granular media. *J. Mech. Sci. Technol.* **21**, 1957–1963 (2007)
8. P. Jongchansitto, I. Preechawuttipong, X. Balandraud, M. Grédiac, Numerical investigation of the influence of particle size and particle number ratios on texture and force transmission in binary granular composites. *Powder Technol.* **308**, 324–333 (2017)
9. H. Wolf, D. König, T. Triantafyllidis, Experimental investigation of shear band patterns in granular material. *J. Struct. Geol.* **25**, 1229–1240 (2003)
10. S.A. Hall, M. Bornert, J. Desrues, Y. Pannier, N. Lenoir, G. Viggiani, P. Besuelle, Discrete and continuum analysis of localised deformation in sand using X-ray  $\mu$ CT and volumetric digital image correlation. *Geotechnique* **60**, 315–322 (2010)
11. G. Schneebeli, Une analogie mécanique pour les terres sans cohésion. *C. R. Hebd. Acad. Sci.* **243**, 125–126 (1956)
12. C. Slominski, M. Niedostatkiewicz, J. Tejchman, Application of particle image velocimetry (PIV) for deformation measurement during granular silo flow. *Powder Technol.* **173**, 1–18 (2007)
13. S.A. Hall, D.M. Wood, E. Ibraim, G. Viggiani, Localised deformation patterning in 2D granular materials revealed by digital image correlation. *Granul. Matter* **12**, 1–14 (2010)
14. V. Richefeu, G. Combe, G. Viggiani, An experimental assessment of displacement fluctuations in a 2D granular material subjected to shear. *Geotech. Lett.* **2**, 113–118 (2012)
15. E. Marteau, J.E. Andrade, A novel experimental device for investigating the multiscale behavior of granular materials under shear. *Granul. Matter* **19**, 77 (2017)
16. R. Hurley, E. Marteau, G. Ravichandran, J.E. Andrade, Extracting inter-particle forces in opaque granular materials: beyond photoelasticity. *J. Mech. Phys. Solids* **63**, 154–166 (2014)
17. R.C. Hurley, K.W. Lim, G. Ravichandran, J.E. Andrade, Dynamic inter-particle force inference in granular materials: method and application. *Exp. Mech.* **56**, 217–229 (2016)
18. N. Karanjgaokar, Evaluation of energy contributions using inter-particle forces in granular materials under impact loading. *Granul. Matter* **19**, 36 (2017)
19. A. Shukla, C. Damania, Experimental investigation of wave velocity and dynamic contact stresses in an assembly of disks. *Exp. Mech.* **27**, 268–281 (1987)
20. K.M. Roessig, J.C. Foster, S.G. Bardenhagen, Dynamic stress chain formation in a two-dimensional particle bed. *Exp. Mech.* **42**, 329–337 (2002)
21. S.A. Mirbagheri, E. Ceniceros, M. Jabbarzadeh, et al., Sensitive photoelastic biocompatible gelatin spheres for investigation of locomotion in granular media. *Exp. Mech.* **55**, 427–438 (2015)
22. C. Chaiamarit, X. Balandraud, I. Preechawuttipong, M. Grédiac, Stress network analysis of 2D non-cohesive polydisperse granular materials using infrared thermography. *Exp. Mech.* **39**, 761–769 (2015)
23. P. Jongchansitto, X. Balandraud, M. Grédiac, C. Beitone, I. Preechawuttipong, Using infrared thermography to study hydrostatic stress networks in granular materials. *Soft Matter* **10**, 8603–8607 (2014)
24. T.S. Majmudar, R.P. Behringer, Contact force measurements and stress-induced anisotropy in granular materials. *Nature* **435**, 1079–1082 (2005)

25. M. Yousefi, X. Balandraud, W.A. Samad, Thermographic stress field investigation of a multiply-loaded disk, in *Residual Stress Thermomechanics & Infrared Imaging, Hybrid Techniques and Inverse Problems*, vol. 7 (Springer, Cham, 2019), pp. 115–117
26. S. Lin, D. Matthys, R.E. Rowlands, Separating stresses thermoelastically in a central circularly perforated plate using an airy stress function. *Strain* **45**, 516–526 (2009)
27. A.A. Khaja, R.E. Rowlands, Experimentally determined stresses associated with elliptical holes using polar coordinates. *Strain* **49**, 116–124 (2013)
28. W.A. Samad, R.E. Rowlands, Full-field thermoelastic stress analysis of a finite structure containing an irregularly-shaped hole. *Exp. Mech.* **54**, 457–469 (2014)
29. W.A. Samad, A.A. Khaja, A. Kaliyanda, R.E. Rowlands, Hybrid thermoelastic stress analysis of a pinned joint. *Exp. Mech.* **54**, 515–525 (2014)
30. B. Foust, R.E. Rowlands, Thermoelastic determination of individual stresses in a diametrically loaded disk. *Strain* **47**, 146–153 (2011)
31. S. Lin, W.A. Samad, A.A. Khaja, R.E. Rowlands, Hybrid thermoelastic stress analysis. *Exp. Mech.* **55**, 653–665 (2015)



## Chapter 18

# Evaluation of Fatigue Crack Growth Behavior and Effect of Repair Work Based on Thermoelastic Stress Analysis for Steel Bridge Members

Takahide Sakagami, Daiki Shiozawa, Yuki Terauchi, Noriyasu Arima, Yoshiaki Mizokami, and Masahiro Hayashi

**Abstract** Evaluation of fatigue damage propagation is necessary to ensure safety and to estimate the remaining life of the aging steel bridges. In this study, thermoelastic stress analysis (TSA) was applied for on-site measurement of stress distributions around fatigue cracks, and the future crack propagation behavior was estimated by the fracture mechanics approach. Experimental studies were conducted for laboratory specimens which modeled a part of welded structure in steel bridges. The stress intensity factors were calculated from stress distributions measured by TSA technique. Further TSA technique was applied to evaluate the effectiveness of repair works for defective portions. Severity reduction in stress distribution around the fatigue crack after treatment was confirmed for actual steel bridge members by TSA.

**Keywords** Thermoelastic stress analysis · Infrared thermography · Fracture mechanics · Fatigue crack · Steel bridges

## Introduction

Inspection of fatigue damage is necessary to ensure safety and estimate the remaining strength of the steel bridges. Nondestructive evaluation (NDE) techniques play an important role in the maintenance programs for steel bridges. Conventional NDT techniques employed for fatigue damage detection include visual testing, magnetic-particle testing and ultrasonic testing. However these are time- and labor-intensive techniques. Further for the effective maintenance of steel bridges structural integrity evaluation is essential for the fitness for service evaluation. Conventional stress- and strain-measurement techniques are insufficient in remote and full-field measurement. Applications of the thermoelastic stress analysis (TSA) are found in structural integrity evaluations for steel structures related with fracture mechanics evaluations [1, 2]. In this study the TSA technique was applied for on-site measurement of stress distributions around fatigue cracks, and the future crack propagation behavior was estimated by the fracture mechanics approach. An experimental study was conducted for laboratory specimens which modeled a part of welded structure in steel bridges. The stress intensity factors were calculated from stress distributions measured by the TSA technique, and the relationship between stress intensity factor ranges and crack growth rates were obtained. Further TSA was applied to evaluate the effectiveness of repair works for defective portions. Severity reduction in stress distribution around the fatigue crack after treatment was confirmed for actual steel bridge members by TSA.

---

T. Sakagami (✉) · D. Shiozawa · Y. Terauchi  
Department of Mechanical Engineering, Kobe University, Kobe, Japan  
e-mail: [sakagami@mech.kobe-u.ac.jp](mailto:sakagami@mech.kobe-u.ac.jp); [shiozawa@mech.kobe-u.ac.jp](mailto:shiozawa@mech.kobe-u.ac.jp); [170t336t@stu.kobe-u.ac.jp](mailto:170t336t@stu.kobe-u.ac.jp)

N. Arima · Y. Mizokami · M. Hayashi  
Honshu-Shikoku Bridge Expressway Company Limited, Kobe, Japan  
e-mail: [noriyasu-arima@jb-honshi.co.jp](mailto:noriyasu-arima@jb-honshi.co.jp); [yoshiaki-mizokami@jb-honshi.co.jp](mailto:yoshiaki-mizokami@jb-honshi.co.jp); [masahiro-hayashi@jb-honshi.co.jp](mailto:masahiro-hayashi@jb-honshi.co.jp)



## Stress Intensity Factor Evaluation Based on TSA

For a crack existing in semi-infinite plate as shown in Fig. 18.1, the equation of the sum of principal stresses around crack tip under mode I loading is given by the series expansion formula as follows.

$$\sigma_r + \sigma_\theta = \left( \sqrt{\frac{2}{\pi r}} \cos \frac{1}{2} \theta \right) K + C_2 + \left( \sqrt{r} \cos \frac{1}{2} \theta \right) C_3 + \dots \quad (18.1)$$

In this study, the first term coefficient  $K$  in Eq. (18.1) was calculated by the least square fitting using numerous data of the sum of principal stresses obtained by TSA technique, thus stress intensity factors  $K$  can be determined.

## Experimental Study for Laboratory Specimen

Experimental studies were conducted for a steel plate weld specimen modeling a part of the bridge structure constituted by the vertical stiffener, the cross beam web and the stringer as shown in Fig. 18.2. Material of the specimen was JIS SM400A. The carbon dioxide gas-shielded arc welding was employed for the fabrication of the specimen. A plate bending loading was applied to the specimen being fixed right end of the specimen on the trestle. The left end of the specimen was subjected to cyclic loading by the shaker with a decentering spindle. The applied stress range was measured by the strain gauge installed on the specimen. The stress ranges initially applied to the weld toe were set from 200 MPa to 600 MPa with stress ratio  $R = -1$ . Loading frequencies were set in the range between 12 Hz and 17.5 Hz. An infrared camera with a QVGA InSb array detector (Type SC7500 by FLIR company, NETD: 20 mK) was employed for the infrared measurement.

The stress intensity factors were calculated from stress distributions measured by TSA technique, and the relationship between stress intensity factor ranges and crack propagation rates were obtained. The obtained results are shown in Fig. 18.3. It is found from the figure that linear relationship was observed on a log-log plot graph with the stress intensity factor range  $\Delta K$  as the abscissa and the crack growth rate  $da/dn$  as the ordinate. It is well known that Paris-Erdogan law relates the stress intensity factor range  $\Delta K$  to the fatigue crack growth rate  $da/dn$  by the following formula,

$$\frac{da}{dn} = C \Delta K^m, \quad (18.2)$$

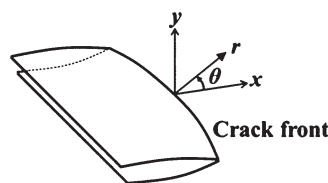


Fig. 18.1 Coordinates near crack front

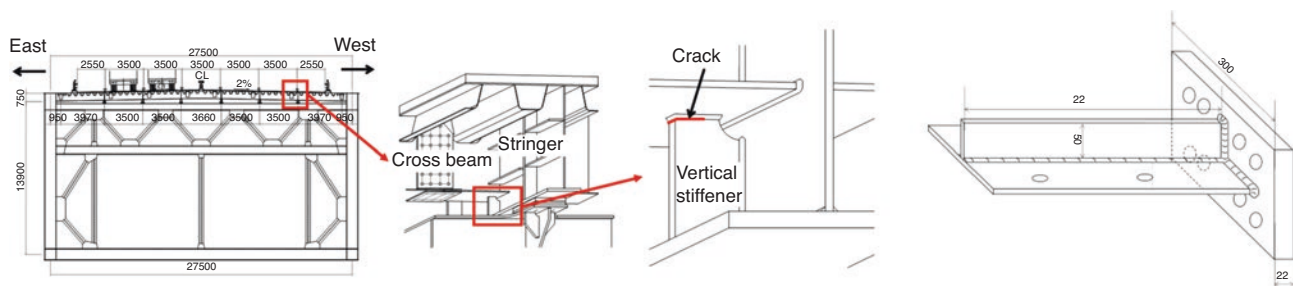


Fig. 18.2 Objective bridge member for evaluating fatigue crack growth and laboratory specimen

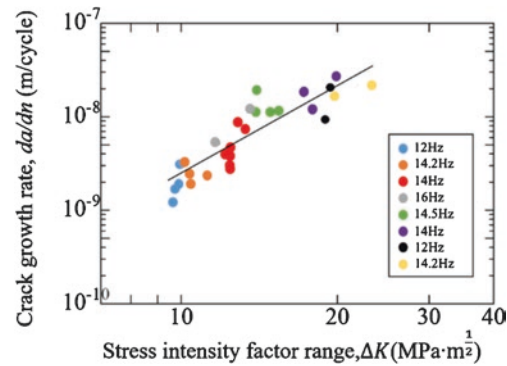


Fig. 18.3 Obtained relationship between stress intensity factor and crack growth rate

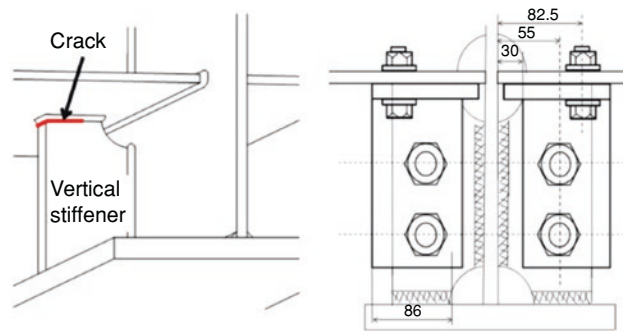


Fig. 18.4 Objective member of evaluating stress severity reduction and repair method

where  $C$  and  $m$  are constants that depend on the material, environment and stress ratio. These values were calculated from the relationship shown in Fig. 18.3. Values of the constants  $C$  and  $m$  are obtained as  $C = 1.45 \times 10^{-12}$ ,  $m = 3.21$ . It is known that the value of  $m$  varies approximately from 2 to 4 for metallic materials. Therefore the reasonable relationship between the stress intensity factor ranges and the crack growth rates was obtained in this study.

## Experimental Study for Actual Steel Bridge

Fatigue cracks were found in the structural members of the long-span steel bridges. Several repair works were applied to the structural members. The stress distributions around the fatigue cracks were measured before and after the repair works by the TSA technique when live loading acted on the bridge and the effectiveness of the severity reduction was investigated [3]. Objective member for evaluating stress severity reduction after the repair work was the vertical stiffener as shown in Fig. 18.4. A fatigue crack was detected at the upper weld part of the vertical stiffener. The employed repair method was the stiffening-plate method; illustration of the method was shown in Fig. 18.4. In this repair method, four angle-stiffener plates were fastened to the vertical stiffeners and the lower cross beam flange using fastening bolts.

The stress distribution on the vertical stiffener was measured before and after the repair. After the repair, the fatigue crack itself was left as it was. The objective structure was loaded with a sprinkler truck with three axles (total vehicle load: 214 kN) driving on the traffic lane of the bridge at a constant speed of 80 kilometers an hour. From the temperature change observed by the infrared camera, the change in the sum of the principal stresses was calculated based on material properties of the structural steel. In this study the obtained sequential infrared data were processed using the self-reference lock-in technique [4] to obtain S/N improved stress distribution images. The obtained results of the self-reference lock-in measurement indicating the stress distributions are shown in Fig. 18.5 with visible image of the structural member before and after the repair. To avoid the problem of the infrared-measurement area being hidden by the angle-stiffener plate, an observation window was

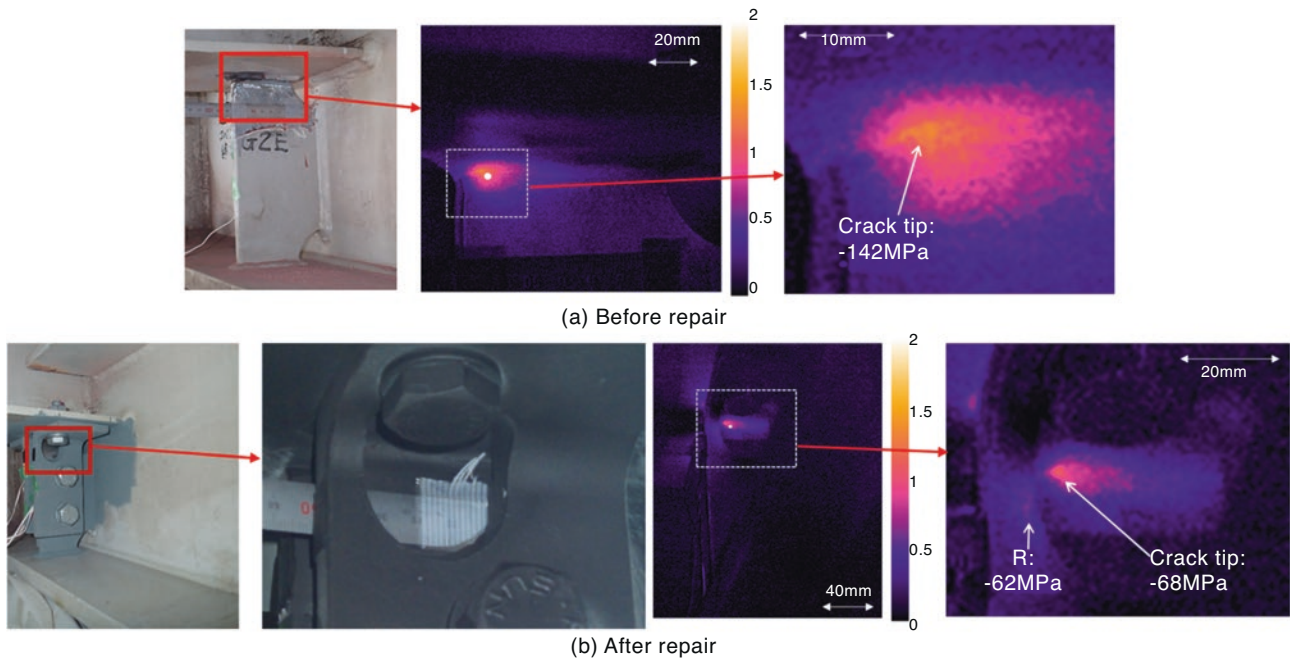


**Fig. 18.5** Results of the thermoelastic stress distribution measurement before and after stiffening-plate repair. (a) Before repair. (b) After repair

made in one of the plates, as shown in the photograph. It is found from Fig. 18.5a that a high stress concentration was observed at the crack tip before the repair. It is found from Fig. 18.5b that a high stress concentration was still observed at the crack tip, however the maximum stress value in the vicinity of the crack tip is drastically decreased after the repair work. The stress intensity factor ranges were calculated from stress distributions measured by the TSA technique for quantitatively evaluating the suppressing effect of fatigue crack propagation by the repair work. The value of the stress intensity factor range  $\Delta K$  before the repair work was  $11.8 \text{ MPa}\sqrt{\text{m}}$ . In contrast  $\Delta K$  was decreased to  $6.7 \text{ MPa}\sqrt{\text{m}}$  after the repair work. According to the relationship between stress intensity factor range  $\Delta K$  and crack propagation rate obtained for the laboratory test, the estimated crack propagation rate was  $4.01 \times 10^{-9} \text{ m/cycle}$  before the repair, and  $6.50 \times 10^{-10} \text{ m/cycle}$  after the repair. It was found that the crack propagation rate was reduced by 83% by the stress mitigation effect of the crack repair that leads to the life prolonging of the cracked steel structures.

## References

1. R.A. Tomlinson, E.A. Olden, Thermoelasticity for the analysis of crack tip stress fields—A review. *Strain* **35**, 49–55 (1999)
2. T. Sakagami, Remote nondestructive evaluation technique using infrared thermography for fatigue cracks in steel bridges. *Fatigue Fract. Eng. Mater. Struct.* **38**, 755–779 (2015)
3. T. Sakagami, Y. Mizokami, D. Shiozawa, T. Fujimoto, Y. Izumi, T. Hanai, A. Moriyama, Verification of the repair effect for fatigue cracks in members of steel bridges based on thermoelastic stress measurement. *Eng. Fract. Mech.* **183**, 1–12 (2017)
4. T. Sakagami, T. Nishimura, S. Kubo, Development of a self-reference lock-in thermography and its application to crack monitoring. *Proc. SPIE* **5782**, 379–387 (2005)



## Chapter 19

# Analysis of Deformations in Crush Tests of Lithium Ion Battery Cells

Marco Sasso, Golam Newaz, Marco Rossi, Attilio Lattanzi, and Sanket Mundhe

**Abstract** Several mechanical tests have been conceived, especially by car manufacturers and related institutions, to assess the hazard level and the general behavior of batteries under severe abuse conditions. No experiments have been reported in the literature for investigating the detailed mechanisms of internal cell deformation and configuration leading to internal shorts due to lateral mechanical deformation. This work aims at determining the maximum deformation inside a lithium-ion battery cell before the onset of the short circuit. Hence, static crushing tests were carried out by means of a hydraulic test machine on pouch type li-ion cell. A semi-spherical punch was used on whole healthy samples, for which it was possible to measure the voltage in real time during the test; a semi-cylindrical punch was used on previously sectioned batteries, for which it was possible to observe the deformations suffered by the various layers that alternate inside the battery. The optical setup used is based on a telecentric lens with in-line illumination and 6X magnification, which permits to reduce the field of view to  $1.2 \times 1.5$  mm. The system has allowed, even with difficulties related to large displacements and loss of focus, to apply the Digital Image Correlation technique to identify the deformation field inside the battery cell. Large local strains were detected, which are responsible of metallic and polymeric layers failure and determine the short circuit.

**Keywords** Li-ion battery · Digital image correlation · Crushing test · Short circuit · Microscopy

## Introduction

In recent years, significant research has been carried out for the employment of advanced batteries as an energy storage device, especially Li-ion batteries, in electric-based transportation. Deep understanding of the behavior of battery pack or cell in case of mechanical damage is mandatory to use such batteries in electric vehicles. In automobile application, it is impossible to guarantee zero deformation of battery cells during a severe crash despite of the amount of protection around the battery pack. Nevertheless, there is still a limited amount of research available in the literature about the mechanical properties and mechanical conditions that lead to a short circuit [1]. Lacking an in-depth understanding of how the batteries fail under mechanical deformation, the current approach is to protect the batteries by heavy, armor-like enclosures.

In this work, we wanted to increase the knowledge regarding the internal deformation of lithium polymer batteries when they are crushed until their internal short cut. Several tests have been carried out in different loading configurations, and different techniques, namely in situ DIC and post-mortem microscopy imaging, have been employed to estimate the battery's internal deformation.

---

M. Sasso (✉) · M. Rossi · A. Lattanzi

Department of Industrial Engineering e Mathematical Sciences, Università Politecnica delle Marche, Ancona, Italy  
e-mail: [m.sasso@univpm.it](mailto:m.sasso@univpm.it); [m.rossi@univpm.it](mailto:m.rossi@univpm.it); [a.lattanzi@pm.univpm.it](mailto:a.lattanzi@pm.univpm.it)

G. Newaz · S. Mundhe

College of Engineering, Wayne State University, Detroit, MI, USA  
e-mail: [gnewaz@eng.wayne.edu](mailto:gnewaz@eng.wayne.edu); [sanket.mundhe@wayne.edu](mailto:sanket.mundhe@wayne.edu)

## Background on Li-Ion Batteries

An electric battery is a device consisting of one or more electrochemical cells with external connections provided to power electrical devices such as flashlights, smartphones, or even electric cars. When a battery is supplying electric power, its positive terminal is the cathode and its negative terminal is the anode. The negative terminal is the source of electrons which, when connected to an external circuit, will flow and deliver energy to an external device. When a battery is connected to an external circuit, ions can move within electrolytes, allowing the chemical reactions to be completed at the separate terminals and so deliver energy to the external circuit. The movement of those ions within the battery allows the current to flow out of the battery.

Pioneering work of the lithium-ion battery began in the early 900s, but only after 1970s non-rechargeable lithium batteries became commercially available, using metallic lithium as anode material. At today, rechargeable Li-ion batteries uses graphite as anode, while a metal oxide is used as the cathode. In 1991 Akira Yoshino invented the first battery that use this technology, the lithium-ion battery, where lithium salt are used as electrolite.

During cell operation, Lithium ions shuttle back and forth between the two electrodes. While discharging, Lithium ions and electrons are extracted (oxidation) from the anode. The ions cross the ion-conductive electrolyte, through a separator, before ending up in the cathode, whereas the electrons flow in the external circuit. The process is reversed during the charging phase. In particular the principal components are:

- The anode (negative pole) which during the discharge, supplies electrons to the external circuit. Lithium oxidizes. Typically, it is made up mostly of graphite.
- The cathode (positive pole) during the discharge, accepts electrons from the external circuit. Lithium is subject to the reduction (Fig. 19.1). It consists of a lithium oxide. The whole cell typology takes its name from the material used for the cathode.
- The electrolyte is an ion (i.e. charged particle) conductor, but an insulator for electrons. It separates the two electrodes and provide the transfer medium of the ions between anode and cathode. In lithium batteries, the electrolyte is an inorganic solvent containing lithium salts. A porous septum separates electrically the two electrodes but allows the transit of ions from one electrode to the other.

Lithium polymer, or more accurately lithium-ion polymer battery (shortened as LiPo), is a rechargeable battery of lithium-ion that uses a polymer-based electrolyte. High conductivity semisolid (gel) polymers forms this type of electrolyte. These batteries are being utilized where weight is a basic element, like tablet, PCs, cell phones.

Different types and designs of battery exist. The cylindrical cell is one of them most commonly used packaging styles. Prismatic cells make optimal use of space by using the layered approach. Other designs are wound and flattened into a pseudo-prismatic jelly roll. Li-polymer cells also come in a flexible foil-type case that resembles a food package (pouch cell). While a standard Li-ion needs a rigid case to press the electrodes together, Li-polymer uses laminated sheets that do not need compression. A foil-type enclosure reduces the weight by more than 20% over the classic hard shell. Moreover, the modern thin film technology unleash the designer fantasy, as the battery can be made into any shape, fitting neatly into the desired shape.

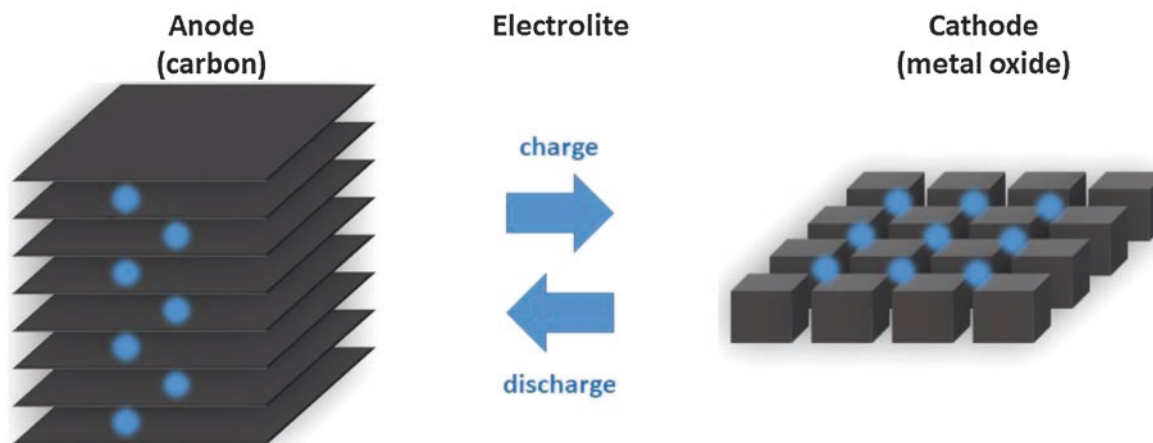


Fig. 19.1 Working mechanism of a lithium-ion battery reaction

## Mechanical Abuse Tests

Engineers are asked to design Li-ion batteries and the supporting structures to remain safe when subjected to impacts. Hence, lithium ion batteries must pass a series of safety tests to be certified for use in a particular application. Safety tests are described in international, national and regional standards. These tests are done to understand and detect possible vulnerabilities when the battery is exposed to extreme loads, and to determine how it will behave under severe abuse conditions [2].

Concerning the mechanical deformation, several tests have been developed to evaluate the safety of Li-ion cells. Some tests, such as the nail penetration, induce internal short circuit on fully assembled cells. The purpose of these tests is to create a small break in the separator, forcing the internal short circuit to occur. Mechanical abuse tests of the Li-ion cells include also dropping and crushing. Crush and impact tests have also been carried out for cells, modules and packs used in electric vehicles. The test results, safety outcomes and ranking of thermal events are usually based on the USABC tables.

Internal displacement and deformation within a battery during a high rate, constant discharge is shown in [3] taking advantage X-ray computed tomography. No experiments are reported in the literature for investigating in real time the detailed mechanisms of internal cell deformation leading to internal shorts during mechanical deformation tests. The main reasons for the lack of mapping of the kinematic processes of internal mechanical deformation of the battery cells are the destructive nature of the mechanical abuse tests and the difficulties associated with freezing the battery state. Opening the cells after mechanical deformation and peeling each layer to find and expose the origin of failure eliminates much of the in-situ deformation information. For most pouch cells, the original deformation cannot be retained as soon as the applied force is removed because of the combination of the spring back of the jellyroll and the flexibility of the pouch enclosure [4].

## Tested Battery

The battery used in this work is a small lithium-polymer (LiPo) pouch cell with a nominal voltage of 3.7 V and nominal capacity of 100 mAh (Fig. 19.2a). The thickness of the battery is 7 mm, with a width of 17 mm and a length of 24 mm.

The layered structure of the battery is shown in Fig. 19.2b. The entire battery includes 30 anode-cathode pairs, divided into alternate layers of aluminum and copper, sandwiched by the active material; layers are stacked one on top of the other, than wrapped in spiral. The separator layers are introduced between the anode and cathodes to prevent short circuits, permitting the lithium ions transfer at the same time. The active material is a slurry made of a polymer gel and graphite. We measured the thickness of each layer with a microscope: the aluminum has a thickness of 0.055 mm and the copper has a thickness of 0.045 mm. The active layers have a thickness of 0.030 mm, and are separated by a 8  $\mu\text{m}$  thick polymeric film. These measurements were repeated over a number of whole batteries, specially cut to this purpose, and resulted reasonably consistent.

Two types of crushing tests were performed in this work: the first type consists in crushing a battery, previously cut, by means of semi-cylindrical punch of 6 mm diameter, as shown in Fig. 19.3; in this way, it is possible to observe the deformation in real time during the test, but the short circuit event cannot be captured. The second type consists in crushing a whole, fully-operative, battery by means of a spherical indenter of 6.35 mm diameter, as shown in Fig. 19.4; in this way it is possible to determine the instant of the short cut, but the internal deformation of the battery can be assessed only by a post-mortem analysis with a microscope.

For the former test type, the battery was first wrapped with an aluminum foil, which helped to keep the layers together during the cutting operation. The created aluminum casing was fixed with epoxy glue, then left to dry for at least 24 h after application.

**Fig. 19.2** (a) Battery used in the test, (b) layered structure

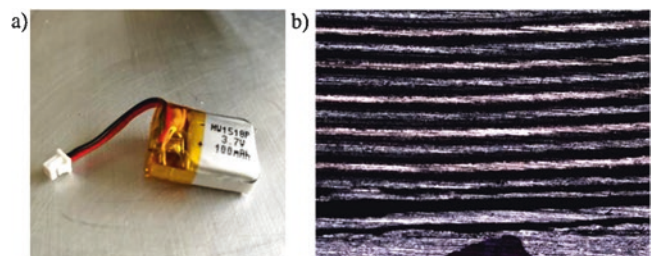


**Fig. 19.3** Crush test of a sectioned battery by a semi-cylindrical punch



**Fig. 19.4** Crush test of a whole battery by a semi-spherical punch



Then, the battery was cut in the front and back, polished with the polishing machine, and left to rest for a week, so that all the active materials can dry completely; this was done to prevent the active semi-solid to squeeze out of the specimen during the test, which would be very harmful for image acquisition. Once the battery is ready, a speckle pattern is created on one lateral face by spraying a thin white paint followed by a dispersion of graphite particles extracted from a laser toner cartridge.

The compression was applied by means of a servo-hydraulic machine (MTS® 858) imposing a displacement speed of 0.15 mm/min. Pictures of the lateral surface of the battery were acquired by a digital camera, storing two frames per second. The camera was equipped with a telecentric lens with in-line illumination and 6X magnification. The field of view was about

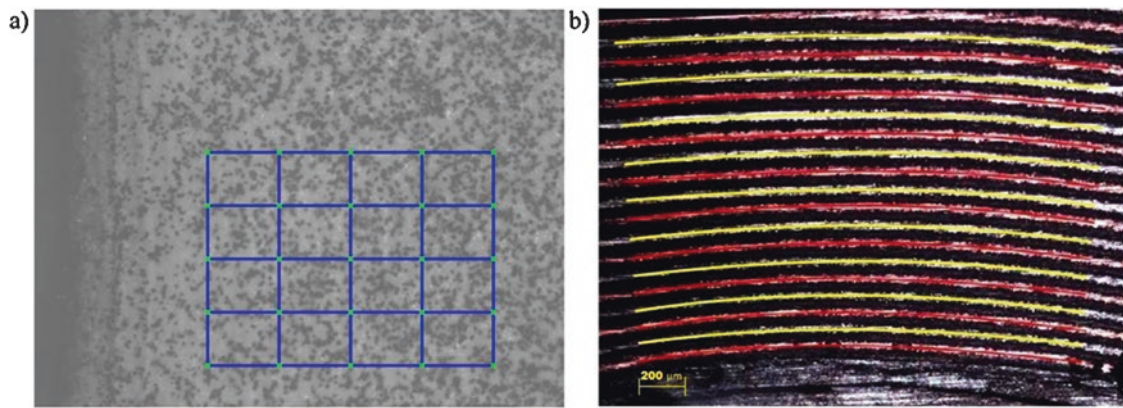


**Fig. 19.5** Pictures acquired (a) during the test by the digital camera and (b) after the test by the microscope

1.5 × 1.2 mm, with a sensor resolution of 1920 × 1440. This optical system was mounted onto high-precision linear stages in order to adjust the image focusing at the beginning as well as during the test. A picture of the undeformed battery, with the DIC subsets grid superimposed, is shown in Fig. 19.5a; each subset encompasses approximately two cathode-anode layer repetitions. The punch (not shown) is on the left.

For the second test type, a relatively thick (0.6 mm) aluminum foil was again used to wrap around the cell in order to help maintaining and freeze the internal mechanical deformation after load removal. The test was conducted by the servo-hydraulic machine imposing a speed of 0.3 mm/min; at this time, the voltage was measured in real time by a digital multimeter, with a significant voltage drop representing the onset of internal short circuit. The deformed cells were cut through the center of indentation by using a diamond blade cutter. These cells were polished using polishing machine and the cross-sectional area were then imaged using optical microscope with a magnification of 5×. An example of picture obtained with a deformed sample is shown in Fig. 19.5b (the punch is at the bottom) together with spline curves that interpolate at best the centerlines of copper and aluminum layers. These interpolating lines have been used to compute the distance between the different layers after the test. In order to estimate the internal strain with this technique, the distance between the metallic layers was also measured by cutting and observing undeformed batteries.

## Experimental Results

Figures 19.6 show the results achieved in the first type of crushing experiment, where the strain was measured by DIC on the lateral surface of the battery. This technique has the advantage to measure the local strain during the deformation process, but the surface preparation prevented from distinguishing the different layers. In the strain distribution contour map (Fig. 19.6a), the punch is on the left, immediately out of the image border. It is noted that the average axial logarithmic strain in the computed zone is about  $-0.35$ , with a maximum value of  $-0.42$  which is achieved in the inner part rather than in the punch-battery contact area. Figure 19.6b shows the load-displacement curve recorded by the testing machine. The red dot corresponds to the instant of the strain result give in Fig. 19.6a; the deformation was 2 mm out of 7 mm thickness of the battery, corresponding to an average logarithmic strain of  $-0.33$ . The test was stopped at 3 mm of crushing, where the curve became nearly horizontal, which is likely to represent to a severe internal damage.

The results of the second type of crushing test, which used the semi-spherical indenter on a whole battery, are shown in Fig. 19.7. The strain contour map, obtained from the post-mortem analysis of the microscope image, shows a strain concentration close to the punch (on the bottom) with a maximum compressive value of  $-0.43$  (Fig. 19.7a). In this test, the machine was stopped after 2.75 displacement, slightly after the occurrence of short circuit, as shown in Fig. 19.7b.

Observing the Fig. 19.7b, it is also noted that a first voltage drop occurred at 2.1 mm displacement, whereas the complete voltage drop, corresponding to the short cut, occurred at about 2.4 mm displacement. This final event is attributed to the failure of the separator film, which is highlighted by the red circle in the enlargement given in Fig. 19.8.



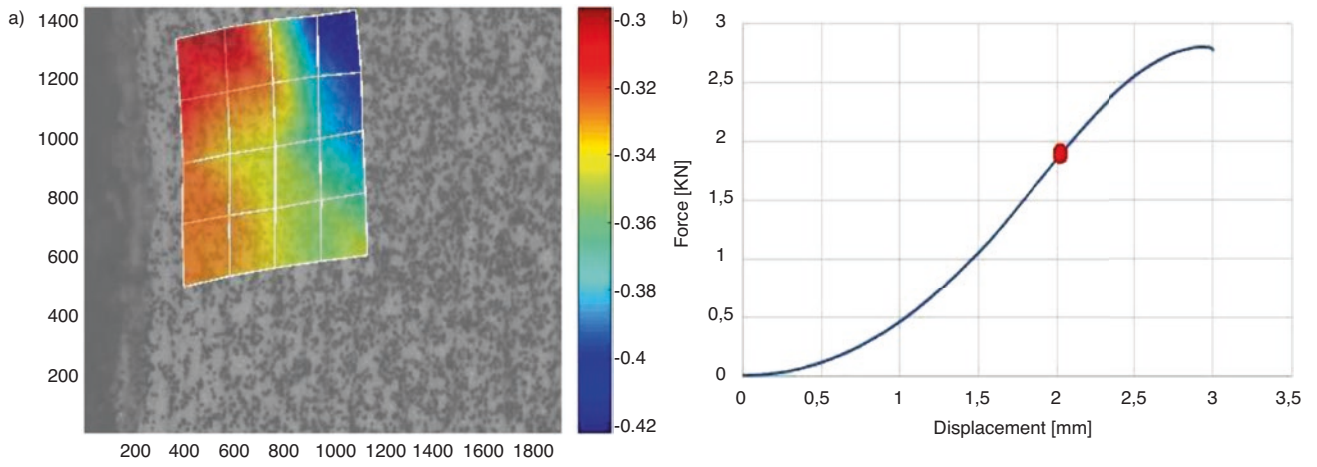


**Fig. 19.6** Results from the crush test with the semi-cylindrical punch, (a) local strain distribution, (b) machine load-displacement curve

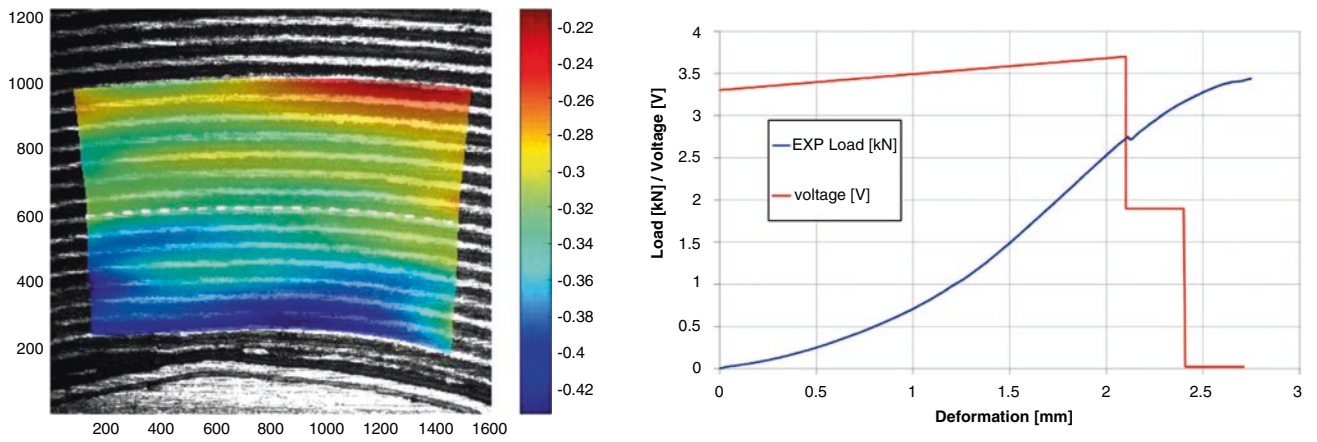
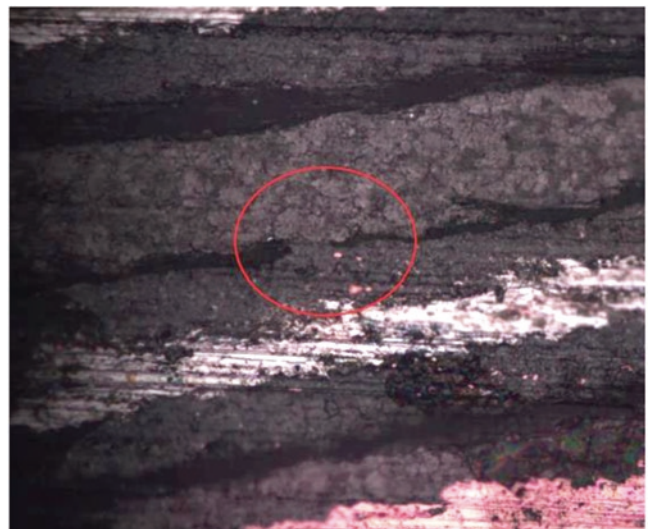


**Fig. 19.7** Results from the crush test with the semi-spherical indenter, (a) local strain distribution, (b) machine load-displacement curve

**Fig. 19.8** Picture obtained with microscope at 50x



## Conclusion

In the paper, two types of crushing tests of LiPo batteries are shown: in the first test, a semi-cylindrical punch crushed a battery previously cut while a digital camera, equipped with a high-magnification telecentric lens, recorded images of the lateral surfaces of the sample; in the second test, a whole fully-operative battery was crushed by a semi-spherical punch while a digital multimeter acquired the voltage at the battery's electrodes in real time. In situ DIC analysis in the former test type, and post-mortem microscopy analysis for the latter test type, permitted to evaluate the internal deformation suffered by the battery. Even if the test geometries are not identical, the two methods provided similar strain level estimation, i.e. 0.3–0.4 compressive logarithmic strain, in the layers close to the punch contact area.

## References

1. E. Sahraei, E. Bosco, B. Dixo, B. Lai, Microscale failure mechanisms leading to internal short circuit in li-ion batteries under complex loading scenarios. *J. Power Sources* **319**, 56–65 (2016)
2. V. Ruiz, A. Pfranga, A. Kristona, N. Omar, P. Van den Bossche, L. Boon-Brett, A review of international abuse testing standards and regulations for lithium ion batteries in electric and hybrid electric vehicles. *Renew. Sust. Energ. Rev.* **81**(1), 1427–1452 (2018)
3. D.P. Finegan, E. Tudisco, M. Scheel, J.B. Robinson, O.O. Taiwo, D.S. Eastwood, P.D. Lee, M. Di Michiel, B. Bay, S.A. Hall, G. Hinds, D.J.L. Brett, P.R. Shearing, Quantifying bulk electrode strain and material displacement within Lithium batteries via high-speed operando tomography and digital volume correlation. *Adv. Sci.* **3**, 1500332 (2016)
4. H. Wang, S. Simunovic, H. Maleki, J.N. Howard, J.A. Hallmark, Internal configuration of prismatic lithium-ion cells at the onset of mechanically induced short circuit. *J. Power Sources* **306**, 424–430 (2016)



## Chapter 20

# In-situ Thermal Monitoring of Printed Components During Rapid Prototyping by Fused Deposition Modeling

K. Pooladvand, A. D. Salerni, and C. Furlong

**Abstract** Full-field-of-view thermography is necessary to effectively monitor and control thermally driven 3D printing processes, such as Fused Deposition Modeling (FDM). The accuracy of thermographic measurements with Infrared (IR) imagers is influenced by the exact knowledge of the emissivity and absorptivity of a given material which varies depending on temperature and color. However, these material properties for ABS, one of the most widely used polymers, still need further investigation. In this paper, we present our efforts to estimate the emissivity of three differently colored ABS polymers between 40 °C and 200 °C. This range of temperatures is critical to the bond formation and welding of the polymer, which eventually defines the mechanical strength of the printed components. Using a calibrated IR imager and thermocouples, we measured the emissivity of different ABS polymeric rings at various temperatures. These measurements are based on the comparison between equivalent emissive power at measured temperatures and the measured emissions from a calibrated blackbody. This allows for the determination of subtle changes in emissivity of the ABS polymer. The estimated emissivity is mapped to correct the full-field temperature readout of the IR imager in-situ and help to accurately monitor the thermal flow. Verification was carried out based on numerical simulations to investigate several slender square blocks (e.g., 3, 7, 11 mm). The emissivity obtained by this method shows improvements in measuring accuracy. Further, our study shows that the emissivity decreases from 0.92 to 0.79 with a slower rate around the glass transition points. This 14% drop in emissivity corresponds to a difference of 36 °C at the readout temperature of 240 °C. Our results also indicate that the emissive heat flux of ABS is dependent on color. The experimentally estimated emissivity can be used in other IR cameras to correctly evaluate the temperature and monitor the thermal flow in real-time. This enables better optimization of the printing parameters to improve the bonding and strength of printed components.

**Keywords** 3D printing · ABS polymers emissivity · Fused deposition modeling (FDM) · IR imaging

## Introduction

Applying real-time monitoring and closed-loop control to Additive Manufacturing (AM) processes can improve component performance and quality while reducing the occurrence of defects [1–4]. With this promising advancement, printing processes are actively controlled, while sensors monitor the critical parameters such as distortion, strain, pool size, heat affected zones, and temperature in-situ. The practical approaches for monitoring include optical (visual or thermal), acoustic, and contact methods [2, 5]. Optical methods offer versatile, non-contact, and full-field sensors with proper spatial and temporal resolutions to measure parameters such as temperature, shape, and distortion [5, 6]. Because 3D printing is a thermally driven process, temperature is one of the essential parameters to monitor in AM processes. Thermal energy flow and dissipation during fabrication affect the physical and mechanical properties of printed components [7–12]. Thus, thermal measurements become an indispensable tool for monitoring 3D printing technologies.

---

K. Pooladvand (✉) · C. Furlong

Center for Holographic Studies and Laser micro-mechaTronics – CHSLT, Worcester Polytechnic Institute, Worcester, MA, USA

Mechanical Engineering Department, Worcester Polytechnic Institute, Worcester, MA, USA

e-mail: [kpooladvand@wpi.edu](mailto:kpooladvand@wpi.edu); [cfurlong@wpi.edu](mailto:cfurlong@wpi.edu)

A. D. Salerni

Center for Holographic Studies and Laser micro-mechaTronics – CHSLT, Worcester Polytechnic Institute, Worcester, MA, USA

Chemical Engineering Department, Worcester Polytechnic Institute, Worcester, MA, USA

e-mail: [asalerni72@wpi.edu](mailto:asalerni72@wpi.edu)

Thermocouples have been conventionally used for accurately measuring the temperature at specific points of interest [10, 13]. On the other hand, thermography offers full-field-of-view, non-contact, and non-invasive measurements. These superior capabilities make thermography one of the most widely used sensors in monitoring and closed-loop control systems in AM technologies [2, 3, 5, 7]. However, the thermal measurement can only measure surface temperature and is very sensitive to environmental fluctuations. Another issue is that accurate measurement requires a reliable understanding of the material properties such as emissivity and absorptivity [14–16].

Infrared (IR) cameras show promising potentials in Fused Deposition Modeling (FDM) processes. Costa et al. [12], Pooladvand and Furlong [7], and Seppala and Migler [17] have used IR cameras to estimate the material, and process properties of different 3D printed objects. In this paper, we presented our efforts to employ an IR camera in-situ to monitor the temperature in an FDM printer. We improved the accuracy of remote temperature measurements by proposing a methodology to estimate the optical properties of Acrylonitrile Butadiene Styrene (ABS) and applied it to correct imager readout in real-time.

## Methodology

### General Plan and Scheme of This Study

Our research combines experimental and computational approaches. In the experimental approach, the emissivity of ABS polymer was obtained empirically. We compared the responses of an IR imager from a calibrated blackbody, and ABS printed washers at different temperatures to estimate the emissivity. We curve fitted the data and used an algorithm to spatially-temporally correct temperature readouts, and map corrected temperature distribution onto specimens during manufacturing.

We also simulated a transient 1D layer-upon-layer deposition using finite difference analysis. In this simulation, boundary conditions are corrected based on the estimated convection coefficient, estimated emissivity, and the Total Heat Transfer Coefficient (THTC). The details of this numerical solution are explained here [7, 18–20]. The corrected temperature readouts were compared with our simulations. The final results illustrate how this algorithm can be used to account for the difference in emissivity and help to improve the thermal readout as a primary monitoring tool in the next generation of smart 3D printing machines.

### Thermography and Infrared Camera

The radiation heat flux depends on direction, wavelength, and temperature. For most engineering materials, one can assume the directional variation is negligible in order to define heat flux in terms of wavelength and temperature, which is known as Planck's law [21, 22].

Infrared (IR) cameras are devices that receive emitted energy from an object of interest and convert them into images. The color and contrast in these images are based on the amount of energy received. The sum of the absorption, reflection, and transmission of radiative energy from each surface is equal to the total incident radiative flux. The IR cameras' detectors measure radiosity, which is a sum of reflection and emission from a particular surface. In addition, the emissivity and transitivity of the media between the source and the detector affect the temperature measurements. In theory, the total received energy contains emission from the object, reflection of other sources, losses due to transmission through and emission of the media [16]. For an object located in the atmosphere, the total energy received by the camera detector is defined as:

$$E_{tot} = \varepsilon_{obj} \cdot \tau_{atm} \cdot E_{obj} + \rho_{obj} \cdot \tau_{atm} \cdot E_{sur} + \varepsilon_{atm} \cdot E_{atm}. \quad (20.1)$$

where,  $E$  is radiation flux,  $\tau$  transitivity,  $\rho$  reflectivity, and  $\varepsilon$  emissivity and subscripts *tot*, *obj*, *atm*, and *sur* denote total, object, atmosphere, and surrounding, respectively. Kirchhoff theory states for each surface the absorptivity,  $\alpha$ , is equal to emissivity,  $\varepsilon$ , in its equilibrium condition [21, 22]. In addition, one can conclude  $\rho_{obj} = 1 - \alpha_{obj}$  for opaque surfaces. The atmosphere also is a transparent medium thus,  $\varepsilon_{atm} = 1 - \tau_{atm}$ . Finally, the Eq. (20.1) is rewritten as:

$$E_{tot} = \varepsilon_{obj} \cdot \tau_{atm} \cdot E_{obj} + (1 - \varepsilon_{obj}) \cdot \tau_{atm} \cdot E_{sur} + (1 - \tau_{atm}) \cdot E_{atm}. \quad (20.2)$$

When the distance between detector and source is less than a meter, the effect of media can be ignored [16], and therefore  $\tau_{\text{atm}}$  is equal to 1.0 and Eq. (20.2) is simplified to:

$$E_{\text{tot}} = \varepsilon_{\text{obj}} \cdot E_{\text{obj}} + (1 - \varepsilon_{\text{obj}}) \cdot E_{\text{sur}}. \quad (20.3)$$

The camera detector receives  $E_{\text{tot}}$  and uses the integrated look-up table to determine the temperature by knowing the emissivity, humidity, and distance. However, if these parameters are not defined correctly, the IR imager generally assumes the case of a blackbody object, and estimates the temperature accordingly. This process leads to an incorrect estimation of the temperature and undervalues the readouts [15, 16]. By knowing the  $\varepsilon$ , these inaccurate readouts can be corrected either during or after recording the measurements.

## Thermal Modeling

Thermal flow in 3D printing has transient three-dimensional physics defined by Furrier law. However, this condition can be simplified to a one-dimensional framework assuming a lumped capacity criterion to estimate the temperature along a length of a slender cylinder or block [7, 8]. In this case, ascribing the only heat source as the advection of the newly deposited material from the extruder, the partial differential equation is obtained as:

$$\frac{\partial \rho u}{\partial t} = \frac{\partial}{\partial z} \left( \kappa \frac{\partial T}{\partial z} \right) + q_s, \quad (20.4)$$

where,  $t$  is time,  $u$  is internal energy,  $\rho$  is mass density,  $\kappa$  is the conductivity,  $T$  is temperature,  $q_s$  is the heat source or sink, and  $z$  is the normal to the cross-section. The heat sink is also defined as the sum of convection and radiation heat transfer ( $q_s = q_{\text{conv}} + q_{\text{radi}}$ ). Equation 20.4 can be simplified by assuming constant area, average deposition velocity along  $z$  direction, and enthalpy formulation ( $du = dh = c_p dT$ ):

$$\rho U c_p \frac{\partial T}{\partial z} = \kappa \left( \frac{\partial^2 T}{\partial z^2} \right) - \frac{4h_t}{d} (T - T_\infty), \quad (20.5)$$

where,  $U$  is average deposition velocity,  $T$  and  $T_\infty$  are the surfaces and environment-wall temperatures, respectively,  $d$  is a diameter or side of the cross-section, and  $h_t$  is THTC. THTC, which is found experimentally, contains both radiation and convection heat transfers. The process that led to estimating the  $h_t$  is explained in our previous work [7].

## Experimental Set-up and Equipment

In our experimental measurements, we wanted to achieve three main goals: calibrating the IR camera, measuring the emissivity of three differently colored ABS polymer, and finally implementing gained knowledge to approximate the surface temperature in-situ. We designed our set up using an IR camera, type-T thermocouple, aluminum block, hot plate, calibrated blackbody, manual thermometer, aluminum tape, computer platform, high-efficiency thermal paste, and home-made cooling accessories as shown in Fig. 20.1.

The IR camera was situated above the hot plate looking to the center of the aluminum block on the hot plate (Fig. 20.1a). In addition, a home-made cooling apparatus consisting of a PVC pipe and a computer fan was utilized above the aluminum block to minimize the effects of the medium, the graphic of this configuration is shown in Fig. 20.1b. The type-T thermocouple installed between the aluminum block and the aluminum adhesive tape as shown in Fig. 20.1c, and it was connected to the DAQ using LabView to record the temperature continuously. The calibrated blackbody and the computer platform is used to determine the sensitivity of the IR camera (Fig. 20.1d).

In order to provide a stable condition, a block of aluminum with  $76.03 \times 121.68 \times 37.70$  mm as shown in Fig. 20.1a, b were located on the hot plate. The top surface of the block was covered with adhesive reflective aluminum tape where the washers were positioned (Fig. 20.1c). Between the adhesive tape and aluminum block, a thermocouple was fixed and situated at the center of the block. A highly conductive thermal paste also covered the distance between the aluminum tape and the washer to guarantee the steady and constant thermal flux between two dissimilar materials and fill all the possible void areas between them.

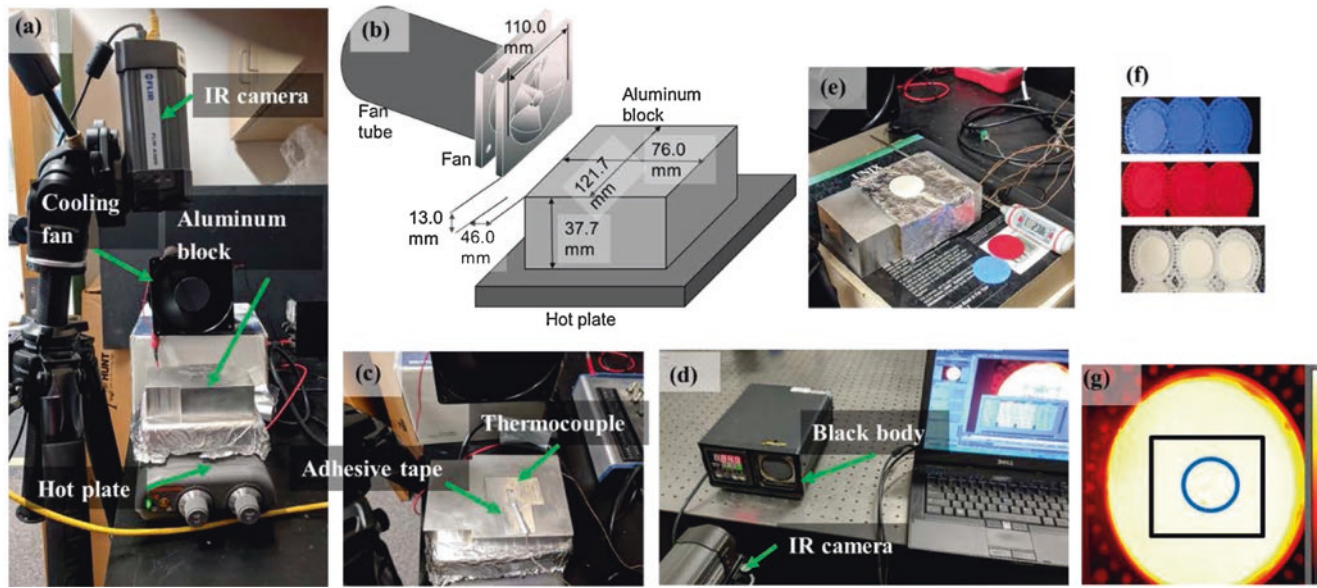


**Fig. 20.1** The configuration of the setup and equipment were used for camera calibration, emissivity estimation, and temperature measurements: (a) IR camera, hot plate, and aluminum block; (b) cooling apparatus; (c) thermocouple installed between the aluminum block and the aluminum adhesive tape; (d) calibrated blackbody and the computer platform; (e) thermometer and the ABS washers; (f) the 3D printed washers consist of three sets of differently colored ABS polymers; and (g) a snapshot of the blackbody captured by the IR camera showing the Area Of Interests

## Results and Discussion

### *IR Camera Calibration and Analysis*

We used a calibrated blackbody to estimate the IR camera's response curve. Assuming the emissivity is 1.0 and the distance between the camera and the blackbody is about 200 mm, the transmissivity of the air is equal to 1.0. Therefore, the total energy received by the detector is equal to the emissive radiation from the surface of the blackbody:

$$E_{tot} = E_{obj} = E_{blackbody}. \quad (20.6)$$

We used a Microbolometer IR camera with a wide spectrum sensitivity in mid-infrared regions (7–18  $\mu\text{m}$ ) [20, 21], and defined the following function to represent the relationship between the camera readout and temperature, knowing that the blackbody total emissive flux follows a power function in a wide spectral range:

$$\text{readout}(T) = aT^b + c \quad (20.7)$$

The initial step was the calibration of the thermal imager under a similar environment to where the rest of the measurements were performed. Figure 20.1d shows such a setup consisted of an IR camera, computer platform, and calibrated blackbody. The temperature of the blackbody changed from 45 to 345  $^{\circ}\text{C}$  in 13 steps both ascending and descending in addition to recording room temperatures. The measurement repeated three times in the laboratory while the room temperature and humidity fluctuated between 20–25  $^{\circ}\text{C}$  and 30–45%, respectively.

At each step, the camera recorded thermograms similar to the one shown in Fig. 20.1g and the data associated with the Area Of Interests (AOI) were recorded for further analysis and curve fitting using MATLAB<sup>®</sup>. The curve fitting results show a strong correlation with the coefficient of determination R-square being above 0.99. Figure 20.2 shows the fitted lines and Table 20.1 lists the results of curve fitting. We did the curve fitting for three different cases, assuming the temperature in Kelvin, and degrees centigrade. Comparing the fitted curve with camera's readout in low temperature, particularly close to room temperature showed a better performance from the degree  $^{\circ}\text{C}$  fitted curve.

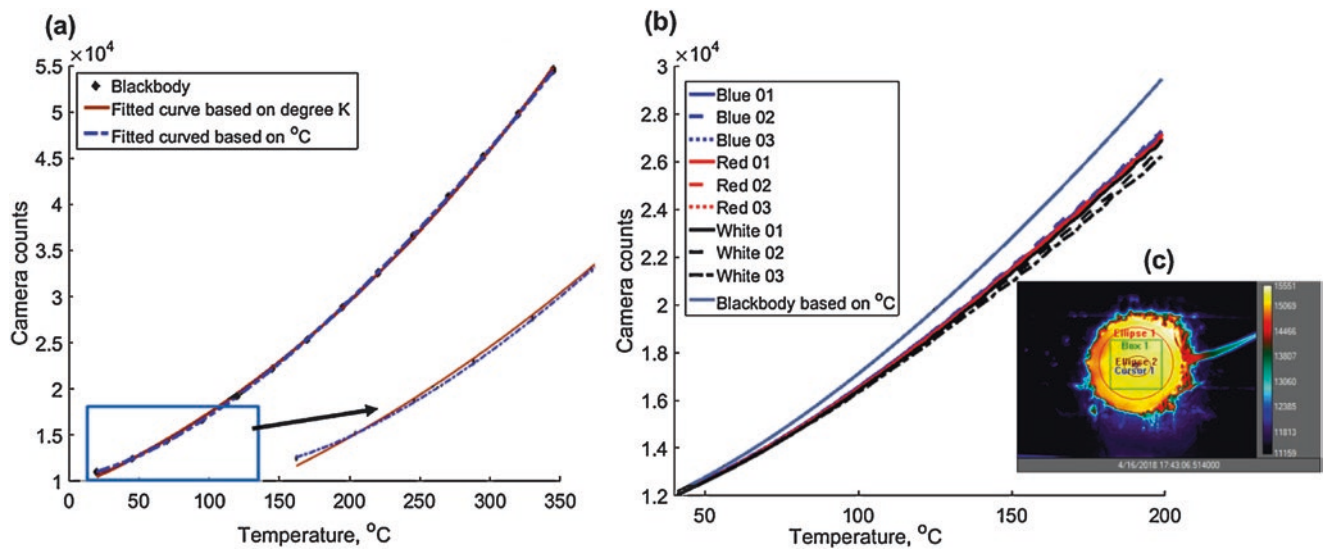


**Fig. 20.2** The acquired data for blackbody and washers along with the fitted curve and snapshot of the IR camera: (a) three measurements of the blackbody with temperature ranging between 25 and 345  $^{\circ}\text{C}$  with the curved fitting based on K and  $^{\circ}\text{C}$ ; (b) the response curve of the blackbody juxtaposed with the nine measurements on the washers with temperatures ranging between 45 and 200  $^{\circ}\text{C}$ ; and (c) a representative snapshot of the IR camera showing the different AOIs used for analyses

**Table 20.1** The derived coefficient and a few statistical information of curve fitting for the rectangular and ellipsoidal AOIs used for estimating the response curves to blackbody radiation

Description	Based on Kelvin	Based on Kelvin assuming $c = 0$	Based on $^{\circ}\text{C}$
Coefficients, a	0.008596	0.02272	5.869
Coefficients, b	2.432	2.286	1.527
Coefficients, c	1899.697	0	10464.94
R-square	0.9997	0.9998	0.9999
Root-mean-square error (RMSE)	240.0865	184.8451	61.1491

After measuring the camera's response curves, we then estimated the emissivity of the 3D printed ABS washers similar to those shown in Fig. 20.1f. We printed nine washers with a thickness of  $0.8 \pm 0.1$  mm and a diameter of  $30.0 \pm 0.5$  mm in three different colors and tested them with the same condition and setup. The aluminum block heated up until its top surface reached 240  $^{\circ}\text{C}$ , after which the washers were carefully situated at the center, where they made contact with the thermocouple. The thermal paste was carefully spread across the area beforehand, and a small aluminum roller was used to ensure the washers were firmly attached.

After about 5 min, the system reached a steady state, at which point the hot plate turned off and measurements started. The DAQ and the LabView<sup>®</sup> program acquired the temperatures with the data acquisition rate of 1MBs. An interface was designed to calculate the average, and standard deviation of the 10,000 subsequent acquired points and store them as a text file. In addition, the IR camera located right above the hot plate at a distance about 200 mm captured the thermograms as well. The Cold Junction (CJ) was set based on the room temperature, which was monitored continuously using a thermometer and the required changes were applied to CJ as needed. The room temperature fluctuated between 18 and 21  $^{\circ}\text{C}$  during different measurements. The humidity also monitored which was always seen as less than 40% during all measurements, though there was no significant effect on the total measurements due to the short distance between the camera and target surface.

Images and temperatures were stored and later used in Matlab for data analysis and curve fitting. The clock of the DAQ and the camera was used for matching the temporally stored data. Knowing the blackbody response at the specific temperature allowed us to measure the emissivity using Eq. (20.3) by estimating  $E_{\text{obj}}$  at the corresponding temperatures, and the IR camera's readout  $E_{\text{tot}}$ . In this equation  $E_{\text{sur}}$  was plugged in based on the room temperature measurements.

As shown in Fig. 20.2c, a few different AOIs were defined on the washer. The curve fitting and analysis were based on the data within the area of "Ellipse 2", which consisted of 732 pixels, and the comparisons among different AOIs did not show any significant differences. The total irradiances off the surface of the washers were measured in camera counts. Figure 20.2a illustrates the total readout counts of the IR camera, while Fig. 20.2b shows the fitted curves for a blackbody and three sets of measurements for white, blue, and red ABS washers. The difference between a blackbody and the ABS washers readout increases as the temperature increases, which indicates that at higher temperatures the emissivity of the ABS decreases. In general, all three different colors show relatively similar trends. Although, white ABS seems less emissive compared to that of blue and red. The difference between the latter two is negligible.

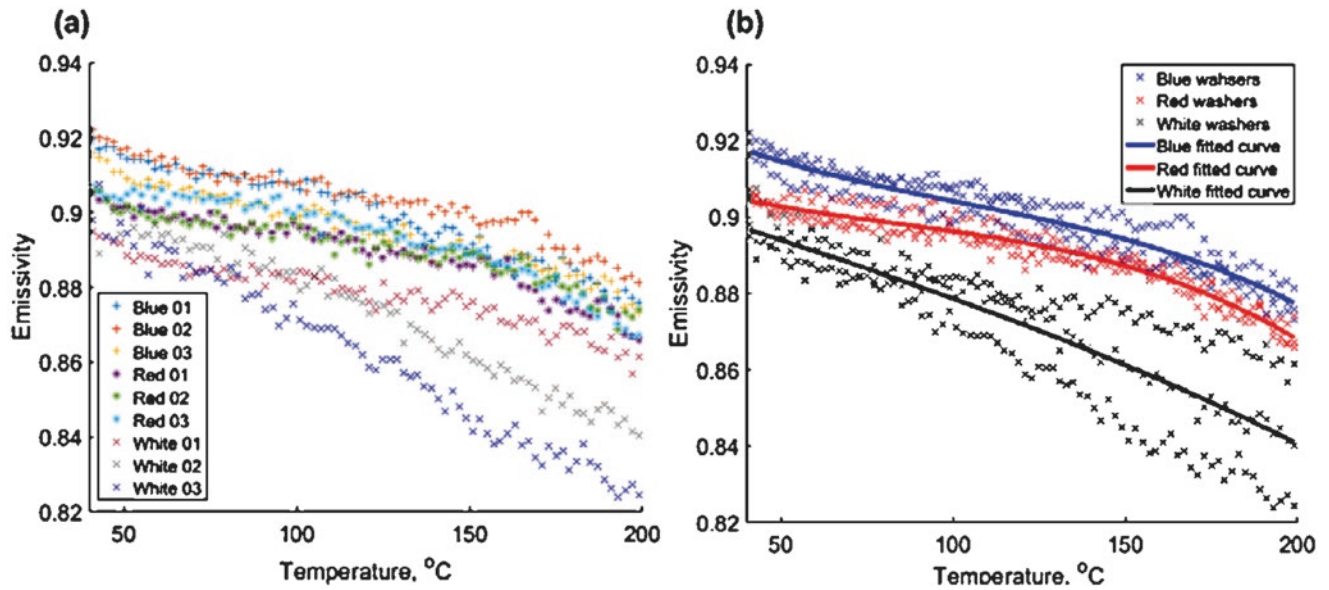


**Fig. 20.3** The estimated emissivity based on the gathered data and fitted curves: (a) scatter plot shows the determined emissivity values of the nine different washers indicating a similarity in trends and effects of the colors; and (b) the entire pool of data for all measurements and the polynomial fitted curve showing the trends and the estimated values

**Table 20.2** Curve fitting coefficient and a few statistical information on curve fitting for the entire obtained points for three different colored washers

Description	Blue washers	Red washers	White washers
Coefficient, a	$-9.916 \times 10^{-9}$	$-1.022 \times 10^{-8}$	$-1.487 \times 10^{-9}$
Coefficient, b	$1.118 \times 10^{-5}$	$1.093 \times 10^{-5}$	$1.252 \times 10^{-6}$
Coefficient, c	-0.00438	-0.004019	-0.0006367
Coefficient, d	1.497	1.405	1.019
R-square	0.8642	0.9199	0.7145
Root-mean-square error (RMSE)	0.0042	0.0028	0.100

The emissivity of these nine samples are determined and shown in Fig. 20.3a. The emissivity, in general, follows a decreasing trend as temperature increases which is similar to the behavior in other materials such as Aluminum. The maximum measured emissivity in room temperature was approximately 0.92, which is less than 0.95, the reported value for polymers at room temperature. The emissivity drops to 0.82 as temperature ascends to 200 °C for white ABS.

Figure 20.3b also illustrates all the measured points of the samples for each color, and the solid line is the fitted curve based on the entire poll of data for the same colors. A polynomial of degree 3 ( $a \times x^3 + b \times x^2 + c \times x + d$ ) was used for the curve fitting.

Table 20.2 lists the coefficients of the polynomial along with some statistical values. The coefficient of determination is above 0.71 for white washers and above 0.86 for red and blue, which indicates a strong correlation between temperature and emissivity. These curves indicate that the difference between blue and red washers decreases as temperature increases. This data also shows that the emissivity of white washers is lower and decreases more dramatically compared to the two others. The curve fitting also exhibits a slowing slope in temperatures between 110 and 130 °C, which is attributed to the glass transition temperature of the ABS polymer.

### *Estimation of the Temperature Distribution Using the Estimated Emissivity in IR Camera*

We printed three different ABS blocks with square cross-sections of 3, 7, and 11 mm while changing two critical printing parameters, printing speed and extruder temperature.

The first experiment was performed on a cube of 3 × 3 mm with a speed of 2000 mm/min (Low) at a temperature of 290 °C (High). The second one carried out on a cube with 7 × 7 mm, with a speed of 4000 mm/min (medium), and a temperature of 265 °C (medium), and the last cube with dimensions of 11 × 11 mm, at a speed of 6000 mm/min (High) and



a temperature of 240 °C (low). By analyzing the captured thermograms, the average deposition velocities in  $z$ -direction were calculated as 15.97, 4.66, and 2.42 mm/min for 3, 7, and 11 mm cubes, respectively. Table 20.3 indicated a few parameters along with other critical information considered for modeling.

The IR camera was installed in front of the FDM machine in a slightly inclined direction but perpendicular to the specimen at the center of the machine. The machine front door was open, and the room temperature and chamber temperature were monitored regularly. The schematic of the camera is shown in Fig. 20.4a. The printing processes were captured with a frame rate of 2 Hz from beginning to a few seconds following the completion of the specimens.

The IR camera captured the process of manufacturing three cubes printed with white ABS filament. The entire process was captured for all three cubes; however, two critical instances, halfway and completion of the printing process for the blocks of 7 and 11 mm, are demonstrated in Fig. 20.5. We wrote an algorithm to correct the IR camera's temperature measurements in-situ. The first column of images in Fig. 20.5a is the initially reported temperatures, the second column are the corrected temperatures based on emissivity, and the last column shows the temperature difference between the corrected and reported values. We used the correlation found for the white ABS polymer to account for the effect of emissivity on temperature measurements. These effects were more pronounced at higher temperatures with a maximum error of 15% in areas with temperatures above 240 °C.

**Table 20.3** Part physical, geometries, and manufacturing parameters considered in this study

Length, $L$	$30 \pm 0.19$ mm	Stacking orientation	Rectilinear, longitudinal ( $0^\circ$ )
Width, $w$	3, 7, and $11 \pm 0.5$ mm	Average ideal time	0.25 s
Material	ABS	Layer thickness	0.19 mm
Color	White	Air gap	0
Specific heat, $c_p$	1300 J/kg-K	Average bulk temperature $T_\infty^a$	35 °C
Density, $\rho$	$948 \pm 5$ kg/cm <sup>3b</sup>	Raft	Yes
Conductivity, $\kappa$	0.16–0.15 W/m-K	Heated-bed temperature $T_b$	70 °C
Polymer-heated bed thermal contact coefficient	4800 W/m <sup>2</sup> K	Bead width	0.40 mm
Coefficient of heat convection for the top layer <sup>c</sup>	3 mm: 90 W/m <sup>2</sup> K 7 mm: 59 W/m <sup>2</sup> K 11 mm: 47 W/m <sup>2</sup> K	Linear deposition velocity for 3D	Low (2000), Medium (4000), and High (6000) (mm/min)
Coefficient of heat convection for other layers <sup>c</sup>	3 mm: 38 W/m <sup>2</sup> K 7 mm: 20 W/m <sup>2</sup> K 11 mm: 7 W/m <sup>2</sup> K	Extruder temperature $T_{\text{Exd}}$	Low (240), Medium (265), and High (290) °C
Printing orientation	Vertical	Cooling	Fan speed 100%

<sup>a</sup>The bulk or envelope temperature was monitored using an analog thermometer and its average calculated accordingly

<sup>b</sup>Density was measured experimentally

<sup>c</sup>The correlation proposed by Churchill [23] is used to estimate the convection coefficient by assuming the velocities of 0.3 and 1.7 m/s for other and top layers, respectively

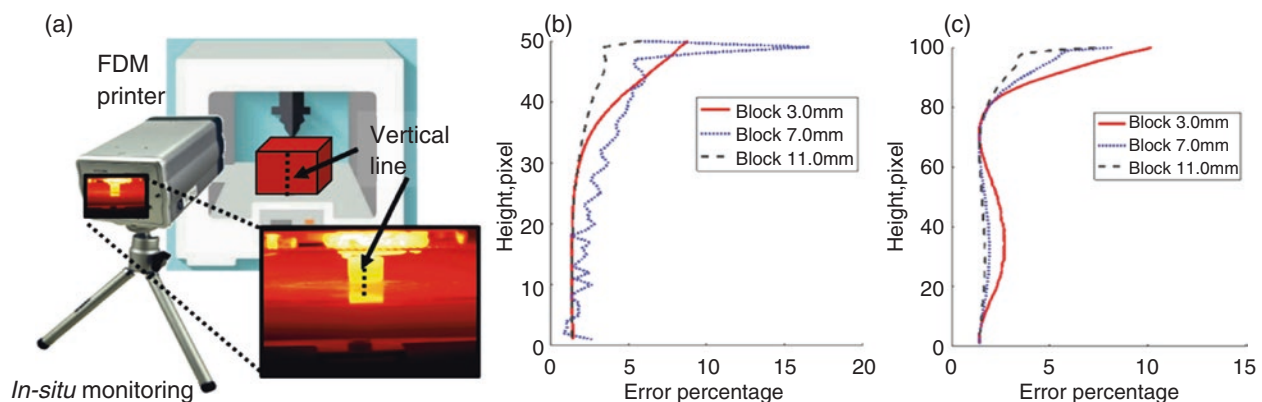


**Fig. 20.4** (a) schematic of the IR camera monitoring fabrication processes in-situ; (b) Error percentage in estimation of the temperature along the height of the blocks of 3, 7, and 11 mm at the halfway point of fabrication; and (c) Error percentage in estimation of the temperature along the height of the block of 3, 7, and 11 mm upon completion of the fabrication process

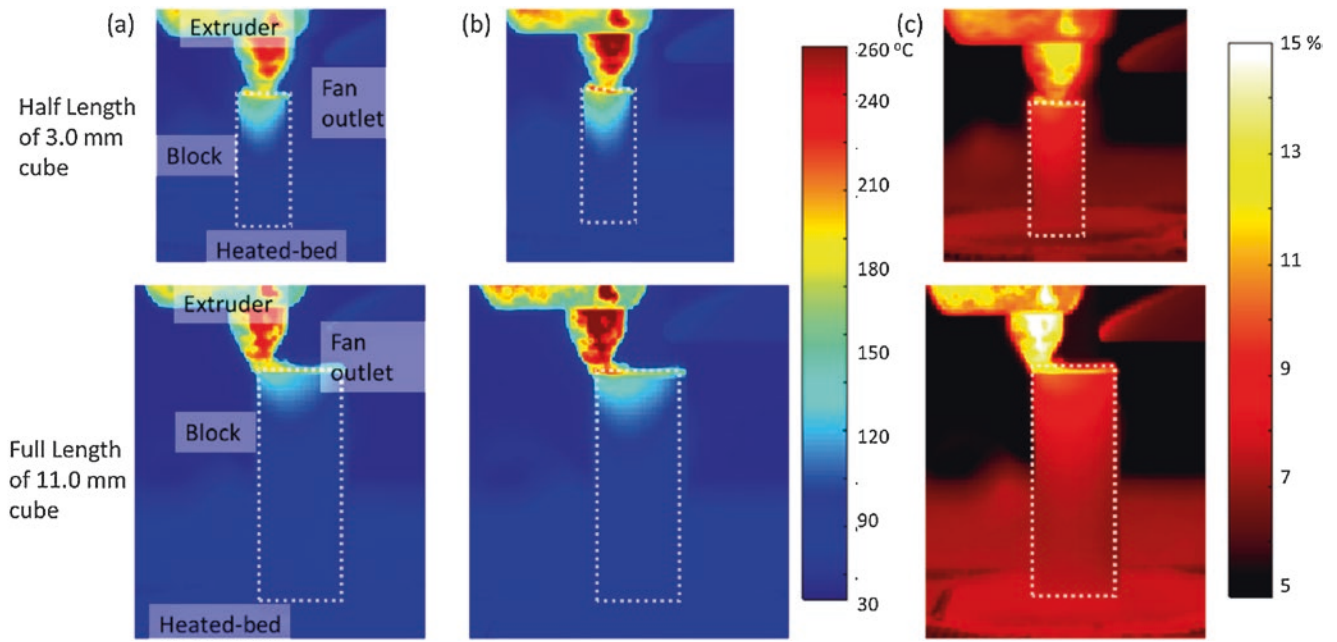


**Fig. 20.5** The first and the second row show the application of the IR camera incorporating the determined emissivity for in-situ temperature measurements at half and full length specimens with 7 and 11 mm, respectively: (a) the original temperature estimated by IR camera; (b) The corrected temperature; and (c) the error percentage

### *Comparison Between Numerical Estimation and IR Measurements*

We developed a simplified 1D simulation to estimate the temperature along the height of three different blocks with the specification mentioned in Table 20.3. The model is based on assuming the lumped capacity for the cross-sections, though this assumption only could be satisfied for the cubical section of  $3 \times 3$  mm. The temperature distribution along the height of these three cases for the half and full length of the blocks are illustrated in Fig. 20.6a, b, respectively.

The results exhibit a strong agreement between the corrected temperature and the estimated temperature for each of the sizes. The maximum difference took place on the top layers of the two larger cubes. This difference can be attributed to the deficiency of a simplified 1D model to capture the dynamics of the deposition or the reflection of the extruder with a higher temperature at the top layers. The corrected temperature, except for the few top layers, are in good agreement with numerical estimation. Looking critically to the numerical model, one can conclude that the lumped capacity model as described here [24] cannot capture the correct temperature distribution and under and overestimates temperature on the lower and top layers, respectively. The temperature distribution on the areas right below the layer of the latest deposited material needs 3-dimensional analyses to be reliably estimated.

### **Conclusions and Future Work**

In this paper, we proposed a methodology for calibration of an IR imager and estimation of the emissivity of ABS polymer using experimental data. The emissivity decreases with increasing temperature and the rates vary around the glass transition temperature of the ABS polymer. The measured emissivity shows the optical properties of ABS also depend on color with darker shades exhibiting a higher emissivity. The emissivity at room temperature is 0.92 which is below the recommended value of 0.95 of ABS commonly used in IR imagers. A script written in Matlab included the camera calibration and obtained emissivities and was incorporated into the IR imager software to correct the temperature measurement in real-time. The results exhibit up to a 15% error in temperatures measurements in temperatures as high as  $240$  °C which translates to  $36$  °C difference between uncorrected and corrected values.

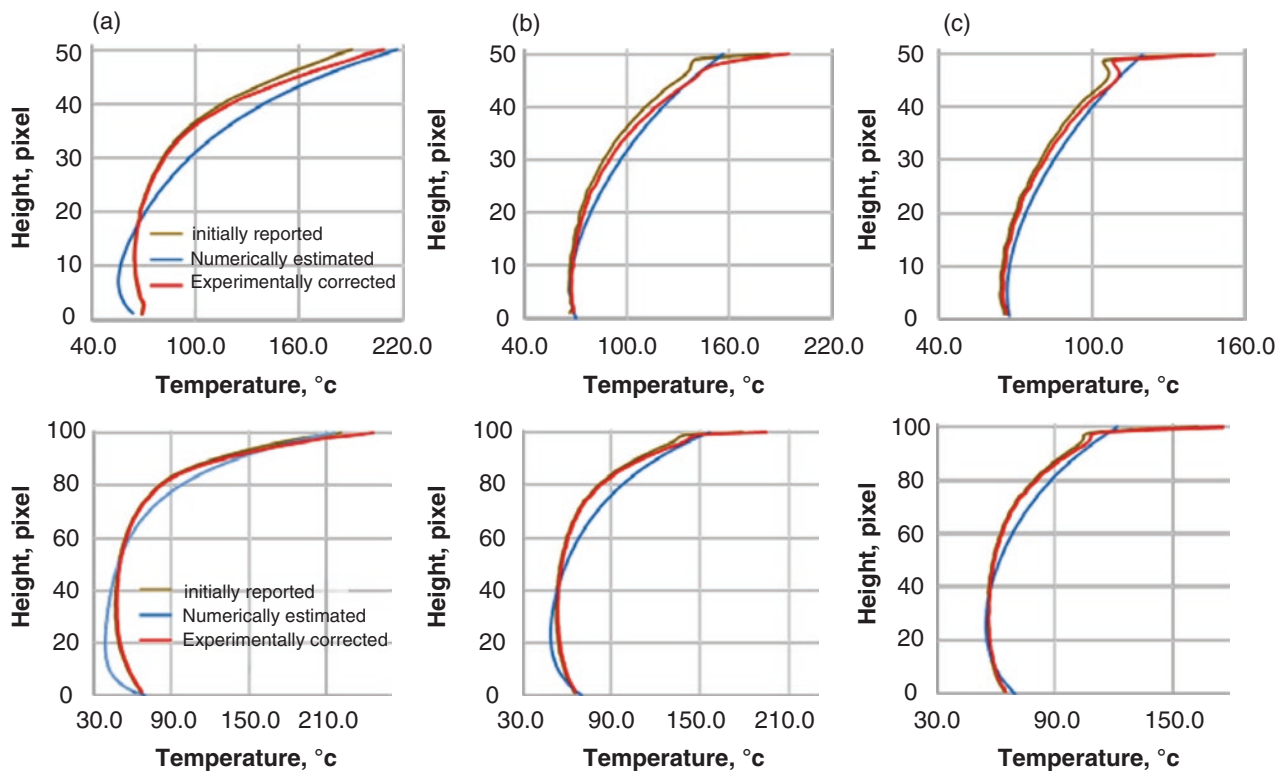


**Fig. 20.6** The comparison between 1D numerical simulations, original, and corrected experimentally measured temperature along the vertical line on the center front-face for the three blocks of sizes 3, 7, and 11 mm at half and full length: (a) 3 mm cube; (b) 7 mm cube; and (c) 11 mm cube

1-D numerical simulations also verified the estimated temperatures, and the results suggest that the corrected temperatures are reliable. The estimated emissivity can be incorporated into other IR imagers monitoring ABS 3D printing processes to account for the dependency on optical material properties for accurate temperature measurements. These corrections help to improve the remote temperature measurements and can be incorporated into future FDM technologies to enable accurate thermal measurements for closed-loop control strategies.

Our results also indicate that the knowledge of the material optical properties is essential for accurate temperature measurements, and failure to incorporate this data leads to erroneous measurements which predict temperatures lower than actual values.

This study exhibits the potential of calibration and numerical modeling in the estimation of accurate thermal measurements during printing which in turn can contribute to the development of a better and more reliable 3D printer in the near future. Although, more investigation is still required to demonstrate the validity of the assumptions made, and the extension of this approach for other polymeric material and metallic 3D printers.

**Acknowledgments** This work has been partially supported by the NSF, award CMMI1428921. The authors would like to gratefully acknowledge the support of the Mechanical Engineering Department of Worcester Polytechnic Institute (WPI) and the contributions by members of the CHSLT.

## References

1. K.D. Migler, R.E. Ricker, Measurement Science Roadmap for Polymer-Based Additive Manufacturing, (*No. Advanced Manufacturing Series (NIST AMS)-100-5*) (2016). <https://www.nist.gov/publications/measurement-science-roadmap-polymer-based-additive-manufacturing>
2. S.K. Everton, M. Hirsch, P. Stravroulakis, R.K. Leach, A.T. Clare, Review of in-situ process monitoring and in-situ metrology for metal additive manufacturing. *Mater. Des.* **95**, 431–445 (2016)
3. R.B. Dinwiddie, L.J. Love, J.C. Rowe, Real-time process monitoring and temperature mapping of a 3D polymer printing process, in *SPIE defense, security, and sensing* (International Society for Optics and Photonics, Bellingham, 2013), p. 87050L
4. C. Kousiatza, D. Karalekas, In-situ monitoring of strain and temperature distributions during fused deposition modeling process. *Mater. Des.* **97**, 400–406 (2016)
5. T. Purtonen, A. Kalliosaari, A.J.P.P. Salminen, Monitoring and adaptive control of laser processes. *Phys. Procedia* **56**, 1218–1231 (2014)
6. K. Pooladvand, C. Furlong, Digital holography and digital image correlation in additive manufacturing, in *ISEM 2015, 5th International Symposium on Experimental Mechanics* (ASEM, Guanajuato, 2015)
7. K. Pooladvand, C. Furlong, Thermo-mechanical investigation of fused deposition modeling by computational and experimental methods, in *Mechanics of Composite and Multi-Functional Materials*, vol. 7 (Springer, Cham, 2017), pp. 45–54
8. K. Pooladvand, C. Furlong, Computational and experimental characterization of 3D printed components by fused deposition modeling, in *Mechanics of Additive and Advanced Manufacturing*, vol. 8 (Springer, Cham, 2019), pp. 87–95
9. N. Shamsaei, A. Yadollahi, L. Bian, S.M. Thompson, An overview of direct laser deposition for additive manufacturing; part II: Mechanical behavior, process parameter optimization and control. *Addit. Manuf.* **8**, 12–35 (2015)
10. Q. Sun, G. Rizvi, C. Bellehumeur, P. Gu, Effect of processing conditions on the bonding quality of FDM polymer filaments. *Rapid Prototyp. J.* **14**(2), 72–80 (2008)
11. M. Griffith, M. Schlienger, L. Harwell, M. Oliver, M. Baldwin, M. Ensz, M. Essien, J. Brooks, C. Robino, e.J. Smugeresky, Understanding thermal behavior in the LENS process. *Mater. Des.* **20**(2), 107–113 (1999)
12. S.F. Costa, F.M. Duarte, J.A. Covas, Estimation of filament temperature and adhesion development in fused deposition techniques. *J. Mater. Process. Technol.* **245**, 167–179 (2017)
13. M.D. Monzón, I. Gibson, A.N. Benítez, L. Lorenzo, P.M. Hernández, M.D. Marrero, Process and material behavior modeling for a new design of micro-additive fused deposition. *Int. J. Adv. Manuf. Technol.* **67**(9–12), 2717–2726 (2013)
14. H. Krauss, C. Eschey, M. Zaeh, Thermography for monitoring the selective laser melting process. In *Proceedings of the Solid Freeform Fabrication Symposium* 999–1014 (2012). <https://sffsymposium.engr.utexas.edu/Manuscripts/2012/2012-76-Krauss.pdf>
15. E. Faye, O. Dangles, S. Pincebourde, Distance makes the difference in thermography for ecological studies. *J. Therm. Biol.* **56**, 1–9 (2016)
16. FLIR, *The Ultimate Infrared Handbook for R&D Professionals* (FLIR Systems Inc., Boston, 2012). www.FLIR.com • 1 866.477.3687, ©2012
17. J.E. Seppala, K.D. Migler, Infrared thermography of welding zones produced by polymer extrusion additive manufacturing. *Addit. Manuf.* **12**, 71–76 (2016)
18. M. Atif Yardimci, S. Güçeri, Conceptual framework for the thermal process modelling of fused deposition. *Rapid Prototyp. J.* **2**(2), 26–31 (1996)
19. L. Li, Q. Sun, C. Bellehumeur, P. Gu, Investigation of bond formation in FDM process. *Solid Freeform Fabr. Proc.* **403**, 400407 (2002)
20. L. Li, Q. Sun, C. Bellehumeur, P. Gu, Composite modeling and analysis for fabrication of FDM prototypes with locally controlled properties. *J. Manuf. Process.* **4**(2), 129–141 (2002)
21. H.R.N. Jones, *Radiation Heat Transfer* (Oxford University Press, Oxford, 2000)
22. J.R. Howell, R. Siegel, M.P. Mengüç, *Thermal Radiation Heat Transfer* (CRC Press, Boca Raton, 2011)
23. S.W.J.A.J. Churchill, A comprehensive correlating equation for forced convection from flat plates. *AIChE J.* **22**(2), 264–268 (1976)
24. C. Bellehumeur, L. Li, Q. Sun, P. Gu, Modeling of bond formation between polymer filaments in the fused deposition modeling process. *J. Manuf. Process.* **6**(2), 170–178 (2004)



## Chapter 21

# Development of an Inverse Identification Method for Identifying Constitutive Parameters by Metaheuristic Optimization Algorithm: Application to Hyperelastic Materials

G. Bastos, A. Tayeb, N. Di Cesare, J.-B. Le Cam, and E. Robin

**Abstract** In the present study, a numerical method based on a metaheuristic parametric algorithm has been developed to identify the constitutive parameters of hyperelastic models, by using FE simulations and full kinematic field measurements. The full kinematic field was measured at the surface of a cruciform specimen submitted to equibiaxial tension. The test was simulated by using the finite element method (FEM). The constitutive parameters used in the numerical model were modified through the optimization process, for the predicted kinematic field to fit with the experimental one. The cost function was then formulated as the minimization of the difference between these two kinematic fields. The optimization algorithm is an adaptation of the Particle Swarm Optimization algorithm, based on the PageRank algorithm used by the famous search engine Google.

**Keywords** Inverse identification · Particle swarm optimization · Hyperelasticity · Digital image correlation

## Introduction

The constitutive parameters of hyperelastic models are generally identified from three homogeneous tests, basically the uniaxial tension, the pure shear and the equibiaxial tension. From about 10 years, an alternative methodology has been developed [1–4], and consists in performing only one heterogeneous test as long as the field is sufficiently heterogeneous. This is typically the case when a multiaxial loading is applied to a 3 branch [1] or a 4-branch [2] cruciform specimen, which induces a large number of strain states at the specimen surface. The Digital Image Correlation (DIC) technique is generally used to characterize the full kinematic field at the specimen surface. The induced heterogeneity is analysed through the distribution of the biaxiality ratio and the maximal eigen value of the strain. Thus, a large number of experimental data is provided for identifying the constitutive parameters of the considered model.

Several methods have been recently developed to identify parameters from experimental field measurements, typically the finite element updating method (FEMU), the constitutive equation gap (CEGM), the virtual fields method (VFM), the equilibrium gap method (EGM) and the reciprocity gap method (RGM). These methods are fully reviewed in [5].

In the present study a new methodology is proposed in order to minimize the cost function in the FEMU approach. The optimization algorithm used is based on the Particle Swarm Optimization (PSO) algorithm and the artificial smart PageRank algorithm used by the famous search engine Google. This algorithm enables us to minimize the full kinematic field differences by modifying the constitutive parameters, while minimizing the CPU calculation time. Even though the final objective is the identification of complex constitutive models, i.e. a large number of constitutive parameters, the two-parameter Mooney's model [6] is presented in this paper to illustrate the methodology.

---

G. Bastos (✉) · A. Tayeb · J.-B. Le Cam · E. Robin  
Univ. Rennes 1, CNRS, IPR (Institut de Physique de Rennes), UMR 6251, Rennes, France  
e-mail: [adel.tayeb@univ-rennes1.fr](mailto:adel.tayeb@univ-rennes1.fr); [jean-benoit.lecam@univ-rennes1.fr](mailto:jean-benoit.lecam@univ-rennes1.fr); [eric.robin@univ-rennes1.fr](mailto:eric.robin@univ-rennes1.fr)

N. Di Cesare  
Université Bretagne Sud, UMR CNRS 6027, IRDL, Lorient, France  
e-mail: [noelie.di-cesare@univ-ubs.fr](mailto:noelie.di-cesare@univ-ubs.fr)

## Experimental Setup

The material considered here is a carbon black filled natural rubber. The specimen geometry is shown in Fig. 21.1. It is a 105 mm long and 2 mm thick cruciform specimen. Figure 21.2 presents an overview of the experimental setup composed of a home-made biaxial testing machine and an optical camera. The machine is composed of four independent RCP4-RA6C-I-56P-4-300-P3-M (IAI) electrical actuators. They were driven by a PCON-CA-56P-I-PLP-2-0 controller and four PCON-CA (IAI) position controllers. The actuators were controlled by an in-house LabVIEW program. Two cell loads, whose capacity is equal to 1094 N, store the force variation in the two perpendicular directions. In the present study, one equibiaxial loading was carried out in such a way that the specimen's centre was motionless for the displacement measurement to be easier. The displacement and loading rate were set at 70 mm and 150 mm/min respectively for the four independent actuators.

Images of the specimen surface at increasing stretches were stored at a frequency equal to 5 Hz with a IDS camera equipped with a 55 mm telecentric objective. The charge-coupled device (CCD) of the camera has  $1920 \times 1200$  joined pixels. The Digital Image Correlation (DIC) technique is used to determine the displacement field at the specimen surface. The software used for the correlation process was SeptD [7], and a uniform cold lighting was ensured by a home-made LED lamp. The spatial resolution, defined as the smallest distance between two independent points was equal to 4 pixels corresponding to 0.343 mm. The Region of Interest (ROI) used for the digital correlation is represented in Fig. 21.3.

**Fig. 21.1** Specimen geometry (dimensions in mm)

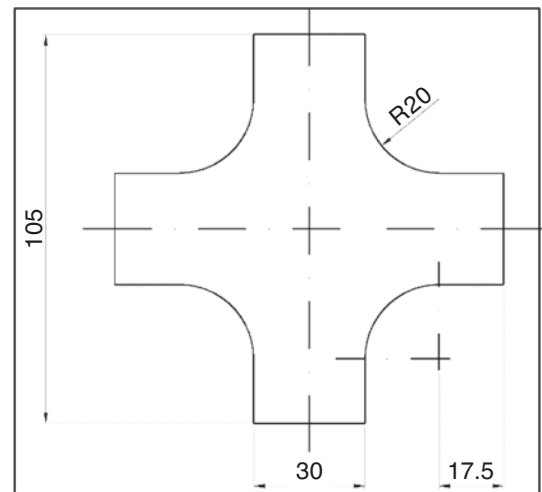


**Fig. 21.2** Home-made biaxial testing machine

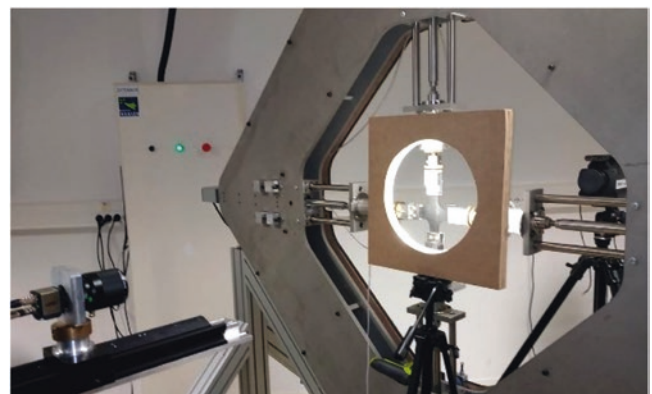
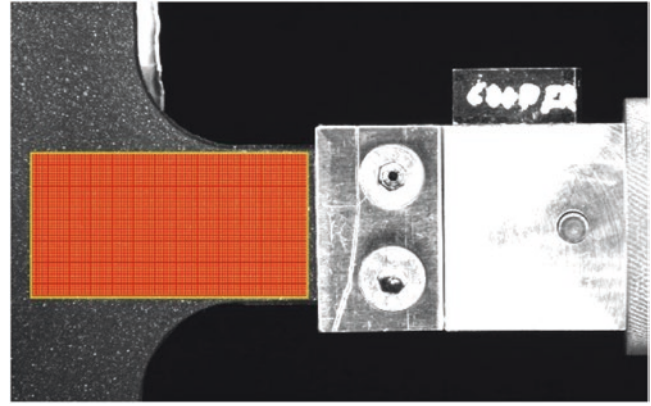


**Fig. 21.3** Region of interest for the DIC technique



## Numerical Model

A finite element calculation is performed by assuming plane stress state and material incompressibility. The four-node PLANE182 ANSYS element is used. The mesh is made of 9600 nodes, and 9353 elements. A biaxial traction load is obtained by prescribing the same displacement of 70 mm on the four branches of the specimen. The two-parameters hyperelastic Mooney model is used for the calculation. The values of the constitutive parameters are changing at each iteration of the optimization process, as described in the next section.

As the spatial resolution between the predicted and the measured kinematic field was different, the experimental kinematic field was fitted by a polynomial-based function. In this way, the predicted kinematic field was compared, for each node, with the experimental field at the same position of the specimen. With the fitting method applied, the difference between the experimental field and the polynomial-based function was less than 0.2 mm whatever the point considered.

## Metaheuristic Optimization Strategy

The aim of the optimization process was here to find the constitutive parameters for the numerical kinematic field to fit the experimental one. The cost function  $f$  was the squared difference between the experimental and the numerical fields, considering the force too, as follows:

$$f = \min \sum_{i=1}^N \frac{1}{N} \left( \frac{U_{x,exp} - U_{x,num}}{U_{x,exp}} \right)^2 + \frac{F_{exp} - F_{num}}{F_{exp}}$$

where  $N$  is the number of nodes in the numerical ROI,  $U_{x,exp}$  is the polynomial-based experimental displacement,  $U_{x,num}$  is the numerical horizontal displacement,  $F_{exp}$  is the experimental horizontal force, and  $F_{num}$  is the numerical horizontal force.

The optimization algorithm used is an adaptation of the classical Particle Swarm Optimization algorithm. In this version, all the particles are influenced by all the others, by considering this influence to be adapted as a function of the respective performance of the particles. The population of PSO particles is then considered as a Markov chain, in which the particles are the nodes, and the transition probabilities between them are the links between them. For each particle, the PageRank value—that is the steady state of the considered Markov chain—is given by the following equation (2). In this way, the PageRank value of each particle is deduced from its performance compared to the best one.

$$\pi_{target}^T = \left| \frac{fitness(\mathbf{G}_{best}) \times 100}{fitness(\mathbf{G}_{best}) - fitness(\mathbf{P}) + \varepsilon} \right|$$

It is then possible to deduce the transition connectivity matrix  $\mathbf{C}$  giving the influence of all the particles on all the others by using a pseudo-random process. The classical equations of PSO are then modified, weighing the influence of all the particles by using the components of  $\mathbf{C}$ , as follow:

$$\mathbf{V}_i^{t+1} = \omega \times \mathbf{V}_i^t + c_1 \times \text{rand}_1 \times (\mathbf{P}_{i,best}^{t+1} - \mathbf{X}_i^t) + c_2 \times \text{rand}_2 \times \sum_{j=1}^n \mathbf{C}_{ij} \times (\mathbf{P}_{j,best}^{t+1} - \mathbf{X}_i^t)$$

$$\mathbf{X}_i^{t+1} = \mathbf{X}_i^t + \mathbf{V}_i^{t+1}$$

where  $\mathbf{V}_i^{t+1}$  is the speed of the  $i$ th particle at iteration  $t + 1$ ,  $c_1$  and  $c_2$  are confident parameters,  $\omega$  is the inertia weight,  $\mathbf{X}_i^{t+1}$  is the position of particle  $i$  at iteration  $t + 1$ ,  $\text{rand}_1$  and  $\text{rand}_2$  are random numbers given in  $[0, 1]$ ,  $\mathbf{P}_{j,best}^{t+1}$  is the personal best position of particle  $i$  at iteration  $t + 1$ , and  $\mathbf{C}$  is the transition connectivity matrix of the considered Markov chain. This Inverse-PageRank-PSO algorithm is fully described in [8].

## Results and Discussion

As the particles are initially randomly defined, the optimization was launched 10 times, to compare the obtained solutions, and be sure that the global minimum of the cost function was reached. The convergence curves of the 10 launched optimization calculation are represented in Fig. 21.4. The obtained values of the cost function and constitutive parameters are given in Table 21.1.

The validation of the optimized results is checked by comparing the experimental displacements and efforts in the sample with the numerical optimized one. In the final numerical model, the values of the constitutive parameters have been set to the mean of the obtained optimized values found in the 10 different calculations launched. Figure 21.5 shows the difference between the experimental polynomial-based kinematic field, and the optimized numerical one, for every point in the ROI.

**Fig. 21.4** Convergence curves of the 10 optimization calculation launched

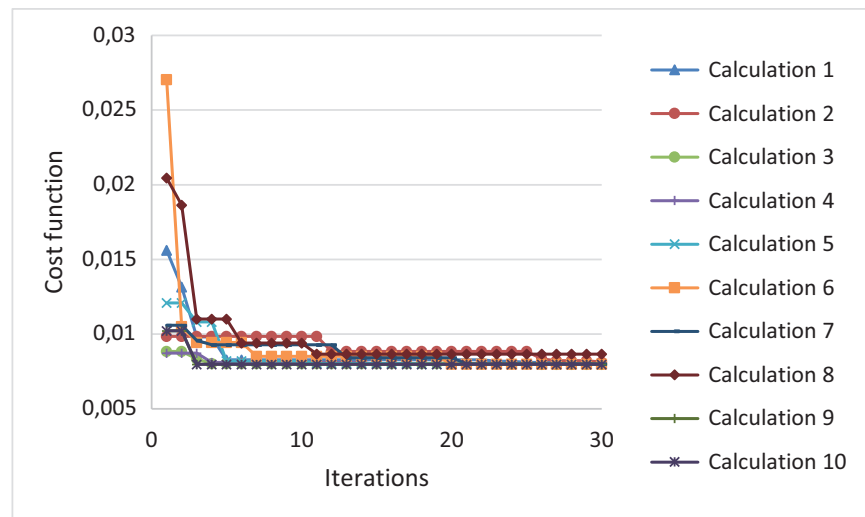


**Table 21.1** Obtained results

Obtained results			
Optimization number	Cost function	C01	C10
1	$8.05 \times 10^{-3}$	0.5159	0.01792
2	$8.13 \times 10^{-3}$	0.5116	0.022541
3	$7.98 \times 10^{-3}$	0.5188	0.020369
4	$7.98 \times 10^{-3}$	0.5197	0.018879
5	$7.98 \times 10^{-3}$	0.5176	0.019914
6	$7.99 \times 10^{-3}$	0.5175	0.020986
7	$8.01 \times 10^{-3}$	0.5153	0.02008
8	$8.03 \times 10^{-3}$	0.5146	0.022146
9	$8.15 \times 10^{-3}$	0.5109	0.021573
10	$7.98 \times 10^{-3}$	0.5202	0.019215
Mean	$8.03 \times 10^{-3}$	$5.16 \times 10^{-1}$	$2.03 \times 10^{-2}$
Std	$6.475 \times 10^{-5}$	$3.19 \times 10^{-3}$	$1.15 \times 10^{-4}$



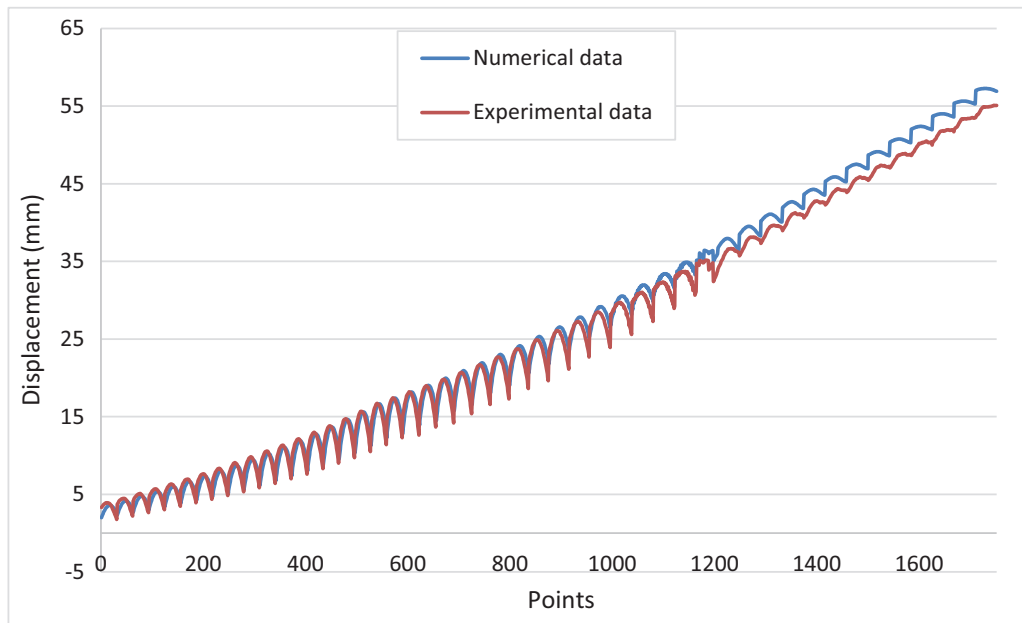
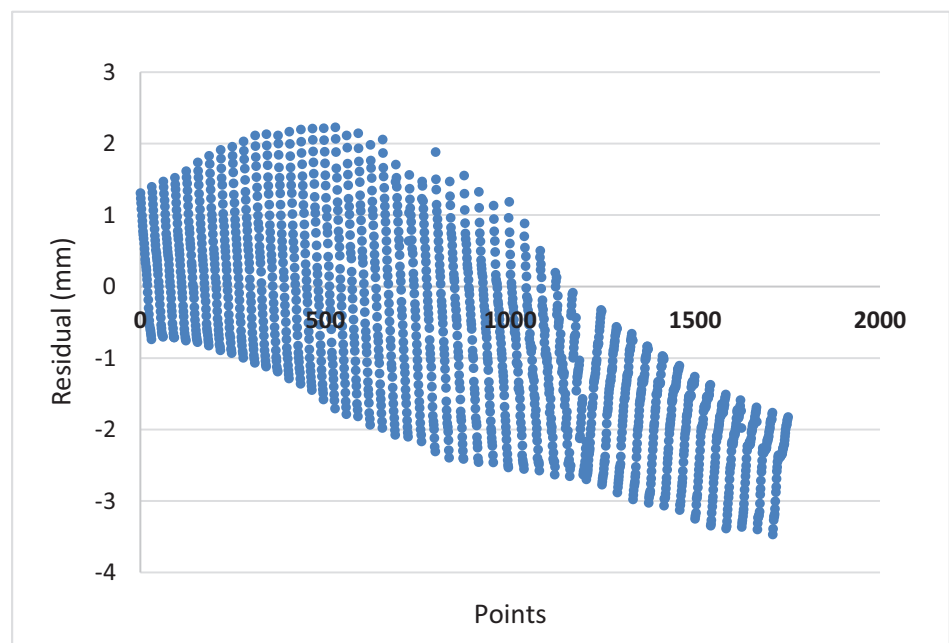


**Fig. 21.5** Comparison between the kinematic fields after the optimization process

**Fig. 21.6** Difference between the kinematic fields for every point of the ROI



This difference is presented in a quantitative way in Fig. 21.6 showing the difference between the two fields for every point of the ROI. One can note that the difference is always less than 6.5% of the experimental kinematic field. Considering the force, the experimental value was 176.02 N, while the numerical value obtained with the optimized values of the constitutive parameters is 176.37 N, which leads to a difference up to 0.4%.

## Conclusions

This work is proposing a new inverse identification method based on the coupling of experimental kinematic fields retrieved by DIC, and the using of a PSO-based parametric optimization algorithm. Experimental and numerical kinematic fields are compared to finally be fitted through the optimization process, while the constitutive parameters are smartly modified.

Applied on a Mooney model, this process is able to find the constitutive parameters reproducing the mechanical response of the specimen, while minimizing the number of optimization iterations. The constitutive parameters found by the optimization process are actually giving a numerical model that retrieves precisely the entire kinematic experimental field.

**Acknowledgements** The authors thank the Region Bretagne, Rennes Métropole and Université Bretagne Loire for their financial support. Cooper Standard is acknowledged for providing the specimens. Authors also thank Dr. Mathieu Miroir, M. Vincent Burgaud, and M. Mickael Le Fur for having designed the biaxial testing machine, Gilles Marckmann and Prof. Michel Grédiac for the fruitful discussions.

## References

1. T. Guélon, E. Toussaint, J.-B. Le Cam, N. Promma, M. Grédiac, A new characterization method for rubbers. *Polym. Test.* **28**, 715–723 (2009)
2. N. Promma, B. Raka, M. Grédiac, E. Toussaint, J.-B. Le Cam, X. Balandraud, F. Hild, Application of the virtual fields method to mechanical characterization of elastomeric materials. *Int. J. Solids Struct.* **46**, 698–715 (2009)
3. M. Johlitz, S. Diebels, *Arch. Appl. Mech.* **81**, 1333–1349 (2011)
4. H. Seibert, T. Scheffer, S. Diebels, *Tech. Mech.* **81**, 72–89 (2014)
5. S. Avril, M. Bonnet, A. Bretelle, M. Grédiac, F. Hild, P. Ienny, F. Latourte, D. Lemosse, S. Pagano, S. Pagnacco, F. Pierron, Overview of identification methods of mechanical parameters based on full-field measurements. *Exp. Mech.* **48**, 381–402 (2008)
6. M. Mooney, A theory of large elastic deformation. *J. Appl. Phys.* **11**, 582–592 (1940)
7. P. Vacher, S. Dumoulin, F. Morestin, S. Mguil-Touchal, Bidimensional strain measurement using digital images. *Proc. Inst. Mech. Eng. C J. Mech. Eng. Sci.* **213**, 811 (1999)
8. N. Di Cesare, D. Chamoret, M. Domaszewski, A new hybrid algorithm based on a stochastic Markov chain model. *Adv. Eng. Softw.* **90**, 127–137 (2015)



# Chapter 22

## MIMO Input Derivations, Optimizing Input Force Against Output Accuracy

Arup Maji

**Abstract** Multi-Input-Multi-Output (MIMO) vibration testing is considered more representative of the true loading environment (flight or wind induced vibration) where the inputs are not through a single point. The derivation of N inputs for testing typically involves matching the response at M locations (outputs). This involves inversion of a  $N \times M$  Transfer Functions (TRF) matrix corresponding to the N input and M output locations. The matrix inversion is affected by both mathematical and physical parameters (ill-conditioned matrix, structural modes, signal noise).

Tikhonov regularization is commonly used in inverting an ill-conditioned  $N \times M$  matrix. A low value of the Tikhonov regularization parameter minimizes the distortion of the original equations while a higher value can minimize error. In practice this introduces an interesting dilemma where obtaining realistic input loads and maintaining accuracy of output are often pitted against each other. A study was conducted using data synthesized from a simply-supported plate structure with known vibration modes with added noise at outputs. The objective of the study was to understand how noise or errors in the output and the Transfer function affect the input. This leads to a more judicious choice of the Tikhonov parameter that can achieve a balance between reducing input loads while preserving desired accuracy of output vibration.

**Keywords** Vibration testing · Multiple input · MIMO

### Introduction

The vibration of a simply supported plate ( $1.0 \times 1.5$  m, 10 cm thick) under multiple input and response locations was studied. Force input was applied at various locations on the grid shown in Fig. 22.1 (the grid lines are equally spaced from  $0.5$  to  $0.95 \times$  length in both x and y axes). Response is also calculated at the same locations. For this specific study the two inputs were applied at locations  $0.25$  and  $0.45 \times$  length (circles in Fig. 22.1). Response was monitored at 4 locations,  $0.25$ ,  $0.45$ ,  $0.65$ , and  $0.85 \times$  length (circles and squares in Fig. 22.1). The response and the input are related by the plate response (Transfer Function TRF) as shown in Eq. (22.1). Input can be derived from response using Eq. (22.2) where  $TRF^{-1}$  is the pseudo-inverse of the rectangular TRF matrix. To invert an ill-conditioned matrix, the Tikhonov regularization parameter is used, which prevents the very low values of TRF from resulting in distorted (nearly singular) values in  $TRF^{-1}$ .

$$[TRF]_{4 \times 2} \times [Input]_{2 \times 1} = [Response]_{4 \times 1} \quad (22.1)$$

$$[TRF]_{2 \times 4}^{-1} \times [Response]_{4 \times 1} = [Input]_{2 \times 1} \quad (22.2)$$

---

Sandia National Laboratories is a multimission laboratory managed and operated by National Technology & Engineering Solutions of Sandia, LLC, a wholly owned subsidiary of Honeywell International Inc., for the U.S. Department of Energy's National Nuclear Security Administration under contract DE-NA0003525.

"This paper describes objective technical results and analysis. Any subjective views or opinions that might be expressed in the paper do not necessarily represent the views of the U.S. Department of Energy or the United States Government."

---

A. Maji (\*)  
 Org1557, Sandia National Laboratories, Albuquerque, NM, USA  
 e-mail: [amaji@unm.edu](mailto:amaji@unm.edu)

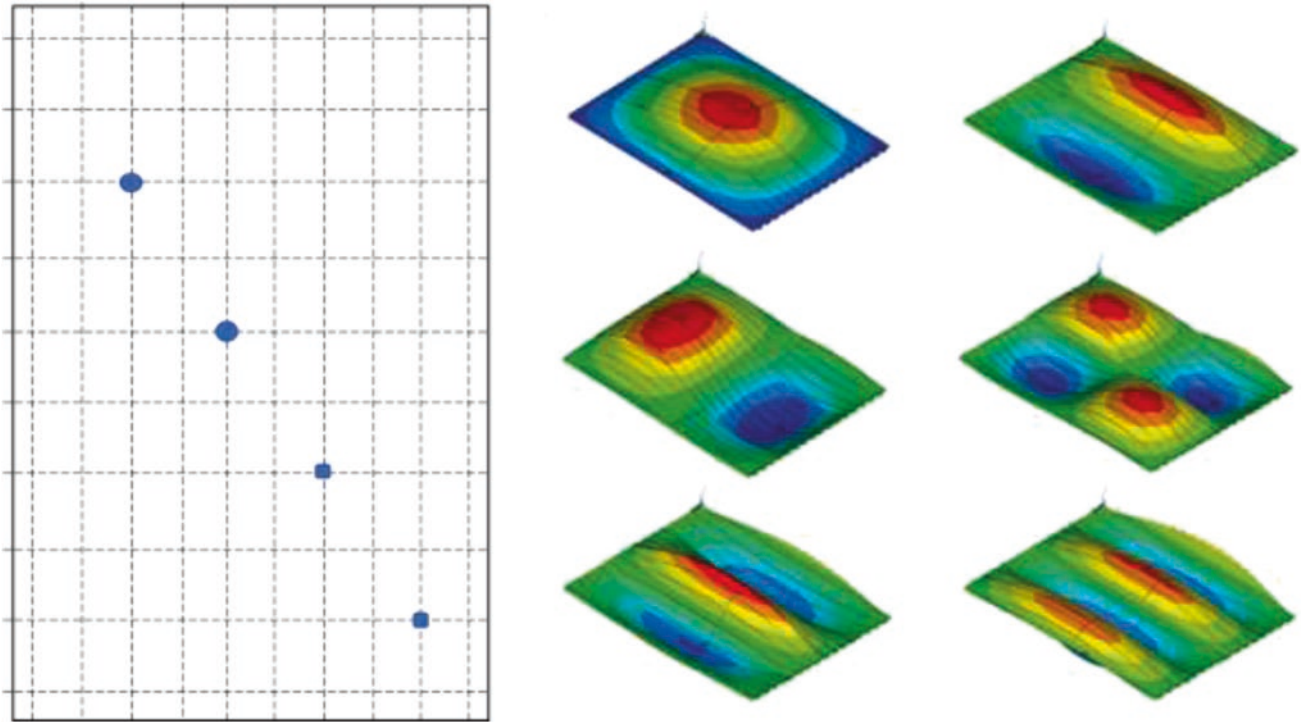


**Fig. 22.1** Simply-supported plate with input and output locations and mode shapes

**Table 22.1** Modes below 300 Hz (numbers refer to values of  $r_1$  and  $r_2$  in equation above)

Modes	1	2	3	4	5
1	34.04	65.46	117.82	191.14	285.39
2	104.73	136.15	188.52	261.83	
3	222.56	253.97			

The frequency domain Response of a simply supported rectangular plate to an input force was determined based on analytical solution provided Fahy and Gardonio [1]. Transverse displacement  $d(\omega)$  at position  $x_2, y_2$  due to a force  $F(\omega)$  at location  $x_1, y_1$  is given by the expression:

$$d(\omega) = \sum_{r=1}^{\infty} \frac{\phi(x_2, y_2) \phi(x_1, y_1)}{M_r [w_r^2 (1 + j\eta)] - \omega^2} F(\omega) \quad (22.3)$$

$w_r = \sqrt{\frac{D}{m} \left[ \left( \frac{r_1 \pi}{l_x} \right)^2 + \left( \frac{r_2 \pi}{l_y} \right)^2 \right]}$  represents the modal frequencies of the plate  $\phi(x, y) = 2 \sin\left(\frac{r_1 \pi x}{l_x}\right) \sin\left(\frac{r_2 \pi y}{l_y}\right)$  Represents a modal shape function.

To obtain velocity instead of displacement the equation is multiplied by  $j\omega$ ; to get acceleration  $a(\omega)$  it is multiplied by  $(-\omega^2)$ .

$D = Eh^3/(12(1 - \nu^2))$ , is plate stiffness,  $E$ ,  $h$  and  $\nu$  are elastic modulus, plate thickness and poisson's ratio.  $m$  is the mass per unit area of the plate,  $l_x$  and  $l_y$  are plate dimensions.  $r_1$  and  $r_2$  are integers representing mode numbers.  $M_r$  is the total mass of the plate.  $\eta$  is damping coefficient. Properties of Aluminum were used ( $E = 70$  GPa,  $\nu = 0.2$ ). Table 22.1 shows the modes <300 Hz.

The following steps were used in these analyses:

- Frequency domain Transfer function (TRF) relating input force to response acceleration was generated using the equation 3 above for all 100 points of the grid shown in Fig. 22.1 (only a few of these were used). This was done for frequency values 1–8192 radians/s.

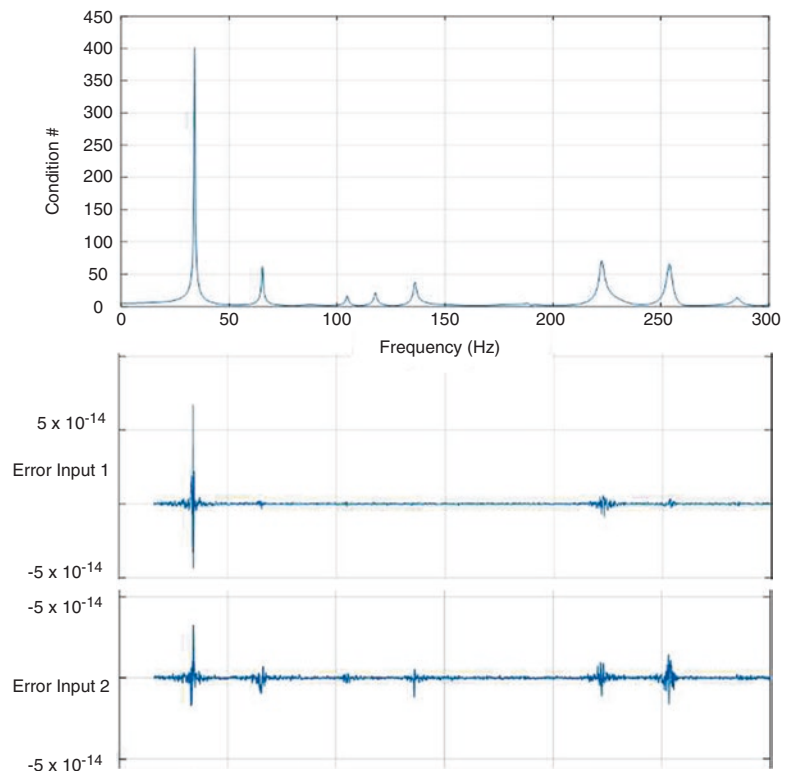
- Frequency domain Input force was generated using random phase (uniformly distributed between  $\pm 180^\circ$ ) and constant amplitude = 100 N. Input force values for the first 100 low frequencies were set to zero such that the length of data was statistically representative. Input force values at high frequencies were also set 0 to satisfy Nyquist criterion.
- The TRF and Input were used to calculate the response as per Eq. (22.1).
- Response was polluted with increasing amounts of white noise at each frequency and the input was recalculated based on Eq. (22.2).
- Error in the new input was determined compared to the original input.
- New Response was calculated using the new input (based on TRF inversion)
- Error in response was calculated relative to the original response.

## Results

Figure 22.2 shows that Input error ( $=\text{True Input}/\text{MIMO-based input}$ ) is correlated with condition # of the TRF; ill-conditioning of the matrix leads to higher error. However, numerical analysis involved in inverting a  $4 \times 2$  matrix results in negligible error (note scale  $5 \times 10^{-14}$  = in Fig. 22.2). It is also worth noting that the relatively higher errors for Input 2 are at frequencies where the input 2 has very little contribution (at location  $0.45 \times \text{length}$  it is close to the node at the center of the plate).

Figure 22.3 shows the effect of adding a noise of amplitude 1.0 and uniformly distributed random phase ( $\pm 180^\circ$ ) to the response at each frequency. The right side of Fig. 22.3 shows that the noise is very low in comparison to the amplitudes of the response (peak response is a 1000), and the response with and without noise is visually indistinguishable. The input error is now considerable. At frequencies of 65, 136 and 254 Hz where Input 2 is near a node it has considerably more error than Input 1. Input 2 has small error at 118, 223, 285 Hz because it is no longer at a node and can contribute to those modes as well as Input 1 can. Also recognizable is the gradual increase in Input error below the 1st mode of 34 Hz, which can be attributed to the lack of motion in the plate.

**Fig. 22.2** Condition # vs. input error with zero noise



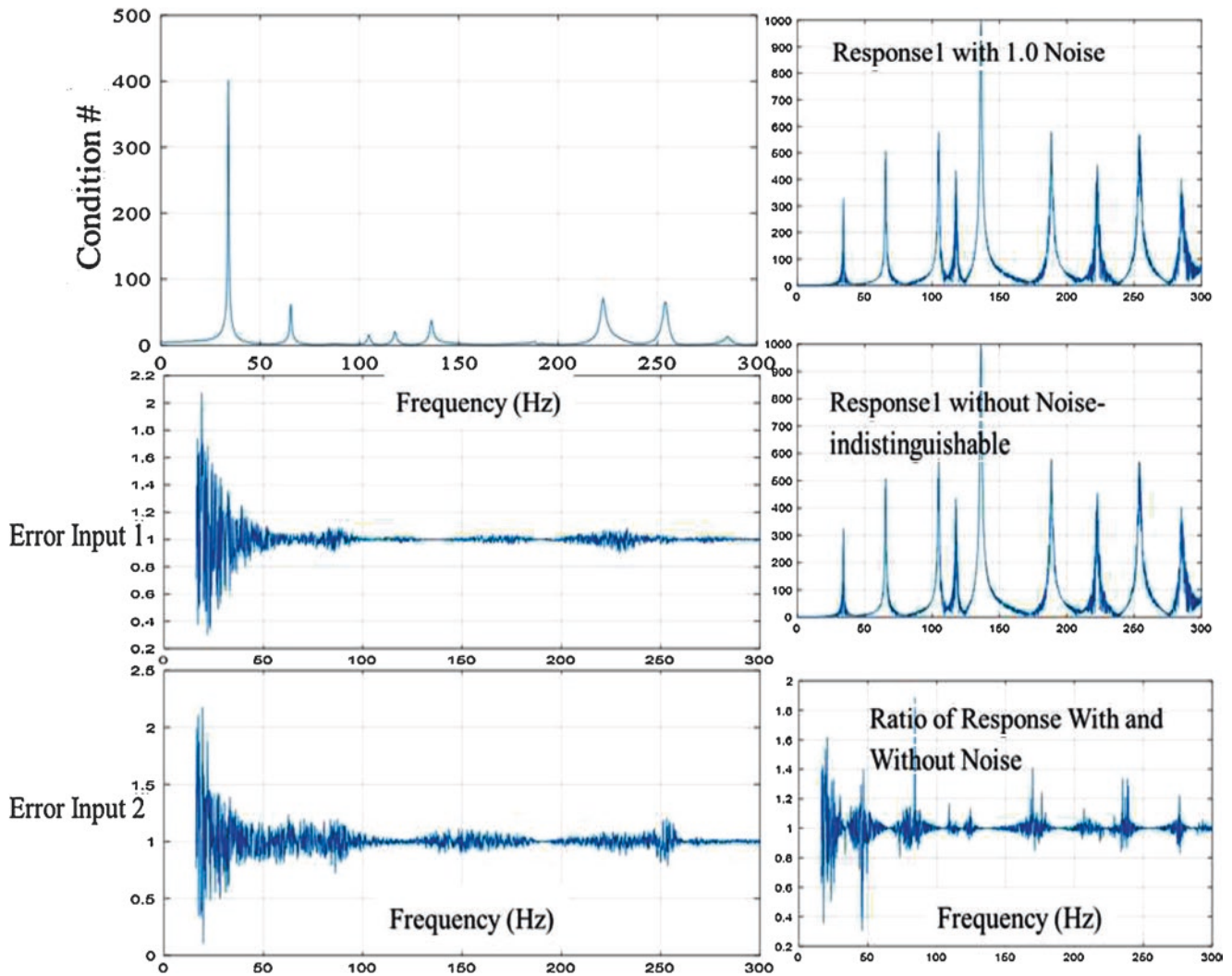


Fig. 22.3 Condition # vs. input error with noise = 1.0

Figure 22.4 shows results with the noise level increased to 10.0 at each frequency. The resulting error in the input is now greater in roughly the same proportion ( $\approx \times 10$  greater than that in Fig. 22.3). The bottom-right plot shows the input error when the tolerance value in the MatLab pseudo-inverse function ‘*pinv*’ is change from 0 to 0.1. This is known as the regularization parameter and referred to in this paper as *tol*. The two plots on the left (in Fig. 22.4) are the same data with the lower figure with a vertical scale matching the one on the lower right for comparison. The input error is significantly lower at and below the 1st mode of 34 Hz. This is because the lower singular values in TRF is set = 0.1 removing the inversion inaccuracies caused by extremely low singular values.

Additional insight can be gained by examining the relationship between the results of the Singular-Value-Decomposition (SVD) of the Transfer Function Matrix (TRF) at each frequency. The high and low singular values are shown in the top right plot of Fig. 22.4 (note long-normal of svd is presented instead of svd to better visualize the effect of singular values and *tol* on the error). The selection of the tolerance value (*tol*) results in selective minimization of input error. So, when *tol* is increased to 0.165 more of the input errors are reduced as seen in the plot in the right-center. The dotted horizontal lines represent the 2 *tol* values relative to the singular values. The circles show the corresponding decrease in the error in Input 2 where the lower svd values are below ( $\ln 0.165 = -1.8$ ). Likewise the two dotted lines below 100 Hz show where the lower svd values are below ( $\ln 0.1 = -2.3$ ) and the corresponding decrease in Input 2 error in those regions.

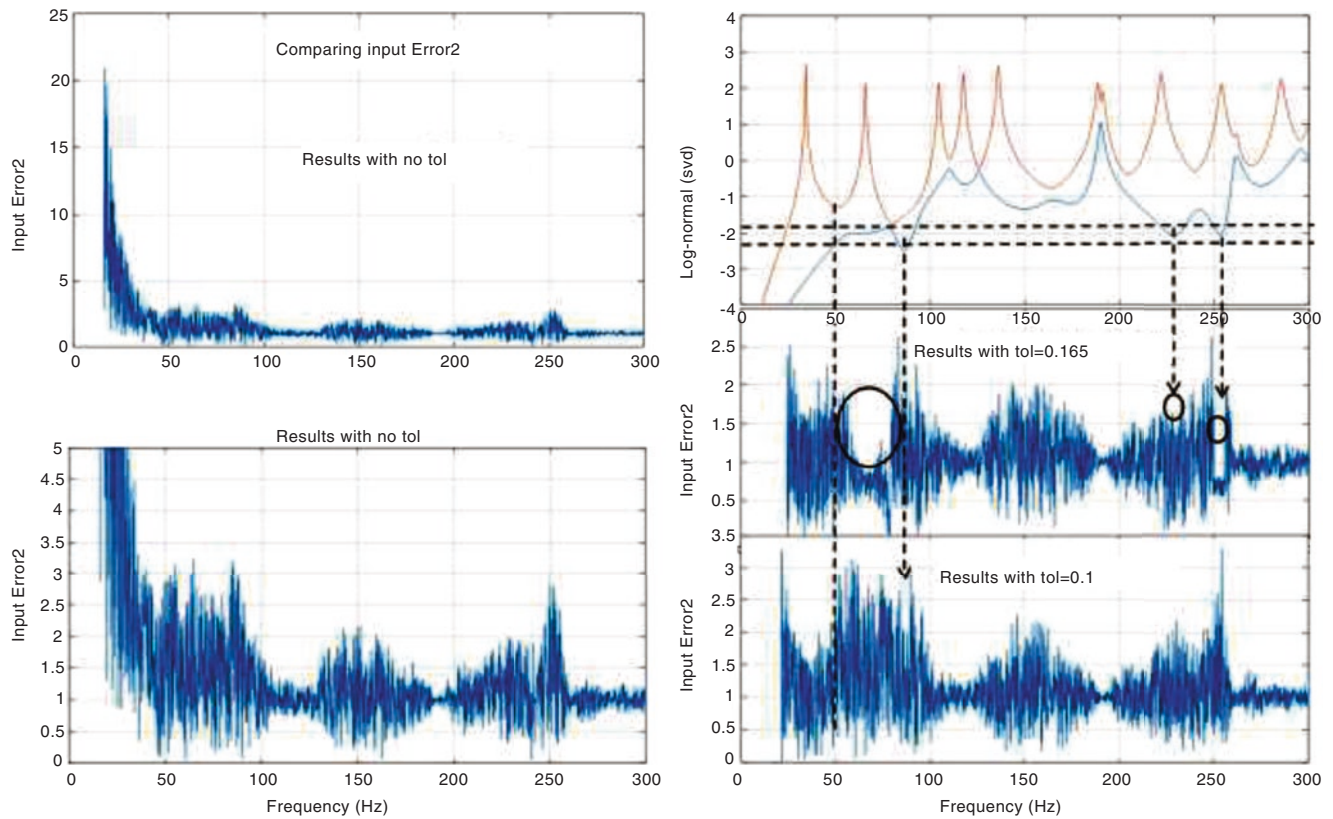


Fig. 22.4 Input error with noise = 10 and effect of regularization parameter

## Conclusions

- Large condition #s associated with resonant modes is the first source of error in MIMO inversion. In the absence of other sources of noise this error is negligible.
- When response is polluted with white noise the input error is in proportion to the relative error in the response (effect of white noise to the response is low at and near resonances).
- Input error at specific frequencies is higher when the input is near a node for that frequency.
- A 10× increase in the noise results in a corresponding 10× increase in the input error.
- Choosing the regularization parameter based on the lower value from singular-value-decomposition of the complex TRF matrix can be used to decrease input error.

## Reference

1. F. Fahy, P. Gardonio, Section 2.4: mobility and impedance functions of thin uniform flat plates, in *Sound and Structural Vibration*, 2nd edn. (Elsevier, Amsterdam, 2007). ISBN# 0-12-373633-1



## Chapter 23

# Evaluation of Sensitivity-Based Virtual Fields for Non-Linear Parameter Identification Including DIC Filtering Effects

Pascal Lava, Jevan Furmanski, Alexander Marek, Francis M. Davis, and Fabrice Pierron

**Abstract** Recently, the issue of automatically defining virtual fields for non-linear constitutive models has been resolved (Marek et al., *Comput Mech* 60:409–431, 2017), relying on a new sensitivity-based approach hereby reducing the influence of noise on the parameter identification. These new set of fields act as weighting factors in the identification process emphasizing the impact of measurement regions with high signal to noise ratios. Conclusions in (Marek et al., *Comput Mech* 60:409–431, 2017) were drawn based on a numerical example involving small strain plasticity. In this presentation, the performance of these newly defined fields is studied when applied to digital image correlation (DIC) measurement data, hereby including the DIC filtering effects through synthetic image deformation (Rossi et al., *Strain* 51:206–222, 2017). Results are presented for both large strain isotropic plasticity and hyperelastic material models.

**Keywords** Digital image correlation · Virtual fields method · Sensitivity-based · Material identification · Non-linearity

## Theoretical Development

For a detailed theoretical development of the sensitivity-based VFs the user is referred to [1]. In summary, the idea behind the proposed approach is that these fields will emphasize regions that carry the most information about the involved constitutive parameters and their time evolution. Each model parameter  $i$  is perturbed in order to determine intrinsic parameter  $\delta\sigma^{(i)}(\boldsymbol{\varepsilon}, \mathbf{X}, t)$  sensitivity and incremental sensitivity  $\delta\tilde{\sigma}^{(i)}(\boldsymbol{\varepsilon}, \mathbf{X}, t)$  maps, with  $\mathbf{X}$  the vector of the model parameters and  $t$  the time step. The virtual displacement  $\mathbf{u}^*$  are then determined from these maps by imposing a virtual mesh on the data point cloud. Next, when the equations for every element in the mesh are collected the following system of equations is produced:

$$\delta\tilde{\sigma}^{(i)} = \mathbf{B}\mathbf{u}^{*(i)} \quad (23.1)$$

where  $\mathbf{B}$  is the global strain-displacement matrix. It is important to stress that every parameter will come with its own sensitivity maps and accordingly will yield a different set of virtual fields.

## Synthetic Images

The regularization properties (subset size, step, shape function, strain method etc.) of full-field measurements as DIC might have a substantial impact on the involved sensitivity maps and accordingly on the performance of the automatically-defined virtual fields. In order to study the impact of DIC filtering effects an identical methodology is adopted as outlined in [2] based

---

P. Lava (✉)  
MatchID NV, Ghent, Belgium  
e-mail: [pascal.lava@matchid.eu](mailto:pascal.lava@matchid.eu)

J. Furmanski  
ExxonMobil Corporate Strategic Research, Annandale, NJ, USA  
e-mail: [jevan.furmanski@exxonmobil.com](mailto:jevan.furmanski@exxonmobil.com)

A. Marek · F. M. Davis · F. Pierron  
Engineering and Physical Sciences, University of Southampton, Southampton, UK  
e-mail: [A.Marek@soton.ac.uk](mailto:A.Marek@soton.ac.uk); [frances.davis@soton.ac.uk](mailto:frances.davis@soton.ac.uk); [F.Pierron@soton.ac.uk](mailto:F.Pierron@soton.ac.uk)



on synthetic image deformation. Hereby, a virtual set of experimental images is created with benchmark input material parameters. The numerical deformed speckle images are created via MatchID's finite element deformation module (<http://www.matchid.eu>), with image deformation expressed in the reference configuration based on the shape functions of the corresponding nodes and end up in integer pixel locations in the deformed image. This not only avoids extra interpolation steps but also guarantees that one naturally arrives at a Lagrangian prescription of the image deformation process [3]. These are then analysed by a DIC platform (<http://www.matchid.eu>) with a quantified set of user variables. Finally, seamlessly feeding the resulting strain fields into the VFM module (<http://www.matchid.eu>) allows material parameter extraction and validation with the known reference parameters.

## Case Study

The method was tested using simulated Abaqus data from a uniaxial tensile test on a double-notched specimen as depicted in [1] and a specimen with a set of circular stress concentrations as in Fig. 23.1. Gaussian noise with a standard deviation of 0.7% was artificially added to the simulated strain data to simulate typical noise levels during an actual experiment. It is important to stress that in contrast to [1], a large strain formulation has been adopted with corresponding stress fields expressed in the first Piola-Kirchoff convention allowing the VFM to apply boundary conditions in the reference configuration.

The applied DIC settings and retrieved strain resolution are summarized in Table 23.1. Additionally, MatchID's missing data compensation technique has been imposed in order to retrieve data up to the edges of the specimen, hereby relying on the subset shape functions.

Table 23.2 contains the results of a basic isotropic Von Mises plasticity model adopting linear hardening, and a hyperelastic first-order Mooney-Rivlin model. The conference presentation will encompass a more broad variety of non-linear model results. It can be depicted from both tables that the sensitivity-based virtual fields outperform the uniform defined ones, reproducing the input parameters with high accuracy despite the involved DIC filtering effects.

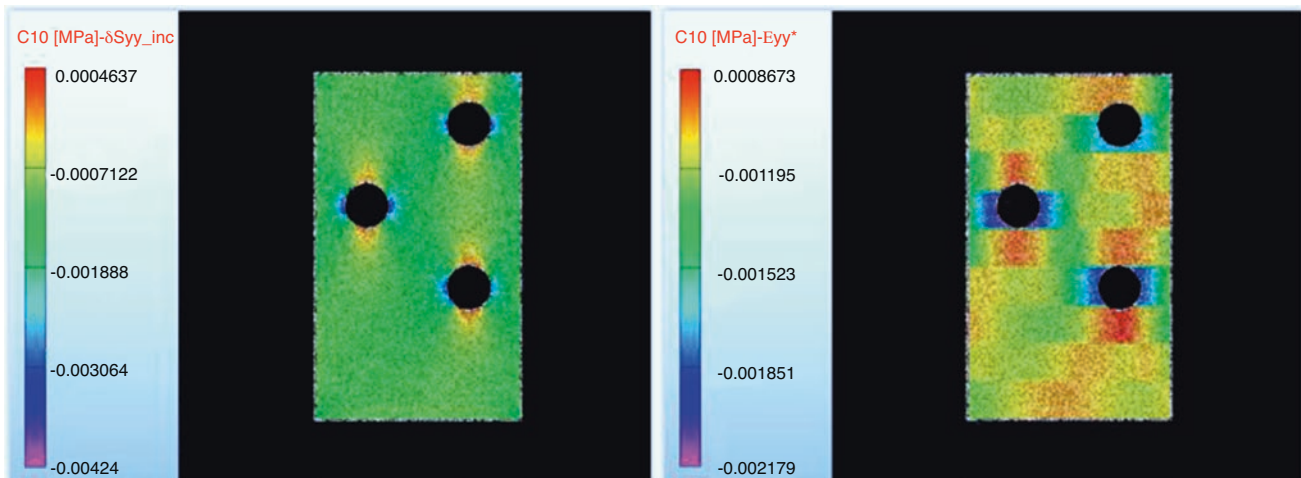


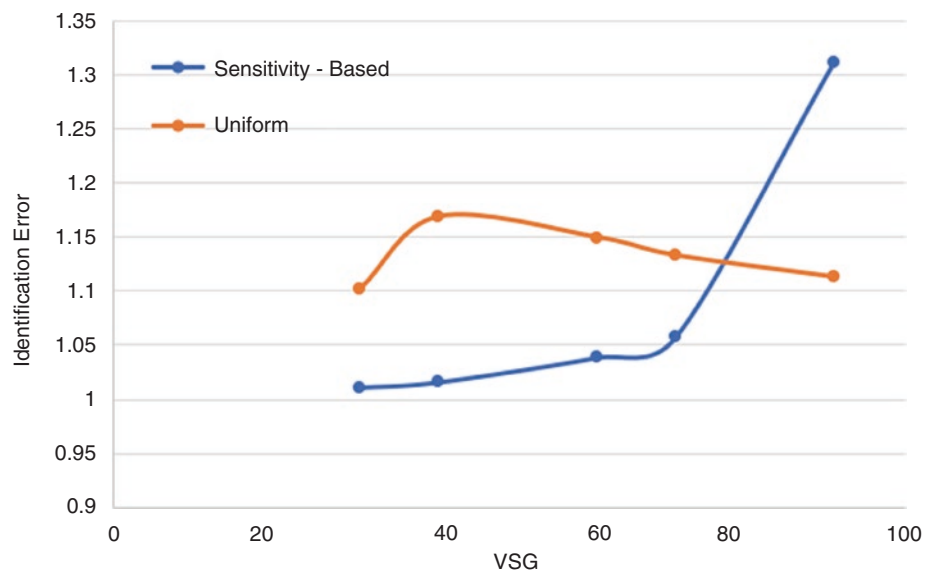
**Fig. 23.1** Incremental stress sensitivity map for C10 at 0.5 N (left panel) and corresponding longitudinal virtual strain field (right panel) adopting a  $9 \times 9$  virtual mesh

**Table 23.1** Adopted DIC settings

Technique used	2D DIC
Pre-filtering	Gaussian–Kernel 5
Subset	21
Step	3
Correlation criterion	ZNSSD
Shape function	Quadratic
Interpolation function	Bicubic splines
Total number of images	50
<i>Strain</i>	
Smoothing method	Polynomial–bilinear
Strain window/VSG	5/43 pixels
Resolution	157 $\mu\text{m}/\text{m}$

**Table 23.2** Identified parameter results

	Plasticity linear hardening		Hyperelastic Mooney-Rivlin	
	$\sigma_0/\sigma_0^{\text{ref}}$	$H/H^{\text{ref}}$	$C_{10}/C_{10}^{\text{ref}}$	$C_{01}/C_{01}^{\text{ref}}$
Uniform	0.94	1.16	1.038	1.1
Incremental sensitivity	1.006	0.987	0.998	1.08

**Fig. 23.2** Averaged material parameter error for both sensitivity-based and uniform virtual fields as a function of virtual strain gauge size

## Impact of DIC Filtering

In order to study the impact of the main DIC regularization parameters (subset, step and strain window) on the final identified properties, a performance analysis was undertaken for the hyperelastic case study. Hereby, various combinations of the abovementioned DIC parameters corresponding to different virtual strain gauge values generated an averaged identification error plot displayed in Fig. 23.2. As can be depicted, the sensitivity-based VF are more dominantly depending on the spatial resolution of DIC compared to the uniform ones. This is due to the fact that they rely on local gradient variations in determining the incremental gradient maps. However, an asymptotic accurate identification trend can be derived towards smaller VSGs. The uniform VF depend less on the VSG size, resulting in a general total error of approximately 10%.

## Conclusion

Sensitivity-based virtual fields act as a weighting factor in the parameter identification process. It is clearly illustrated that these fields outperform their uniform counterparts. Moreover, this method allows to reproduce input parameters with high accuracy despite the involved DIC filtering effects if a DIC convergence study is made. The adopted method is computationally very efficient and does not require a non-straightforward coupling to finite element solvers as in inverse model updating schemes. In the future, more complicated material models will be investigated, as e.g. the calibration of a non-linear viscoplastic three-network-model [4].

## References

1. A. Marek, F. Davis, F. Pierron, Sensitivity-based virtual fields for the non-linear virtual fields method. *Comput. Mech.* **60**, 409–431 (2017)
2. M. Rossi, P. Lava, F. Pierron, D. Debruyne, M. Sasso, Effect of DIC spatial resolution, noise, and interpolation error on identification results with the VFM. *Strain* **51**, 206–222 (2017)
3. P.L. Reu et al., DIC challenge: developing images and guidelines for evaluating accuracy and resolution of 2D analyses. *Exp. Mech.* **58**(9), 1067–1099 (2018)
4. J. Bergstrom, An advanced thermomechanical constitutive model for UHMWPE. *Int. J. Struct. Chang. Solids* **2**(1), 31–39 (2010)



# Chapter 24

## Identification of Inhomogeneous Plastic Constitutive Models of Friction Stir Welded Aluminum Alloy Sheets Using Virtual Fields Method

Chanyang Kim, Jin-Hwan Kim, and Myoung-Gyu Lee

**Abstract** In this study, heterogeneous material properties of friction stir welded (FSWed) aluminum alloy sheet were identified using the virtual fields method. As a feasibility study before application to real experiment, finite element simulation was carried out to generate deformation data as a virtual mechanical test. For inputs of mechanical properties including plasticity properties, spatially heterogeneous strain hardening data were obtained from reference micro-indentation data of FSWed aluminum alloy sheet. From the finite element simulation result (which replaces real experiment), the boundary of welding zone and spatial distribution of plastic parameters in the welded region could be identified using virtual fields method (VFM). The calculated material parameters in the weld zone agreed well with target material parameters (used for inputs of FE simulation), which validates the potential application of VFM to identify the mechanical properties of heterogeneous materials.

**Keywords** Friction stir welding (FSW) · Virtual fields method (VFM) · Inverse analysis method · Inhomogeneous mechanical properties · Aluminum alloys

### Introduction

Friction stir welding (FSW) is a solid-state joining technology applied to hard-to-weld metal alloys with conventional welding techniques. The mechanical properties of the welded joint in the metal sheets are naturally inhomogeneous due to spatial distributions of temperature history during the welding process. For example, the FSWed joint consists of thermo-mechanically affected zone (TMAZ) and heat affected zone (HAZ). Therefore, accurate identification of mechanical properties of welded joint such as plastic yielding and hardening is important for the design of automotive part forming process with FSWed sheet metals. This is particularly true because the welded zone in FSWed sheet is wider than that of other welding techniques, and thus the forming simulation should consider the effect of inhomogeneous mechanical properties. To characterize the mechanical properties of FSWed joint, several methods have been introduced, which include micro-indentation [1], tensile test using a miniature specimen, and numerical inverse approach with finite element method. In this study, the feasibility of extracting plastic properties of FSWed aluminum alloy sheet joint using the virtual fields method (VFM) [2, 3], as one of the inverse approaches, was investigated.

### Methodology

The virtual fields method (VFM) is based on the weak form equilibrium equation, the principle of virtual work. The principle of virtual work for statics under a plane stress condition can be written as follows.

$$t \int_S \boldsymbol{\sigma}(\boldsymbol{\varepsilon}) \boldsymbol{\varepsilon}^* ds = \int_S \mathbf{F} \mathbf{u}^* ds \quad (24.1)$$

---

M.-G. Lee (✉) · C. Kim

Department of Materials Science and Engineering and RIAM, Seoul National University, Seoul, South Korea  
e-mail: [myounglee@snu.ac.kr](mailto:myounglee@snu.ac.kr); [c.kim@snu.ac.kr](mailto:c.kim@snu.ac.kr)

J.-H. Kim

Graduate Institute of Ferrous Technology, POSTECH, Pohang, South Korea  
e-mail: [jjinkim@postech.ac.kr](mailto:jjinkim@postech.ac.kr)

where  $t$  is specimen thickness,  $\boldsymbol{\sigma}$  stress tensor,  $\boldsymbol{\epsilon}$  strain tensor, and  $\boldsymbol{F}$  external traction vector. Also,  $\boldsymbol{\epsilon}^*$  and  $\boldsymbol{u}^*$  are virtual strain tensor and displacement vector, respectively. In Eq. (24.1) strains can be obtained using a full-field measurement such as the digital image correlation (DIC) technique. In this study, as the preliminary theoretical approach, ideal deformation data was generated by finite element simulation, which were used for the inputs of the VFM. Also, a linear interpolation scheme used in the finite element method [3, 4] was introduced to calculate local strains. Local stress values, which depend on material parameters are calculated based on tangent stiffness stress update algorithm [3, 5].

The virtual displacement  $\boldsymbol{u}^*$  and strain  $\boldsymbol{\epsilon}^*$  can be assigned by the user of VFM with necessary constraints. In this study, simple tension-type virtual fields are employed as in Eq. (24.2).

$$u_x^* = 0, u_y^* = y, \epsilon_{xx}^* = 0, \epsilon_{yy}^* = 1, \epsilon_{xy}^* = 0 \quad (24.2)$$

In Eq. (24.1), the left-hand side term is called the internal virtual work ( $W_{int}$ ) and the right-hand side term is the external virtual work ( $W_{ext}$ ). Therefore, a cost function for the optimization of material parameters for an equilibrium condition is used as follows.

$$\omega = \sum_{i=0}^{i=n} (W_{int}^i - W_{ext}^i)^2 \quad (24.3)$$

where  $i$  denotes time step in the time-discretized data set, and  $n$  is a total number of the time steps. By minimizing the cost function, required material parameters can be identified. In this study, the Matlab<sup>®</sup> built-in non-linear least squares optimization function was used.

In the FSWed, mechanical properties in the region far away from the weld centerline are much less affected by the welding process and can be assumed as those of base material. Therefore, it is computationally efficient to find a boundary between based and welded regions before identifying heterogeneous material parameters of welding affected zone including TMAZ and HAZ. The boundary is identified using the cost function  $\omega$ . If the calculated  $\omega$  value with the mechanical properties of the base material, which is prior known, is nearly zero, it can be assumed as the base material. By successive scanning the region where  $\omega$  is smaller than a prescribed critical value, the boundary can be identified. Once the boundary between the base and the welded zone is known, the material parameters of the remaining welding affected zone are identified. The whole welding affected zone is discretized into a number of sub-domains, and the material parameters of each sub-domain are identified independently. For the optimization of material parameters, the Matlab<sup>®</sup> built-in non-linear least squares optimization function was utilized. The overall procedure is schematically illustrated in Fig. 24.1.

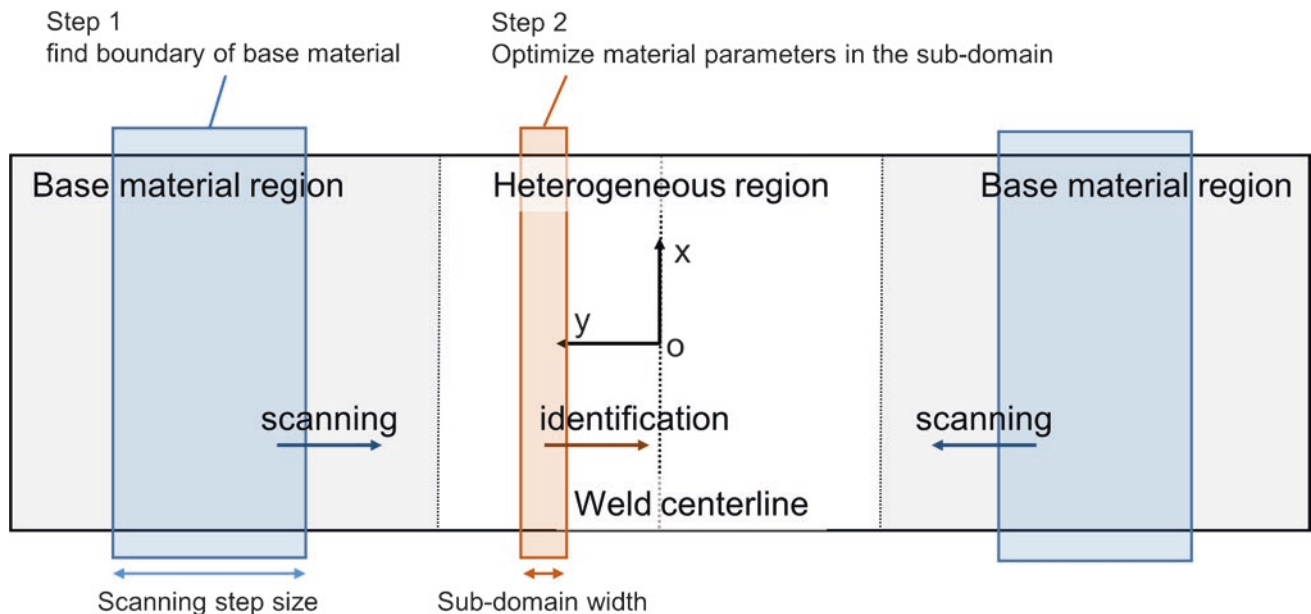


Fig. 24.1 Schematics of FSWed material parameters identification procedure

## Material Model

The virtual target material properties of FSWed specimen is generated based on [1]. For the elastic properties, Young's modulus of 70 GPa and Poisson ratio of 0.33 are assumed. The isotropic von Mises yield function is used with the Voce strain hardening law in Eq. (24.4).

$$\bar{\sigma} = \sigma_0 + k(1 - e^{-b\bar{\epsilon}}) \quad (24.4)$$

where  $\bar{\sigma}$  and  $\bar{\epsilon}$  are equivalent stress and strain, respectively, and  $\sigma_0$ ,  $k$ , and  $b$  are material parameters. The virtual spatial distribution of material parameters are generated based on the reference micro-indentation data fitted with Fourier series. For example, Fig. 24.2 shows the distribution of yield stress of the investigated FSWed sheet along sample coordinate.

## Finite Element Simulation

For a virtual tension test (which replaces the real experiment), finite element simulation is conducted under the plane stress condition. The ASTM E8 standard tension test specimen is used and a commercial finite element software ABAQUS/Standard is used. The input heterogeneous material properties are implemented using the user subroutines UHARD and USDFLD. Plane stress linear triangle elements (CPS3) are used and the total number of elements is 280,624 with an average element size of 0.1 mm. A weld centerline is located in the center of specimen vertical to the specimen length direction and the origin of global coordinates is selected as the specimen center.

## Result

The identified boundary of base material zone presents an exact match with input (target) value. In addition, the spatial distributions of material parameters for the Voce strain hardening law give a very good agreement with target values as shown in Fig. 24.3a. The distributions of equivalent stress corresponding to the several levels of equivalent strain also agree well with input values (Fig. 24.3b).

**Fig. 24.2** Yield stress distribution of virtual material based on reference data [1]

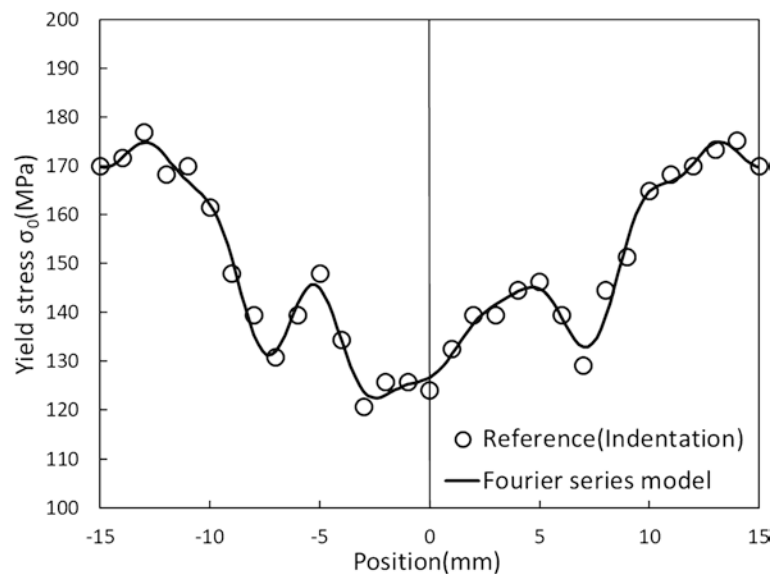
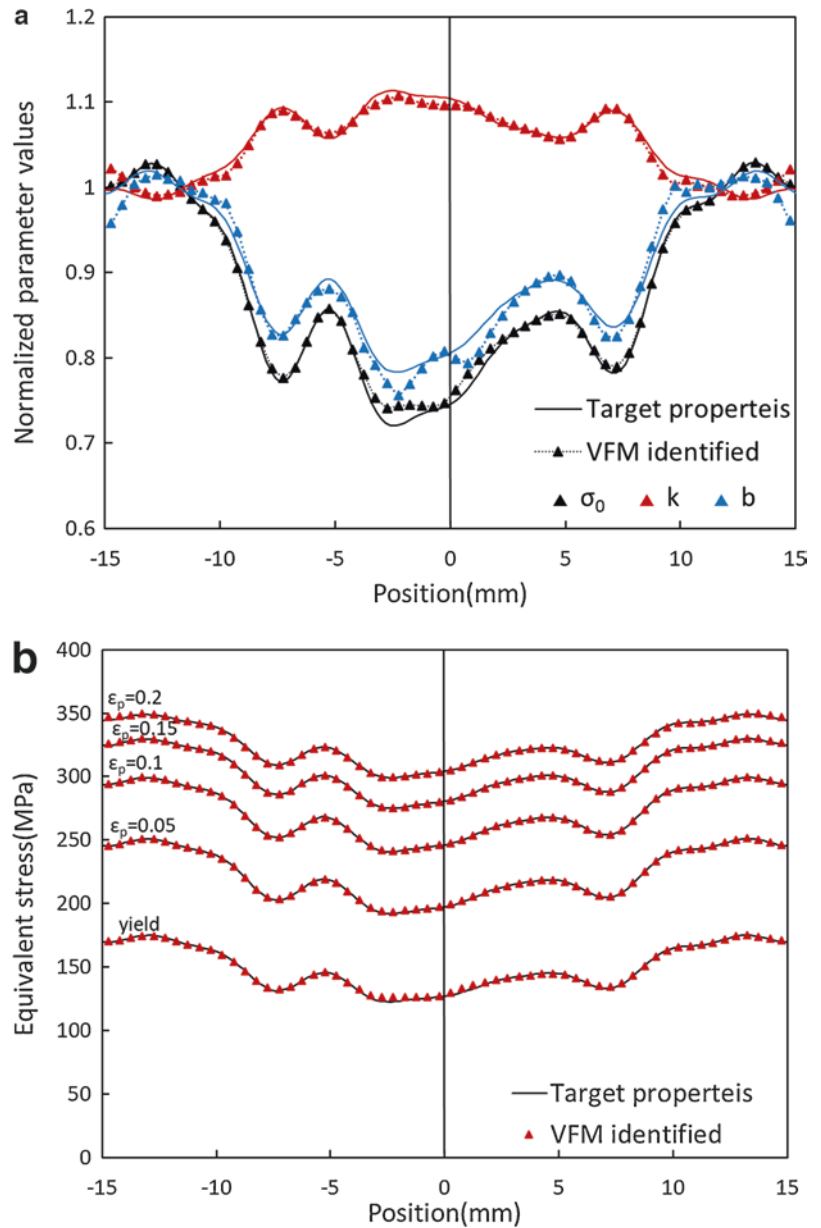


**Fig. 24.3** VFM identification results (a) distribution of material parameters, and (b) distribution of equivalent stress



## Conclusion

The feasibility study for identifying plastic properties of FSWed aluminum alloy sheet joint using the virtual fields method (VFM) is presented. The proposed method consists of two-step procedure: as a first step the location of boundaries between base and weld zones is searched, and the subsequent identification of inhomogeneous mechanical properties is followed through the discretized VFM approach. The identified plastic properties including the yield stress and plastic hardening using the proposed procedure show good agreement with target input values, which confirms the feasibility of the VFM approach for extracting mechanical properties of welded joints.

**Acknowledgments** This research is supported by a grant funded from National Research Foundation of Korea (NRF- 2017R1A2A2A05069619).

## References

1. C. Kwansoo et al., Macro-performance evaluation of friction stir welded automotive tailor-welded blank sheets: part I—material properties. *Int. J. Solids Struct.* **47**(7-8), 1048–1062 (2010)
2. M. Grediac et al., The virtual fields method for extracting constitutive parameters from full-field measurements: a review. *Strain* **42**(4), 233–253 (2006)
3. J.-H. Kim et al., Characterization of the post-necking strain hardening behavior using the virtual fields method. *Int. J. Solids Struct.* **50**(24), 3829–3842 (2013)
4. S. Avril, P. Badel, A. Duprey, Anisotropic and hyperelastic identification of in vitro human arteries from full-field optical measurements. *J. Biomech.* **43**(15), 2978–2985 (2010)
5. M.A. Sutton et al., Determination of elastic-plastic stresses and strains from measured surface strain data. *Exp. Mech.* **36**(2), 99–112 (1996)





## Chapter 25

# Accuracy Improvement of Thermoelastic Stress and Dissipation Energy Measurement by Motion Compensation with Optical-Infrared Synchronous Measurement

Yuji Uchid, Daiki Shiozawa, Mitsuhiro Hori, Kazuki Kobayashi, and Takahide Sakagami

**Abstract** On the infrared thermography image, an apparent temperature change caused by the relative displacement between moving object and infrared camera is obtained. This paper shows the motion compensation system with the optical-infrared synchronous measurement. Displacement information of the specimen is calculated from the series of optical image using the digital image correlation method. The displacement information on the optical image is reflected to the infrared image by the homography conversion. For obtaining the displacement information by digital image correlation method, random pattern on the surface of measured object is required. In this study, white random pattern was drowned by the sputtering painting method. The motion compensation system was applied to the thermoelastic stress analysis and dissipated energy measurement. It was confirmed that the apparent temperature change and edge effect can be removed by using developed motion compensation system.

**Keywords** Thermoelastic stress analysis · Dissipated energy measurement · Digital image correlation method

## Introduction

When cyclic loading is applied to the materials, temperature change caused by the thermoelastic effect was measured by infrared thermography. The measured temperature change makes it possible to analysis the magnitude and distribution of stress in non-contact condition [1]. In addition, the temperature change due to energy dissipation which caused by microplastic deformation can be measured [2]. The fatigue limit rapidly estimation based on the measurement of energy dissipation has been studied by a lot of researcher [3–8]. When the loading is applied to the materials, an interested point in the measuring object moves in the view of infrared thermography by the rigid body movement and deformation of an object. This relative moving is measured as a fake and apparent temperature change. This apparent temperature change is a noise component in thermoelastic stress analysis or dissipated energy evaluation. In order to improve accuracy of thermoelastic stress analysis and dissipated energy measurement, the motion compensation system with the optical-infrared synchronous measurement was developed. This paper described the motion compensation system and the effect of this system on the thermoelastic stress analysis and energy dissipated measurement.

## Apparent Temperature Change

In the thermoelastic stress analysis, the change of the principal stress  $\Delta\sigma$  on the material can be determined from the temperature change  $\Delta T_E$  based on the thermoelastic effect as shown in the following equation.

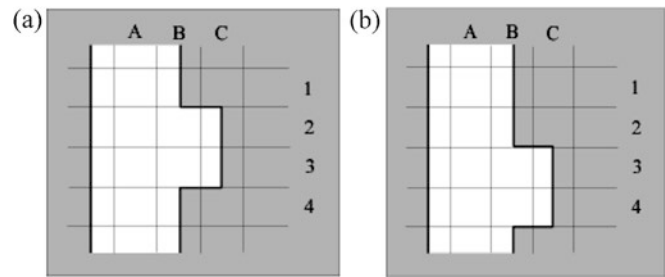
$$\Delta T_E = -kT\Delta\sigma \quad (25.1)$$

---

Y. Uchid (✉) · M. Hori · T. Sakagami  
Ergovision Corporation, Osaka, Japan  
e-mail: [yuj@ergovision.co.jp](mailto:yuj@ergovision.co.jp); [holy@ergovision.co.jp](mailto:holy@ergovision.co.jp); [sakagami@mech.kobe-u.ac.jp](mailto:sakagami@mech.kobe-u.ac.jp)

D. Shiozawa · K. Kobayashi  
Department of Mechanical Engineering, Kobe University, Kobe, Japan  
e-mail: [shiozawa@mech.kobe-u.ac.jp](mailto:shiozawa@mech.kobe-u.ac.jp); [181t332t@stu.kobe-u.ac.jp](mailto:181t332t@stu.kobe-u.ac.jp)

**Fig. 25.1** Difference of the measurement locations caused by the displacement



$T$  and  $k$  indicates the absolute temperature of the materials and thermoelastic coefficient, respectively. The temperature rise due to irreversible energy dissipation  $\Delta T_D$  occurs at the maximum tensile stress and at the maximum compressive stress. Thus, the measured temperature change  $T(t)$  on the surface includes  $\Delta T_E$  and  $\Delta T_D$ . Therefore, temperature change due to dissipated energy  $\Delta T_D$  can be obtained as the component having double frequency of the load signal using basically Fourier analysis [3, 8].  $\Delta T_D$  is related to the fatigue damage, so that the fatigue limit of the materials can be estimated by the rapid estimation method based on the dissipated energy measurement.

Since rigid body movement and deformation due to the applied force are occurring in the material, an interested point of measuring object moves in the field of view as shown in Fig. 25.1. The pixel (B, 2) of infrared thermography in Fig. 25.1a obtained the temperature at the edge of material. By rigid body movement and deformation of material due to applied force, the pixel (B, 2) measured the background radiation as shown in Fig. 25.1b. The temperature change at pixel (B, 2) in Fig. 25.1 is an apparent temperature change, which called as edge effect. The observation point located at the pixel (A, 1) in Fig. 25.1a moves to the pixel (A, 2) in Fig. 25.1b, so that the pixel (A, 1) doesn't measure the accuracy temperature change at the observation point. The time-series data obtained at the pixel (A, 1) is apparent temperature change and it indicates the difference in emissivity of the measuring object.

## The Motion Compensation System with the Optical-Infrared Synchronous Measurement

Various position correction methods have been proposed to remove apparent temperature change. Sakagami et al. [9] have proposed a method of position correction by DIC(digital image correlation) using feature pattern in infrared images. Chen et al. [10] and Wang [11] developed a method of position correlation using images captured by optical camera and infrared thermography respectively. In this study, the motion compensation system with the optical-infrared synchronous measurement was developed. Developed system consists of recording system and image processing software. A schematic illustration of the recording system is shown in Fig. 25.2.

In the developed recording system, the infrared thermography and the visible-light video camera are driven by the shutter pulse supplied from the synchronized shutter pulse generator, so that synchronous imaging becomes possible. Two personal computers were prepared for data recording and system control, and they were connected to each of the two video cameras. These PCs are connected via a network, and each software in PC works in conjunction. Table 25.1 shows the specifications of employed infrared thermography and visible-light video camera.

Synchronized shutter pulse generator has following functions in addition to supplying shutter pulse to the two video cameras. The microcomputer in the shutter pulse generator analyzes the frequency and phase of the input loading waveform and creates a correspondence table between the load signal phase of the fatigue testing controller and the shutter pulse number. The loading signal waveform and the correspondence table are sent to visible light recording and PC for controlling system. With the synchronous shooting function and this correspondence table, it is possible to provide synchronized visible and infrared thermographic images and the phase of the load waveform for subsequent image processing software.

Our goal is to correct the infrared thermography of the deforming specimen to image before deformation. This correction becomes possible by detecting the movement vector of each pixel (optical flow vector) of the reference and observation image using DIC. However, it is difficult to detect optical flow vector in infrared image with high accuracy, because the spatial resolution of infrared thermography is low and there is no fine feature pattern in infrared image for DIC. Therefore, we used visible-light camera to obtain an optical flow vector for each pixel in infrared thermography. The feature pattern on test specimen was drawn with a paint not affecting infrared thermography, and it was taken with visible-light camera to acquire an optical flow vector. Figure 25.3 shows these processes.

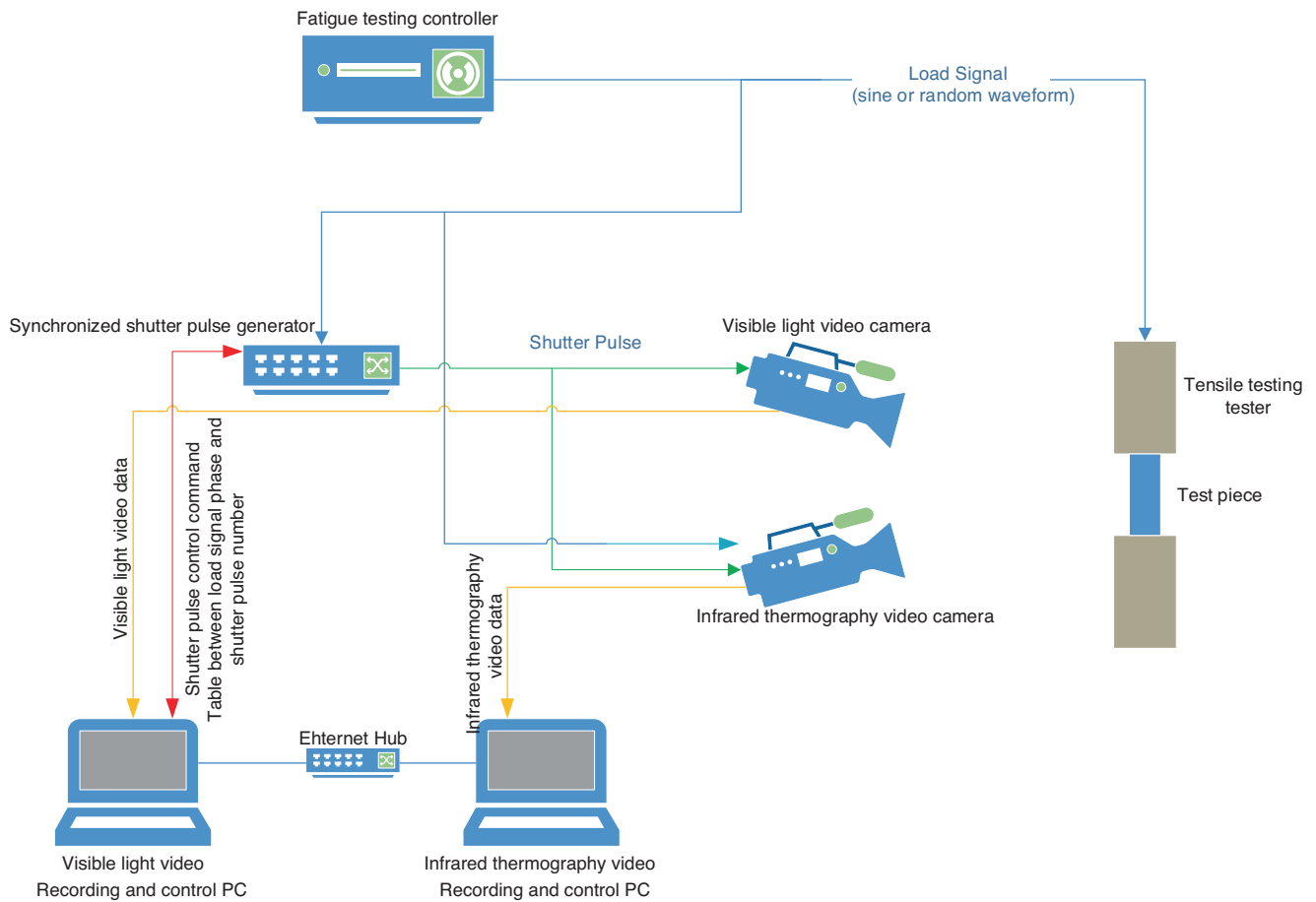


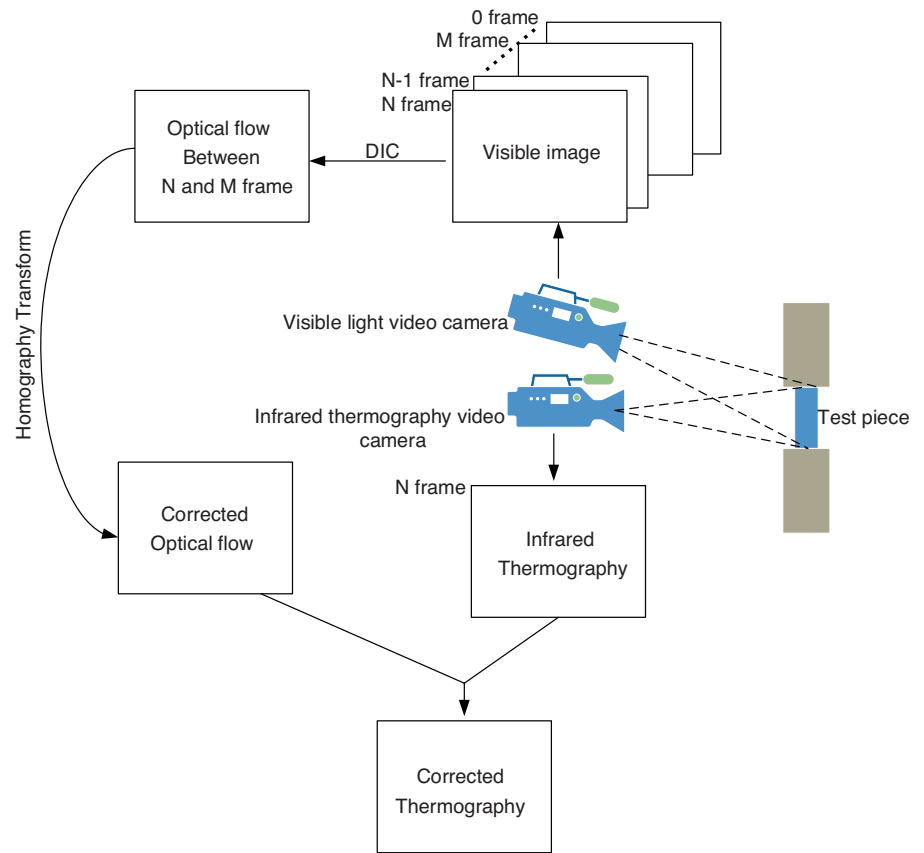
**Fig. 25.2** Schematic illustration of optical-infrared thermography synchronous measurement system

**Table 25.1** Specifications of employed infrared thermography and visible-light camera

	Infrared thermography camera	Visible-light camera
Manufacturer and model number	Fliar SC7500	DIRECT HAS U2
Image sensor	InSb	CMOS
Number of pixels	320 × 256	2592 × 2048 (max) 640 × 480
Maximum frame rate	350 Hz	1000 Hz (640 × 480)
Minimum exposure time	10 μs	10 μs
Temperature resolution	0.02 K	
Lense focal distance	100 mm	50 mm

$M$  frames of visible-light image taken synchronously with infrared thermography are used as reference frames. The optical flow vectors between arbitrary frame ( $N$ -th frame image) and reference  $M$  frames are calculated using DIC. The position correction in the thermography image are carried out based on the optical flow vectors obtained by visible-light image. In the previous study, the visible-light image and infrared image are taken respectively, by photographing difference faces [10] and shooting by switching cameras [11]. In this study, the visible-light image and infrared image are taken for same face in sync. There is a parallax difference between visible-light camera and infrared thermography camera, so that the optical flow vector obtained by optical image cannot be directly reflected to the thermography image. A homography transformation was introduced to solve these problems under the condition that the surface of the test piece was flat.

**Fig. 25.3** Position correction of infrared thermography with DIC



A homography transformation convert the optical flow vector in the visible-light image to the infrared image. The advantage of the homography transformation is that it is possible to obtain homography transformation matrix  $H$  from the captured image without knowing the position, posture, focal length, etc. of each camera. By acquiring four pairs of coordinates on the two images where the same point of the test piece, the homography transformation matrix  $H$  is calculated as in following equation,

$$H \begin{pmatrix} x \\ y \\ 1 \end{pmatrix} = \begin{pmatrix} sx' \\ sy' \\ s \end{pmatrix} \quad (25.2)$$

In Eq. (25.2),  $H$  denotes a homography transformation matrix,  $(x, y)$  denotes a coordinate on the image of the visible-light camera, and  $(x', y')$  denotes a coordinate on the image of the infrared thermography.

$H$  is obtained from the point pairs given in following way.

$$\begin{bmatrix} x & y & 1 & 0 & 0 & 0 & -xx' & -yx' \\ 0 & 0 & 0 & x & y & 1 & -xy' & -yy' \end{bmatrix} \begin{bmatrix} h_{11} \\ h_{12} \\ h_{13} \\ h_{21} \\ h_{22} \\ h_{23} \\ h_{31} \\ h_{32} \end{bmatrix} = \begin{pmatrix} x' \\ y' \end{pmatrix} \quad (25.3)$$

**Fig. 25.4** Selecting four points pairs. (a) Visible image. (b) Infrared thermography

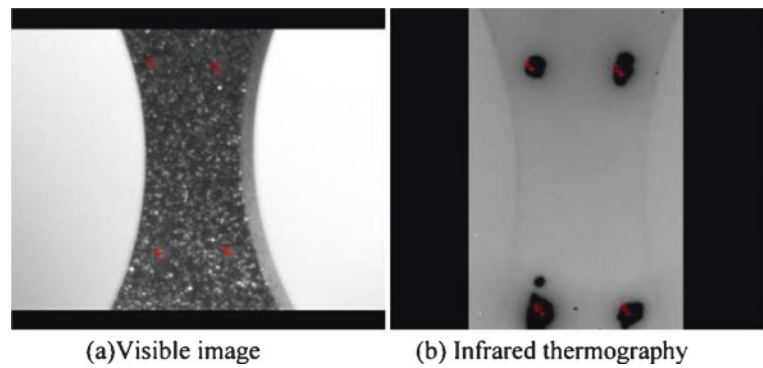
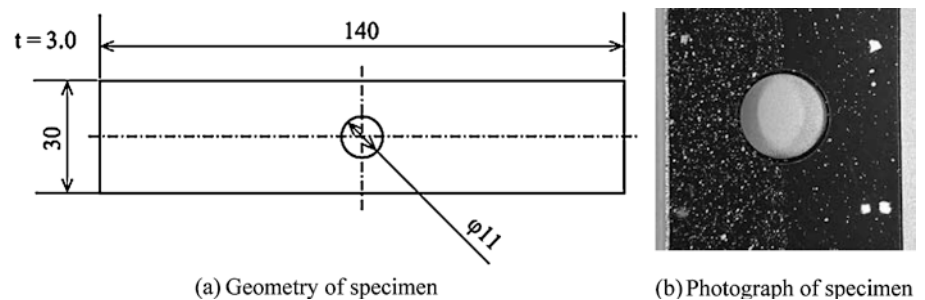


**Fig. 25.5** Geometry and photograph of specimen. (a) Geometry of specimen. (b) Photograph of specimen



Components  $h_{ij}$  is an element of a homography transformation matrix  $H$ . Since two equations are obtained for eight unknown parameters  $h_{ij}$ , if four or more pairs of  $(x, y)$  and  $(x', y')$  are obtained, Eq. (25.3) can be solved and a homography transformation matrix  $H$  is obtained. The visible-light image and infrared image are shown in Fig. 25.4.

Using the homography transformation matrix  $H$ , the optical flow vector of the visible-light image is converted into it viewed from the viewpoint of the infrared thermography camera. Then using this optical flow vector, we correct frame  $M$  of the infrared thermography to N-th frame.

## Experiments

The geometry of the test specimen (aluminum alloy A5052) used in the experiment is shown in Fig. 25.5. The loading condition was a sinusoidal stress waveform with stress ratio  $R = -1$  and loading frequency  $f = 5$  Hz, and the nominal stress amplitude was set to  $\sigma_a = 50$  MPa. As the measurement conditions, the frame rate of the visible-light camera and infrared thermography were set to 100 Hz and the photographing time was set to 10 s. Frequency analysis was performed on the measured The time-series data, and thermoelastic stress amplitude is obtained as the temperature change that is synchronized with the reference loading signal, and the double frequency component of the reference loading signal was taken as the dissipated energy. A visible-light image of the test specimen surface is shown in Fig. 25.5b.

The sum of principal stress distribution and the dissipated energy distribution are shown in Figs. 25.6 and 25.7, respectively. Displacement of about  $120 \mu\text{m}$  occurred in the lower part of the circular hole by DIC in visible-light image. From the sum of principal stress distribution in the case where the position correction is not applied, it was found that high stress appears in the edge portion of the lower portion of the circular hole. On the other hand, in the case where the position correction is applied, high stress due to the edge effect does not appear. Similarly in the dissipated energy distribution, high dissipated energy which seems to be an edge effect does not appear due to position correction. In the distribution of the dissipated energy, the dissipated energy in the vicinity of the circular hole is reduced by applying the position correction. It was considered that noise components of dissipated energy due to apparent temperature change can be removed.

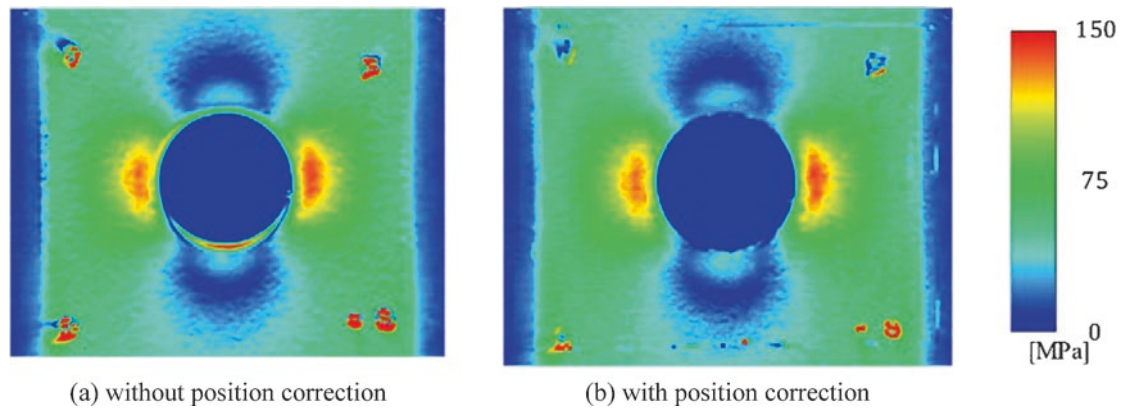


**Fig. 25.6** Distributions of measured stress amplitude ( $\sigma = 50$  MPa). (a) without position correction. (b) with position correction

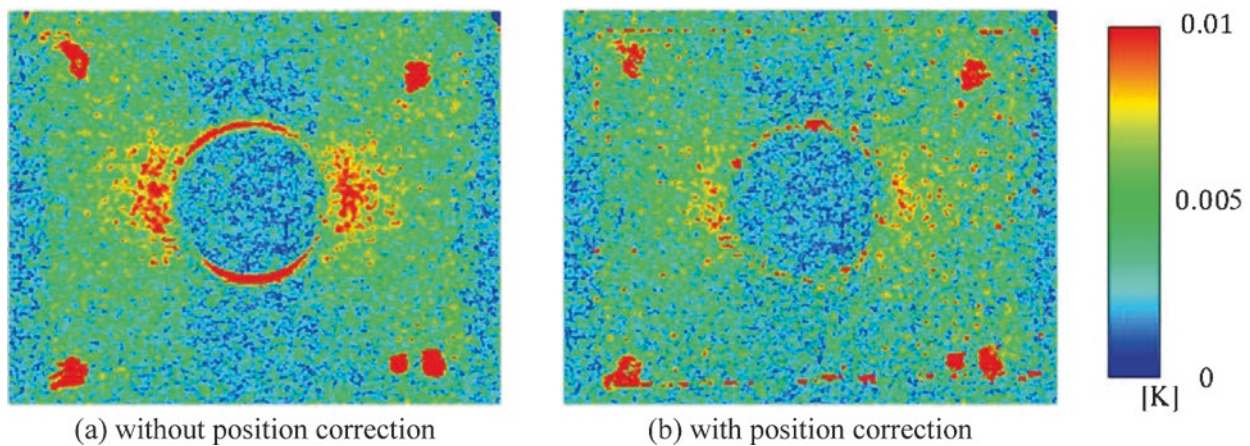


**Fig. 25.7** Distributions of dissipated energy ( $\sigma = 50$  MPa). (a) without position correction. (b) with position correction

## Conclusion

The motion compensation system with optical-infrared infrared synchronous measurement was developed. In this study, the visible-light image and infrared image are taken for same face in sync, and the optical flow vector obtained in visible-light image was reflected to the infrared image. There is a parallax difference between visible-light camera and infrared thermography camera, so that a homography transformation convert the optical flow vector in the visible-light image to the infrared image. As a result of measuring with developed system, it was found that it is possible to remove the edge effect and the apparent temperature change.

## References

1. T. Sakagami, Remote nondestructive evaluation technique using infrared thermography for fatigue cracks in steel bridges. *Fatigue Fract. Eng. Mater. Struct.* **38**, 755–779 (2015)
2. T. Sakagami, S. Kubo, E. Tamura, T. Nishimura, Identification of plastic-zone based on double frequency lock-in thermographic temperature measurement, in *Proceedings of ICF11* (2005)
3. P. Bremond, P. Potet, Lock-in thermography: a tool to analyze and locate thermomechanical mechanism in materials and structure. *Proc. SPIE* **4360**, 560–566 (2001)
4. M.P. Luong, Infrared thermographic scanning of fatigue in metals. *Nucl. Eng. Des.* **158**, 363–376 (1995)
5. G. La Rosa, A. Risitano, Thermographic methodology for rapid determination of the fatigue limit of materials and mechanical components. *Int. J. Fatigue* **22**(1), 65–73 (2000)

6. J.-C. Krapez, D. Pacou, Thermography detection of damage initiation during fatigue tests. *Proc. SPIE* **4710**, 435–449 (2002)
7. K. Hayabusa, K. Inaba, H. Ikeda, K. Kishimoto, Estimation of fatigue limits from temperature data measured by IR thermography. *Exp. Mech.* **57**(2), 185–194 (2017)
8. D. Shiozawa, T. Inagawa, T. Washio, T. Sakagami, Accuracy improvement in dissipated energy measurement by using phase information. *Meas. Sci. Technol.* **28**(4), 044004 (2017)
9. T. Sakagami, N. Yamaguchi, S. Kubo, T. Ninimura, A new full-field motion compensation technique for infrared stress measurement using digital image correlation. *J. Strain Anal. Eng. Des.* **43**, 539 (2008)
10. D. Chen, S. Sun, J.M. Dulieu-Barton, Q. Li, W. Wang, Crack growth analysis in welded and non-welded T-joints based on lock-in digital image correlation and thermoelastic stress analysis. *Int. J. Fatigue* **110**, 172–185 (2018)
11. W. Wang, R.K. Fruehmann, J.M. Dulieu-Barton, Application of digital image correlation to address complex motions in thermoelastic stress analysis. *Strain* **51**, 405–418 (2015)